Espen Tjønneland Wefring

Lead-Free Ferroelectric Materials based on $BiFeO_3$ and $Bi_{0.5}K_{0.5}TiO_3$

Thesis for the degree of Philosophiae Doctor

Trondheim, June 2015

Norwegian University of Science and Technology
Faculty of Natural Sciences and Technology
Department of Materials Science and Engineering

NTNU – Trondheim
Norwegian University of
Science and Technology

NTNU
Norwegian University of Science and Technology

Thesis for the degree of Philosophiae Doctor

Faculty of Natural Sciences and Technology
Department of Materials Science and Engineering

978-82-326-1016-7 (print)
978-82-326-1017-4 (digital)
1503-8181

Doctoral theses at NTNU, 2015:180

IMT-Report 2015:215

Printed by NTNU Grafisk senter

This thesis has been submitted to

Department of Materials Science and Engineering
Norwegian University of Science and Technology

in partial fulfilment of the requirements
for the academic degree

Philosophiae Doctor

April 2015

Acknowledgements

First of all I wish to express my gratitude towards my main supervisor Professor Tor Grande for excellent guidance through almost four years. I have enjoyed our collaboration and especially appreciate your endless optimism and enthusiasm. It is impossible to leave your office without a more optimistic view on the tasks ahead. This also applies to my co-supervisor Professor Mari-Ann Einarsrud, I am very grateful for the significant role you had during my first year and the insightful comments to all of my work. I am also thankful for the acceptance you both show for my desire to take on other responsibilities and duties in addition to my PhD-work.

Secondly, I want to thank Jr. Professor Dr. Kyle Grant Webber for accepting me as a guest at the Technische Universität Darmstadt and including me in the group. Your guidance during my stay was truly valuable. I also appreciate the significant assistance from Florian Schader and Dipl. Ing. Daniel Isaia with respect to the use of Little Chuck and any technical challenges I could come up with. A special thanks to Florian for showing me the outskirts of Darmstadt, I really enjoyed our trips! A general thank you is also extended to all members of the NAW-group for my warm welcome. I will forever regret the BBQ I was not able to host.

The years here in KII (and KI) would not have been the same without the Inorganic Materials and Ceramics Research Group. I have benefited a lot from the collective experience obtained in this group over the years by engineers, PhD-candidates, post-docs, professors and everyone else. The open doors and friendly people makes KII a great place to be. I especially want to acknowledge Dr. Maxim Morozov for sharing his extensive experience with ferroelectrics. I have enjoyed our discussions, both the scientific and the more political/philosophical ones. I also had the pleasure of co-supervising Eva Rise, Mads Christensen and Duy Che as master students. I have learned a lot from our collaboration and enjoyed working with you. My office mates through the last four years; Guttorm Ernst Syvertsen, Sophie Weber, Ahmet Tezel, Susanne Linn Skjærvø, Nikola Kanas and Xinzhi Chen, you have been great companions in the everyday life.

Our department football team PolyCrystal Palace also deserves to be mentioned. I truly appreciate playing with all of you despite my mediocre skills.

I also want to thank Mr. and Ms. Beer for founding the DoktorandØl and Maria Stepanova for organizing in Mr. Beers's absence. How else would I have learned about cricket? To my friends, to Høiskolens Chemikerforening and to TapHel&Toddy, thank you for making these soon to be nine years in Trondheim worth it.

To my dear family; Thank you mum and dad for showing me the possibilities but never pushing. Thanks to Ola and Marte for maintaining the farm so that I always have a recreational place to disconnect and re-charge. Thanks to Gry and Åsmund for always having a bed available whenever it is needed. Thanks to farmor, farfar and Beste for always being interested in what I do and how I'm doing and thanks to Kaja for calling me just to talk.

And finally Helene, thank you for getting me home and for reminding me of the life outside the office. Thank you for understanding when I'm exhausted and for brightening the day whenever it is needed! Thank you for the love and care in the time passed and years to come :)

Preface

The work in this thesis was carried out from September 2011 until April 2015, including 6 months teaching responsibilities, one month service as faculty board member, one month as a stand-in XRD staff engineer and 2.5 months of unpaid leave for farming. The main supervisor was Professor Tor Grande with Professor Mari-Ann Einarsrud as co-supervisor at the Department of Materials Science and Engineering, Norwegian University of Science and Technology (NTNU). All experimental work was performed at NTNU except the mechanical stress-strain measurements, which were performed at Technische Universität Darmstadt in Germany.

The work was funded by The Research Council of Norway as part of the project ”Lead-free ferro- and piezoelectric $K_{0.5}Na_{0.5}NbO_3$” (grant number 197497/F20).

The author has performed all the experimental work with three exceptions; High temperature X-ray diffraction data were collected with assistance from Dr. Julian Tolchard (NTNU), TEM sample preparation and characterization were performed by Dr. Per Erik Vullum (SINTEF Materials and Chemistry) and parts of the sample preparation for mechanical characterization which was performed by Michael Heyse (Technische Universität Darmstadt)

Parts of this thesis have been published (included in Appendix A). The author prepared the manuscripts and performed all experiments included in the papers.

Paper I:
Wefring ET, Morozov MI, Einarsrud M-A and Grande T, ”Solid-state synthesis and properties of relaxor (1-x)BKT-xBNZ ceramics,” *J. Am. Ceram. Soc.*, **97**, 2928-2935 (2014)

Paper II:
Wefring ET, Einarsrud M-A and Grande T, ”Electrical conductivity and thermopower of (1-x)$BiFeO_3$ - x$Bi_{0.5}K_{0.5}TiO_3$ (x = 0.1, 0.2) ceramics near the ferroelectric to paraelectric phase transition,” *Phys. Chem. Chem. Phys*, **17**, 9420-9428 (2015)

Trondheim, April 7th 2015
Espen Tjønneland Wefring

Summary

Piezoelectric materials are widely used in high-tech specialized instruments and consumer electronics today, and the most common piezoelectric material is lead-based $Pb(Zr_{1-x}Ti_x)O_3$. Concerns regarding the harmful effects of lead on human health and the environment have promoted the development of lead-free piezoceramics. Several lead-free piezoelectric materials have been investigated intensively in recent years, but the properties are still inferior to those of the lead-based piezoelectric materials.

This thesis is comprised of two parts where the first part aimed at investigating the possible presence of a morphotropic phase boundary (MPB) in the (1-x)$Bi_{0.5}K_{0.5}TiO_3$ - x$Bi_{0.5}Na_{0.5}ZrO_3$ (BKT-BNZ) system where improved piezoelectric performance was expected. Dense and phase pure materials along the (1-x)BKT - xBNZ composition join were synthesized by a conventional solid state method. The crystal structure, determined by X-ray diffraction (XRD), changed from tetragonal ($x \leq 0.15$) to orthorhombic ($x > 0.8$) with a pseudo-cubic structure for intermediate compositions. The dielectric performance ($x \leq 0.50$) was investigated as a function of frequency ($1\text{-}10^6$ Hz) and temperature (up to 600 °C). All the investigated BKT-BNZ materials displayed a relaxor-like behavior where the dispersion of the permittivity maximum increased with increasing BNZ-content. The highest dielectric constant was observed for $x = 0.15$. The electromechanical properties were also characterized ($x \leq 0.50$) and the highest electric field induced strain and polarization were observed for $x = 0.10$. The electromechanical response was increasingly electrostrictive with increasing BNZ-content. The composition region with the best dielectric and piezoelectric performance coincides well with the change from tetragonal to pseudo-cubic crystal structure.

The second and major part of the thesis was focused on the electrical conductivity and point defect chemistry of $BiFeO_3$ (BFO) based materials. BFO is a promising lead-free piezoelectric material with an intrinsic high polarization and strain, but practical application is hindered by a high coercive electric field and a high leakage current. BKT-substituted BFO was chosen as a model system, following reports that the formation of parasitic secondary phases, typically found in pure BFO, was suppressed by BKT-substitution. Dense and phase pure BFO-BKT ceramics (10 and 20 mol% BKT) were

prepared by solid state synthesis along with ceramics where Ti^{4+} and Fe^{3+} were used as donor and acceptor substituents, respectively. The materials were isostructural to BFO (rhombohedral R3c) with a decreasing lattice distortion with increasing BKT content and Ti-donor substitution. High temperature X-ray diffraction revealed that the lattice distortion of 80 and 90 mol% BFO was retained up to 550-600 °C. The ferroelectric to paraelectric phase transition temperature (T_C), determined by a combination of high temperature XRD, thermal analysis and dielectric spectroscopy, decreased with BKT-substitution but remained relatively high. Smaller variations of the phase transition temperature were observed with donor/acceptor substitution. The retention of the high phase transition temperature and lattice distortion is important for the high temperature applicability of BFO and BFO-based materials.

The isothermal DC electrical conductivity of BFO-BKT (10 and 20 mol% BKT) was measured as a function of temperature and partial pressure of oxygen (P_{O_2}). A minimum in the conductivity was observed when gradually changing from oxidizing to inert atmosphere. This behavior is typical for the change from p-type to n-type semiconductor. The change of the main charge carrier was confirmed by a positive and negative Seebeck coefficient in oxidizing and inert atmosphere, respectively. This is the first direct evidence of n-type conductivity in bulk BFO-based materials. The isothermal conductivity was successfully described by a simple point defect model by considering relevant point defect equilibria with electrons (Fe^{2+}) and electron-holes (Fe^{4+}) as the major charge carriers. The model also included oxygen and cation vacancies. Furthermore, the electrical conductivity was reduced/increased by donor/acceptor substitution in line with the point defect model. The point defect model provides a physical understanding of electrical conductivity of BFO-based materials including pure BFO.

The high coercive electric field of BFO has been related to a hard ferroelectric behavior. The ferroelastic properties of non-substituted and donor substituted BFO-BKT materials were investigated up to 400 °C to elucidate the corresponding ferroelastic properties of BFO-based materials. Aging was confirmed by varying the thermal history of the materials, and it was substantiated that the aging is related to oxygen vacancies. The coercive stress was > 700 MPa at room temperature and increased with donor substitution. The materials became ferroelastically softer with increasing temperature which decreased the coercive stress and increased the remanent strain. Finally, it was shown that the ferroelastic properties could be manipulated

by annealing in varying P_{O_2} and subsequently quenching from above T_C.

Investigation of the microstructure of selected materials by transmission electron microscopy revealed a complex domain structure and that the grains of BFO - BKT (20 mol% BKT) were not chemically homogeneous. A final study of a third composition series with 30 mol% BKT using substantially longer sintering times to improve the chemical homogeneity was performed. The Fe:Ti- and A:B-ratio in the material (30 mol% BKT) was also varied. The conductivity was reduced by donor substitution, in line with earlier results. Surprisingly, addition of excess A-cations increased the conductivity and is probably related to a slight A-excess in the as-synthesized materials. The grain size increased and the chemical homogeneity was significantly improved with increasing sintering time. The longer sintering time also resulted in a nearly cubic crystal structure based on XRD along with a lower conductivity and a more temperature stable permittivity. The variation of Fe:Ti- or A:B-ratio resulted in systematic changes in the electrical conductivity, while no significant effect was observed with respect to chemical homogeneity, phase transition temperature and crystal structure.

The work presented herein provides an important insight to the point defect chemistry of BFO and BFO-based materials. The work demonstrates the importance of considering both thermal and atmospheric history of the materials in relation to the point defect chemistry and functional properties.

Contents

Abbreviations and symbols

0._BNZ=xBNZ	(1-x)BKT - xBNZ
0.7BFTyez	$(Bi_{0.85}K_{0.15})_{1+z}(Fe_{0.7-y}Ti_{0.30+y})O_3$
0.8BFTy	$Bi_{0.90}K_{0.10}Fe_{0.8-y}Ti_{0.2+y}O_3$
0.9BFTy	$Bi_{0.95}K_{0.05}Fe_{0.9-y}Ti_{0.1+y}O_3$
a	Lattice parameter
AC	Alternating current
b	Lattice parameter
BFO	$BiFeO_3$
BKT	$Bi_{0.5}K_{0.5}TiO_3$
BKZ	$Bi_{0.5}K_{0.5}ZrO_3$
BNT	$Bi_{0.5}Na_{0.5}TiO_3$
BNZ	$Bi_{0.5}Na_{0.5}ZrO_3$
BS	$BiScO_3$
BT	$BaTiO_3$
c	Lattice parameter
$\mathbf{C}_i$	Concentration of charge carriers
d	Piezoelectric coefficient, small signal
d*	Piezoelectric coefficient, large signal
DC	Direct current
DTA	Differential thermal analysis
e	Electrons
E	Electric field
$\mathbf{E}_C$	Coercive electric field
EDS	Energy dispersive X-ray spectroscopy
EELS	Electron energy loss spectroscopy
FWHM	Full-width-half-maximum
h	Electron-holes
HTXRD	High temperature XRD
KNN	$K_{0.5}Na_{0.5}NbO_3$
LF	$LaFeO_{3-\Delta}$
LSF	$La_{0.75}Sr_{0.25}FeO_{3-\Delta}$
MPB	Morphotropic phase boundary
n	Concentration of Fe^{2+}
p	Concentration of Fe^{4+}
P	Polarization

$\mathbf{P}_D$	Polarization defect dipoles
PNR	Polar nanoregion
$\mathbf{P}_{O_2}$	Partial pressure of oxygen
PPT	Polymorphic phase boundary
$\mathbf{P}_S$	Spontaneous polarization
PT	$PbTiO_3$
PZT	$Pb(Zr_{1-x}Ti_x)O_3$
$\mathbf{q}$	Electrical charge
$\mathbf{S}$	Seebeck coefficient
S1-S6	Sintering procedure, see Table 3.3
SAED	Selected area electron diffraction
SEM	Scanning electron microscopy
STEM	Scanning TEM
$\mathbf{t}$	Goldschmidt tolerance factor
$\mathbf{tan}\ \delta$	Dielectric loss
$\mathbf{T}_C$	Curie temperature
$\mathbf{T}_d$	Depolarization temperature
TEM	Transmission electron microscopy
$\mathbf{T}_m$	Temperature of permittivity maximum
$\mathbf{V}_O^{\cdot\cdot}$	Oxygen vacancy
XRD	X-ray diffraction
$\boldsymbol{\Delta_r H}$	Enthalpy of reaction
$\boldsymbol{\epsilon}$	Strain
$\boldsymbol{\epsilon_{(b/u)max}}$	Maximum E-induced strain (bipolar/unipolar)
$\boldsymbol{\epsilon_r}$	Remanent strain
$\boldsymbol{\epsilon^r_{sw}}$	Maximum switching strain, rhombohedral
$\boldsymbol{\varepsilon'}$	Real relative dielectric permittivity
$\boldsymbol{\varepsilon'_{max}}$	Maximum real relative dielectric permittivity
$\boldsymbol{\varepsilon'_{RT}}$	Room temperature real relative dielectric permittivity
$\boldsymbol{\mu_i}$	Mobility charge carrier, (e)lectrons/electron-(h)oles
$\boldsymbol{\sigma}$	Mechanical stress
$\boldsymbol{\sigma_c}$	Coercive mechanical stress
$\boldsymbol{\sigma_{max}}$	Maximum applied mechanical stress
$\boldsymbol{\sigma'_{AC}}$	Real alternating current electrical conductivity
$\boldsymbol{\sigma_{DC}}$	Direct current electrical conductivity
$\boldsymbol{\sigma_{e/h}}$	Electrical conductivity of electrons/electron-holes
$\boldsymbol{\sigma_{min}}$	Isothermal minimum in DC electrical conductivity
$\boldsymbol{\sigma_{tot}}$	Total electrical conductivity of a semiconductor
$\boldsymbol{\chi}$	Dielectric susceptibility

Chapter 1

Background

The direct piezoelectric effect (conversion of mechanical energy to electrical energy) was discovered as early as 1880, closely followed by the discovery of the converse piezoelectric effect (conversion of electrical energy to mechanical energy). Any material that is exposed to mechanical stress (compressive or tensile) will develop strain but piezoelectrics will develop a charge in addition to strain through the direct piezoelectric effect. The converse piezoelectric effect allows for the generation of strain through application of an electric field (Figure 1.1). Ferroelectricity, where a spontaneous polarization could be reoriented by an electric field, was later discovered in Rochelle salt.[1]

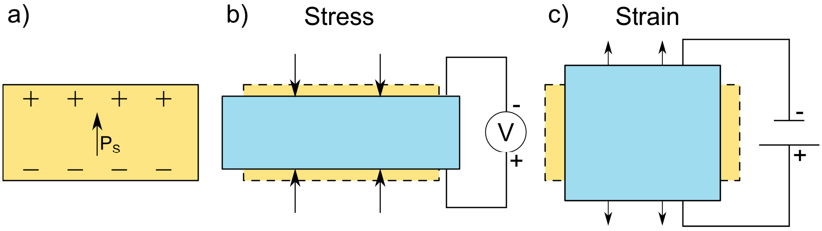

Figure 1.1: Schematic view of the piezoelectric effect. The initial state of a poled ceramic (a), the direct effect where charge is generated by application of mechanical stress (b) and the converse effect where strain is generated by an applied electric voltage (c). Figure adapted from Haugen.[2]

Although discovered in 1880, the technological development of piezoelectrics did not commence until the 1940s with the discovery of high dielectric constant $BaTiO_3$ and the poling process for ceramics.[3] Common for all applications is the utilization of the link between electrical and mechanical energy, provided by the direct and converse piezoelectric effects. Piezoelectric materials are utilized in many modern technological applications such as capacitors, transducers, radio and communication filters, gas ignitors, sensors and ultrasonic motors.[3] Piezoelectrics are found in both high tech specialized instruments (e.g. atomic resolution transmission electron microscopes) and consumer electronics such as cell phones, computers and inkjet printers.[4,5] Piezoelectric devices installed in vibrating environments such as floors, shoes (Figure 1.2), cars, roads and so on may also function as energy harvesters by scavenging the otherwise wasted vibrational energy.[6] The global market for piezoelectric actuators alone was US\$$\sim$6.5 billion in 2009.[7] For piezoelectrics in total the market has been estimated to US\$21 billion in 2012 and a near doubling is expected in 2017.[5]

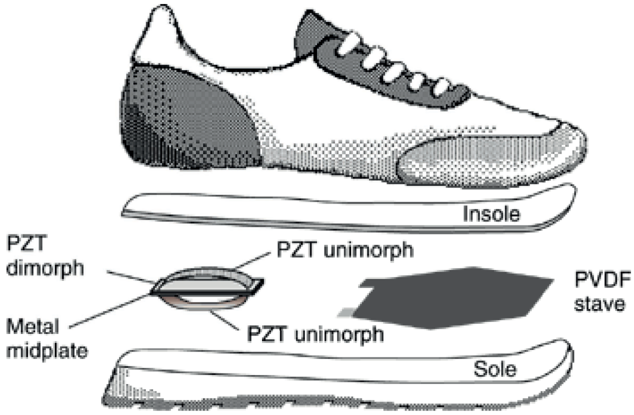

Figure 1.2: Piezoelectric device for energy harvesting from a shoe.[8]

Lead zirconate titanate ($Pb(Zr_{1-x}Ti_x)O_3$, PZT) is the most commonly used piezoelectric today where the Zr:Ti ratio is normally near the morphotropic phase boundary (MPB) of $x \approx 0.48$, separating the tetragonal and rhombohedral structure as shown in Figure 1.3.[1,7] The MPB of PZT follows an almost vertical line in the phase diagram up to the Curie temperature (T_C) where the structure becomes cubic and the piezoelectric properties vanish. PZT is very versatile as the properties can be tuned by compositional variations and iso- or aliovalent doping or substitution.[1,3,9] Another interesting feature of PZT is the 6s electron lone pair of Pb^{2+} which is shown to stabilize a covalent bond between Pb and O in $PbTiO_3$ and enhance the lattice distortion.[10,11]

There are concerns regarding the harmful effects of lead on humans and the surrounding environment, both with respect to production of lead containing components and the increasing amount of electronic waste from consumer electronics where piezoelectric components are used.[13–15] Restrictions on the use of lead in electronics were approved by the European Union in 2002 with the "Directive on the restriction of the use of certain hazardous substances in electrical and electronic equipment" and the "Waste electrical and electronic equipment directive", also revised in 2011 and 2012, respectively.[16–19] Other countries have adopted similar regulations.[13,15] In these regulations, the use of lead containing piezoelectrics is not limited as there are at present no satisfactory lead-free alternatives to replace PZT. The use of PZT will

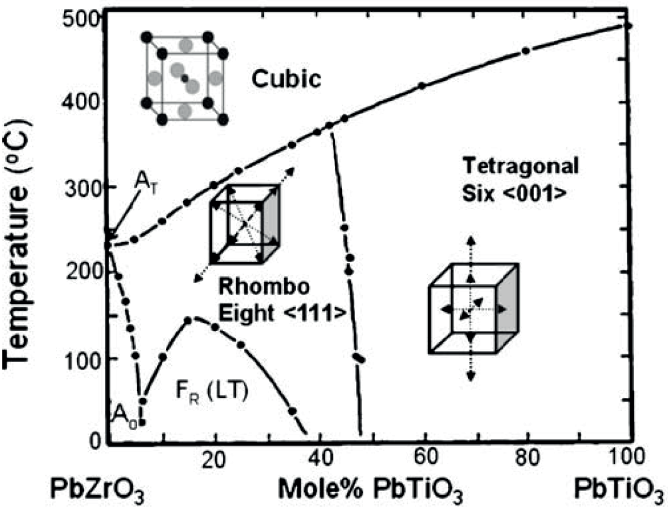

Figure 1.3: Phase diagram of PZT showing the MPB composition at ∼48 mol% $PbTiO_3$ and the ferro- to paraelectric Curie temperature.[12]

though be restricted once viable lead-free alternatives are developed. Another limitation of PZT is the relatively low T_C (≈386 °C) near the MPB.[1] Above this temperature the piezoelectric properties disappear, limiting the high temperature applicability of PZT.

The pending ban on the use of PZT has spiked the interest for development of lead-free piezoelectrics.[12,13,20–28] Rödel *et al.*[13] have summarized a set of considerations that should be taken into account when investigating new, or improving already established, lead-free piezoelectrics including toxicity and cost of elements (Figure 1.4), crystal structure and electronic structure. The vast majority of the lead-free materials investigated today are perovskites based on $Bi_{0.5}K_{0.5}TiO_3$ (BKT), $Bi_{0.5}Na_{0.5}TiO_3$ (BNT), $BiFeO_3$ (BFO), $BaTiO_3$ (BT) and/or $K_{0.5}Na_{0.5}NbO_3$ (KNN). The crystal structures of these perovskite materials are tetragonal (BKT, BT), rhombohedral (BNT, BFO) and orthorhombic (KNN) which presents a number possible binary and ternary combinations. In addition, the perovskite structure itself allows for many different dopants or substituents to be introduced into the material.[13] Rhombohedral-tetragonal MPBs (analogous to the MPB of PZT) have been identified for the solid solutions of e.g. BNT-BT and BNT-BKT.[29,30] The electronic structure of Pb^{2+} and Bi^{3+} shows important similarities in that they both possess a 6s electron lone pair. This lone pair has been related the stability of PZT, naturally making investigation of Bi-based

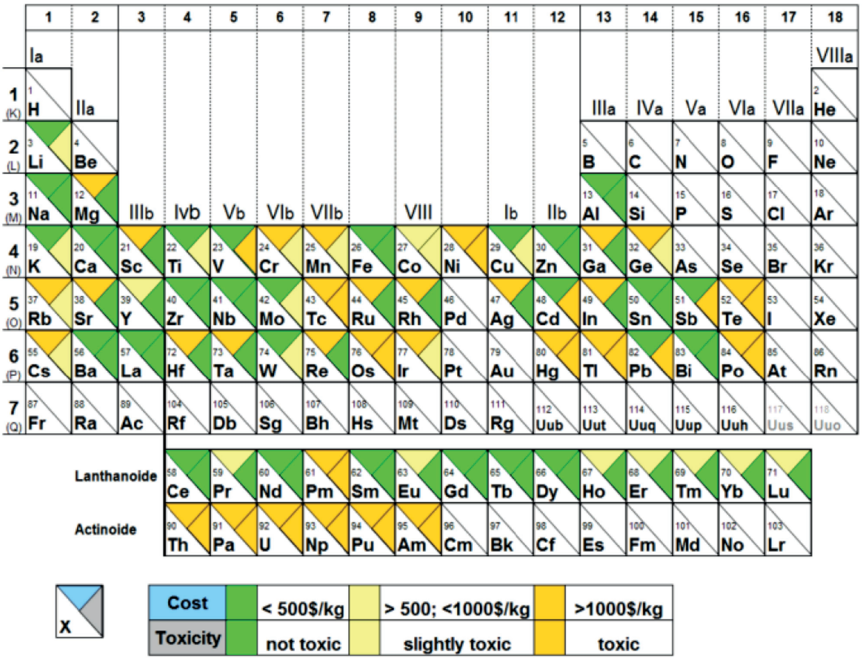

Figure 1.4: Toxicity and cost of elements interesting for lead-free piezoelectrics.[13]

piezoelectrics interesting.[10,11,13] The large rhombohedral distortion and ionic displacements in BFO, resulting in potentially very large polarization, is stabilized by the lone pair making BFO a very interesting end-member for piezoelectric solid solutions with a possible MPB.[28,31,32]

The first material system investigated in this thesis was BKT - $Bi_{0.5}Na_{0.5}ZrO_3$ (BNZ) which is a ternary reciprocal system comprised of BKT (tetragonal ferroelectric),[33,34] BNT (rhombohedral relaxor ferroelectric),[35–37] BNZ (orthorhombic)[38] and $Bi_{0.5}K_{0.5}ZrO_3$ (BKZ, cubic).[39] An MPB has previously been observed along the BKT-BNT composition line and addition of Zr to BKT-BNT is reported to improve the properties near the MPB.[29,40] The different crystal structure of the end-members, the large difference in Goldschmidt tolerance factor (t) of e.g. BKT (t=0.99) and BNZ (t=0.89) and the presence of Bi are all important parameters that motivate a further study of the BKT-BNZ system, in light of the guidelines discussed by Rödel *et al.*[13]

The second system investigated in this thesis was the solid solution of rhombohedral BFO and tetragonal BKT. Pure BFO has a high T_C (825 °C), a high polarization and high strain,[28,31,41–43] but application of BFO as a lead-free piezoelectric has been hampered by high electrical conductivity, high coercive electric fields and challenges related to parasitic phases.[28,41,44,45] Extensive in-house experience was available with respect to bulk BFO,[45–48] and initial studies of the BFO-BKT system were promising.[49,50] An MPB was anticipated based on the crystal symmetry of the two end-members and a composition region of maximum electromechanical performance had been found.[50] The thesis work was motivated by several studies which indicate that the electrical conductivity and coercive electric field are related to point defects,[41,51,52] but a comprehensive understanding of the point defect chemistry of BFO was still lacking. The solid solution of BFO-BKT was chosen as a model system because it allows the use of conventional synthesis methods while retaining the rhombohedral symmetry of BFO and avoiding parasitic phases commonly observed in BFO.[45,50]

The work described in this thesis is part of the LEAD-FREE project funded by The Research Council of Norway (FRINATEK grant no. 197497/F20). The overall goal of the project is to develop lead-free piezoelectrics that can replace PZT, taking advantage of amongst other the significant in-house knowledge on ceramics processing. One part of the project focused on synthesis and characterization of KNN thin films by an environmentally friendly aqueous precursor solution,[53] another part was focused on synthesis and characterization of textured lead-free ceramics[2] and a third part was focused on synthesis and characterization of Bi-based lead-free piezoelectrics.

Aim of Work

This thesis is comprised of two parts where the first part is the synthesis and characterization of materials in the system (1-x)BKT - xBNZ (Chapter 4). The aim of this study was to investigate the possible existence of an MPB along the binary composition join between tetragonal BKT and orthorhombic BNZ. Moreover, the two end-members have respectively a high and low tolerance factor which further substantiates the presence of an MPB. The investigation encompassed characterization of the crystal structure, dielectric and electromechanical properties along the (1-x)BKT - xBNZ composition line. The investigation concluded that no signature of an MPB was observed and further work was therefore discontinued.

The attention was subsequently shifted to the (1-x)BFO - xBKT system, where considerable studies had already been carried out in the LEAD-FREE project. The investigation in this system was aimed at determining the major point defects in BFO-materials and how the point defect chemistry is related to the functional properties of the material. First, successful synthesis of dense BFO-ceramics with 10 and 20 mol% BKT by the solid state method was confirmed (Chapter 5). The effect of subsequent Ti-substitution on crystal structure, microstructure, phase purity and the ferroelectric to paraelectric phase transition temperature was investigated as these are important properties for the piezoelectric performance and high temperature applicability of the materials.

BFO with 10 and 20 mol% BKT was chosen as an appropriate model system to investigate the point defect chemistry of BFO-materials (Chapter 6). The aim was to determine the temperature and atmosphere dependence of the DC electrical conductivity and the Seebeck coefficient. The results were applied to outline a point defect model describing the electrical conductivity based on a mass action treatment of relevant point defect equilibria in the materials. The reported p-type conductivity of BFO-based materials suggests that the electrical conductivity may be reduced by donor substitution. The effect of donor substitution by Ti^{4+} on the temperature and atmosphere dependent electrical conductivity was therefore investigated to further elucidate the point defect chemistry and reduction of electrical conductivity upon donor substitution (Chapter 6).

The ferroelastic properties of BFO-BKT materials (10 and 20 mol% BKT) were investigated for the first time (Chapter 7). This part of the study aimed to elucidate whether BFO-materials possess hard ferroelastic behavior analogous to the hard ferroelectric behavior of BFO. It was also aimed at investigating the effect of thermal and atmospheric history on the ferroelastic properties, in light of the previously established point defect chemistry. Finally, the study intended to investigate if donor substitution of BFO-materials displays a similar ferroelastic softening effect as reported for PZT.

Transmission electron microscopy (TEM) was conducted in order to investigate the microstructure and domain structure in the materials (Chapter 8). The TEM investigation revealed a complex domain structure and inhomogeneous chemical composition of the grains.

Finally, based on the established point defect chemistry, a series of experiments were performed to elucidate the separate and combined effect of donor substitution by Ti^{4+} and varying the A:B-ratio. These materials were also sintered for longer times to investigate the effect of grain growth during sintering on the chemical homogeneity (Chapter 9).

Chapter 2

Introduction

2.1 Piezo- and Ferroelectricity

An ideal dielectric is a non-conducting electrostrictive material where polarization (P) and strain (ϵ) can be induced by an electric field (E). The induced polarization is proportional to the dielectric susceptibility (χ), Eq. 2.1.[54]

$$P = \chi E \tag{2.1}$$

The strain on the other hand is proportional to the square of the electric field or polarization as given in Eq. 2.2.[54,55]

$$\epsilon = mE^2 \quad / \quad \epsilon = QP^2 \tag{2.2}$$

Here, m and Q are electrostrictive coefficients. This results in a strain that is independent of the polarity of the electric field. Piezoelectric materials are dielectrics with additional symmetry restrictions such that polarization (or electrical displacement, D) can be induced by applying a mechanical stress (the direct effect, Eq. 2.3) and strain may be induced by applying an electric field (the converse effect, Eq. 2.4), as shown in Figure 1.1.[1,54,55]

$$D = \frac{q}{A} = d\sigma \tag{2.3}$$

$$\epsilon = dE \tag{2.4}$$

Here, q is charge, A is area, d is the piezoelectric coefficient expressed in pC/N or pm/V, respectively, and σ denotes mechanical stress. Both the polarization and strain developed by the piezoelectric effect are linearly dependent on the direction of stress and electric field, respectively. The parameters presented above are directional quantities such that d is often presented as d_{ij} where i (=1,2,3) denotes the direction of D or E (Cartesian reference frame) and j (=1,2..,6) denotes the direction of σ or ϵ where j=1,2,3 refer to stresses along the i-axis' and j=4,5,6 refer to shear stresses.[55]

The symmetry restrictions of piezoelectrics are such that out of the 32 crystallographic point groups there are 21 which are non-centrosymmetric. Out of these there are 20 point groups that allow piezoelectricity. 10 out of these 20 point groups are pyroelectric, meaning that each unit cell will develop a spontaneous polarization (P_S) when cooled below the paraelectric to pyro-/ferroelectric phase transition temperature, T_C. If the direction of P_S in a pyroelectric material can be permanently reoriented by an external force (electric field or mechanical stress) the material is ferroelectric. All ferroelectrics are pyroelectric and piezoelectric, but not all piezoelectrics and pyroelectrics are ferroelectric etc., as described in Figure 2.1.[1,3,54,55]

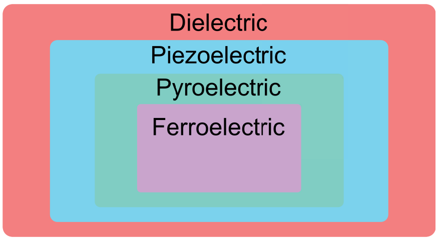

Figure 2.1: Hierarchy of dielectric, piezoelectric, pyroelectric and ferroelectric crystals.

2.1.1 Piezo- and Ferroelectric Ceramics

Four material classes make up the vast majority of the studied piezo- and ferroelectric ceramics; perovskites, bismuth layered structures, $LiNbO_3$ type ferroelectrics and tungsten bronzes.[13] The perovskite structure is the basis for the most industrially important materials such as PZT and BT,[1,3,56] and the most promising lead-free ferroelectrics.[13,15,28] The paraelectric cubic perovskite unit cell with the formula unit ABO_3 and the ferroelectric tetragonal polymorph are shown in Figure 2.2a and 2.2b, respectively. Perovskites are highly versatile in that they can accommodate a large variety of different cations of different size and charge, resulting in a wide range of different distortions of the ideal aristotype.[57]

The crystal structure of perovskites can to some extent be predicted using the Goldschmidt tolerance factor, given in Eq. 2.5.[58,59]

$$t = \frac{r_A + r_O}{\sqrt{2}(r_B + r_O)} \tag{2.5}$$

Here, r_A, r_B and r_O are the ionic radii of the A, B and oxygen ions for their respective coordination numbers. The ionic radii of the A and B cations are

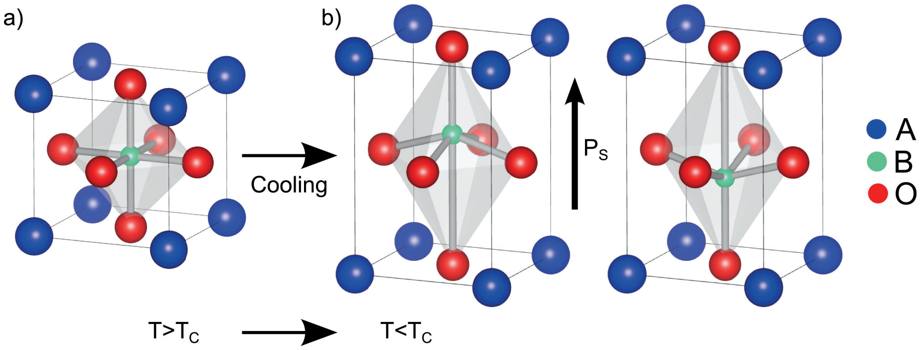

Figure 2.2: The cubic paraelectric perovskite unit cell (a) and a ferroelectric tetragonal polymorph where the B cation is displaced along the [001] axis (b). The direction of the spontaneous polarization, P_S, is shown by the thick black arrow, corresponding to the displacement of the B cation.

such that t = 1 for an ideal cubic perovskite while t typically ranges from 1.1 to 0.8.[59] If the size of the A-cation is too small, $t < 1$ which typically gives tetragonal, rhombohedral or orthorhombic symmetry depending on the size of the cations relative to the anions. An A cation that is too large will give $t > 1$ and tetragonal or hexagonal structure can be expected.[55,57,60] The adopted crystal structure is important for ferroelectrics as it, e.g., determines the number of allowed crystallographic directions of P_S; 6 for tetragonal (Figure 2.3a), 12 for orthorhombic (Figure 2.3b), 8 for rhombohedral (Figure 2.3c), 24 for monoclinic and 48 for triclinic crystals.[13] A link has also been suggested between the tolerance factor and T_C of ferroelectric materials for $PbTiO_3$-based (PT) materials and bismuth layered materials, where a lowered t results in a higher T_C.[61,62]

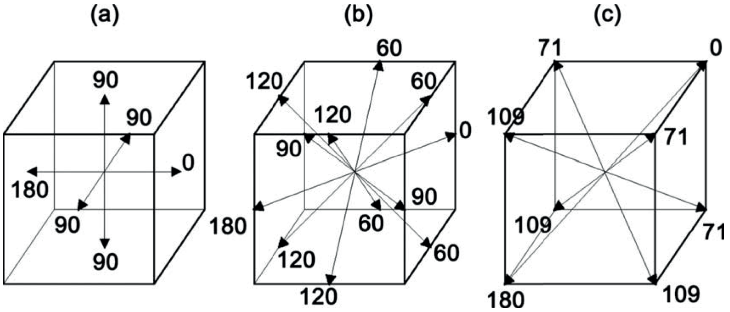

Figure 2.3: Direction of spontaneous polarization in tetragonal (a), orthorhombic (b) and rhombohedral (c) perovskites. Adapted from Marton *et al.*[63]

2.1.2 Morphotropic Phase Boundary

Enhanced piezoelectric performance is commonly observed near a phase transition in ferroelectrics, and two types of phase transitions are of particular interest; MPBs and polymorphic phase transitions (PPT). An MPB is an abrupt compositionally dependent and temperature independent phase transition between two phases in a solid solution, while a PPT is a temperature driven phase transition.[1,13,55] The qualitative origin of the enhanced performance is dielectric softening of the ferroelectric crystal which increases the dielectric susceptibility (polarizability). The increased polarizability occurs as the energy difference between the two phases at the transition composition/temperature is lowered and even small fields are able to reorient polarization, even that of a non-polar axis. While the origin of the effect is the same, MPB-ferroelectrics are often preferred in practical applications as they are not limited by a narrow temperature range.[13,64]

A well known MPB is the one that separates the rhombohedral and tetragonal polymorphs of PZT (Figure 1.3), where prominent properties are observed. Several mechanisms have been suggested as the source of the improved properties, including a mixture of several phases or a monoclinic phase in the transition region (increasing the number of allowed directions of P_S), a maximum in the dielectric constant ($\approx \chi$ in ferroelectrics,[54] allowing increased polarizability), and a maximum in mechanical compliance.[3,55,64] MPBs have also been identified in lead-free perovskites such as BKT-BNT,[29] BT-BNT,[30] BT-KNN[65] and BKT-KNN.[66] Figure 2.4a displays a peak for the dielectric constant at the MPB in the xBT - (1-x)BNT system, while a peak in the piezoelectric constant and coupling factor (k) at the MPB in the xBNT - (1-x)BKT material system is shown in Figure 2.4b.

One method to identify new potential MPBs is to simply consider the crystal structure and tolerance factor of known ferroelectric end-member materials and examine the properties in the composition region of the phase transition.[13] The rhombohedral to tetragonal transition of PZT is an example of this where the free energy of the two phases is equal at the MPB, allowing easy polarization switching.[54] A more goal-oriented strategy has been applied for e.g. PT-Bi(B'B")O_3 where the tolerance factor is used to predict the composition region of an MPB more accurately (B = transition metals).[60] Another method is to chemically modify a ferroelectric so that the stable temperature region of the MPB composition is adapted to a range which allows practical application.[13,61]

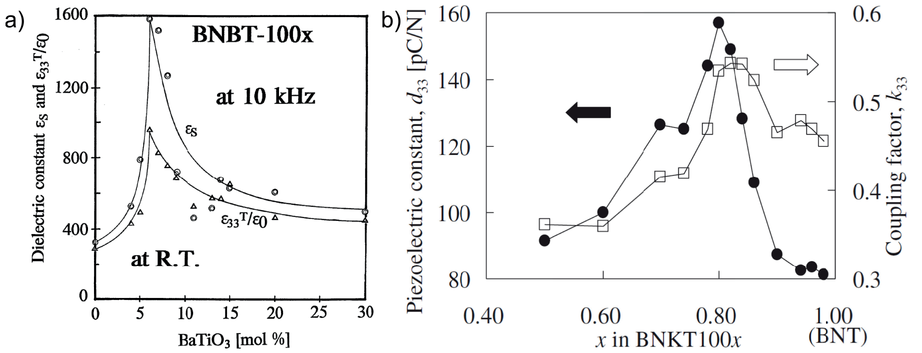

Figure 2.4: The dielectric constant of xBT - (1-x)BNT as a function of composition (a), and the d_{33} and k_{33} of xBNT - (1-x)BKT (b) across the respective MPBs of the systems.[30,67]

2.1.3 Ferroelectric Domains

All orientations of P_S will point in the same direction when an ideal infinite single crystal is cooled below T_C as this would minimize the energy related to the ionic displacement. This would result in a crystal with macroscopic $P = P_S$. A displacement of the B cation along the [001] axis of a tetragonal unit cell (Figure 2.2) will alter the energy seen by the neighboring unit cell, but this is compensated by corresponding displacements in the neighboring cells. A real crystal will, however, be spatially limited by a surface and the ionic displacement of the unit cell at the surface will hence not be energetically compensated in the same way as a bulk unit cell. This is resolved by formation of ferroelectric domains which are defined as volume units in the material where the direction of P_S of all unit cells is the same, and domains are separated by domain walls. The formation of domains results in a macroscopic P = zero, although $P_{domain} \neq$ zero for each individual domain. It is mentioned for completeness that if the ferroelectric was not dielectric (high mobility of free charges) the depolarization field would be formed by free charges migrating to the surface and effectively screening any macroscopic polarization.[68]

The domain structure of a ferroelectric is determined by many factors. The depolarization field would disappear completely if each individual unit cell was an individual domain, but this is prevented by the energy cost related to formation of domain walls (dipolar and elastic energy). The resulting structure will hence be a balance between depolarization field and domain wall energy. The type of domain wall is governed by symmetry restrictions and the requirement that the spontaneous strain of neighboring domains must be equal in the plane of the domain wall.[68] This results in 90° and 180° walls for tetragonal crystals, 60°, 90°, 120° and 180° for orthorhombic crystals and 71°, 109° and 180° for rhombohedral crystals, as can be derived from Figure 2.3.[69]

The domain formation discussed above is related to a perfect single crystal. Commercially it is significantly more interesting to consider polycrystals as they are easier to produce.[13] All the aspects discussed above will be valid for each grain, but the overall behavior of the material will also depend on the interaction between grains. The different grain orientations and sizes will introduce additional strains in the material such that the microstructure will be important for domain size and material performance, as demonstrated, e.g., for PZT, BKT and BT.[70–72]

2.1.4 Ferroelectric Hysteresis

Macroscopic polarization in a non-polar (as-cooled) ceramic can be induced by application of an electric field over the material. The electric field will destabilize domains with P_S oriented away from the direction of the field and stabilize domains with P_S oriented close to the direction of the field. The stabilized domains will start to grow at the expense of the destabilized ones giving $P \neq$ zero. The result is "the fingerprint" of a ferroelectric material, given by the polarization vs. electric field behavior, the P-E loop. The development of the P-E loop of an as-fabricated ferroelectric ceramic (P = zero) is shown schematically in Figure 2.5a and experimentally for PZT in Figure 2.5b. Upon application of $E > 0$, domains will start to reorient and the macroscopic polarization will increase as long as the electric field is increased. The initial increase is linear (small fields) before a non-linear behavior is observed. When all switchable domains are reoriented in accordance with the electric field, the ferroelectric will behave as linear dielectric upon further increasing E. The saturated polarization (P_{sat}) of the ferroelectric may be estimated by extrapolation of the saturated P-E curve back to zero electric field. The remanent polarization (P_r) is on the other hand the macroscopic polarization left after the electric field is removed. The polarization behavior is perfectly symmetric for positive and negative electric fields in an ideal ferroelectric; application of $E < 0$ will first result in $P = 0$, which defines the coercive electric field (E_C), before $P < 0$ is observed. P_r is

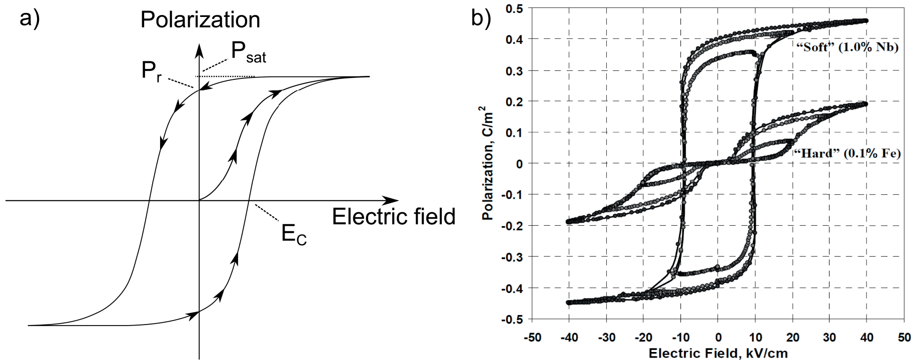

Figure 2.5: Schematic representation of a ferroelectric P-E hysteresis loop (a) and a comparison of soft (donor substituted) and hard (acceptor substituted) PZT (b).[74]

smaller than P_{sat} because some domains cannot be permanently reoriented by the electric field as further discussed below. The zero field macroscopic polarization will not return to zero before the material is again heated to the paraelectric state above T_C where all polarization disappears and the domain structure is erased.[73]

The hysteretic nature of the P-E loop is also reflected in the strain-electric field loop (ϵ-E loop/butterfly loop), as depicted schematically in Figure 2.6a and experimentally for ceramic BFO in Figure 2.6b. Upon application of a positive electric field over a ferroelectric ceramic, starting in point A of Figure 2.6a, a negative strain will develop because not all domains are oriented along the direction of the electric field. Domains will start to reorient to a direction which is better aligned with the field when E_c is surpassed (point G). A positive strain will now develop (H) and continue to increase as long as E increases (C). The strain will decrease back to the remanent strain (ϵ_r) once the electric field is removed (C to A). The same sequence is repeated for negative electric fields. The change from G to H will not be as abrupt in reality because different domains may have different E_c.[54]

The developed strain stems from electrostriction and the converse piezoelectric effect (Eq. 2.2 and 2.4). The square dependence of electrostriction on the electric field implies both that it only develops positive strain and that the piezoelectric effect will be dominating. The development of butterfly loops requires domain reorientation and consequently domain wall motion. Point defects may be highly important for domain wall movement in ferroelectrics, as discussed further in Chapter 2.2.

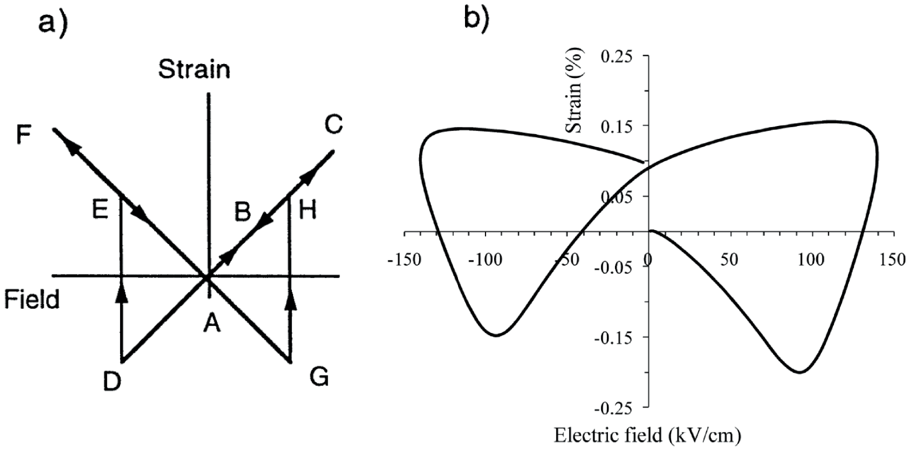

Figure 2.6: Schematic representation of a ferroelectric strain-electric field butterfly loop (a) and the experimentally measured electric field induced strain of ceramic BFO (b).[42,54]

2.1.5 Piezoelectric Response of Ferroelectrics

The response of a ferroelectric material to a small field (electrical or mechanical) is important and can be described by χ or more commonly for small electric fields, by the complex relative dielectric permittivity $\varepsilon(\omega)$ as shown in Eq. 2.6.[75]

$$\varepsilon(\omega) = \varepsilon'(\omega) - i\varepsilon''(\omega) = \chi(\omega) + 1 \tag{2.6}$$

Here, ω is frequency, ε' is the real relative dielectric permittivity and $i\varepsilon''$ is the imaginary relative dielectric permittivity. The term permittivity will be used interchangeably with relative dielectric permittivity throughout this thesis, though it is noted that permittivity is in fact equal to $\epsilon(\omega)\epsilon_0$ (ϵ_0 is the permittivity of vacuum). The intrinsic permittivity of a material will depend solely on lattice effects through polarizability.[54,55] The intrinsic permittivity of piezoelectrics is hence normally higher than in other dielectrics due to an increased polarizability and the strong coupling between electric field and strain (Eq. 2.4).[55] The permittivity in ferroelectrics normally peak near a phase transitions, as shown for an MPB in Figure 2.4a, and for several PPTs in BT in Figure 2.7.

The intrinsic permittivity of ferroelectrics is important because it directly influences the piezoelectric coefficient which may be estimated by Eq. 2.7.[55]

$$d \approx 2Q\varepsilon_0\varepsilon' P_r \tag{2.7}$$

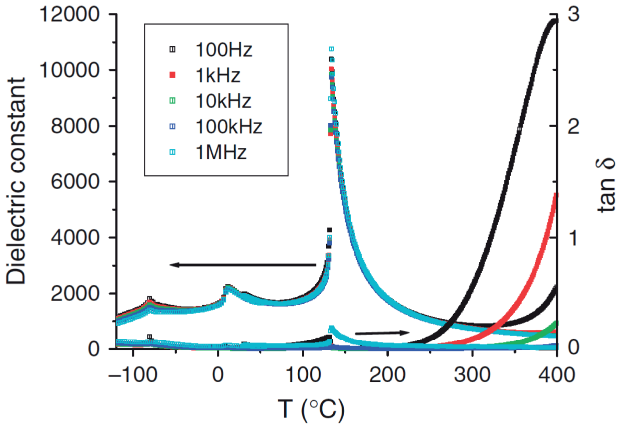

Figure 2.7: Temperature and frequency dependence of the dielectric constant for ferroelectric BT.[76]

It is evident from Eq. 2.7 that a high P_r and ε' is desirable for materials where a high d is desired, such as for sonars or ultrasonic transducers.[1,3] This further explains the interest towards identifying MPBs in solid solution systems where these properties are seen to increase (Chapter 2.1.2). Furthermore, d (in pC/N or pm/V) is defined as the small signal piezoelectric coefficient while d* (in pm/V) is sometimes used in the literature to denote the large signal piezoelectric coefficient.

The extrinsic contributions to the piezoelectric performance of ferroelectrics are all other effects than lattice effects, including those of non-180° domain wall motion, impurities and interfacial effects.[54,55] Displacement of domain walls is the most important of these, but the contribution is normally smaller than the intrinsic lattice contribution.[54,64] Domain wall motion is also an origin for dielectric or mechanical loss, defined by the loss angle δ (Eq. 2.8), which is the phase shift angle of an applied sinusodial field across a dielectric.[54,75]

$$\tan\delta = \frac{\varepsilon''(\omega)}{\varepsilon'(\omega)} \tag{2.8}$$

The measured permittivity of a ferroelectric will include contributions from factors such as electrical conductivity, in addition to the contributions from the piezo- and ferroelectric nature of the material. This results in a measured $\varepsilon(\omega)$ where the real term of Eq. 2.6 also includes contributions from alternating current (AC) conductivity (σ_{AC}) and Maxwell-Wagner relaxations while the imaginary term includes contributions from direct current (DC) conductivity (σ_{DC}), σ_{AC} and dielectric losses (domain wall motion).[9,28,75] Throughout this thesis ε will be treated as the measured ε and the (ω) will be omitted for simplicity.

Correspondingly to Eq. 2.6, the electrical conductivity of the material ($\sigma(\omega)$) may be represented as a complex number where $\sigma'(\omega)$ is the real contribution and $i\sigma''(\omega)$ is the imaginary contribution, and the conductivity is a function of the permittivity as shown in Eq. 2.9.[9]

$$\sigma(\omega) = \sigma'(\omega) + i\sigma''(\omega) = \left[\omega\varepsilon_0\varepsilon''(\omega) + \sigma_{DC}\right] + i\left[\omega\varepsilon_0\varepsilon'(\omega)\right] \tag{2.9}$$

Finally, the piezoelectric coupling factor (k) is a direct measurement of the energy efficiency of the electromechanical coupling and is defined in Eq. 2.10.[1]

$$k = \sqrt{\frac{\text{Electrical output energy}}{\text{Mechanical input energy}}} \quad or \quad \sqrt{\frac{\text{Mechanical output energy}}{\text{Electrical input energy}}} \tag{2.10}$$

2.2 Hard/Soft Ferroelectrics and the Aging Process

A material that exhibit a P-E loop as shown in Figure 2.5a is characterized as a soft ferroelectric, exemplified also by 1% Nb substituted PZT in Figure 2.5b. The antithetical concept is hard ferroelectrics where the P-E loop is pinched at zero field, also shown in Figure 2.5b for 0.1% Fe substituted hard PZT.

The development of macroscopic polarization in ferroelectrics requires reorientation of domains; consequently movement of domain walls as one domain grows at the expense of another. The origin of the pinched P-E loop is a stabilization of the domain walls by point defects which hinder domain wall movement and inevitably prevents domain reorientation.[77] Domain wall movement is an important extrinsic contribution to the piezoelectric performance of a material, as established in Chapter 2.1.5. Hard ferroelectrics normally obtain a lower P_r due to reduced domain wall movement and reorientation of P_S, which directly affects the piezoelectric constant through Eq. 2.7. A high E_c is also observed, which is challenging e.g. with respect to "high conductivity" ferroelectrics.[28,44] The pinched hysteresis loops of hard ferroelectrics should incidentally not be interchanged with the loops of anti-ferroelectric materials where the origin of the apparent pinching is a fundamentally different domain structure.[73]

Aging is the mechanism that gives hardening of ferroelectrics and is a generic process where material properties change over time as external factors such as temperature, electric field or mechanical environment are altered.[9,78] The driving force for aging in ferroelectrics is the spontaneous polarization that arise as the material is cooled from the paraelectric to the ferroelectric phase. The spontaneous polarization that develops will alter the energy associated with the different lattice sites in the crystal. This promotes migration of intrinsic or extrinsic point defects to more energetically favorable lattice sites where they are stabilized and may act to hinder domain wall movement. Computational studies on PT show that both association of positive and negative point defects, and the accumulation of isolated and coupled point defects at 180 ° domain walls is energetically favorable.[79,80] The importance of domain walls has been confirmed by studies on hard and soft PZT from low temperature (4.2 K) up to room temperature. At low temperature, where domain wall motion is not expected to contribute significantly to the piezoelectric properties, hard and soft PZT show similar properties. As the temperature gradually increases, the piezoelectric performance of soft PZT improves much more than that of hard PZT, in line with a higher domain wall contribution.[81] The type of point defect is of importance as this can influence the type of aging mechanism.[9,79] The three mechanisms for aging that are generally discussed in the literature, either alone or in combination, are[78,79]:

The bulk effect which is characterized by point defects associating to form defect dipoles with a defect dipole moment (P_D) within single unit cells that stabilize orientations of P_S parallel to P_D. These defect dipoles will then pin domain walls and effectively prevent polarization switching at low electric fields. The bulk effect is described more in detail below. This effect has been found to be the cause of hardening observed e.g. in BT and PZT.[9,82,83]

The domain wall effect which is manifested by point defects that migrate into the domain walls of ferroelectrics.[78,84] The driving force may be to relieve lattice mismatch from a dopant, strain effects at the domain wall or charge compensation. Calculations have shown that both single point defects and associated point defects are energetically stabilized at 180° domain walls relative to the bulk domain in tetragonal PT.[79] The effect can also be related to charge compensation at the domain wall, as domain walls have been shown to possess a different electronic configuration than the bulk domains.[85,86]

The grain boundary effect which is related to surface charges that develop at the grain boundaries. These may develop as a consequence of secondary phases or an increased point defect concentration at the grain boundaries during fabrication of the ceramic.[78,87]

An example of the bulk effect is given by comparing an ideal defect-free ferroelectric (Figure 2.2) and a ferroelectric containing point defects (Figure 2.8). In the case of an ideal defect-free ferroelectric, all oxygen lattice sites are energetically degenerate in the paraelectric state (Figure 2.2a). All the six possible orientations of P_S are equally favorable and no aging is observed as there are no point defects that may act to pin domain walls (Figure 2.2b). Figure 2.8a illustrates a paraelectric unit cell with an acceptor substituted B site and a charge compensating oxygen vacancy. In the paraelectric state, the oxygen vacancy may locate at any of the six octahedral sites as they are all degenerate. This degeneracy is removed below T_C where the B site is displaced in the [001] direction (Figure 2.8b). Given sufficient mobility, the oxygen vacancy with positive effective charge may migrate to a more energetically favorable site where it is stabilized and forms a defect dipole together with the acceptor substituted B site, which has a effective negative charge (Figure 2.8c).[82] The resulting P_D will either hinder the reorientation of P_S when an external field is applied or, if the field is able to reorient P_S, act as a recovering force that switches P_S back when the field is removed. An acceptor substituent is used in this example and computational investigations suggest that the energy difference between defect dipoles where the oxygen vacancy occupies the different oxygen sites may depend on the type of acceptor substituent.[80] The acceptor substituent may also be a cation vacancy which is highly relevant when working with volatile elements such as Pb or Bi.[41,79]

The hard/soft characteristic of ferroelectrics may be altered in several ways through aging/de-aging, e.g. by chemical substitution as observed for PZT. In this case, donor substitution is expected to reduce the point defect concentration, which consequently reduces the concentration of defect dipoles and results in a softer ferroelectric. The opposing effect is observed for acceptor substitution where the ferroelectric becomes harder. The P-E loop of PZT where the hard/soft characteristic is tuned by chemical substitution is shown in Figure 2.5b. The thermal history of a ferroelectric is also important for the hard/soft behavior, as mobility of point defects is higher at higher temperature. This makes high T_C ferroelectrics more prone to hardening relative to low T_C ferroelectrics because the driving force for hardening (P_S)

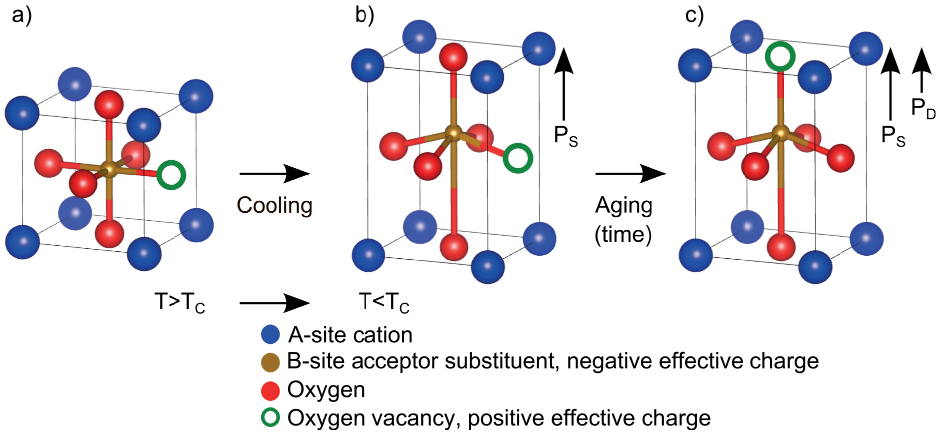

Figure 2.8: Schematic depiction of aging by the bulk effect in a tetragonal perovskite. The cooling from the paraelectric (a) to the ferroelectric (b) state is subsequently followed by an aging process where the oxygen vacancy migrates to an energetically preferred site (c) and forms a defect dipole, P_D, that stabilizes the spontaneous polarization, P_S.

arises at a higher temperature where the point defect mobility is higher. An example of the effect of high T_C is the actively induced hardening of BT which required five days of annealing just below $T_C = 128$ °C where the point defect mobility is low (Figure 2.9a).[82,83] On the other hand, BFO shows hard behavior when cooled normally from $T_C = 825$ °C. The high T_C enables oxygen vacancy mobility in the polar state (Figure 2.9b, non-quenched). Hardening of BFO can be reduced by quenching the ceramics from above T_C down to room temperature. The fast cooling to low temperature reduces the time in which the point defects have sufficient mobility to migrate and form e.g. defect dipoles, leaving the quenched sample softer than the non-quenched one (Figure 2.9b).[41] A third method of de-aging is electric field cycling where P_D becomes more evenly distributed and domain walls are possibly released from the pinning effect of P_D (Figure 2.9c).[77,78]

2.3 Relaxor Ferroelectrics

Relaxor ferroelectrics is a class of materials that differ from normal ferroelectrics in that P_S is gradually lost with increasing temperature, as opposed to the abrupt loss of P_S at T_C for normal ferroelectrics. Relaxors are identified by three characteristics; (1) the temperature of maximum permittiv-

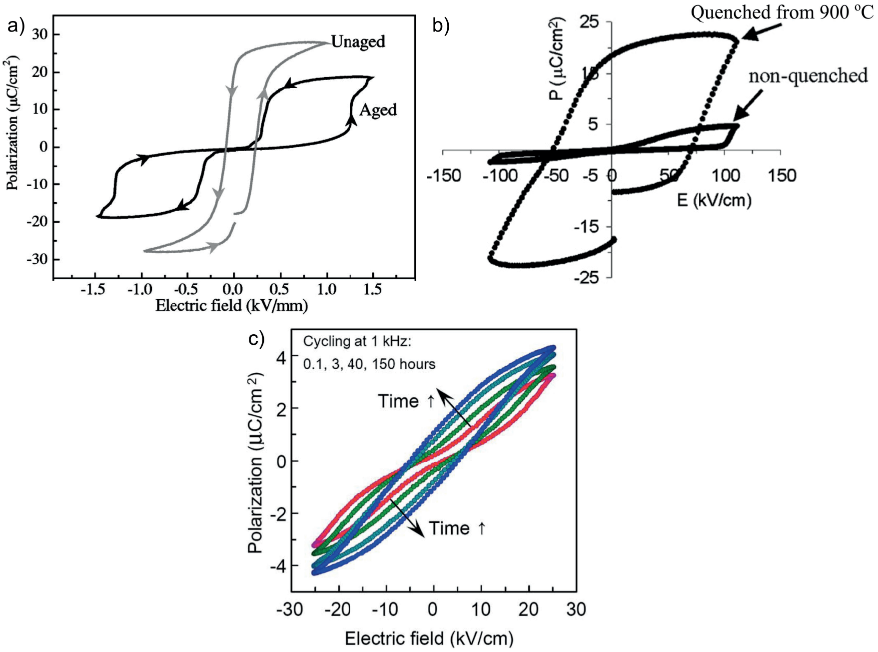

Figure 2.9: Aged (hard) and unaged (soft) Mn-doped BT single crystal where aging is introduced intentionally by annealing just below T_C (a).[83] Aged (non-quenched, hard) and unaged (quenched, softer) BFO where aging is intentionally avoided by quenching (b).[41] Deaging of a PZT ceramic at room temperature by electric field cycling (c).[77]

ity (T_m) is frequency dependent (Figure 2.10) as opposed to the frequency independent T_m observed for normal ferroelectrics (Figure 2.7); (2) the ferroelectric hysteresis curve will gradually close with increasing temperature and (3) macroscopic ferroelectric behavior is apparent although a paraelectric long range crystallographic order is observed by e.g. X-ray diffraction (XRD).[88]

The proposed models to describe this relaxor behavior can be separated into two categories, as summarized by Bokov and Ye[89]. One set of models assume compositional disorder which results in polar nanoregions (PNR) embedded in a non polar matrix (Figure 2.11a). Due to the compositional differences, these nanoregions will attain different Curie temperatures and hence smear out the ferro- to paraelectric phase transition. The second category of models argue that the PNRs are separated by domain walls instead of a non-polar phase (Figure 2.11b).

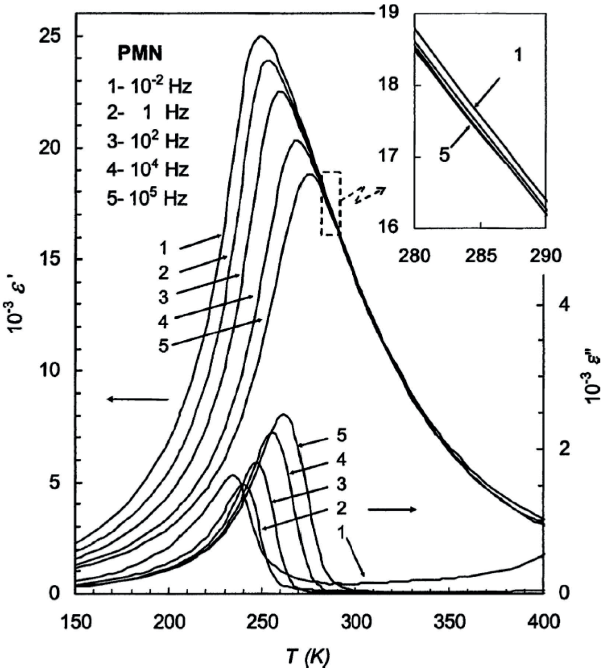

Figure 2.10: Temperature and frequency dependent dielectric permittivity of the relaxor ferroelectric $\mathrm{Pb(Mg_{1/3}Nb_{2/3})O_3}$.[89]

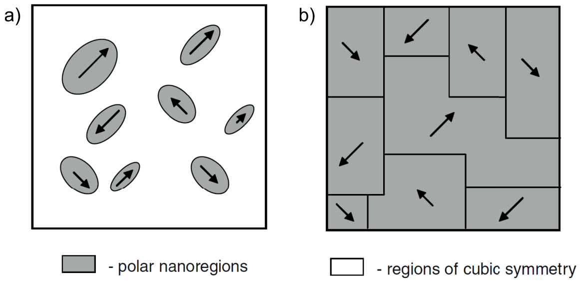

Figure 2.11: Schematic models of relaxor ferroelectrics; PNRs embedded in a non polar matrix (a) and PNRs separated by domain walls (b).[89]

2.4 Ferroelasticity in Ferroelectrics

Ferroelectric materials with non-180° domain walls are also ferroelastic. Ferroelastics are materials which develop spontaneous strain upon cooling from the paraelastic to the ferroelastic state, which will cause formation of ferroelastic domains in a similar way to the formation of ferroelectric domains.

Ferroelastic materials possess a non-linear mechanical stress induced strain contribution, analogous to the non-linear polarization that is induced by an electric field in ferroelectrics (Eq. 2.3). The ferroelastic hysteresis curve for compressive stress, given schematically in Figure 2.12, is qualitatively equal to the ferroelectric hysteresis curve (Figure 2.5).[90] However, the stress-strain hysteresis curve of ferroelastics is often provided as one loading cycle of compressive stress.

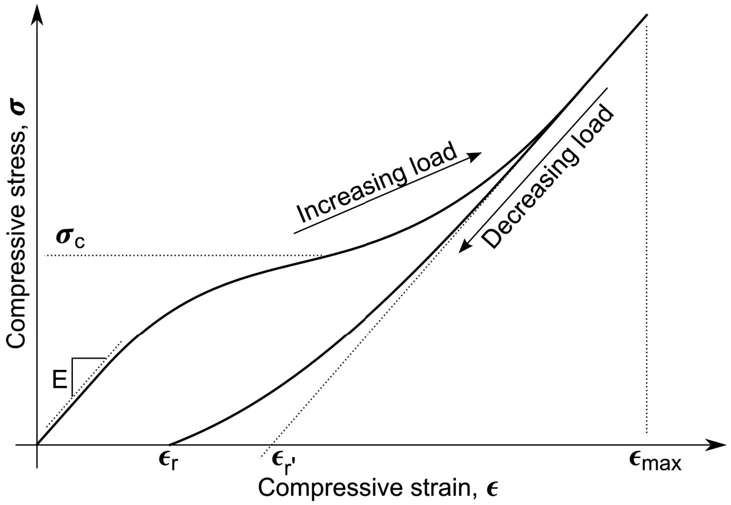

Figure 2.12: Schematic representation of a ferroelastic hysteresis loop.

During application of a compressive stress, a linear elastic strain will develop at small stress levels, and the slope of the stress-strain curve is proportional to the Youngs modulus (E-modulus) of the material. At a given stress level, a non-linear elastic strain will develop due to domain reorientation in the material. At this point, domains oriented parallel to the direction of the applied stress are destabilized and domains perpendicular to the stress direction are stabilized. The non-linear behavior will persist until all available domains are reoriented, at which the stress-strain curve is saturated and a further increase of the stress will provide a linear behavior. The remanent strain, ϵ_r, is defined as the residual strain after removal of the applied stress (analogous to ϵ_r for ferroelectrics when the electric field is removed). The difference ϵ_r'-ϵ_r (defined in Figure 2.12) denotes the degree of backswitching during unloading, and is an indication of how much of the non-linear strain was obtained due to irreversible domain switching. A hard ferroelectric-ferroelastic, where the domain walls are immobilized by point defects (see Chapter 2.2), will show more backswitching and a higher coercive stress (σ_c)

than a soft ferroelectric-ferroelastic.[91] It has however been suggested that domain wall pinning is only relevant up to a threshold stress level. Above this stress, the domain walls are no longer stabilized by point defects and hard and soft materials behave similar.[91] Furthermore, the coercive stress is defined as the minimum of $d\sigma/d\epsilon$ which is where the domain reorientation rate is highest, as shown in Figure 2.12. It is noted that this is not the true coercive stress corresponding to the E_c of a P-E loop, as this would require a measurement of the full stress-strain loop with both compressive and tensile stress. A study of the E_c/σ_c and P_r/ϵ_r of PZT has shown that they behave qualitatively similar across the MPB.[92]

The macroscopic strain developed under stress is comprised of the intrinsic (elastic) and extrinsic (ferroelastic) contributions.[93] The ferroelastic contribution with reorientation of domains will give a maximum switchable strain for tetragonal (ϵ^t_{sw}) and rhombohedral (ϵ^r_{sw}) symmetry which is given by Eqs. 2.11 and 2.12, respectively.[94,95]

$$\epsilon^t_{sw} = \frac{c_t}{a_t} - 1 \tag{2.11}$$

$$\epsilon^r_{sw} = \frac{d_{111}}{d_{11\bar{1}}} - 1 \tag{2.12}$$

Here, a_t and c_t are the tetragonal lattice parameters while d_{111} and $d_{11\bar{1}}$ are lattice plane spacings of the pseudo-cubic unit cell.

The theoretical maximum fraction of this switching strain that can be obtained by compressive stress for polycrystals when assuming randomly oriented domains, is 0.269 and 0.285 for tetragonal and rhombohedral structures, respectively.[95] The real ϵ_r developed under compressive stress in ferroelastics is determined by how easy it is to reorient a domain, in addition to the theoretical strain produced from each switching event.[96]

The effect of temperature on ϵ_r is determined by the influence of temperature on all the different processes involved in strain development.[96] It has been shown for soft PZT that the contribution from the linear elastic regime is relatively constant up to 200 °C, while the extrinsic contribution showed a clear decrease with increasing temperature.[93] The decreasing extrinsic contribution (domain wall movement) was correlated to the decreasing lattice distortion observed in PZT with increasing temperature and shows the importance of Eqs. 2.11 and 2.12.[91,97]

2.5 Lead-Free Piezoelectrics

2.5.1 Overview

The first lead-free piezoelectric material investigated and subsequently utilized in many practical applications was BT.[1] Recent concerns regarding the harmful effects of lead has led to legislation that limits the allowed amount of lead in electronics, but for the time being there is an exception for piezoelectrics due to the lack of alternatives to PZT.[16–19] This has motivated a renewed interest for the development of lead-free piezoelectrics that may replace PZT.[13,15] The most important perovskites at present, in addition to BT, is KNN, BKT, BNT and BFO as summarized by several recent reviews.[3,12,13,20–25,27,28]

BKT and BNT are tetragonal ferroelectric and rhombohedral relaxor materials at room temperature, respectively. BKT becomes paraelectric at a relatively high temperature ($T_m \approx 400$ °C), while the depolarization temperature (T_d, where the polar displacement disappears) of BNT is relatively low ($T_d \approx 180$ °C).[33,34,98,99] A relatively high coercive electric field, piezoelectric properties that are inferior to PZT and challenges related to the synthesis make BKT and BNT more interesting as part of a solid solution than as pure compounds.[13,34,100,101] BKT and BNT are reviewed in more detail in Chapter 2.5.2 and 2.5.3, respectively. BFO is a rhombohedral multiferroic at room temperature.[28,44,102] High ferroelectric polarization and strain have been reported for BFO ceramics, but practical application is hampered by a high E_c and leakage currents.[28,31,42,43] The high T_C of BFO (825 °C) is also of interest as it will allow high temperature application of ferroelectrics.[28] BFO is reviewed in more detail in Chapter 2.5.5. BT shows a high dielectric permittivity of ~1400, making it suitable for capacitors.[1,3] It is a tetragonal ferroelectric at room temperature with a relatively low T_C (120-135 °C).[1,21] The low T_C and the additional PPTs upon cooling (tetragonal to orthorhombic at 0 °C and further to rhombohedral at -90 °C), presents a challenge with respect to a narrow operating temperature range.[1,3,13] Chemical modifiers can be used to tune T_C and the performance of BT to specific applications.[3] Ca and Zr substituted BT is the lead-free piezoelectric with the highest reported $d_{33} = 620$ pC/N at present.[103] KNN is a room temperature ferroelectric solid solution of $KNbO_3$ and $NaNbO_3$. KNN shows peak performance at the 50-50 composition, where it is reported to be orthorhombic or monoclinic.[13,104,105] It shows a relatively high T_C of ~400 °C and transforms from the room temperature symmetry to tetragonal at a PPT near 200 °C.[104,105] The synthesis of KNN is challenging with respect to the density of polycrystals and the volatility of the alkali oxides, and the piezoelectric properties of conventional KNN are inferior to PZT.[1,13] A renewed interest in KNN was however seen in the wake of the report by Saito *et al.*[106] where piezoelectric properties comparable to those of PZT were reported for chemically modified and textured KNN ceramics (Figure 2.13).

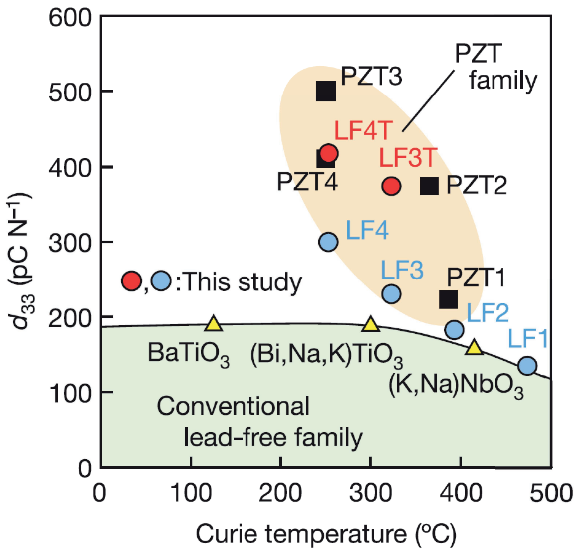

Figure 2.13: Comparison of the d_{33} of lead-free and lead containing piezoelectric ceramics. LF(1-3) denote Li and Ta substituted KNN-materials, LF4 is substituted with Sb in addition to Li and Ta, and LF(3-4)T are the corresponding textured materials.[106]

Although some of the lead-free piezoelectrics may be used as a single compound, a large number of binary or ternary solid solutions have been reported with lead-free piezoelectric end-members. Some, such as BNT-BKT, BFO-BT and BFO-BKT, are inspired by the rhombohedral-tetragonal MPB of PZT. BNT-BKT has been intensively studied for several years due to the enhanced piezo- and ferroelectric properties at the MPB of 16-20 mol% BKT.[29] The BNT-BKT system is reviewed in Chapter 2.5.4. BFO-PT shows complete solid solution and an MPB with enhanced piezoelectric performance at ~30 mol% BT where a transition from rhombohedral to (pseudo) cubic structure is observed. The permittivity is seen to increase and T_C decreases with increasing BT content, as could be expected from the end-member properties. The application of BFO-BT is hampered by high leakage currents which makes poling difficult.[107–109] BFO-BKT has received significant attention in recent years.[50,110,111] It shows structural transitions similar to those of BFO-BT, but it is unclear whether an MPB is present at the rhombohedral to pseudo-cubic transition with 30-40 mol% BKT. The characterization of the ferroelectric performance of BFO-BKT is also hampered by a high leakage current, but T_C is seemingly less sensitive to the addition of BKT relative to BT. BFO-BKT is reviewed in more detail in Chapter 2.5.6.

In addition to the above mentioned solid solutions, there are reports on a large variety of other end-member combinations of lead-free piezoelectrics. The reader is referred to several recent review articles where these are described.[21–24]

2.5.2 $Bi_{0.5}K_{0.5}TiO_3$

BKT is a room temperature ferroelectric tetragonal perovskite which was discovered around 1960.[33,112,113] The original report of Ivanova *et al.*[33] revealed a tetragonal to pseudo-cubic phase transition at 270 °C (T_2) and a pseudo-cubic to cubic transition at 410 °C (Figure 2.14). The structural transitions have been confirmed by later reports while the exact transition temperatures vary around ~300 °C and ~400 °C.[114] The T_2 phase transition is suggested to be of first order and the pseudo-cubic to cubic transition of second order.[115,116] Selected structural and other properties of BKT are summarized in Table 2.1.

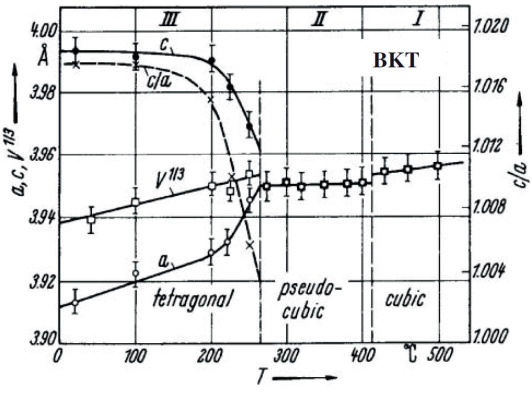

Figure 2.14: Lattice parameters of BKT as a function of temperature.[33]

Table 2.1: Structural, dielectric, piezoelectric and ferroelectric properties of BKT prepared by conventional solid state synthesis (values after hot-pressing in parenthesis). The tolerance factor is calculated from the given reference with A-site coordination of 8.

Property	Value	Reference
Room temperature symmetry	Tetragonal, P4mm	[33,115,117]
a_t, [Å]	3.9388	[117]
c_t, [Å]	3.9613	[117]
Tetragonality c_t/a_t, [-]	1.006	[117]
Tolerance factor, t [-]	0.99	[118]
T_2, [°C]	$\sim$ 300	[33,34,113,114]
T_m, [°C]	$\sim$ 400	[33,34,113,114]
P_r, [$\mu C/cm^2$]	25 (14-22)	[34,100]
E_c, [$\mu C/cm^2$]	52 (47-53)	[34,100]
d_{33}, [pC/N]	81 (70)	[34,100]
k_{33}, [-]	0.35 (0.28)	[29,34]
ε' (10 kHz), [-]	666 (600)	[34,119]

It has been reported by several that BKT shows poor sinterability when synthesized by conventional methods.[13,34,120,121] However, it has recently been shown that high density BKT ceramics can be obtained from solid state synthesis by careful consideration of the particle size of the precursors.[100]

A second challenge related to synthesis of BKT is the evaporation of Bi_2O_3 and K_2O at elevated temperatures.[122] It has been suggested that the volatility leads to a non-stoichiometric material. The non-stoichiometry shifts the overall composition into a three phase region where BKT is in equilibrium with a Bi-rich and a Ti-rich phase, as shown in Figure 2.15.

A relaxor-type behavior is apparent from the frequency dispersion of the dielectric permittivity with increasing temperature (Figure 2.16a). The gradual phase transition between T_2 and T_m is reflected by an abrupt drop for the coupling factor when heating up to T_2 (Figure 2.16b), after which a gradual decrease is observed up until T_m. Although the cubic state is observed at a relatively high temperature ($\sim$400 °C), the gradual disappearance of the tetragonal structure from $\sim$300 °C limits the high temperature applicability of BKT. The piezoelectric and ferroelectric properties of BKT are such that the pure material is not very useful as a single compound, but may rather act as an important constituent to solid solutions.[13]

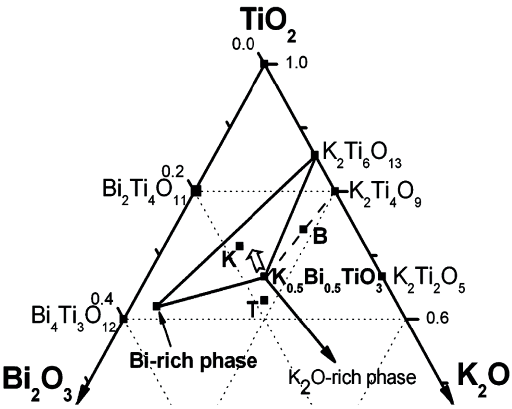

Figure 2.15: Suggested three phase region of a Bi-rich and Ti-rich phase, in addition to BKT as a result of Bi_2O_3 and K_2O losses during fabrication of BKT.[122]

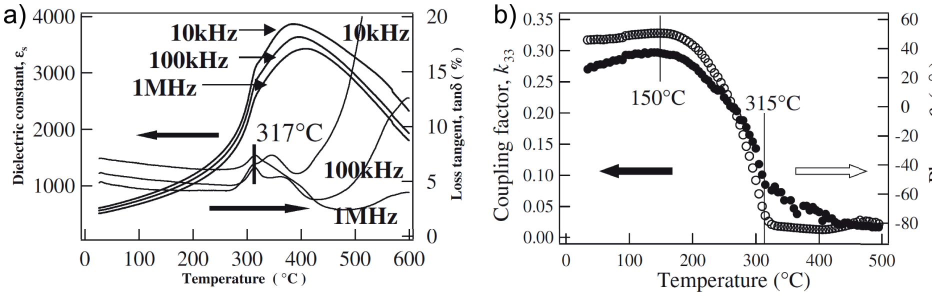

Figure 2.16: Dielectric constant (a), and k_{33} and θ of BKT hot pressed at 1080 °C. Adapted from Hiruma *et al.*[34]

2.5.3 $Bi_{0.5}Na_{0.5}TiO_3$

BNT is a relaxor ferroelectric discovered along with BKT in the early 1960s.[112] The room temperature rhombohedral structure transforms to a tetragonal structure through a diffuse phase transition between 200 °C and 320 °C before a cubic structure is adopted at 540 °C.[13,98] However, recent reports suggest a monoclinic symmetry at room temperature[123,124] and there are discussions related to the structural development in the 200-320 °C temperature range.[13,35,125] Crystal structure and selected properties of BNT are summarized in Table 2.2. BNT shows a higher P_r and E_c and comparable d_{33} to that of BKT. Poling has been reported to be difficult due to the high E_c and high leakage currents.[13,21]

Similar to BKT, it is expected that Bi_2O_3 and Na_2O may evaporate during synthesis of BNT (sintering temperature ~1100-1200 °C), leaving an A:B-ratio < 1. A Na deficient homogeneity region has been observed for $Bi_{0.5}Na_{0.5-x}TiO_{3-x/2}$ with $0 \leq x \leq 0.3$.[21,126] Small deviations from the nominal 50:50 Bi:Na-ratio have also been shown to give a cubic-like long range structure and Bi:Na-ratio < 1 was detrimental for the polarization response to an electric field.[127] The thermal history of BNT is also of importance for the perceived long range order as rhombohedral and monoclinic structures were observed after calcination and sintering, respectively.[124]

2.5.4 (1-x)$Bi_{0.5}K_{0.5}TiO_3$ - x$Bi_{0.5}Na_{0.5}ZrO_3$ Solid Solution

The BKT-BNZ ternary reciprocal system consists of the four end-members BKT, BNT, BKZ and BNZ. Structural parameters for BKZ and BNZ are provided in Table 2.3.

The BKT-BNT composition line is the most studied in this system after an MPB was proposed for 16-20 mol% BKT by Sasaki *et al.*[29] The evolution of the room temperature crystal structure along the composition line has been

Table 2.2: Structural, dielectric, piezoelectric and ferroelectric properties of BNT prepared by conventional solid state synthesis. The tolerance factor is calculated from the given reference with A-site coordination of 8.

Property	Value	Reference
Room temperature symmetry	Rhombohedral, R3c	98
a_h, [Å]	5.4887	98
c_h, [Å]	13.5048	98
Lattice distortion c_{pc}/a_{pc}, [-]	1.004	98
Tolerance factor, t [-]	0.95	118
T_d, [°C]	200	98
T_m, [°C]	320	98
T_{cubic}, [°C]	540	98
P_r, [μC/cm^2]	34-39	101,126
E_c, [μC/cm^2]	69-72	101,126
d_{33}, [pC/N]	68-82	99,101,116,126
k_{33}, [-]	0.45	99
ε' (10 kHz), [-]	536	101

Table 2.3: Structural properties of BKZ and BNZ. The tolerance factor is calculated from the given reference with A-site coordination of 8.

	BKZ[39,119]	BNZ[38]
Room temperature symmetry	Cubic, $Pm\bar{3}m$	Orthorhombic, Pnma
a, [Å]	4.1582	5.77
b, [Å]	-	8.14
c, [Å]	-	5.70
Tolerance factor, t [-][118]	0.94	0.89

studied by several authors, as summarized by Jones *et al.*[117] The rhombohedral to tetragonal transition is suggested to occur directly, by a bridging pseudo-cubic phase, the coexistence of rhombohedral and tetragonal structure or a second bridging rhombohedral phase.[117] The displacement of Ti in the oxygen octahedron is shown to decrease with increasing Na-content.[128] The depolarization temperature at the MPB is at the level of BNT, while T_m decreases with respect to both end members. The P_r, d_{33}, k_{33} and ε' are all seen to increase and the E_c decreases, but the properties are still inferior to PZT.[1,29,99,101] Substitution of Ti with small amounts of Zr near the MPB of BKT-BNT has shown to increase the electric field induced strain significantly and a $d_{33}^* = 614$ pm/V was reported, while the polarization and permittivity were decreased with increasing Zr substitution.[40]

The available literature related to BKZ and BNZ is limited although both materials were suggested as ferroelectrics already in 1961.[112] The low tolerance factor for both materials and the difference in crystal symmetry suggest a possible MPB in solid solution with BKT or BNT, but the BKZ and BNZ end-members cannot be piezoelectric due to their non-polar crystal symmetry. Along the BKT-BKZ composition line, the tetragonal symmetry prevails up to 5-11 mol% BKZ.[119,129] The rhombohedral structure of BNT transforms to orthorhombic symmetry at 58-60 mol% BNZ.[129–131]

Substitution of 5-10 mol% BKT/BNT with BKZ/BNZ increases the dielectric constant slightly while the d_{33} of both BKT and BNT is reduced with the introduction of Zr.[119,129,132]

2.5.5 $BiFeO_3$

Phase Stability and Crystal Structure

The phase diagram of Bi_2O_3 - Fe_2O_3 is shown in Figure 2.17. BFO is a line compound with no solid solution and a first order ferro- to paraelectric phase transition at T_C = 825 °C, where an orthorhombic structure is adopted.[44,102,133] The T_C is high compared to PZT (T_C = 386 °C)[1], BT (T_C = 120-135 °C)[21] and other lead-free ferroelectrics.[13] The synthesis of phase pure BFO ceramics is notoriously challenging because of $Bi_2Fe_4O_9$ (mullite) and $Bi_{25}FeO_{39}$ (sillenite) which forms on the Fe_2O_3 and Bi_2O_3 rich side of the BFO line in the Bi_2O_3-Fe_2O_3 phase diagram, respectively. These two phases are slightly more thermodynamically stable than BFO in the 447-767 °C temperature range.[45] This temperature range is highly relevant with respect to synthesis of BFO by several different techniques.[134] A reaction pathway for BFO formation was suggested by Bernardo *et al.*[135] where the limiting factor that resulted in Bi/Fe-rich phases was the slow diffusion of Fe into Bi. Rojac *et al.*[28] have also provided a thorough discussion related to the phase purity of BFO. The sillenite phase may be removed by high temperature annealing, but it is believed that this is a result of Bi_2O_3 evaporation, resulting in a sub-stoichiometric material with a Bi:Fe-ratio < 1. Several alternative synthesis methods have been proposed but synthesis challenges still prevail.[28,134]

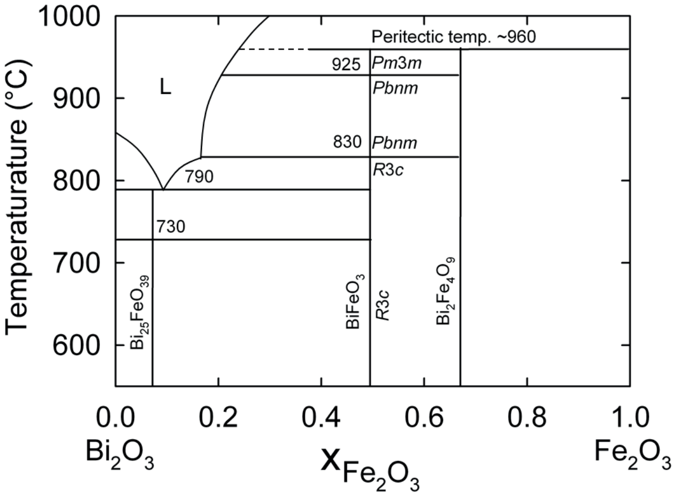

Figure 2.17: Binary phase diagram of Bi_2O_3 - Fe_2O_3.[48]

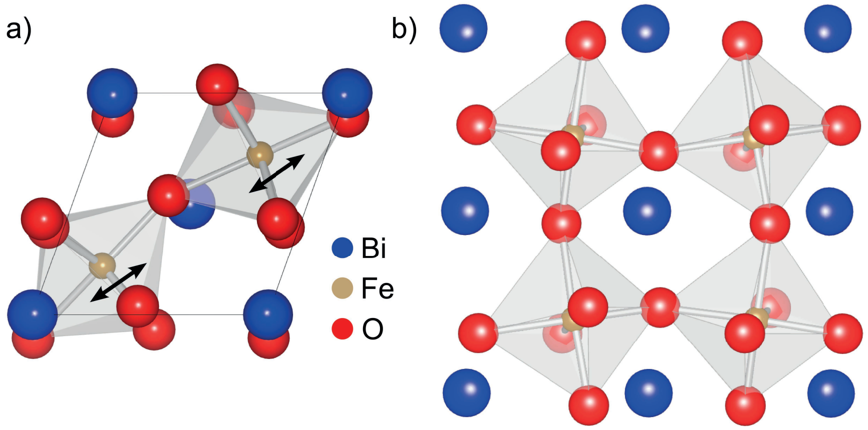

Figure 2.18: The rhombohedral representation of the BFO unit cell seen along the rhombohedral $[100]_r$ (a) and the pseudo-cubic $[100]_{pc}$ (b) crystallographic directions (adapted from Selbach[48]). Atomic positions taken from Kubel and Schmid.[102] The black arrows indicate the direction of P_S, $[111]_r$.

The crystal structure of BFO is rhombohedral R3c at room temperature, also denoted as the α-phase of BFO.[102,133] The structure is a distorted simple cubic perovskite with an antiferrodistortive rotation of the oxygen octahedra around the threefold rhombohedral polar axis ($[111]_r$). The Bi^{3+} and Fe^{3+} are in addition shifted cooperatively along the polar axis resulting in a doubled unit cell relative to the cubic aristotype.[102] The primary unit cell of BFO is shown in Figure 2.18 and structural parameters are summarized in Table 2.4. The room temperature structure transforms to the orthorhombic Pbnm β-phase at ~825 °C and further to a cubic or orthorhombic symmetry at ~ 930 °C.[136,137]

The symmetry of BFO can be represented by rhombohedral (r) and hexagonal (h) axes as shown in Figure 2.19. The rhombohedral lattice parameters may also be reduced to a pseudo-cubic representation. The axis of the different representations are related through the polar axis where $[111]_r \parallel [111]_{pc} \parallel [001]_h$.

Normalized pseudo-cubic lattice parameters relating to the hexagonal unit cell are obtained by $a_{pc} = 2^{-1/2} a_h$ and $c_{pc} = 12^{-1/2} c_h$ which allows the calculation of the lattice distortion by c_{pc}/a_{pc}.

Table 2.4: Structural and functional parameters of BFO. The data are given for polycrystalline ceramics if not otherwise stated. The tolerance factor is calculated from the given reference with A-site coordination of 8.

Property	Value	Reference
Room temperature symmetry	Rhombohedral, R3c	[102]
a_h, [Å]	5.57874(16)	[102]
c_h, [Å]	13.8688(3)	[102]
Lattice distortion c_{pc}/a_{pc}, [-]	1.015	[102]
Tolerance factor, t [-]	0.90	[118]
T_C, [°C]	825	[28]
ε', [-]	30-10000	[28]
DC conductivity, [S/cm]	10^{-2} - 10^{-8}	[28]
Seebeck coefficient (air), [μV/K]	~600	[138]
d_{33}, [pC/N]	2 - 60	[28]
P_r, [μC/cm^2]	20-60	[28]
E_c, [kV/cm]	~75	[28]
P_r, [μC/cm^2] single crystal	65 $[010]_{pc}$ ≈100 $[111]_{pc}$	[43]
E_c, [kV/cm] single crystal	11 $[010]_{pc}$	[43]

Dielectric and Electromechanical Properties

The room temperature dielectric permittivity of BFO at GHz frequencies is relatively low with $\varepsilon' \approx 30$.[44] The permittivity at lower frequencies is normally higher due to Maxwell-Wagner relaxations,[140] and domain wall and conductivity contributions.[28,44,141]

The early macroscopic investigations of the electric field dependent ferroelectric properties of BFO reported a $P_r = 6.1$ μC/cm^2 for a single crystal.[142] A renewed interest for BFO as a ferroelectric arose with the report of Wang *et al.*[143] which reported P_r of 50-60 μC/cm^2 for epitaxial thin films. A $P_r > 60$ μC/cm^2 along the $[010]_{pc}$ crystallographic direction of a single crystal has been reported more recently.[43] This corresponds to a $P_r \approx 100$ μC/cm^2 along the polar $[111]_{pc}$ axis, in line with values of polarization determined by computational methods for bulk BFO.[31,43] Selected properties of BFO materials are included in Table 2.4.

The macroscopic electric field induced strain of ceramic BFO is shown in Figure 2.20a. The large strain has been attributed to polarization reversal and domain wall movement, ruling out a phase transition as the source of the

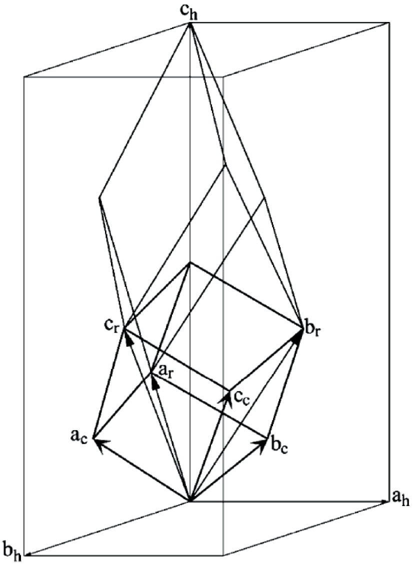

Figure 2.19: The hexagonal, rhombohedral and pseudo-cubic representation of the BFO unit cell.[139]

large strain.[28] The high strain is comparable to what is observed for PZT.[1] The obtained peak-to-peak strain of BFO is seen to decrease significantly with increasing frequency (Figure 2.20b), a trend that is also observed for the small signal piezoelectric coefficient.[28,144]

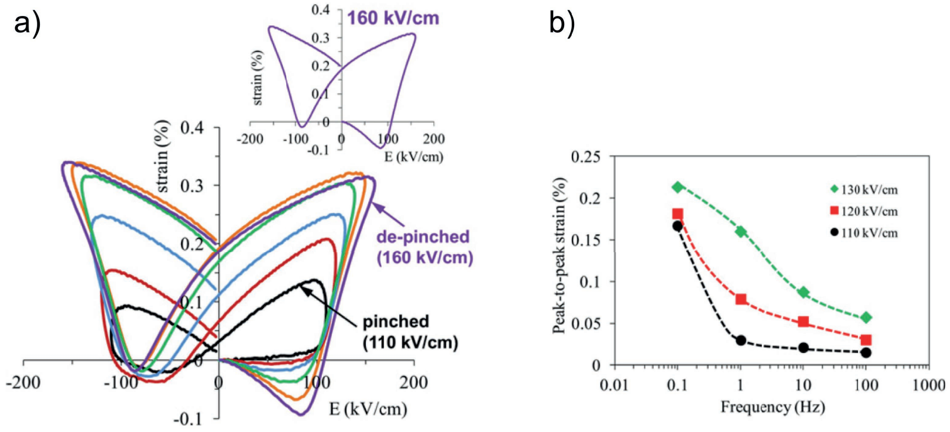

Figure 2.20: The electric field induced strain (a) and the frequency dependence of the peak-to-peak strain (b) for increasing electric fields.[28]

Aging and Hard/Soft Characteristics of BFO

BFO is considered a hard ferroelectric with a pinched P-E loop for conventionally prepared samples (Figure 2.9b). This, in addition to the high E_c combined with high leakage currents, makes it difficult to determine the true P_r of conventionally prepared BFO. A coercive electric field of >70 kV/cm is commonly observed for BFO ceramics while $E_c \approx 12$ kV/cm has been reported in single crystals.[28,41,43] Ferroelastic domains of a single crystal have, however, been fully reoriented "by means of a pair of tweezers" without any further specification by the authors.[145]

Several important characteristics related to aging in BFO have been studied by Rojac and co-workers.[28,41,42,144] Deaging/softening of originally hard BFO can be achieved by thermal quenching (Figure 2.9b), by electric field cycling and by thermal annealing at high temperature. An effect of all three methods can be observed for both large and small signal properties (e.g. d_{33} and P_r).[41,42] Hardening of originally soft BFO has also been reported after thermal annealing, analogous to BT (Figure 2.9a).[82,146]

The mechanism of hardening/softening of BFO is, however, not fully understood.[28] For example, the softening effect of donor substitution in PZT is related to the reduced concentration of point defects.[9] The softening of BFO by high temperature annealing does not directly correlate with this as high temperature annealing is expected to increase the point defect concentration (Eq. 2.13) and hence provide more domain wall pinning sites. The softening by high temperature annealing suggests that there may be other or additional mechanisms governing the domain wall movement/pinning in BFO relative to PZT.[28,86] Factors such as the accumulation of charge on the domain wall, the pinning effect of "B-site acceptor"-"oxygen vacancy" vs. "A-site acceptor"-"oxygen vacancy" point defect couples and the possibility of tuning the concentration of Fe^{2+}-"oxygen vacancy" point defect couples have been discussed.[28,144,147]

Electrical Conductivity

$BiFeO_3$ is a room temperature semiconductor with a band gap of ~2.5 eV and has been suggested to become metallic at temperatures higher than 920 °C.[44,133] The DC conductivity of BFO varies significantly over several orders of magnitude, ranging from 10^{-2} to 10^{-10} S/cm.[28,42,148–150] Small polaron hopping by localized charge carriers, which depends on the presence of an element with at least two valence states,[57] has been suggested to be the conductivity mechanism.[51,150–152] This is reasonable in the case in BFO when considering the point defect chemistry, and further connects the electrical conductivity of BFO to the partial pressure of oxygen (P_{O_2}, see Chapter 2.6). Both p-type and n-type conductivity in BFO has been observed experimentally[51,138,153–155] and predicted theoretically[52,156,157] but there are no systematic studies of the P_{O_2} dependency of the conductivity of BFO.

The domain wall conductivity of BFO thin films differ from the domain bulk conductivity, and is suggested to be of n-type due to its dependency on the concentration of oxygen vacancies.[85,154,155,158] An increased concentration of oxygen vacancies along the domain wall relative to the domain bulk may be reasonable, e.g. to relieve additional stresses at the domain wall. This would facilitate a local reduction of Fe^{3+} to Fe^{2+} along the domain wall, where Fe^{2+} is known to be the dominating charge carrier in related n-type semiconductors such as $LaFeO_3$. The formation of non-neutral domain walls have been suggested as the pinning mechanism of domain walls in thin films of BFO (domain wall effect, Chapter 2.2).[78,159] Rojac *et al.*[86] recently demonstrated conductive domain walls in as-sintered and poled bulk BFO ceramics. The observation of conductive domain walls also after poling suggest that domain wall movement in BFO involves charge transfer. Theoretical studies indicate that movement of charged domain walls may be promoted or hindered depending on the charge density at the domain wall.[160]

Point Defect Chemistry

The point defect chemistry is highly relevant for the performance of BFO as a ferroelectric material because point defects have been related to both the high coercive electric field and the high leakage currents.[28,41,150] In addition to the indirect experimental data that substantiate the formation of point defects,[41,122] there are computational studies which confirm that point defect formation is favorable in BFO.[52,156,157] There are, however, no reports on preferential ordering of point defects along, e.g., grain boundaries or domain walls.

The point defect chemistry of BFO is expected to originate from the loss of Bi_2O_3, and the accompanying formation of point defects, at elevated temperatures as described by Eq. 2.13.

$$2Bi_{Bi}^{\times} + 3O_{O}^{\times} \xrightarrow{\text{Heat}} 2V_{Bi}''' + 3V_{O}^{\cdot\cdot} + 2Bi(g) + {}^{3}\!/_{2}O_2(g) \tag{2.13}$$

Here, V_{Bi}''' and $V_{O}^{\cdot\cdot}$ are Bi- and O-vacancies with negative and positive effective charge, respectively, and Kröger-Vink notation is used to describe the point defects. Kröger-Vink notation is commonly used to include point defects in crystalline solids in chemical equilibria, and require a lattice site balance in addition to the mass and charge balance required for conventional chemical equations. Species that are not a part of the crystalline lattice are treated as in normal chemical equilibria (e.g. O_2 (g)) while additional nomenclature is adopted for the lattice species. Subscript denotes a given lattice site and which element that nominally occupies it (e.g. Bi- or O-sites). Superscript × denotes that the lattice site is occupied by an element with the same valence as the element that nominally occupies the site (e.g. Bi^{3+} on a Bi^{3+}-site, $Bi_{Bi}^{\times}$). Furthermore $'$ and $^{\bullet}$ denote an effective negative and positive charge, respectively, when the lattice site is occupied by an element with a different charge than nominally occupies the site, or by a vacancy, V (e.g. a vacancy on a Bi^{3+}-site, V_{Bi}'''). The $V_{O}^{\cdot\cdot}$ in Eq. 2.13 is formed to ensure charge balance resulting in an oxygen deficient material.

The defect chemistry is further governed by the electroneutrality condition (Eq. 2.14) and the mass balance of Fe (Eq. 2.15) as Fe is a multivalent ion.

$$n + 3\left[V_{Bi}'''\right] = p + 2\left[V_{O}^{\cdot\cdot}\right] \tag{2.14}$$

$$\left[Fe_{Fe}\right] = n + \left[Fe_{Fe}^{\times}\right] + p \tag{2.15}$$

Here, n is the concentration of Fe^{2+}, $\left[Fe_{Fe}^{\times}\right]$ is the concentration of Fe^{3+} and p is the concentration of Fe^{4+}. The ratio of Fe^{2+}:Fe^{3+}:Fe^{4+} is directly linked to the concentration of $V_{O}^{\cdot\cdot}$ through Eq. 2.16 and 2.17.

$$2Fe_{Fe}' + {}^{1}\!/_{2}O_2(g) + V_{O}^{\cdot\cdot} \rightleftharpoons 2Fe_{Fe}^{\times} + O_{O}^{\times} \tag{2.16}$$

$$2Fe_{Fe}^{\times} + {}^{1}\!/_{2}O_2(g) + V_{O}^{\cdot\cdot} \rightleftharpoons 2Fe_{Fe}^{\cdot} + O_{O}^{\times} \tag{2.17}$$

Element Doping/Substitution

The R3c symmetry of BFO is lost at relatively low amounts of substituent elements, as summarized by Silva *et al.*[134] Isovalent substitution of Bi is often motivated by an increased BFO phase stability and a reduced stability of the sillinite and mullite parasitic impurities. The R3c symmetry of BFO is normally conserved up to 10-20 mol% Bi-substitution by, e.g., rare earth substituents, coupled by a significant reduction of T_C.[134,161] An MPB in $Bi_{1-x}Sm_xFeO_3$ has, however, been suggested around x = 0.14 where peak dielectric and piezoelectric response was observed in a thin film.[162] It was recently shown that Sm^{3+} substitution of Bi^{3+} in BFO ceramics gives a softening effect and reduces the frequency dependence of the electric field induced strain.[163] Isovalent substitution of Fe by e.g. Mn is stable up to ~30 mol% Mn, which is relatively high for BFO.[134,136]

Aliovalent substitution of Fe is highly relevant with respect to the high conductivity of BFO (Chapter 2.5.5 - "Electrical conductivity"). The effect of donor substituents such as W^{6+}, Nb^{5+} and Ti^{4+} on the homogeneity and phase purity of BFO has been examined by Bernardo et al.,[164] showing that Ti^{4+} gives the least amount of secondary phases. It was later shown that the Ti-substituted ceramics may develop inhomogeneous ~40 nm sized grains with a Ti-enrichment on the grain boundaries.[148]

The p-type behavior of BFO argues that donor substitution should reduce the number of charge carriers and reduce conductivity while acceptor substitution should increase the number of charge carriers and increase conductivity. Ti^{4+}, Nb^{5+} and W^{6+} are donor *substituents* commonly reported to reduce the conductivity of BFO[149,150,152,165,166] while acceptor *substitution* by Ni^{2+} is shown to increase conductivity.[150] The opposite effect, i.e. an increasing conductivity by donor *substitution* and decreasing conductivity by acceptor *substitution* has also been reported and was attributed to the atmosphere during synthesis (N_2).[167] Both acceptor and donor *doping* has shown to decrease the conductivity of BFO.[168]

The terms *doping* and *substitution* are readily used interchangeably despite their different meaning. Substitution should be used when one element deliberately is replaced by another during synthesis, i.e. $BiFe_{1-x}Ti_xO_3$ where Fe is substituted by Ti. Doping refers to the case when an element is added in excess, i.e. when 1 mol% Ni is added to stoichiometric $BiFeO_3$ with the Bi:Fe ratio 1:1. The mixing of substitution and doping may make it challenging to evaluate the effect of doping/substitution.[169] The observed effect of substitution on conductivity is commonly explained in literature by; (i) an alteration of the concentration of $V_O^{\cdot\cdot}$ and the average valency of Fe (Fe^{3+} reduced to Fe^{2+}) and (ii) an effect of secondary phases.[28,150,153,167,170,171] Recent studies have shown that the presence of Fe^{4+} is likely at high P_{O_2}, giving p-type conductivity, and that n-type conductivity (due to Fe^{2+}) would arise at low P_{O_2}.[51,52,138,153,156,172,173] The maximum concentration of Fe^{2+} in BFO before decomposition has been found to be 2 mol%.[174]

2.5.6 (1-x)BiFeO$_3$ - xBi$_{0.5}$K$_{0.5}$TiO$_3$ Solid Solution

Crystal Structure and Phase Stability

Complete solid solubility along the (1-x)BFO - xBKT composition line has been reported by several groups in recent years where the rhombohedral crystal structure of BFO prevails for $x < 0.4$-0.6 and the tetragonal structure of BKT is observed for $x > 0.75$-0.9. A pseudo-cubic region is reported between the rhombohedral and tetragonal phases.[50,110,111,175–177] The onset of the pseudo-cubic structure at $x = 0.4$ has been confirmed by TEM observations of polar nanoregions in an otherwise non-polar matrix.[176] Bennet et al.,[111] however, found that the rhombohedral structure prevailed for $x < 0.6$. Figure 2.21 shows room temperature XRD patterns of (1-x)BFO - xBKT for $x = 0.1$-0.9 where the (113) super-reflection due to rhombohedral symmetry is visible for $x \leq 0.3$. The high T_C of BFO (825 °C) decreases with increasing BKT content and reaches 400-450 °C at $x = 0.4$ which is on the level of pure BKT.[28,110,177,178]

Matsuo *et al.*[110] suggested an MPB at $x \approx 0.4$ based on an enhanced P_r and effective piezoelectric strain coefficient but the same behavior was not observed for the permittivity and ϵ_{max}/E_{max} (ϵ_{max} is the maximum strain induced by the applied field, E_{max} is the maximum electric field). Later reports point towards an MPB for $x \approx 0.75$ where a maximum of the room temperature permittivity and electric field induced polarization and strain is observed.[50] However, it is noted that as x decreases, it may be difficult to separate the effect of altered piezoelectric/ferroelectric properties from the effect of increasing leakage currents and E_C, making comparable characterization more challenging.

The rhombohedral lattice distortion of (1-x)BFO - xBKT ($x = 0.2$) varies with relatively small variation of the A:B-ratio.[179] While addition of ≤1 mol% excess A-cations provided materials with little rhombohedral distortion, addition of 2 mol% excess A-cations provided a significant rhombohedral splitting. This corresponds to the observations in BNT where the lattice distortion is also observed to be dependent on small variations of the nominal composition.[127]

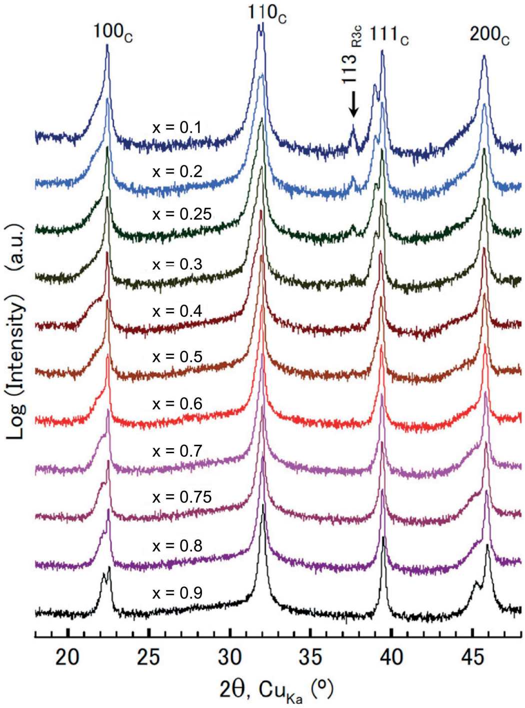

Figure 2.21: XRD patterns along the (1-x)BFO - xBKT composition line showing the transition from tetragonal (BKT) via pseudo-cubic to rhombohedral (BFO) crystal structure. Adapted from Morozov *et al.*[50]

Electrical Conductivity

The room temperature electrical conductivity of (1-x)BFO - xBKT in air decreases with increasing BKT content for x = 0.2-0.6.[110] The atmosphere and temperature dependent conductivity for x = 0.3-0.9 has been investigated by Morozov *et al.*[178,180] Heating ceramics with $x \leq 0.6$ in a low P_{O_2} atmosphere (N_2) will first reduce the conductivity from ~400 °C before continued heating above ~600 °C leads to an increased conductivity, all relative to the conductivity in air. The process was reversible upon heating in a high P_{O_2} atmosphere (O_2).[180] Figure 2.22 further demonstrates that the room temperature conductivity is highly sensitive to thermal annealing in various atmospheres with x = 0.3.[178] The behavior corresponds well with the point defect chemistry of BFO described previously and is also analogous to what has been reported with respect to p-/n-type semiconductor behavior of BFO, as discussed in Chapter 2.5.5. Annealing in varying P_{O_2}

is expected to change the concentration of $V_O^{\cdot\cdot}$ and the valence state of Fe in BFO (Eqs. 2.16 and 2.17), which will influence the conductivity of a material with a hopping type mechanism. Furthermore, adding excess A-cations has shown to increase the conductivity of 0.8BFO - 0.2BKT while excess B-cations decreased the conductivity.[179]

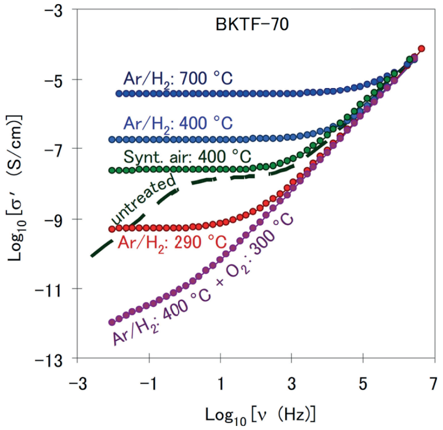

Figure 2.22: Real AC conductivity of 0.7BFO - 0.3BKT as a function of frequency at room temperature after different thermal and atmospheric treatments.[178]

Dielectric and Electromechanical Properties

A maximum in the room temperature permittivity for (1-x)BFO - xBKT was observed at x = 0.75 as summarized in Figure 2.23a. The temperature dependent permittivity has been investigated by several and shows a sharper peak near T_C or T_m when approaching the BFO end-member, corresponding to the pseudo-cubic to rhombohedral symmetry transition (Figure 2.23b).[175,177,178]

Maxwell-Wagner type relaxations resulting in giant permittivity peaks at T < 300 °C have been reported for x=0.1-0.9.[178] The origin of the giant permittivity was suggested to be a charge depletion layer near the oxide-electrode interface which could be reversibly removed and induced by annealing in selected atmospheres.

The macroscopic electric field induced polarization and strain of (1-x)BFO - xBKT were shown by several authors to decrease with increasing BFO content for x < 0.75, with $P_r \approx 12\ \mu C/cm^2$ at x = 0.4.[50,111,177] Matsuo *et al.*[110] on the other hand observed peak $P_r = 52\ \mu C/cm^2$ at x = 0.4 for

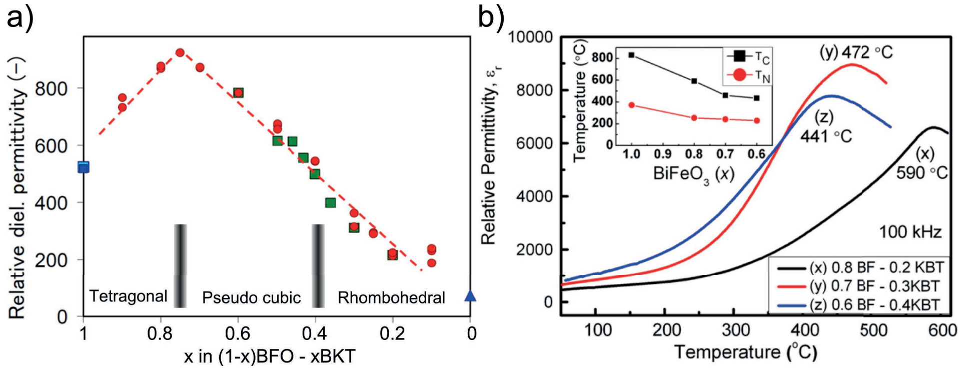

Figure 2.23: Relative dielectric permittivity of (1-x)BFO - xBKT at room temperature (a) and the relative dielectric permittivity as a function of temperature (100 kHz) for x = 0.2 - 0.4 (b). Data in (a); red circles,[50] blue square,[34] green squares[110] and blue triangle.[41] Figures adapted from Morozov *et al.*[50] and Bennett *et al.*[177], respectively.

the investigated range x = 0.2-0.6. A discrepancy with respect to composition has also been reported for the d_{33} vs. the d^*_{33} which shows peak values at x = 0.4 and 0.6, respectively.[111] The electric field induced strain in conventionally fabricated 0.7BFO - 0.3BKT ceramics is reported as < 0.12 % for unipolar measurements at 100 kV/cm and < 0.07 and ~0 % peak-to-peak for bipolar measurements at 85 and 60 kV/cm, respectively.[50,110,111,177] The strain is also dominated by electrostrictive effects with a small negative strain, as noted by Bennett *et al.*[111]

Recently the electric field induced strain of (1-x)BFO - xBKT (x = 0.3) ceramic annealed in N_2 showed peak-to-peak values > 0.25 % from bipolar measurements, values that are on the level of pure BFO.[42,180] It has also been reported that doping (1-x)BFO - xBKT (x = 0.4) with CuO contributes to opening of the P-E loop.[181] The large variation in observed performance illustrates that it is challenging to characterize these materials, especially in the BFO rich end of the composition line. The thermal and atmospheric history of the material is important and small variations in the synthesis method were recently shown to influence the leakage current characteristics of x = 0.4 ceramics.[180,182]

Recent reports have shown that substitution of BKT with PT in (1-x)BFO - xBKT ($x \approx 0.44$, the pseudo-cubic relaxor part of the composition line) promotes a long range ferroelectric order.[111] The compositions lie along the line between the MPBs of BFO-BKT and BFO-PT. The tetragonality increases with increasing PT content, along with ferroelectric contributions to electric field induced strain and the squareness of the P-E loop.[111] A high electric field induced strain of 0.805 % was obtained.[183] Relatively high d_{33} values up to 228 pC/N was also reported in this system with T_C exceeding that of PZT.[183,184]

2.6 Electrical Conductivity of Sub-Stoichiometric Oxides

The development of lead-free piezoelectrics and ferroelectrics is to a large extent focused on perovskites that contain volatile A-site elements (Bi, Na and K). It is hence expected that the as-produced ceramics will be sub-stoichiometric if the loss of volatile elements is compensated for.[13,41,122,126] Point defects are important for the performance of piezo- and ferroelectric material through aging and domain wall pinning as discussed in Chapter 2.2, but can also be directly relevant for the electrical conductivity of the material. Sub-stoichiometric oxides such as $LaFeO_{3-\Delta}$ (LF), where Δ denotes the deviation from nominal oxygen stoichiometry, have been investigated for many years due to the close relation between electrical conductivity and the point defect chemistry. This relation has, however, gained little attention in the piezo- and ferroelectric community. The total electrical conductivity in semiconductors (σ_{tot}) with localized charge carriers (such as LF) is given by the concentration of charge carriers (C), their mobility (μ) and the charge of each charge carrier (Eq. 2.18).[185]

$$\sigma_{tot} = \sum_i C_i \mu_i q_i \tag{2.18}$$

Here, i denotes the charge carrier species. The dominating charge carriers in LF are electrons and electron-holes localized at iron lattice sites, giving Fe^{2+} and Fe^{4+}, respectively.[185] The concentration of electrons and electron-holes is governed by the electroneutrality condition and the mass balance of Fe as given by Eq. 2.14 and 2.15, respectively. In the case of LF, V_{Bi}''' in Eq. 2.14 would be exchanged with lanthanum vacancies. Additionally, the concentration of $V_O^{\cdot\cdot}$ in materials with a multivalent cation, such as Fe in LF, is related to the P_{O_2} through Eq. 2.16 and 2.17. The multivalent cation allows the concentration of charge carriers to be controlled by controlling the P_{O_2} and hence the electrical conductivity of the material (Eq. 2.18).

Figure 2.24a shows how the conductivity of $La_{0.75}Sr_{0.25}FeO_{3-\Delta}$ (LSF) varies with P_{O_2} at several temperatures. The conductivity is first reduced when changing from a high to a low P_{O_2} and passes through a minimum before it subsequently increases. The minimum in conductivity is the crossover from p-type to n-type conductivity where the dominating charge carrier changes from electron-holes to electrons. This crossover is accompanied by a change of the sign of the Seebeck coefficient (S; Figure 2.24b) which is positive when the dominating charge carrier is positive and negative when the dominating charge carrier is negative.[185–187]

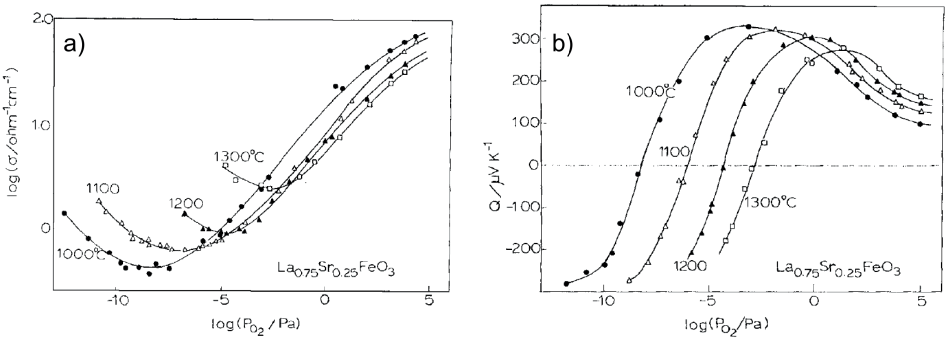

Figure 2.24: The DC electrical conductivity (a) and Seebeck coefficient (b) of LSF as a function of temperature and P_{O_2}.[186]

In summary, the volatility of A-site elements in lead-free ferroelectrics, and especially in BFO, point towards a P_{O_2} dependent electrical conductivity. Both p- and n-type conductivity in BFO have been observed experimentally[51,138,153–155] and predicted theoretically[52,156,157] but there are no systematic studies of the P_{O_2} dependency of the electrical conductivity of BFO.

Chapter 3

Experimental

3.1 Material Synthesis

3.1.1 BKT-BNZ

(1-x)BKT-xBNZ powders (x = 0, 0.05, 0.10, 0.15, 0.20, 0.30, 0.40, 0.50, 0.60, 0.70, 0.80, 0.90 and 1, batch size ~ 50 g) and sintered ceramics were produced by conventional solid state synthesis as outlined in Figure 3.1 from oxide and carbonate precursors. Abbreviations and compositions of all the materials are defined in Table 3.1. The precursors, Bi_2O_3 (99.9%, Aldrich, Germany), Na_2CO_3 (99.99%, Aldrich), K_2CO_3 (99.99%, Aldrich), TiO_2 (99.9%, Aldrich) and ZrO_2 (Tosoh, Japan), were dried in a vacuum furnace (200 °C, ~12 h) prior to weighing of stoichiometric amounts. Mixing was performed by ball milling with 5 mm yttria-stabilized zirconia balls (Tosoh, Japan) in isopropanol (~24 h). The ZrO_2 precursor was premilled the same way to break up agglomerates before drying, weighing and mixing with the other precursors. The ball milled slurry of precursors was dried using a rotavapor (Buchi, Switzerland) and the powder mixture was subsequently calcined in an alumina crucible covered by an alumina lid. The calcined powder was ball milled by the same procedure as for the precursor mixture. The calcined and milled powders were dried using a rotavapor and a drying furnace (100 °C). The dried powder was sieved through a 250 μm sieve. Green bodies were formed by uniaxial pressing (50-100 MPa, 2 min) and subject to cold isostatic pressing (200 MPa, 2 min). The green bodies were surrounded by sacrificial powder of the same composition during sintering. The calcination and sintering was done in a chamber furnace (ambient air). The temperatures and duration of the calcination and sintering steps were optimized to obtain dense and phase pure ceramics for each composition, as given in detail in Table 3.1. The heating and cooling rate was kept constant at 300 °C/h.

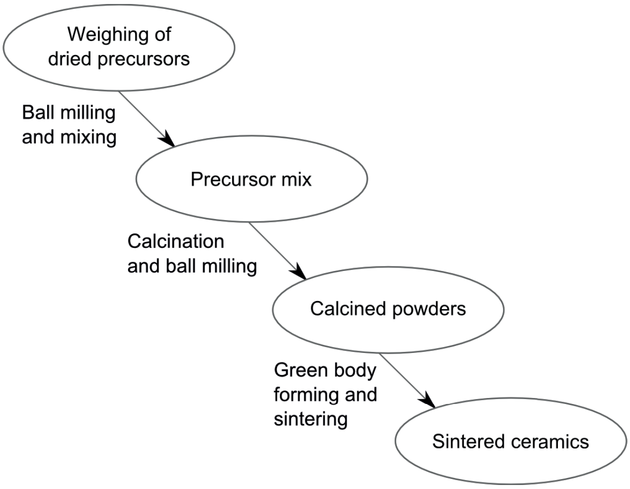

Figure 3.1: Solid state synthesis route for fabrication of powders and ceramics.

3.1.2 BFO-BKT

(1-x)BFO - xBKT powders (x = 0.1, 0.2 and 0.3, batch size ∼ 50 g) and sintered ceramics were produced by conventional solid state synthesis as outlined in Figure 3.1 from oxide and carbonate precursors. The Fe:Ti-ratio of the materials was varied according to the following compositions; $Bi_{0.95}K_{0.05}Fe_{0.9-y}Ti_{0.1+y}O_3$ and $Bi_{0.90}K_{0.10}Fe_{0.8-y}Ti_{0.2+y}O_3$ (0.9BFTy and 0.8BFTy, respectively) by Fe/Ti-substitution. Excess A-cation materials were also produced where the Fe:Ti- and A:B-ratio was varied according to the following composition; $(Bi_{0.85}K_{0.15})_{1+z}(Fe_{0.7-y}Ti_{0.30+y})O_3$ (0.7BFTyez). For all composition series, y = -0.01, 0, 0.01, 0.03, 0.06 and z = 0, 0.005. Abbreviations and compositions of all the materials are defined and summarized in Table 3.2. The precursors, Bi_2O_3 (99.9% and 99.999%, Aldrich, Germany), K_2CO_3 (99.99%, Aldrich), TiO_2 (99.9% and 99.99%, Aldrich) and Fe_2O_3 (99.999%, Aldrich), were dried in a vacuum furnace (200 °C, ∼12 h) prior to weighing of stoichiometric amounts. The higher purity chemicals were used for all experiments except for y = -0.01 and 0.06 and measurement of DC conductivity, Seebeck coefficient, atmosphere dependent dielectric spectroscopy of 0.8BFTy and high temperature XRD. Mixing was performed by ball milling with 5 mm yttria-stabilized zirconia balls (Tosoh, Japan) in isopropanol (∼16 h). The ball milled slurry of the mixture of precursors was dried using a rotavapor (Buchi, Switzerland) and the powder mixture was subsequently calcined in an alumina crucible covered by an alu-

Table 3.1: Calcination and sintering temperature for materials in the (1-x)BKT - xBNZ system, abbreviated xBNZ, for x = 0.05, 0.10, 0.15, 0.20, 0.30, 0.40, 0.50, 0.60, 0.70, 0.80 and 0.90, and BKT and BNZ for x = 0 and 1, respectively.

Abbreviation	Composition	Calcination	Sintering
BKT	$Bi_{0.5}K_{0.5}TiO_3$	700 °C - 3 h	1060 °C - 3 h
0.05BNZ	$Bi_{0.50}K_{0.475}Na_{0.025}Ti_{0.95}Zr_{0.05}O_3$	700 °C - 3 h	1050 °C - 10 h
0.10BNZ	$Bi_{0.50}K_{0.45}Na_{0.05}Ti_{0.90}Zr_{0.10}O_3$	700 °C - 3 h	1050 °C - 3 h
0.15BNZ	$Bi_{0.50}K_{0.425}Na_{0.075}Ti_{0.85}Zr_{0.15}O_3$	700 °C - 3 h	1050 °C - 10 h
0.20BNZ	$Bi_{0.50}K_{0.40}Na_{0.10}Ti_{0.80}Zr_{0.20}O_3$	700 °C - 3 h	1050 °C - 10 h
0.30BNZ	$Bi_{0.50}K_{0.35}Na_{0.15}Ti_{0.70}Zr_{0.30}O_3$	750 °C - 3 h	1000 °C - 10 h
0.40BNZ	$Bi_{0.50}K_{0.30}Na_{0.20}Ti_{0.60}Zr_{0.40}O_3$	750 °C - 3 h	980 °C - 10 h
0.50BNZ	$Bi_{0.50}K_{0.25}Na_{0.25}Ti_{0.50}Zr_{0.50}O_3$	750 °C - 3 h	980 °C - 10 h
0.60BNZ	$Bi_{0.50}K_{0.20}Na_{0.30}Ti_{0.40}Zr_{0.60}O_3$	750 °C - 3 h	980 °C - 10 h
0.70BNZ	$Bi_{0.50}K_{0.15}Na_{0.35}Ti_{0.30}Zr_{0.70}O_3$	750 °C - 3 h	980 °C - 10 h
0.80BNZ	$Bi_{0.50}K_{0.10}Na_{0.40}Ti_{0.20}Zr_{0.80}O_3$	750 °C - 3 h	875 °C - 3 h
0.90BNZ	$Bi_{0.50}K_{0.05}Na_{0.45}Ti_{0.10}Zr_{0.90}O_3$	700-1050 °C - 3 h	-
BNZ	$Bi_{0.5}Na_{0.5}ZrO_3$	750 °C - 3 h	850 °C - 3 h

Table 3.2: Calcination and sintering temperature for materials in the (1-x)BFO - xBKT system with y = -0.01, 0, 0.01, 0.03, 0.06 and z = 0, 0.005. Abbreviations are defined such that 0.9BFT0 denotes y = 0, 0.9BFT1 denotes y = 0.01 and so on, while 0.7BFT1e5 denotes y = 0.01 and z = 0.005. The sintering procedures are defined in Table 3.3.

Abbreviation	Composition	Calcination	Sintering procedure
0.9BFTy	$Bi_{0.95}K_{0.05}Fe_{0.9-y}Ti_{0.1+y}O_3$	800 °C - 5 h	S7
0.9BFT0	$Bi_{0.95}K_{0.05}Fe_{0.90}Ti_{0.10}O_3$		
0.9BFT1	$Bi_{0.95}K_{0.05}Fe_{0.89}Ti_{0.11}O_3$		
0.9BFT3	$Bi_{0.95}K_{0.05}Fe_{0.87}Ti_{0.13}O_3$		
0.9BFT6	$Bi_{0.95}K_{0.05}Fe_{0.84}Ti_{0.16}O_3$		
0.8BFTy	$Bi_{0.90}K_{0.10}Fe_{0.8-y}Ti_{0.2+y}O_3$	820 °C - 5 h	S1, S2
0.8BFT0	$Bi_{0.90}K_{0.10}Fe_{0.80}Ti_{0.20}O_3$		
0.8BFT1	$Bi_{0.90}K_{0.10}Fe_{0.79}Ti_{0.21}O_3$		
0.8BFT3	$Bi_{0.90}K_{0.10}Fe_{0.77}Ti_{0.23}O_3$		
0.8BFT6	$Bi_{0.90}K_{0.10}Fe_{0.74}Ti_{0.26}O_3$		
0.7BFTyez	$(Bi_{0.85}K_{0.15})_{1+z}(Fe_{0.7-y}Ti_{0.30+y})O_3$	790 °C - 5 h	S1, S2, S3, S4, S5, S6
0.7BFT0e0	$(Bi_{0.85}K_{0.15})_{1.000}(Fe_{0.70}Ti_{0.30})O_3$		
0.7BFT1e0	$(Bi_{0.85}K_{0.15})_{1.000}(Fe_{0.69}Ti_{0.31})O_3$		
0.7BFT0e5	$(Bi_{0.85}K_{0.15})_{1.005}(Fe_{0.70}Ti_{0.30})O_3$		
0.7BFT1e5	$(Bi_{0.85}K_{0.15})_{1.005}(Fe_{0.69}Ti_{0.31})O_3$		

mina lid. The calcined powder was ball milled by the same procedure as for the precursor mixture. The calcined and milled powders were dried using a rotavapor and a drying furnace (100 °C). The dried powder was sieved through a 250 μm sieve. The particles that were to large to pass through the sieve were crushed with a mortar and put back in the sieve until everything passed through the sieve. Green bodies were formed by uniaxial pressing with the pressure kept as low as possible to avoid delamination, and subsequently cold isostatic pressing (200 MPa, 2 min) before sintering. The green bodies were surrounded by sacrificial powder of the same composition during sintering. The calcination and sintering was performed in a chamber furnace (ambient air) at temperatures and duration as given in Table 3.2. The sintering procedures, specified for each material in Table 3.2, are defined in Table 3.3. All 0.9BFTy ceramics were sintered by the S7 procedure while all 0.8BFTy ceramics were sintered by the S1 procedure unless otherwise is specifically stated. The heating/cooling rates were 300 °C/h during calcination and 120 °C/h during sintering.

Table 3.3: Sintering procedures used for production of BFO-BKT ceramics.

Sintering procedure	Temperature, [°C]	Time, [h]	Sacrificial powder
S1	1010	2	Yes
S2	1010	10	Yes
S3	1010	20	Yes
S4	1020	2	No
S5	1010	2	No
S6	1010	10	No
S7	980	2	Yes

3.2 Characterization

3.2.1 X-ray Diffraction

The crystal structure of all materials was investigated using powder X-ray diffraction (XRD) on powder that was prepared by crushing sintered pellets and subsequently annealing the crushed powder above T_C. (1-x)BKT - xBNZ (x = 0-1) was annealed at 600 °C for 12 h, 0.7BFTyez and 0.8BFTy were annealed at 800 °C for 6-12 h and 0.9BFTy was annealed at 850 °C for 6 h. Room temperature X-ray diffractograms were obtained for 2θ = 10-90° (with exceptions 0BNZ, 0.10BNZ and 0.20BNZ: 15-110°; 0.90BNZ and 1BNZ: 20-60°) with a step size of 0.0078 and 5.2-15.6 s/step on a Siemens 5005 diffractometer with CuK$_\alpha$ radiation source and a secondary monochromator (Karlsruhe, Germany). The powder was dispersed on a Si single crystal sample holder using ethanol.

High temperature powder XRD (HTXRD) of BKT, 0.8BFT0 and 0.9BFT0 was performed using a Bruker D8Advance diffractometer with CuK$_\alpha$ radiation, a VANTEC-1 position sensitive detector and an MRI Physikalische Geräte GmbH high temperature camera (Karlsruhe, Germany) on crushed and annealed pellets. BKT was dispersed on a Pt heating strip and heated to 600 °C (200 °C/h) while diffractograms were recorded for 2θ = 15-100° with step size 0.016° and 2 s/step. A diffractogram was recorded before and after heating, every 20 °C up to 260 °C, every 10 °C from 270 to 520 °C and every 20 °C from 520 to 600 °C. 0.8BFT0 and 0.9BFT0 were packed in an alumina sample holder and heated to 760 °C (200 °C/h) by a radiant heater placed within the high temperature camera (MRI Physikalische Geräte GmbH). The temperature was calibrated against an Al_2O_3 standard and gave an estimated error of ±15 °C. Diffractograms were collected over an angular range of 20-75° 2θ with step size 0.016° and 1 s/step. A diffractogram was collected before and after the heating cycle, every 50 °C up to 510 °C and every 10 °C above 510 °C.

Lattice parameters were determined by Pawley refinement using the Topas software.[188] A simple axial model with modified Thompson-Cox-Hastings psudo-Voigt (TCHZ) peak shapes was used for room temperature patterns where lattice parameters were allowed to converge before sample displacement and peak shapes were added to the refinement. Chebychev background polynomials (8-10 orders) were used and the LP factor was set to 26.6. The HTXRD patterns of 0.8BFT0 and 0.9BFT0 were refined using a full axial model with TCHZ peak shapes. The lattice parameters were allowed to converge before sample displacement and peak shape were refined. Chebychev background polynomials (12 orders) were used. The full-width-half-maximum (FWHM) of selected diffraction lines (background signal subtracted) was determined using the DIFFRAC.EVA software.[189]

3.2.2 Density

The density of sintered ceramics was measured by the Archimedes method (ISO 5017:1998(E)) in isopropanol and the theoretical density was calculated from lattice parameters obtained by refinement of XRD data.

3.2.3 Scanning Electron Microscopy

Phase purity, microstructure and homogeneity were investigated on polished or thermally etched ceramics using scanning electron microscopy (SEM; Hitachi S-3400N, Japan). SiC paper was used to grind off the as-sintered surface (200-300 μm) to remove any surface effects after sintering. The surface was subsequently polished using diamond suspensions with consecutive particle diameters $9 \rightarrow 3 \rightarrow 1$ μm and finally a colloidal silica suspension (MD-Plan, Dur, Nap and Chem polishing cloths with corresponding suspension, Struers). Thermally etched samples were annealed 50-100 °C below the sintering temperature for 5-15 min.

Phase purity was examined by SEM using backscattered electrons on polished (not thermally etched) sintered ceramics. The microstructure was examined on thermally etched samples using secondary electrons in the SEM. The chemical composition of polished ceramics (not thermally etched) was examined by energy dispersive X-ray spectroscopy (EDS; X-MAX, Oxford Instruments, UK). Samples were typically covered by a thin carbon layer to provide sufficient conductivity and an acceleration voltage of 15-25 kV was used. No standards were used for the EDS analysis.

3.2.4 Transmission Electron Microscopy

0.8BFT0 and 0.8BFT-1 ceramics were examined by TEM. The 0.8BFT0 sample was prepared by mechanical tripod wedge polishing followed by low-energy Ar^+-ion milling with liquid N_2 cooling of the sample during milling, as described by Eberg *et al.*[190] The 0.8BFT-1 sample was prepared by mechanical grinding, dimpling and Ar^+-ion milling with liquid N_2 cooling of the sample during milling and the acceleration voltage of the Ar^+-ions was progressively reduced from 3.5 kV to 1.0 kV at the final stage of the milling.

TEM was performed on a cold-FEG JEOL ARM 200F with both probe and image spherical aberration correction operated at 200 kV. The TEM was equipped with a large solid angle (0.98 sr) Centurio silicon drift detector for EDS and a fast Quantum ER GIF with DualEELS which allows for simultaneous acquisition of EDS and electron energy loss spectroscopy (EELS) data. EDS and EELS data were obtained in scanning TEM (STEM) mode with a 5C probe (probe size 1 Å), 40 μm condenser aperture (probe current 120 pA) and 1.5 cm camera length. Selected area electron diffraction (SAED) was used to investigate the local crystal structure.

3.2.5 Differential Thermal Analysis

Differential thermal analysis (DTA; STA 449 C, Netzsch) of crushed and annealed samples was used to determine phase transition temperatures. An alumina crucible was filled with 100-300 mg powder and heated to 750 °C at 40 °C/min (0.7BFTyez), 750 °C at 10 and 40 °C/min (0.8BFTy) or 800 °C at 10 °C/min (0.9BFTy) in synthetic air (30 mL/min) and held at the maximum temperature for 5 min before cooling with the same rate as heating. The temperature was calibrated versus the melting points of Zn, Al and Au.

3.2.6 DC Electrical Conductivity

The DC conductivity of 0.8BFT0 and 0.9BFT0 was measured by the four point method using an in-house built setup previously described by Wærnhus.[191] Figure 3.2 shows a schematic of the sample mounting and key features.

Sintered bars were ground to dimensions of about 22 x 4.5 x 3 mm using #220 SiC carbide grinding paper and Pt-paste was used to ensure sufficient contact between the current probes and the sample. A DC voltage of 1.4-1.5 V was applied (GW Instek GPS3030DD) over the sample. The resulting voltage drop and current across the sample was measured by the voltage electrodes (placed 5 mm apart) and current electrodes, both connected to Keithley 2000 multimeters. The temperature was controlled by an S-type thermocouple. The isothermal DC conductivity was allowed to stabilize at 700, 750 and 800 °C at a constant P_{O_2} before the temperature was reduced to 650 °C where the conductivity again was allowed to nearly stabilize before a new P_{O_2} was introduced. The gas flow and P_{O_2} was controlled (Brooks 0154 Flow controller) by mixing N_2 and O_2 (Yara Praxair, 5.0) to give P_{O_2} = 1, 0.2,

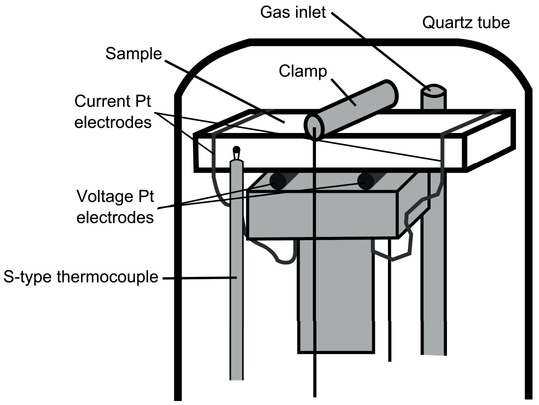

Figure 3.2: Schematic setup for four point measurement of DC conductivity. Adapted from Wærnhus.[191]

0.02, 0.002, 0.000002 atm with flow rates of 50, 250, 250, 500, 500 mL/min, respectively. The sequence of P_{O_2} was 0.2, 1, 0.02, 0.002 and 0.000002 atm (0.8BFT0) and 1, 0.2, 0.02, 0.002 and 0.000002 atm (0.9BFT0). The electrical conductivity was measured continuously, also when temperature or atmosphere was altered, for a total time of 640 and 770 h for 0.8BFT0 and 0.9BFT0, respectively.

3.2.7 Seebeck Coefficient

The Seebeck coefficient of 0.8BFT0 and 0.9BFT0 was measured at 650, 700, 750 and 800 °C on ceramic bars similar to those used for DC conductivity measurements. The sample was mounted vertically in a Probostat^{TM} setup (NorECs AS, Norway) as shown in Figure 3.3a and covered by an outer alumina tube, allowing controlled atmosphere. The setup was placed inside a tubular furnace where the middle thermocouple was connected to the temperature controller. All measurements in a given P_{O_2} were finished at all temperatures before the temperature was reduced to 650 °C. A new atmosphere was introduced after a stable sample response was observed at this low temperature. The measurements were first done in O_2, then in N_2 and finally in synthetic air (Yara Praxair, 5.0) with manual flow control. Total measurement time from start to finish was 533 h and 159 h for 0.8BFT0 and 0.9BFT0, respectively. The top and bottom thermocouple and electrodes were connected to a computer through a multimeter (Kiethley 2000). The Omega software (NorECs AS, Norway) was used to read the voltage difference between the top and bottom electrode (ΔV) and the temperature difference between the top and bottom S-type thermocouples (ΔT, typically 20-25 °C). The Seebeck coefficient was then calculated as S = ΔV/ΔT.

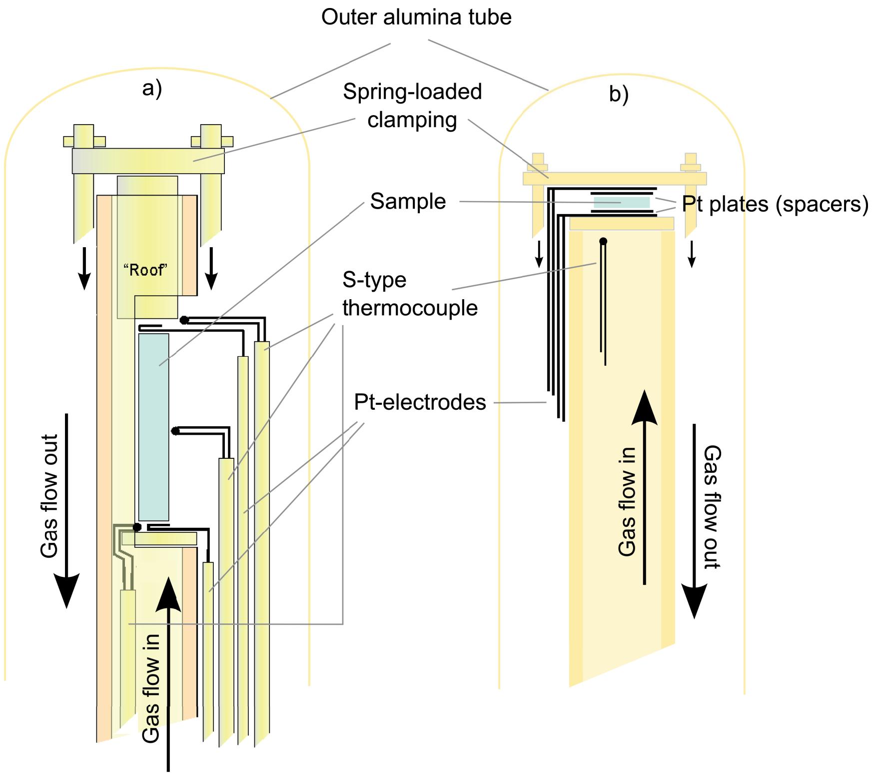

Figure 3.3: Schematic sample setup for Seebeck measurements (a) and for dielectric spectroscopy (b). Figure a) adapted from NorECs AS.[192]

3.2.8 Dielectric Spectroscopy

Dielectric properties of all materials (except 0.30BNZ, 0.40BNZ and 0.50BNZ) were investigated using a frequency analyzer (Alpha-A high performance frequency analyser, Novocontrol Technologies, Germany) connected to a Probostat^{TM} (NorECs AS, Norway) mounted in a vertical tubular furnace. A combined electrode and heating unit (Novotherm, Novocontrol Technologies, Germany) was used instead of the Probostat^{TM} and the tubular furnace for 0.30BNZ, 0.40BNZ, 0.50BNZ. Surface effects after sintering were ground off (200-300 μm) by SiC paper from both faces of disk shaped ceramic pellets (diameter 7-9 mm). The discs were subsequently cleaned in an ultrasonic bath and electroded by gold sputtering.

Measurements in both heating setups were performed during continuous heating/cooling (120 °C/h) every 30 s at frequencies $10^6 \to 1$ Hz with 1 AC Volt driving voltage. A room temperature scan was carried out before and after every heating cycle at frequencies $10^7 \to 10^{-2}$ Hz. The dielectric response of 0.30BNZ, 0.40BNZ, 0.50BNZ ($T \leq 400$ °C) was measured in ambient air (2-wire mode) limited by the experimental equipment. All measurements performed using the Probostat$^{\text{TM}}$ setup in 4-wire mode were done in a controlled atmosphere of synthetic air, N_2 and/or O_2 (Yara Praxair, 5.0) with manual flow control. The setup is shown in Figure 3.3b and data was collected and analyzed using the software provided together with the frequency analyzer (WinDETA, Novocontrol Technologies, Germany). The reported data for the BKT-BNZ materials are recorded after one heating cycle to the maximum temperature. For BFO-BKT samples, an initial heating cycle to $T > 300$ °C was performed in synthetic air to remove Maxwell-Wagner relaxations.[178] The reported temperature dependent data are from a second heating cycle to the maximum temperature and the room temperature data were recorded after this second heating with some exceptions. The atmosphere dependent conductivity of 0.8BFTy (Figure 6.6 and 6.7) is reported after the materials were heated one time in synthetic air, N_2 and finally O_2. The temperature dependent dielectric properties of 0.7BFT0e0 sintered by different sintering procedures (Figure 9.8) is reported after only one heating to 720 °C and the room temperature data were recorded after this one heating. The atmosphere dependent dielectric properties of 0.7BFT0e0 were obtained after several heating cycles to 720 °C in synthetic air before different atmospheres were introduced (Figure 9.11). The samples were not removed from the experimental setup between consecutive heating cycles.

3.2.9 Ferroelectric Characterization

The electric field induced polarization and stain was investigated using a piezoelectric evaluation system (TF Analyzer 2000, aixACCT Systems GmbH, Germany). The samples were submerged in silicone fluid (Wacker AK 100, Darwin Vertriebs, Germany) during testing to avoid arcing.

Disc shaped ceramic BKT-BNZ pellets (diameter 7-8 mm) were prepared by grinding off at least 200-300 μm from the major faces, cleaning (acetone and ultrasonic bath) and application of a silver electrode (cured at 200 °C, 12 h). Several bipolar measurements were performed at each electric field strength to allow the polarization and strain response to stabilize, before increasing the electric field (5 kV/cm increments). Unipolar measurements were subsequently performed, starting at low field strengths where the response was allowed to stabilize before increasing the electric field (5 kV/cm increments). The field strength was increased to a maximum (60 kV/cm) before the field was reduced (5 kV/cm decrements) with stabilization of the response at each field strength. Dielectric breakdown was typically observed for electric field $>$ 60 kV/cm, however, a few samples were exposed to 80 kV/cm before breakdown was observed. The frequency of the applied field was 0.25 Hz.

Disc shaped ceramic 0.7BFTyez pellets (diameter $\sim$4 mm) were prepared by grinding off at least 200-300 μm from the major faces, cleaning (acetone and ultrasonic bath) and application of gold electrode by sputtering. In addition to as-sintered 0.7BFTyez ceramics, pellets were annealed in air at 710 °C (30 min), 710 °C (24 h) and 1000 °C (30 min) and quenched to ambient temperature by removing them from the furnace, before being prepared for ferroelectric characterization by grinding and electroding. Two sets of 0.7BFTyez pellets were prepared by grinding to the final thickness before annealing in $P_{O_2} = 0.01$ at 710 °C (30 min) and quenching to ambient temperature. One of these sample sets were electroded before the annealing and one was electroded after the annealing.

3.2.10 Mechanical Characterization

Stress-strain measurements were performed to investigate the ferroelastic properties of 0.8BFTy and 0.9BFTy. The samples were prepared by grinding cylindrical ceramics to remove any surface effects from sintering and to obtain uniform dimensions ($\sim$6 mm hight, 5.8 mm diameter). Special care was taken to ensure parallel faces of the cylinder. The samples were subsequently heated (300 °C/h) above T_C in air using a chamber furnace to 710 °C (0.8BFTy) and 780 °C (0.9BFTy) and kept at this temperature for 30 min to relieve stresses induced by the grinding. Cooling was either done in the furnace (300 °C/h) or by quenching to ambient temperature where the sample was removed from the furnace at $T>T_C$. The annealing above T_C was repeated between each stress-strain measurement and all samples were tested within 14 h after cooling. The samples were placed on an alumina plate covered by an alumina crucible during heat treatment (in the presence of sacrificial powder) to reduce the loss of Bi_2O_3 and K_2O.

A separate set of 0.8BFTy ceramics were annealed in different atmospheres before mechanical stress-strain measurements were done at 100 °C. These ceramics were first annealed in air for 30 min before being quenched to ambient temperature from the same furnace as described above. Mechanical stress-strain measurements were performed before the samples were annealed in N_2 at 740 °C for 3 h 40 min using tube furnace with manual flow control for the gas. The sample was subsequently quenched to ambient temperature by removing it from the furnace. The same procedure was followed when finally annealing in O_2 at 740 °C for 3 h 12 min. The temperature of the two different furnaces was calibrated against each other.

The stress-strain measurements were performed in a load frame (Z030, Zwick GmbH & Co.KG, Germany) fitted with a split furnace for heating (SV800, Thermal Technology GmbH).[93] The setup is shown in Figure 3.4. The sample and the above conical tungsten carbide load bearing was centered on a tungsten carbide plate by two alignment fixtures before a small preload (100 N / ~3.8 MPa) was applied to ensure contact and alignment. The strain developed during loading was measured by two alumina rods in contact with the top and bottom tungsten carbide load bearings and two linear variable differential transducers (LVDT, Figure 3.4). The strain originating from the sample and the tungsten carbide was then taken as the difference between the strain measured by the two LVDTs. The true sample strain was extracted by calibration of the setup using Al_2O_3 cylinders. The error of the measured remanent strain and coercive stress is normally 2 % and 5 %, respectively, based on previous measurements with this setup.[93,193]

The loading and unloading rates were constant (4 MPa/s) throughout a measurement loading cycle. However, some loading cycles were aborted before the programmed maximum stress (σ_{max}) was reached to avoid potential breakage of sample and subsequently equipment. Measurements at elevated temperature (100, 200, 300 and 400 °C) were done by heating to the set temperature (300 °C/h) and letting the temperature stabilize for 5-15 min (longer time for lower temperatures). An experiment was also performed where quenched 0.8BFT0 was mounted in the setup and kept at 400 °C for 2 and 7 h before a load cycle was applied. The temperature was controlled by a K-type thermocouple and all stress-strain measurements were done in ambient air.

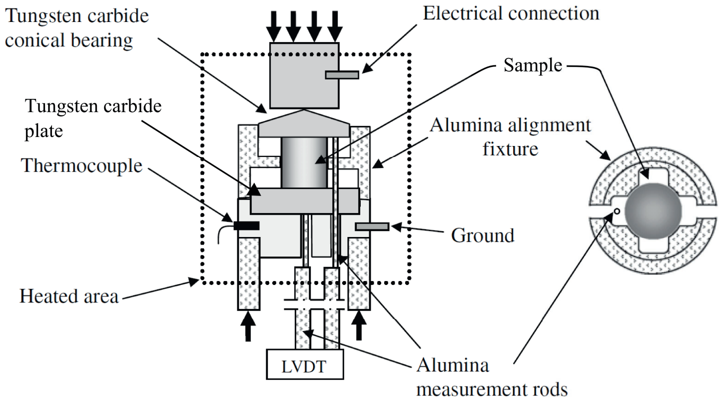

Figure 3.4: Schematic setup and sample loading for compressive stress-strain measurements. Adapted from Webber *et al.*[93]

The coercive stress was determined by finding the minimum of $d\sigma/d\epsilon$ (numerical derivation) which was smoothed by a 20 point moving average. The smoothed curve was fitted to a polynomial and the minimum of this polynomial was taken as the coercive stress.

A non-linear behavior at low stress levels ($< \sim 100$ MPa) was observed in the stress-strain hysteresis loop after some experiments. This stems from an instrument artifact and results in a larger maximum strain at σ_{max} than is provided by the sample alone. ϵ_r is, however, not affected because it is obtained after stress removal.

Chapter 4

Solid-State Synthesis and Properties of Relaxor BKT-BNZ Ceramics

4.1 Results

4.1.1 Crystal Structure and Microstructure

Solid state synthesis was used to produce materials along the (1-x)BKT - xBNZ composition line (x = 0-1) as described in Chapter 3.1.1. The calcination and sintering temperatures are given in Table 3.1. Room temperature X-ray diffractograms for the whole series of materials are shown in Figure 4.1 and Pawley refinement was used to determine the lattice parameters which are summarized in Table 4.1 and shown in Figure 4.2. The diffractograms were indexed and refined with the tetragonal P4mm space group for $x \leq 0.10$, the cubic $Pm\bar{3}m$ space group for the pseudo-cubic region ($0.15 \leq x \leq 0.80$) and the orthorhombic Pnma space group for x = 1 (BNZ). The space groups used for BKT and BNZ are in line with previous reports.[33,38,117] An increasing lattice parameter is apparent with increasing BNZ content, corresponding to the leftward shift of diffraction lines in Figure 4.1.

The nominal chemical composition for $x \leq 0.50$ was confirmed by EDS on polished ceramics. The materials were phase pure at high BKT content but a small amount of secondary phase was observed for $x \geq 0.20$ (Figure 4.1). The secondary phase observed for x = 0.80 and 1 is suggested to be $Bi_2Zr_2O_7$[194] based on EDS analysis.

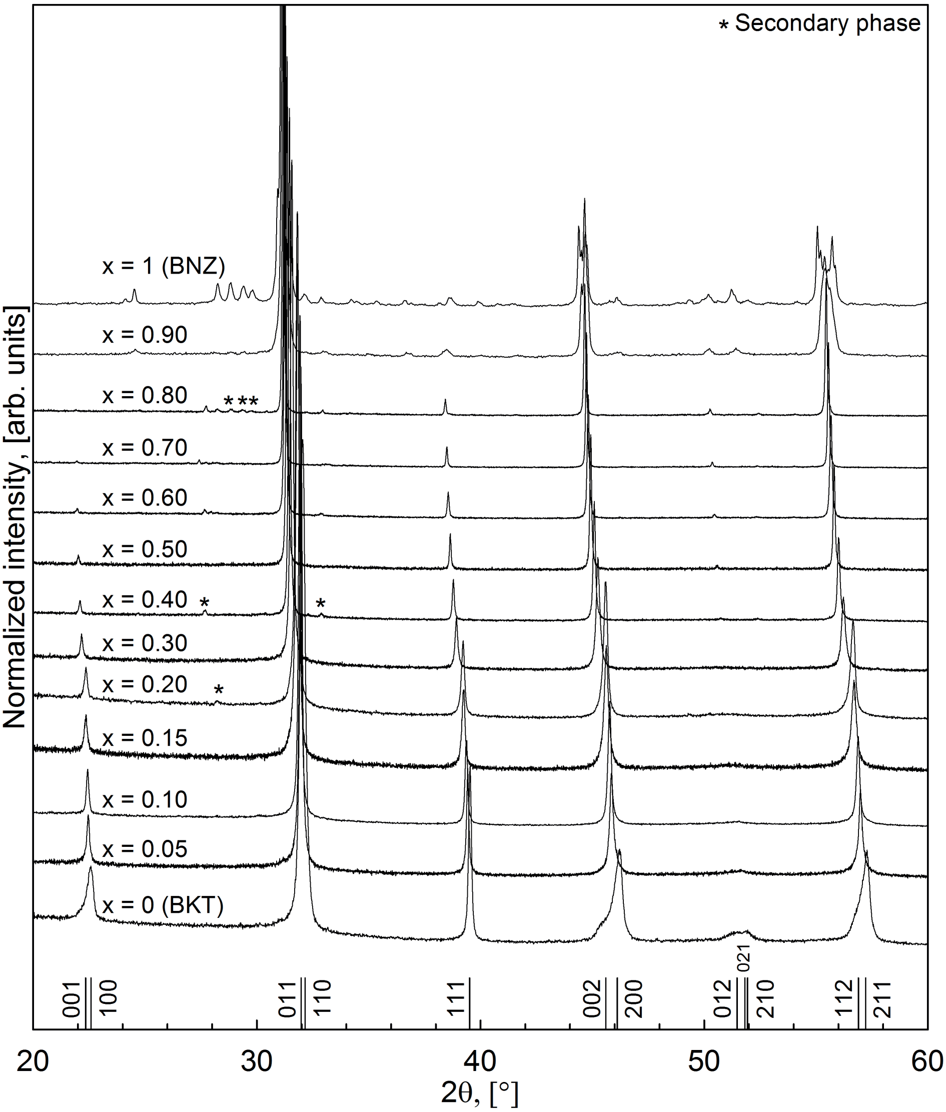

Figure 4.1: Room temperature X-ray diffractograms for (1-x)BKT - xBNZ with x = 0-1. The indices are obtained by Pawley refinement of the tetragonal BKT (x = 0) diffractogram and the diffractograms are normalized to the maximum intensity of the (011)/(110) reflection.

Table 4.1: Tabulated unit cell parameters, piezoelectric (60 kV/cm) and dielectric data for the (1-x)BKT - xBNZ materials.

Composition	Cell parameters, [Å]			P_{max} [μC/cm^2]	$\epsilon_{b,max}$ [%]	$\epsilon_{u,max}/E_{max}$ [pm/V]	ε'_{max} @ 10 kHz
	a	b	c				
x = 0 (BKT)	3.933(3)	-	3.975(4)	12	0.03	46	2575 (368°C)
x = 0.05	3.954(6)	-	3.962(8)	14	0.04	62	2954 (319°C)
x = 0.10	3.96(2)	-	3.96(2)	21	0.08	116	3296 (298°C)
x = 0.15	3.975(1)	-	-	13	0.04	61	3507 (255°C)
x = 0.20	3.9799(8)	-	-	14	0.04	61	2555 (233°C)
x = 0.30	4.0042(7)	-	-	10	0.02	36	1788 (212°C)
x = 0.40	4.0186(4)	-	-	7	0.01	16	1217 (232°C)
x = 0.50	4.0325(4)	-	-	4	0.01	9	906 (251°C)
x = 0.60	4.0416(3)	-	-	-	-	-	-
x = 0.70	4.0508(2)	-	-	-	-	-	-
x = 0.80	4.0585(3)	-	-	-	-	-	-
x = 1 (BNZ)	5.787(4)	8.162(5)	5.694(3)	-	-	-	-

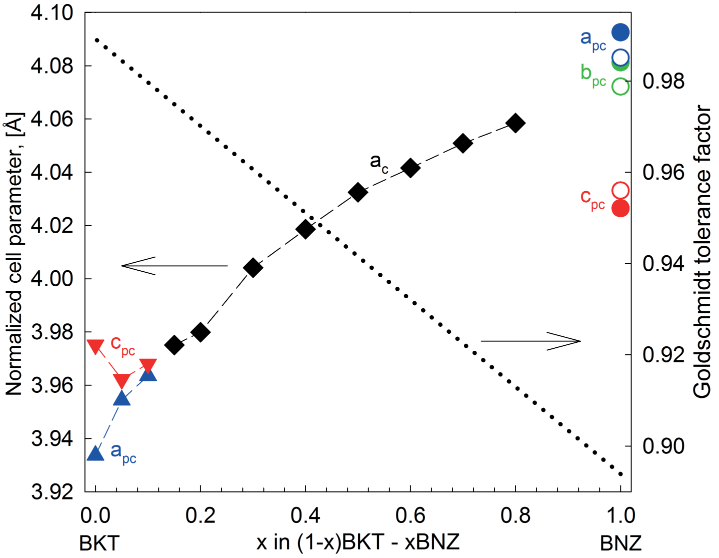

Figure 4.2: Pseudo-cubic (a_{pc}, b_{pc} and c_{pc}) and cubic (a_c) lattice parameters of (1-x)BKT - xBNZ (x = 0-1) determined by Pawley refinement. Tetragonal lattice parameters are given as $a_t = a_{pc}$ and $c_t = c_{pc}$ while orthorhombic lattice parameters are normalized by $a_{pc} = 2^{-1/2}a_{orth}$, $b_{pc} = 0.5b_{orth}$ and $c_{pc} = 2^{-1/2}c_{orth}$.* The filled symbols are from this work and open circles from Jaiban *et al.*[38] The dotted line is the Goldschmidt tolerance factor and the dashed line is a guide to the eye.

Dense ceramics (relative density ≥ 96 %) were obtained for materials of compositions $x \leq 0.50$, $x = 0.80$ and $x = 1$, as listed in Table 4.2. The grain size was relatively constant for $x \leq 0.30$ while significantly larger grains were observed for $x = 0.40$ and $x = 0.50$ (Table 4.2). SEM micrographs of the microstructure, shown for selected compositions of $x \leq 0.50$ in Figure 4.3, reveal exaggerated grain growth resulting in an inhomogeneous grain size.

Selected diffractograms from powder HTXRD of BKT ($x = 0$) are presented in Figure 4.4. The tetragonal splitting of the (100)/(001) diffraction lines gradually decreases with increasing temperature, and completely disappears between 300 and 400 °C in line with the phase transitions discussed in Chapter 2.5.2.

---

[*] The lattice parameters are here normalized as pseudo-cubic to facilitate comparison but are not related to a_{pc} and c_{pc} for BFO defined in Chapter 2.5.5.

Table 4.2: Relative density and grain size for the (1-x)BKT - xBNZ materials as obtained using the optimized synthesis protocols.

Composition	Density, [%]	Grain size, [μm]
x = 0 (BKT)	97 ± 0.6	0.2 ± 0.01
x = 0.05	97 ± 0.4	0.2 ± 0.02
x = 0.10	96 ± 0.9	0.3 ± 0.03
x = 0.15	98 ± 0.8	0.4 ± 0.01
x = 0.20	96 ± 0.7	0.5 ± 0.05
x = 0.30	96 ± 1	0.6 ± 0.06
x = 0.40	96 ± 0.7	2.0 ± 0.1
x = 0.50	96 ± 0.6	4.8 ± 0.5
x = 0.60	92 ± 2	-
x = 0.70	93 ± 0.5	-
x = 0.80	96 ± 0.5	-
x = 0.90	-	-
x = 1 (BNZ)	96 ± 1	-

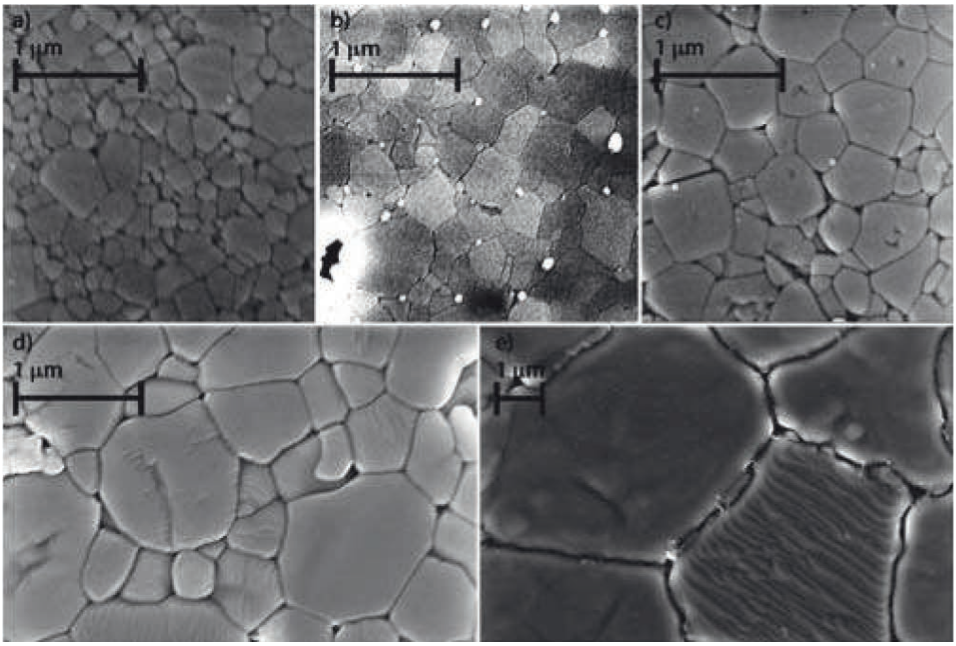

Figure 4.3: SEM micrographs (secondary electrons) of thermally etched surfaces of ceramics obtained for BKT (x = 0) (a), 0.10BNZ (b), 0.15BNZ (c), 0.30BNZ (d) and 0.50BNZ (e, note the larger scale).

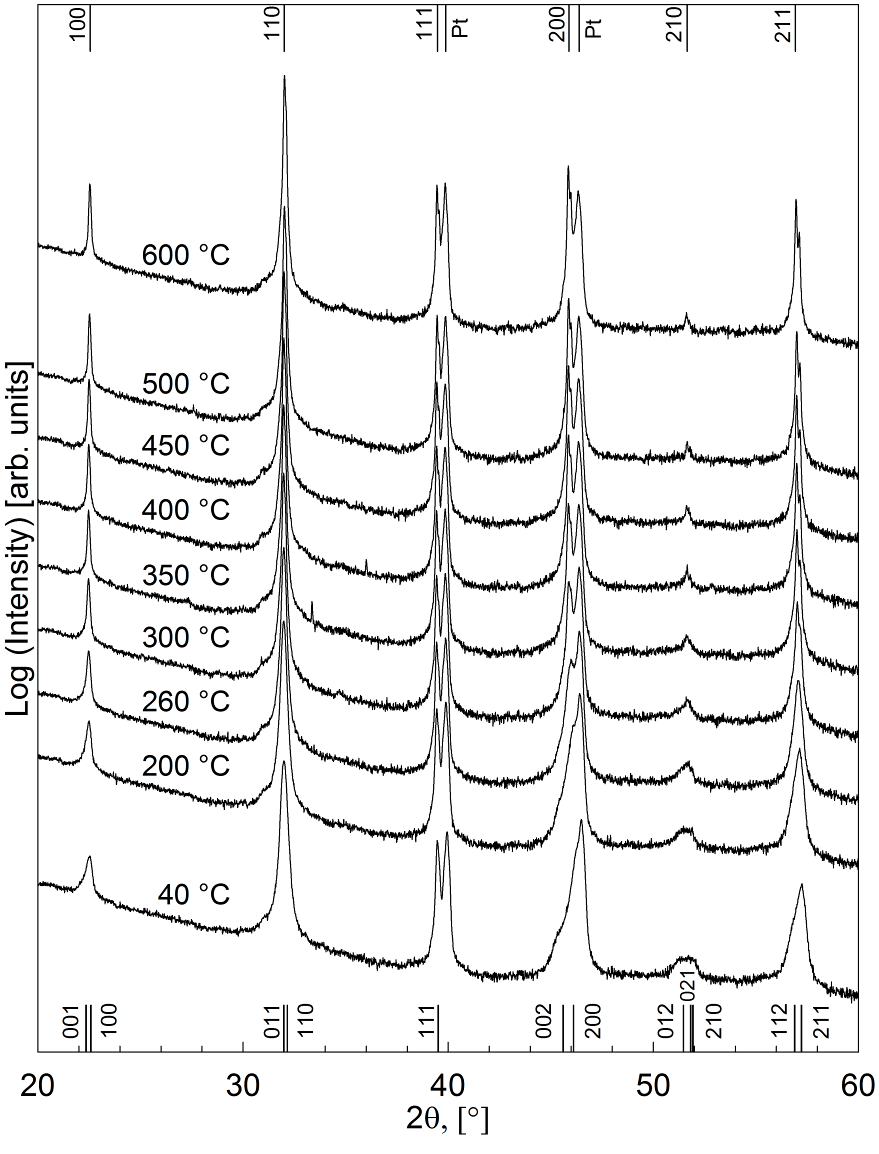

Figure 4.4: Powder HTXRD diffractograms of BKT (x = 0). The lower indices are tetragonal diffraction lines as determined by Pawley refinement of a room temperature pattern while the upper indices are related to the cubic high temperature phase. The diffraction lines resulting from the Pt-sample stage are also included.

4.1.2 Dielectric and Electromechanical Response

The dielectric permittivity and loss, ε' and tan δ respectively, were investigated for x = 0-0.50. The room temperature ε' and tan δ are shown in Figure 4.5a and 4.5b, respectively. The permittivity is in reasonable agreement with other reported values for the ternary reciprocal BKT-BNZ system (see also Figure 4.11). Some variation of the permittivity and loss is observed between the compositions but there is no systematic variation.

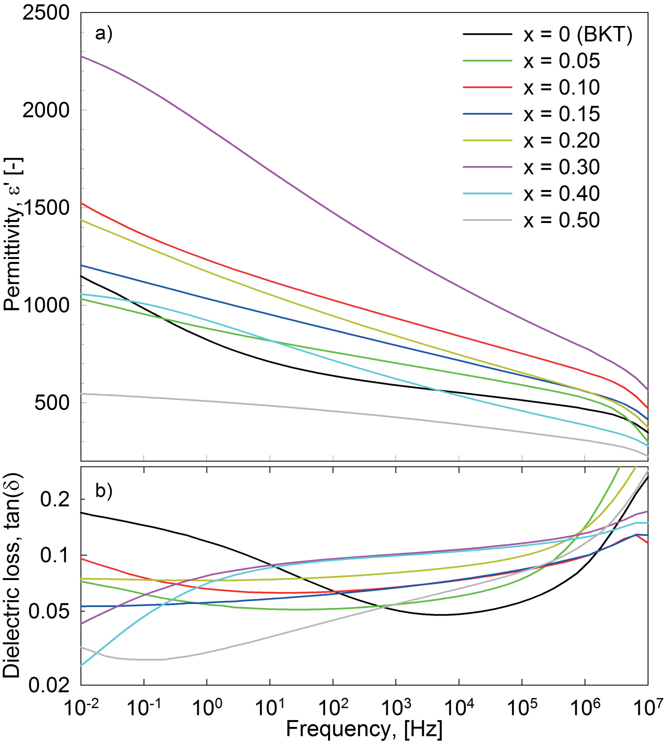

Figure 4.5: Room temperature permittivity (a) and dielectric loss (b) as a function of frequency of the samples used for electromechanical testing for (1-x)BKT - xBNZ (x=0-0.5).

The high temperature ε' at 10 kHz for x = 0-0.15 and 0.20-0.50 is shown in Figure 4.6a and 4.6b, respectively. The permittivity at T_m increases with increasing BNZ content up to x = 0.15, where $\varepsilon' = 3507$ is observed at 255 °C. The permittivity peaks and the maximum ε' (ε'_{max}) are less pronounced for x > 0.15 and it is difficult to identify a clear T_m for x = 0.4 and 0.5. The T_m decreases continuously with increasing BNZ content, as summarized along with the corresponding ε'_{max} in Table 4.1. The frequency dependent permittivity and dielectric loss versus temperature of 0.15BNZ is shown in Figure 4.6c and 4.6d, respectively. The large variation of T_m and ε' with frequency substantiates a relaxor-type behavior, which was also observed in all other investigated compositions.

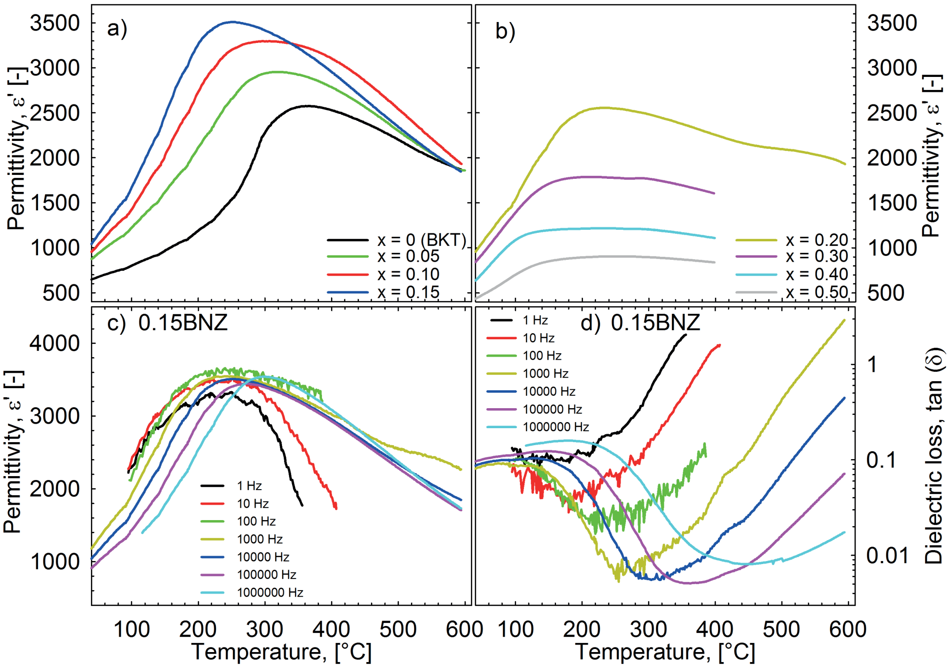

Figure 4.6: Temperature dependence of the permittivity for (1-x)BKT - xBNZ (x=0-0.5) at 10 kHz (a and b) and frequency and temperature dispersion of the permittivity and dielectric loss of 0.15BNZ (c and d).

The electric field induced polarization of x = 0-0.10 and x = 0.15-0.50 is shown in Figure 4.7a and 4.7b, respectively. The polarization increased with increasing BNZ content up to x = 0.10 where P_{max} = 20.5 μC/cm^2, before decreasing towards x = 0.50 where P_{max} = 4.4 μC/cm^2 (at 60 kV/cm). The bipolar electric field induced strain displayed the same trend as the polarization (Figure 4.7c and 4.7d). The highest bipolar strain ($\epsilon_{b,max}$) was observed for x = 0.10 with $\epsilon_{b,max}$ = 0.08 % at 60 kV/cm and decreased significally with increasing BNZ content for x $\geq$ 0.15. P_{max} and $\epsilon_{b,max}$ are summarized in Table 4.1. The ferroelectric nature of the material decreases with the addition of BNZ, as is evident from the lack of negative strain for x $>$ 0.10.

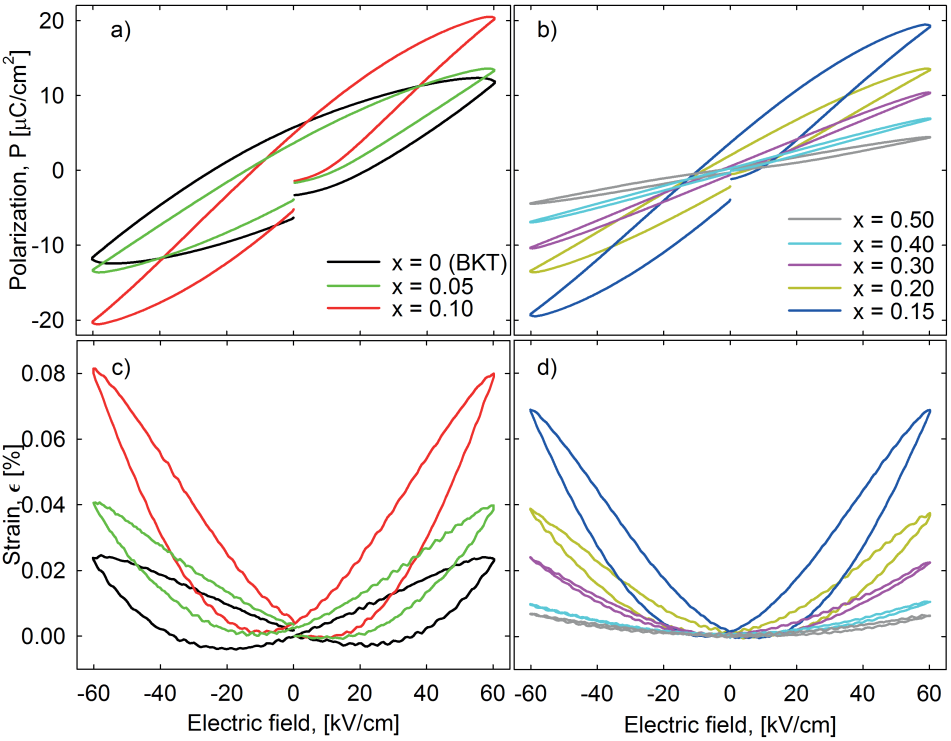

Figure 4.7: Electric field induced bipolar polarization (a and b) and strain (c and d) for sintered ceramics of composition (1-x)BKT - xBNZ (x=0-0.5).

The gradual evolution of bipolar and unipolar polarization induced by an increasing electric field strength is shown in Figure 4.8a and 4.8b, respectively, with the corresponding electric field induced strain shown in Figure 4.8c and 4.8d. The polarization increases gradually and, although the loops are not fully saturated, it is clear that ferroelectric switching occurs at the higher electric field values. The strain increases gradually with increasing electric field and shows a maximum value of 0.1 % at 70 kV/cm bipolar measurements and 0.07 % at 60 kV/cm unipolar measurements.

The peak in piezoelectric performance is also observed for the unipolar electric field induced strain which is quantified by $\epsilon_{u,max}/E_{max}$ where $\epsilon_{u,max}$ is the maximum unipolar strain with the remanent strain subtracted. The $\epsilon_{u,max}/E_{max}$ of xBNZ (x = 0-0.50) is summarized in Table 4.1 and shows the highest value for 0.10BNZ with $\epsilon_{u,max}/E_{max}$ = 116 pm/V.

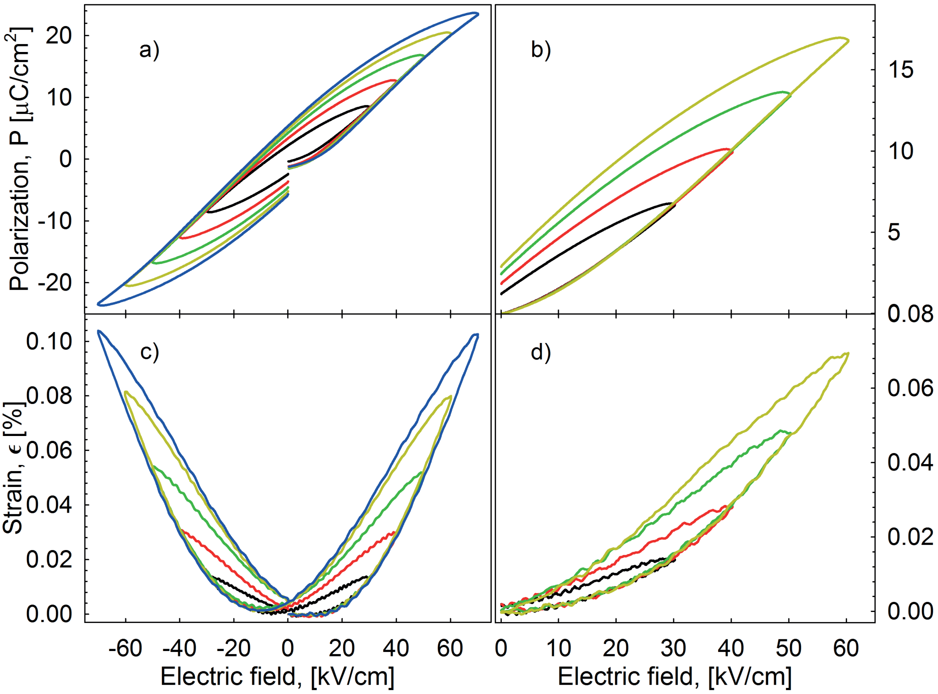

Figure 4.8: Electric field induced bipolar and unipolar polarization (a and b) and strain (c and d) for 0.10BNZ at increasing field strength.

4.2 Discussion

4.2.1 Phase Stability

Peak performance for xBNZ (x = 0-0.50) was observed at x = 0.15 with respect to ε' and x = 0.10 with respect to electric field induced polarization and strain. This is the composition region that coincides with the tetragonal to pseudo-cubic transition observed by XRD (Figure 4.1 and 4.2). A phase transition along the BKT-BNZ composition line was expected based on the different crystal structure and tolerance factor of BKT (tetragonal, t = 0.99) and BNZ (orthorhombic, t = 0.89). A phase transition where the tetragonal structure of BKT is lost has been observed in several other solid solutions as well, e.g. BKT-BKZ,[119,129] BFO-BKT,[50] BKT-BiScO$_3$[195] (BS) and BKT-BNT.[29,116,196] Common for all, including this work, is that the tetragonal structure is lost at t ≈ 0.96-0.98. The composition of the phase transition in BKT-BNT is still under debate (Chapter 2.5.4). A phase diagram for the ternary reciprocal system BKT-BNZ is suggested in Figure 4.9 based on this work and literature data. The phase diagram shows a large region with cubic/pseudo-cubic phase dominance, suggesting that a large amount of substitution of BNZ for BKT is not beneficial. The tetragonal region is constrained close to BKT which is the area of higher tolerance factor. The transition from tetragonal to pseudo-cubic occurs at x ≈ 0.10 along the BKT-BNZ composition joint and does not show the characteristics of an MPB as the transition occurs gradually.

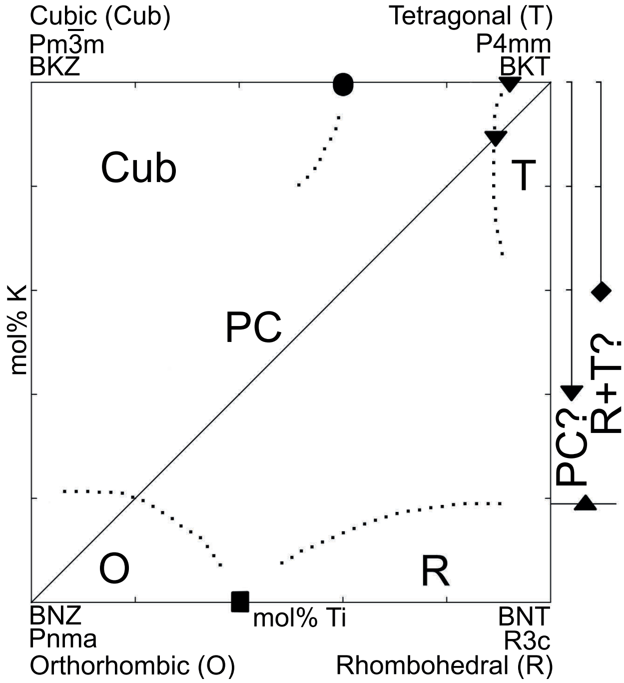

Figure 4.9: Tentative structural phase diagram in the ternary reciprocal system BKT-BNZ based on reported crystal symmetries. Solid marks along the binary joints represent reported phase transitions (PC = pseudo-cubic); circle PC-Cub,[119] triangle down T-PC[119,197] and this work, diamond T-(R+T?),[116] triangle up (PC?)/(R+T?)/T-R[29,116,197] and square R-O.[129,198] Dotted lines separate possible phase dominance areas.

All the investigated materials show relaxor-like behavior with a T_m that depends on the frequency of the driving field. This is exemplified for 0.15BNZ in Figure 4.6c where a broad frequency dependent permittivity peak is observed, typical for relaxors. The data are, however, not sufficient to attribute the behavior to any specific class of relaxors (see e.g. Bokov and Ye[89]). The dielectric dispersion increases with increasing BNZ content and both T_m and ε' decrease significantly (Table 4.1). This compositional dependence corresponds well with the transition from tetragonal to cubic/pseudo-cubic structure and a gradual loss of ferroelectricity. An apparent relaxor-like behavior has also been observed in solid solutions of BKT with BFO, BKZ or BS.[50,119,195]

The relaxor behavior observed for BKT corresponds to the crystal structure development with increasing temperature and is in accordance with earlier reports.[34,114,119] The (112)/(211) diffraction lines are split in two for the tetragonal room temperature symmetry and merge to one (211) line in the high temperature cubic symmetry (Figure 4.4). The FWHM values of the (112)/(211) reflections are shown in Figure 4.10a as a function of temperature, as extracted from the HTXRD experiment on BKT. An abrupt drop is observed at ~300 °C corresponding to the tetragonal to pseudo-cubic transition (T_2) of BKT, after which the FWHM value decreases more gradually up to and above the pseudo-cubic to cubic transition at ~400 °C.

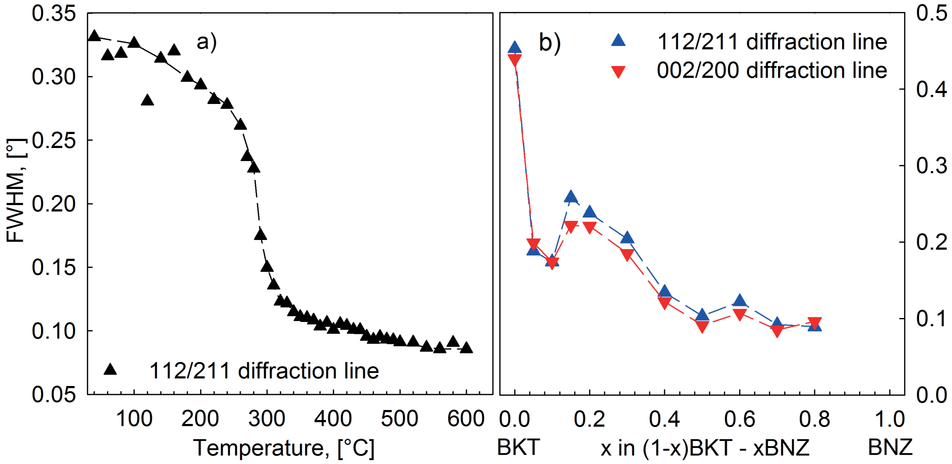

Figure 4.10: Full width half maximum of the a); (112)/(211) XRD reflections as a function of temperature for BKT (x=0) and b); (112)/(211) and (002)/(200) XRD reflections as a function of composition of (1-x)BKT - xBNZ (x=0-0.8). Dashed lines are added as guide to the eye.

The FWHM of the (112)/(211) and (002)/(200) XRD reflections along the (1-x)BKT - xBNZ composition line is included in Figure 4.10b. It is apparent that the tetragonality of BKT drops significantly already at x = 0.05 and further for x = 0.10, as would be expected for the tetragonal to pseudo-cubic transition. The increased FWHM at 0.15BNZ may originate from PNRs that are known to exist in pseudo-cubic materials. These PNRs may introduce small lattice strains that will interfer with the long range order of the cubic matrix phase and subsequently provide a "size effect" which results in peak broadening. The "size effect" induced by the PNRs will gradually disappear as the structure becomes more cubic (less PNRs are present), resulting in a more constant FWHM for x = 0.50-0.80. It cannot be ruled out, however, that the FWHM observed for x = 0.15-0.40 originates from a change of symmetry, but this was not resolved by the current XRD analysis.

It is suggested that the pseudo-cubic to orthorhombic transition in (1-x)BKT-xBNZ occurs for $0.80 < x \leq 0.90$, based on the observed orthorhombic super reflections observed for 0.9BNZ (Figure 4.1). This transition occurs in the same tolerance factor range as the rhombohedral to orthorhombic transition in BNT-BNZ.

4.2.2 Dielectric and Electromechanical Performance

The room temperature permittivity (ε'_{RT}) of BKT found in this study corresponds well with literature data (Table 2.1). The ε'_{RT} of BKT-BNZ materials summarized in Figure 4.11 show that the highest ε'_{RT} is observed in Ti-rich compositions and that substitution of Ti with large amounts of Zr in general reduces ε'_{RT}. A small amount of Zr was however found beneficial near the MPB of BKT-BNT by Hussain *et al.*[40] The 0.15BNZ composition shows the second highest permittivity of the BKT-BNZ system behind the MPB region of BKT-BNT.

Comparing the findings in this work with literature reveals that the ε'_{RT} of BKT-BNT (80 % BNT), BKT-BFO (25 % BFO) and BKT-BS (15 % BS) all show an ε'_{RT} in the range of 0.15BNZ, which is higher than the ε'_{RT} of the respective end-members.[49,99,119,195] At elevated temperatures, however, the BKT-BNT and BKT-BFO solid solutions show an ε' 2-3 times higher than what is observed for BKT-BNZ and BKT-BS.

The electric field induced polarization and strain correspond well with earlier reports on BKT.[34,120,195] Both polarization and strain increase with increasing BNZ content up to x = 0.10, however, the effect of BNZ is smaller than e.g. BFO and BNT.[50,99,110] The reduced opening of the hysteresis loops with increasing BNZ content is attributed to the increasing cubic character of the crystal structure (Figure 4.1) which reduces the lattice polarizability

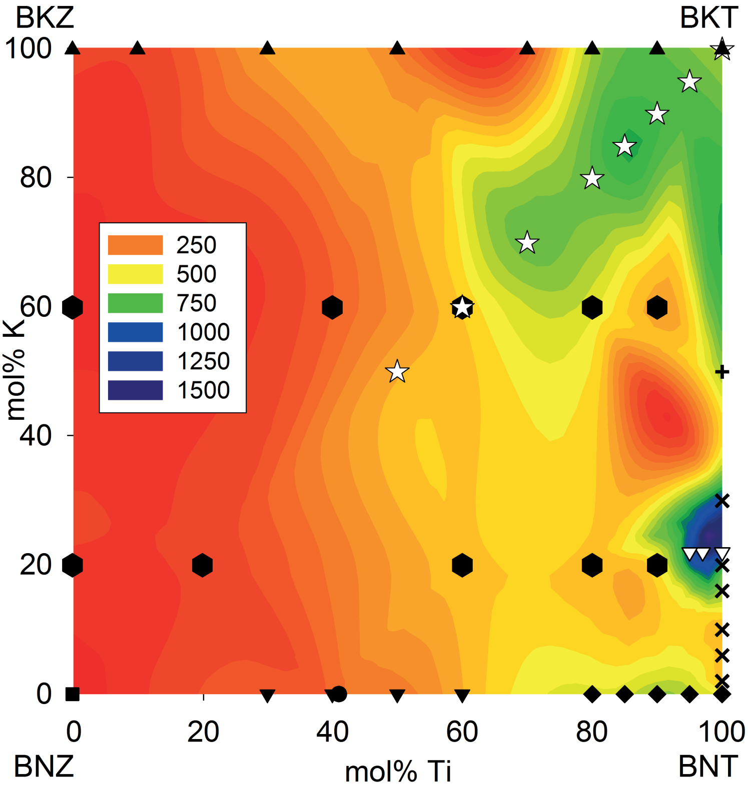

Figure 4.11: Contour plot of room temperature dielectric constants in the BKT-BNZ system. Data are gathered from the following literature (frequency = 10 kHz if not stated otherwise): stars (this work), triangle up,[119] filled triangle down,[198] open triangle down,[40] hexagons (100 kHz),[129] plus (1 MHz),[101] cross,[99] diamond,[132] square[199] and circle.[200]

and the strain effect from domain reorientation. A reduced opening of the hysteresis loops was also observed e.g. in BKT-BFO (with increasing BFO content). This is, however, probably related to domain wall pinning with high BFO content.[41,50] The size of the cations should also be accounted for with respect to the electromechanical response. The average size of the A-cation decreases while that of the B-cation increases with increasing BNZ content in BKT-BNZ, reducing the tolerance factor (Eq. 2.5 and Figure 4.2). The reduction of the tolerance factor is accommodated by tilting the oxygen octahedra. Hence the potential ferroelectric displacement of Ti^{4+} is reduced and consequently the ferroelectric response of the material decreases.[128]

The total electric field induced strain in a dielectric material is the sum of the electrostrictive contribution (Eq. 2.2) and the piezoelectric contribution (Eq. 2.4). Electrostriction may only produce positive strain due to its square dependence on the electric field while piezoelectric strain may be both positive and negative. A clear transition from piezoelectric strain response with open butterfly loops and negative strain to an electrostrictive response with more parabolic ϵ-E is apparent with increasing BNZ content (Figure 4.7c and 4.7d). The increasingly electrostrictive response is further illustrated in Figure 4.12 where electric field induced strain is plotted against the square of the applied electric field. An increasingly linear behavior is observed with increasing BNZ content which confirms that electrostriction dominates over piezoelectricity. This is rationalized by the transition from tetragonal to pseudo-cubic structure for x $\geq$ 0.15 where piezoelectric strain stems from PNRs within a non-polar cubic matrix. As the BNZ content increases, these PNRs will gradually disappear and electrostriction will have an increasingly dominating role. This is the same gradual transition that occurs in BKT where the ferroelectric domains gradually disappear between 280 and 450 °C.[114] Tetragonal to pseudo-cubic transition has also been suggested for BKT-BNT,[197] BKT-BKZ,[119] BKT-BFO[50] and BKT-BS[195] solid solutions when moving away from the BKT rich region.

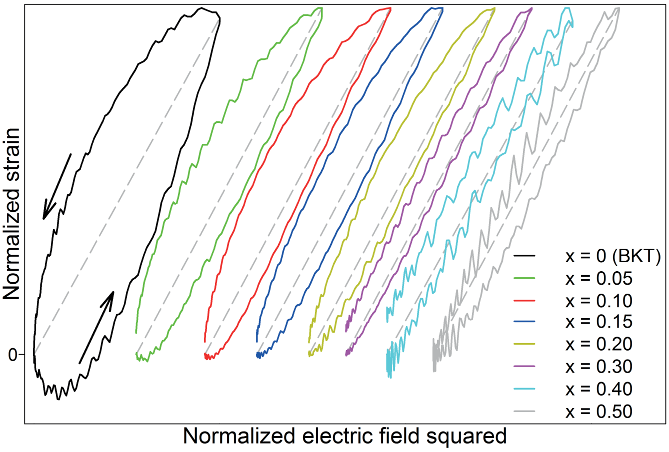

Figure 4.12: Normalized strain vs. normalized electric field squared for the positive half of a bipolar measurement. The measurements were done at 60 kV/cm and the values are normalized to the maximum value. The plots are shifted along the x-axis for clarity while the dashed grey lines are added as a guide to the eye and show the linear path from minimum to maximum electric field. The black arrows indicate the path during application of the field.

The ferroelectric polarization response observed in Figure 4.7a and 4.7b is only partly saturated and show some evidence of non ferroelectric contributions (dielectric loss), giving a rounded shape of the P-E loop.[201] However, it is argued that the measurements described herein are sufficient to consider trends for relevant properties along the (1-x)BKT - xBNZ composition joint. The P-E loops of 0.10BNZ open and the saturation increases gradually with increasing electric field strength, as shown in Figure 4.8. The measurement of electromechanical properties was normally stopped at 60 kV/cm as dielectric breakdown typically occurred at higher fields. The qualitative shape of the P-E loops did, however, not change drastically for samples that were exposed to 70 kV/cm ($x = 0.05$) or 80 kV/cm ($x = 0.10$). In addition, the coercive field of BKT is ∼50 kV/cm and it is not expected that this increases with the addition of BNZ, as BNZ reduces the tetragonality of the system.[34,100] It can also be established that the variation of electric field induced polarization is not a manifestation of losses. The dielectric loss was measured for all samples prior to ferroelectric testing (Figure 4.5b) and no trend was observed that corresponds to the trend in induced polarization (Table 4.1 and Figure 4.7a and 4.7b).

The dielectric and piezoelectric properties of (1-x)BKT-xBNZ for $x = 0.60$-1 were not studied in detail due to the observed trend up to $x = 0.50$ and challenges related to the production of ceramics of sufficient quality.

4.2.3 Microstructure

It has been noted in previous reports that the densification of BKT is challenging and hot pressing has shown to be effective to obtain highly dense BKT ceramics.[13,34,120,121] No problems were experienced with respect to the sinterability of BKT in this work. The synthesis procedure was optimized to find the lowest calcination temperature giving phase pure powders and a subsequent ball milling step was added to obtain small BKT particles. Small particles are beneficial during sintering as it increases the driving force for densification. Tabuchi *et al.*[100] have recently demonstrated the importance of small precursor particles to obtain dense BKT.

The microstructure of sintered BKT ceramics shows a grain size in line with previous reports.[34,71] The grain size increases gradually with increasing BNZ content up to $x = 0.30$ before a significant increase is observed for $x = 0.40$ and $x = 0.50$. The origin of the increased grain size is unclear. The liquidus temperature of the alkali-carbonate mixture decreases with increasing BNZ-content and is lower than the calcination temperature for x = 0.40 and 0.50, suggesting the presence of a transient liquid during calcination.[202] The effect of a liquid phase during calcination is expected to be coarsening of the calcined powder and possibly reduced density. The density was not lower for 0.40BNZ and 0.50BNZ than for the other compositions. The origin of the large grain size was not investigated further.

Chapter 5

Crystal Structure, Microstructure and High Temperature Stability of BFO-BKT

5.1 Results

5.1.1 Crystal Structure

Solid state synthesis was used to prepare (1-x)BFO - xBKT (x = 0.2, 0.1) perovskite materials with Ti^{4+}/Fe^{3+} as donor/acceptor substituents, using the procedure described in Chapter 3.1.2. The compositions are abbreviated 0.8BFTy and 0.9BFTy where y denotes the level of donor/acceptor substitution, as given in Table 3.2. Times and temperatures for calcination and sintering of all the compositions are summarized in Table 3.2. Room temperature X-ray diffractograms for 0.8BFTy and 0.9BFTy are shown in Figure 5.1 where the lower indices refer to the room temperature crystal structure of BFO. The rhombohedral splitting of the diffraction lines decreased with increasing Ti-substitution (and increased with decreasing Ti-substitution, i.e. y = -0.01), as is apparent from Figure 5.1. The decreasing/increasing splitting is also highlighted for selected reflections in Figure 5.2. The secondary phase observed for 0.8BFT3 and 0.9BFT6 was not observed by XRD on bulk as-sintered ceramics but appeared upon XRD analysis of crushed and thermally annealed powders. The secondary phase was identified as an Aurivillius type phase.

The effect of Ti-substitution on the rhombohedral distortion is further reflected in the room temperature lattice parameters of 0.8BFTy and 0.9BFTy, shown in Figure 5.3a and summarized in Table 5.1. The diffractogram for all materials could be fitted to the rhombohedral R3c symmetry. The lattice parameters display a significant contraction of the unit cell for both 0.8BFTy and 0.9BFTy with increasing Ti-substitution, where the effect is most pronounced for 0.8BFTy. The lattice distortion (c_{pc}/a_{pc}) is correspondingly reduced with increasing Ti-substitution as is presented in Figure 5.3b and summarized in Table 5.1.

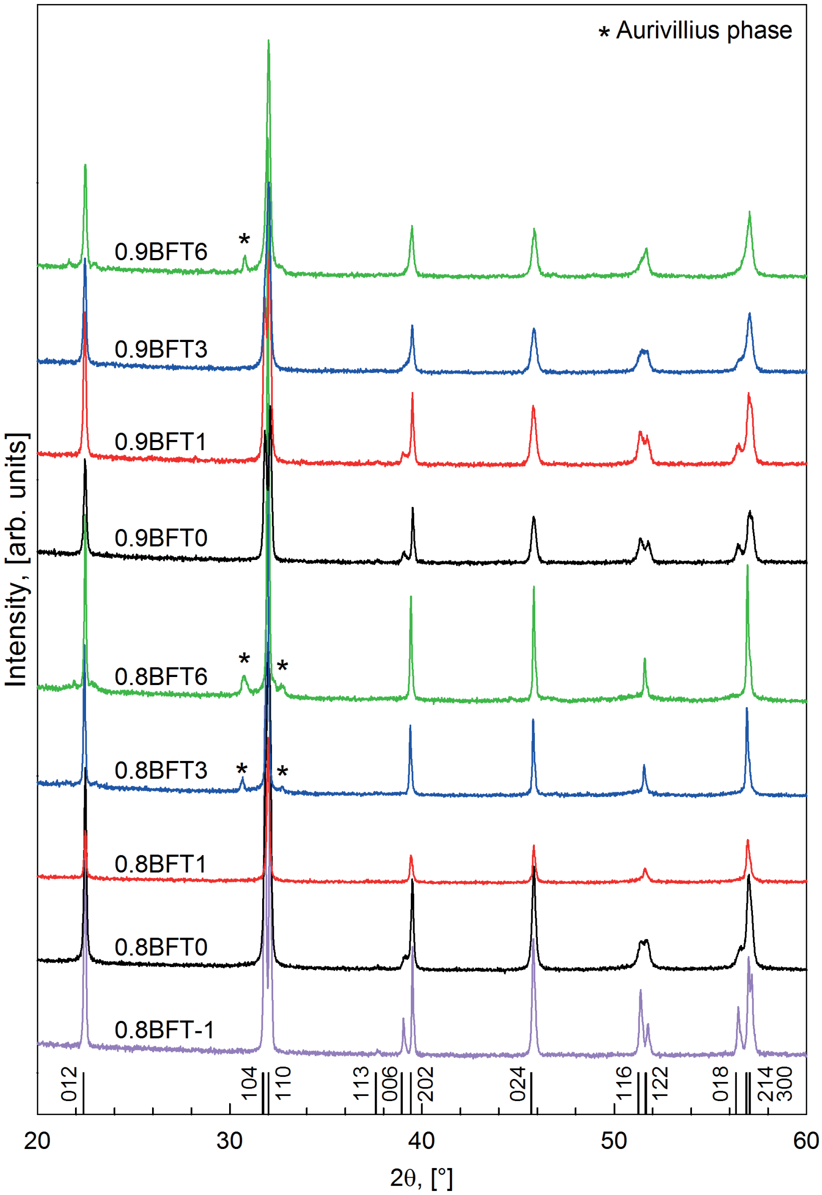

Figure 5.1: Room temperature X-ray diffractograms of 0.8BFTy and 0.9BFTy. The secondary phases in 0.8BFT3 and 0.9BFT6 appeared after thermal annealing above T_C before XRD analysis. The indices refer to the room temperature structure of BFO (ICDD nr. 04-009-3445).

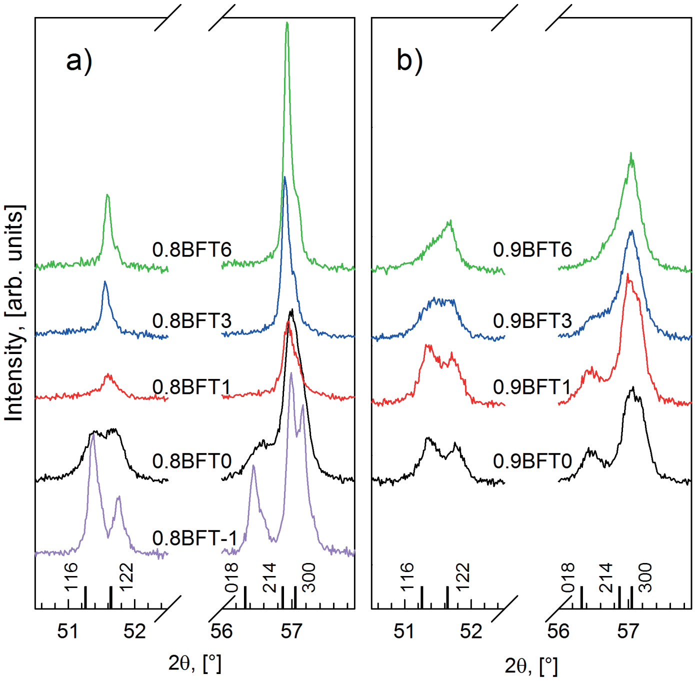

Figure 5.2: Selected diffraction lines of 0.8BFTy (a) and 0.9BFTy (b) emphasizing the decreased rhombohedral splitting with increasing Ti-substitution (increasing y). The indices refer to the room temperature structure of BFO (ICDD nr. 04-009-3445).

5.1.2 Microstructure

Dense and phase pure polycrystalline ceramics with composition 0.8BFTy and 0.9BFTy were successfully prepared from the powder made by solid state synthesis. The relative density of all the materials was ≥ 96 %. The microstructure of thermally etched 0.8BFTy and 0.9BFTy ceramics is displayed in Figure 5.4 and the grain sizes are summarized in Table 5.1. A submicron grain size is apparent for all materials except 0.8BFT-1 and 0.8BFT6, where significant grain growth was observed for 0.8BFT-1. The grain size distribution is seemingly more homogeneous in materials with higher Ti-substitution level.

Figure 5.5a and 5.5b display SEM micrographs of the surface of a polished (not thermally etched) 0.9BFT3 ceramic obtained by secondary and

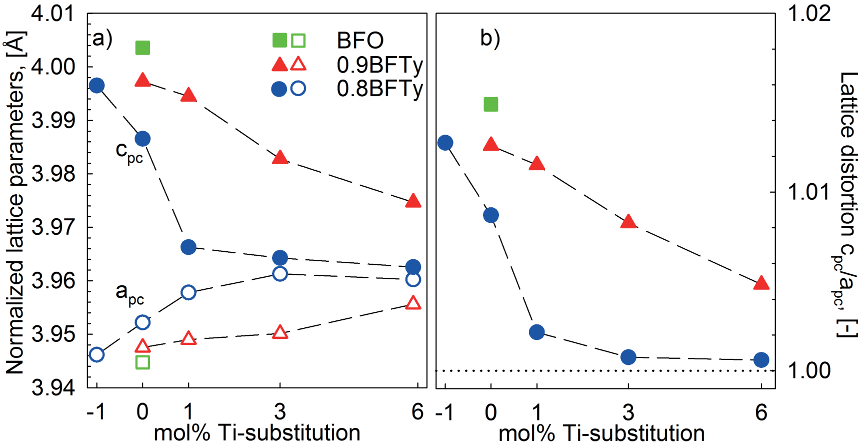

Figure 5.3: Room temperature lattice parameters (a) and the corresponding lattice distortion c_{pc}/a_{pc} (b) of 0.8BFTy and 0.9BFTy as a function of Ti-substitution. Data for pure BFO is included from Selbach *et al.*[136] Lattice parameters were normalized as follows; $a_{pc}=2^{-1/2}a_h$ and $c_{pc}=12^{-1/2}c_h$. Dashed lines are guides to the eye.

Table 5.1: Room temperature lattice parameters of 0.8BFTy and 0.9BFTy along with lattice distortion and grain size.

Material	Lattice parameters a_h, [Å]	Lattice parameters c_h, [Å]	Lattice distortion c_{pc}/a_{pc}, [-]	Grain size [μm]
0.8BFT-1	5.580(7)	13.844(3)	1.013	5.5 ± 0.2
0.8BFT0	5.589(2)	13.809(8)	1.009	0.9 ± 0.09
0.8BFT1	5.597(2)	13.74(0)	1.002	0.7 ± 0.1
0.8BFT3	5.602(1)	13.73(2)	1.001	0.9 ± 0.08
0.8BFT6	5.600(6)	13.72(7)	1.001	1.2 ± 0.09
0.9BFT0	5.582(7)	13.847(0)	1.013	0.6 ± 0.03
0.9BFT1	5.584(7)	13.837(3)	1.012	0.6 ± 0.05
0.9BFT3	5.586(3)	13.79(7)	1.008	0.6 ± 0.02
0.9BFT6	5.594(1)	13.76(9)	1.005	0.7 ± 0.04

backscattered electrons, respectively, which are representative images for both composition series. Moreover, Figure 5.5c and 5.5d show SEM micrographs (backscatter electrons) at higher magnification of the polished surfaces of 0.9BFT3 and 0.8BFT0, respectively. The nominal composition of 0.8BFTy and 0.9BFTy was confirmed by EDS. SEM micrographs of 0.8BFT6 are presented in Figure 5.5e and 5.5f, where the presence of a secondary phase is evident by the observation of elongated grains. The chemical composition of this phase corresponded to an Aurivillius phase as determined by EDS, supporting the observations by XRD (Figure 5.1).

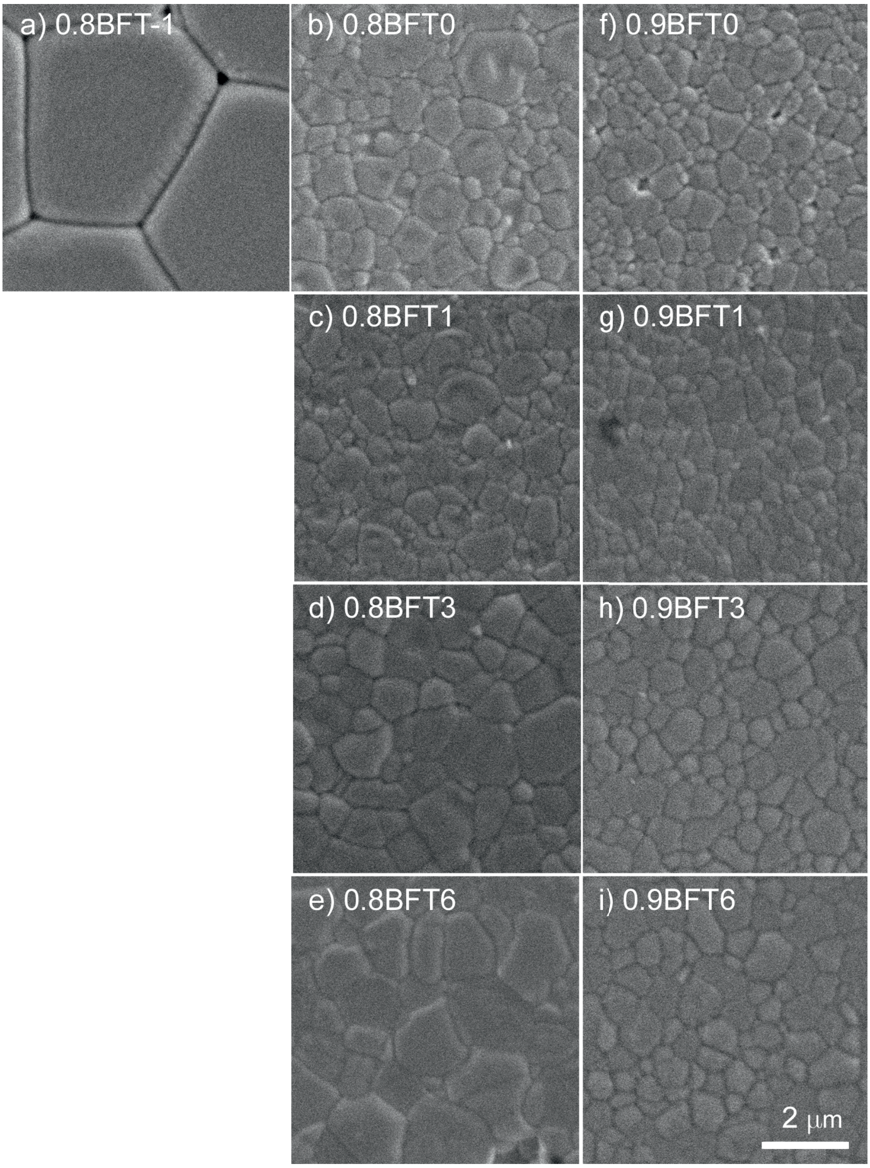

Figure 5.4: SEM micrographs of the thermally etched surface of 0.8BFTy (a-e) and 0.9BFTy (f-i) ceramics (secondary electrons).

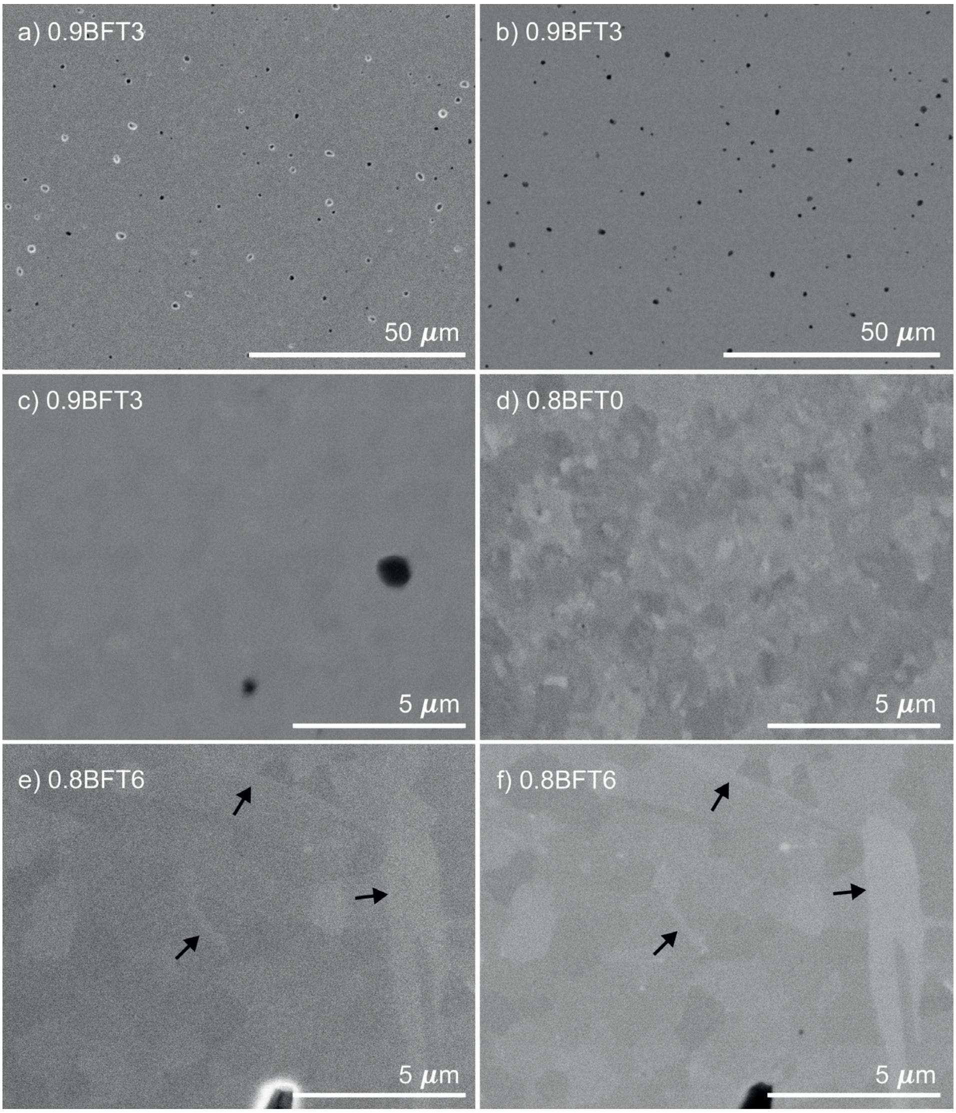

Figure 5.5: SEM micrographs of polished ceramics of composition 0.9BFT3 (a-c), 0.8BFT0 (d) and 0.8BFT6 (e and f) obtained from secondary electrons (a, e) and backscattered electrons (b, c, d, f). The arrows in e and f point towards a secondary phase.

5.1.3 Ferro- to Paraelectric Phase Transition

Selected X-ray diffractograms illustrating the thermal evolution of the crystal structure of 0.8BFT0 and 0.9BFT0 are given in Figure 5.6 and 5.7, respectively. The diffractograms were indexed to the R3c space group up to the ferroelectric to paraelectric phase transition, which occurs at 630 and 676 °C for 0.8BFT0 and 0.9BFT0, respectively. The thermal evolution of the (006)/(202) diffraction lines are shown in the insets to highlight the reduced splitting with increasing temperature. The materials were refined to the cubic Pm$\bar{3}$m space group above the phase transition. BFO has been reported to be orthorhombic Pbnm above T_C,[137] but no super-reflections related to this symmetry were observed.

The thermal evolution of the pseudo-cubic lattice parameters a_{pc} and c_{pc} of 0.8BFT0 and 0.9BFT0 is compared to those of pure BFO in Figure 5.8a. Both a_{pc} and c_{pc} increase linearly with temperature far below T_C, while a strong contraction of c_{pc} is apparent at temperatures close to T_C. A discontinuous change of the unit cell volume near the phase transition is demonstrated in the insert in Figure 5.8a, in line with the behavior of pure BFO.[46] The contraction of the c_{pc} parameter is further reflected in the abrupt change observed for the lattice distortion as shown in Figure 5.8b for 0.8BFT0, 0.9BFT0 and BFO.

The ferroelectric to paraelectric phase transition temperature was further investigated by DTA where an endothermic (exothermic) peak was observed during heating (cooling), as shown in Figure 5.9. The onset temperature and the temperature at the peak maximum/minimum is summarized for all materials in Table 5.2. The first order nature of the transition is confirmed by the hysteresis between heating and cooling for all materials. The double peak observed for 0.8BFT0 and 0.9BFT0 may be related to the successive phase transitions of BFO.[136,137] The phase transition is significantly sharper for the acceptor substituted 0.8BFT-1 and is also seen to become sharper with increasing Ti-substitution relative to the unsubstituted materials. The phase transition temperatures are shifted to slightly higher temperatures with increasing Ti-substitution but the variations are relatively small (summarized in Table 5.2), in line with earlier work on Ti-substituted BFO.[166]

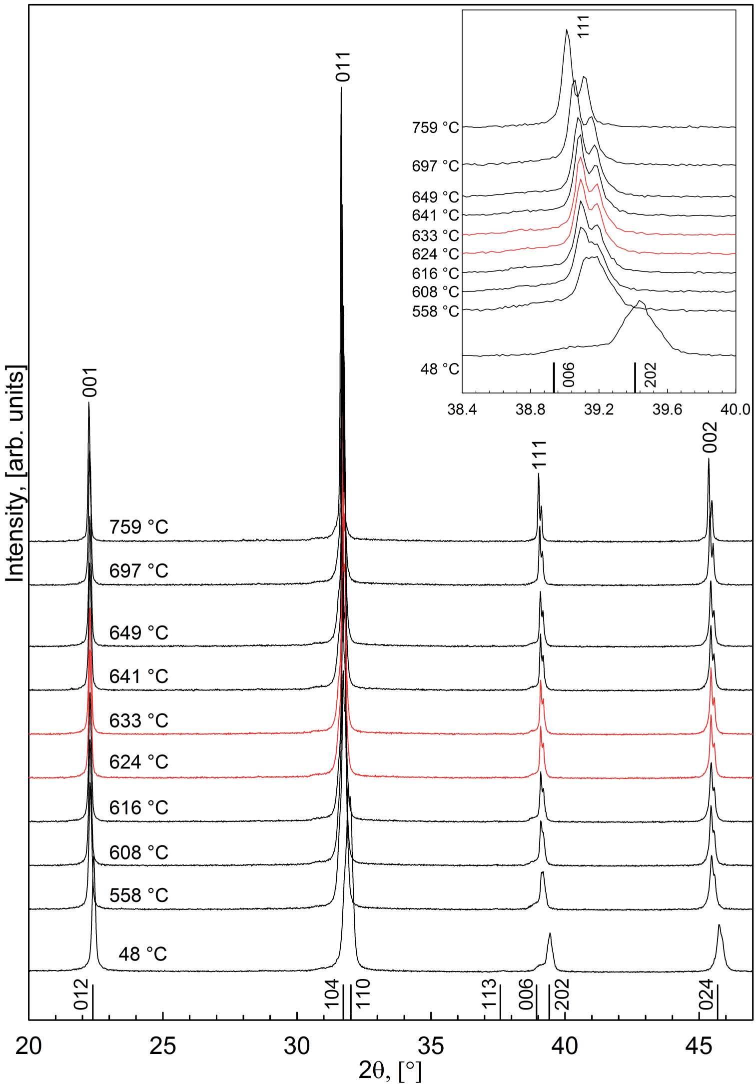

Figure 5.6: X-ray diffractograms of 0.8BFT0 at selected temperatures. The vertical bars denote the position of room temperature reflections of BFO and the corresponding Miller indices (ICDD 04-009-3445). The upper indices refer to the high temperature cubic symmetry. The temperature range of the ferroelectric to paraelectric phase transition is highlighted by red diffractograms. The inset shows the (006)/(002) diffraction line in detail.

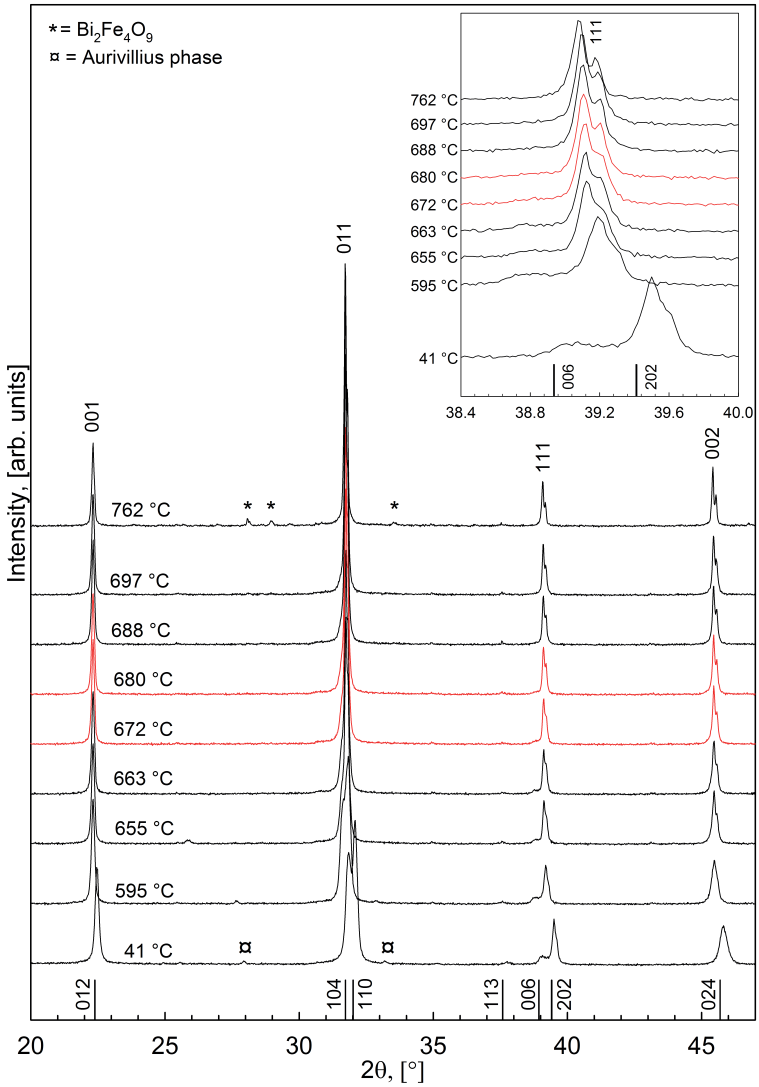

Figure 5.7: X-ray diffractograms of 0.9BFT0 at selected temperatures. The vertical bars show the position of room temperature reflections of BFO and the corresponding Miller indices (ICDD 04-009-3445). The upper indices refer to the high temperature cubic symmetry. The temperature range of the ferroelectric to paraelectric phase transition is highlighted by red diffractograms. The inset shows the (006)/(002) diffraction line in detail. The secondary phase seen at $2\theta \approx 28^\circ$ was not present after sintering, but appeared after thermal annealing above T_C prior to HTXRD analysis.

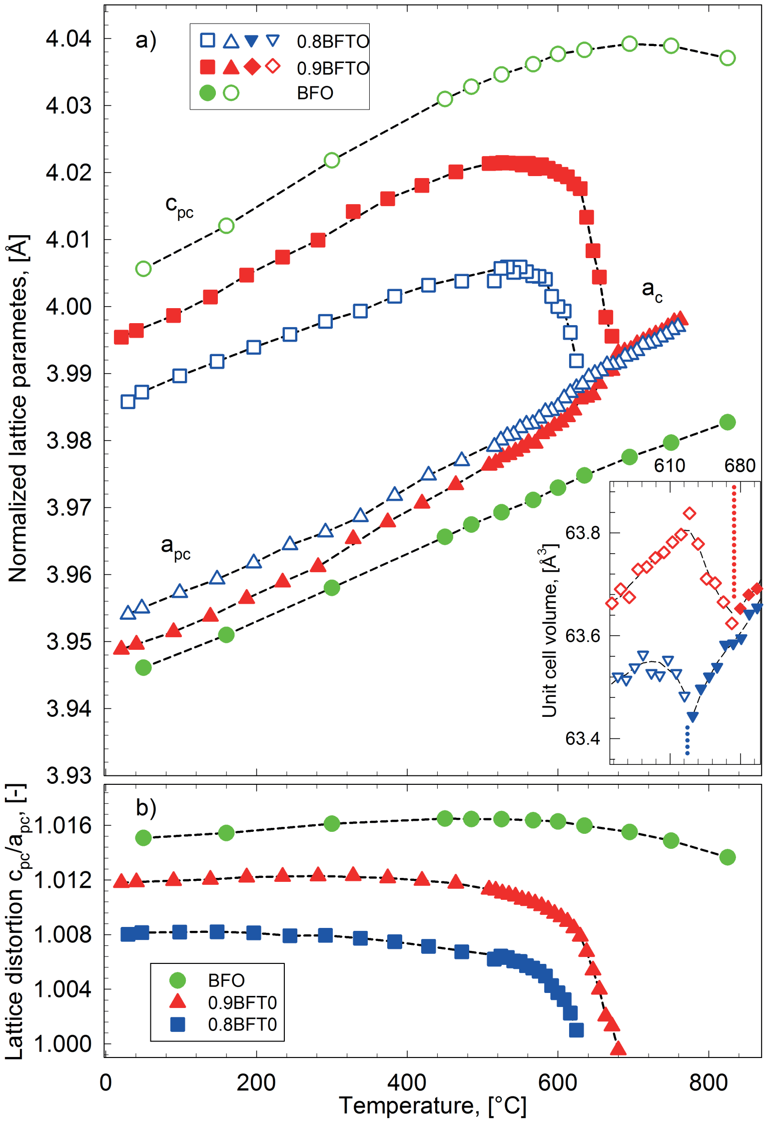

Figure 5.8: Thermal evolution of the normalized lattice parameters (a) and the lattice distortion c_{pc}/a_{pc} (b) of 0.8BFT0 and 0.9BFT0. Data for BFO is taken from Selbach *et al.*[46] The inset in (a) shows the unit cell volume below (open symbols) and above (filled symbols) the ferroelectric to paraelectric phase transition (marked by dotted lines). Lattice parameters were normalized as follows; $a_{pc}=2^{-1/2}a_h$ and $c_{pc}=12^{-1/2}c_h$. Dashed lines are guides to the eye.

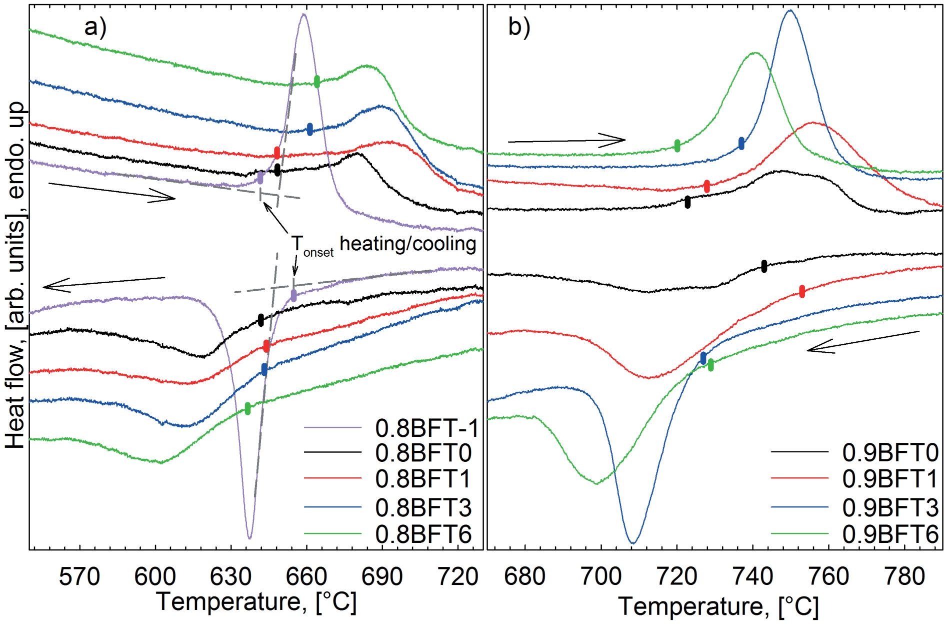

Figure 5.9: DTA heat flow signal for 0.8BFTy (a) and 0.9BFTy (b) materials during heating and cooling. The onset of each peak was taken as the midpoint between the crossing of the dashed grey lines and the point where the ”horizontal” grey line is separated from the measurement curve. The heating/cooling rate was 10 °C/min.

The ferroelectric to paraelectric phase transition of 0.8BFTy and 0.9BFT6 was also observed by a maximum in the dielectric permittivity (Figure 5.10). T_C during heating and cooling does not display a strong dependence on the Ti-substitution level except for 0.8BFT-1, where T_C is shifted to lower temperatures. The non-substituted 0.8BFT0 also shows a larger hysteresis with respect to heating and cooling compared to the other materials. The transition temperatures are summarized in Table 5.2. The high conductivity of 0.9BFTy with y<0.06 prevented measurements of permittivity near the phase transition. The origin of the small anomalies observed for 0.8BFT0 and 0.8BFT1 at ∼580 °C and for 0.9BFT6 near 680 °C is not known. The anomalies of 0.8BFT0 and 0.8BFT1 were shifted to higher temperatures for each heating cycle and may originate from interactions between the sample and the electrode.

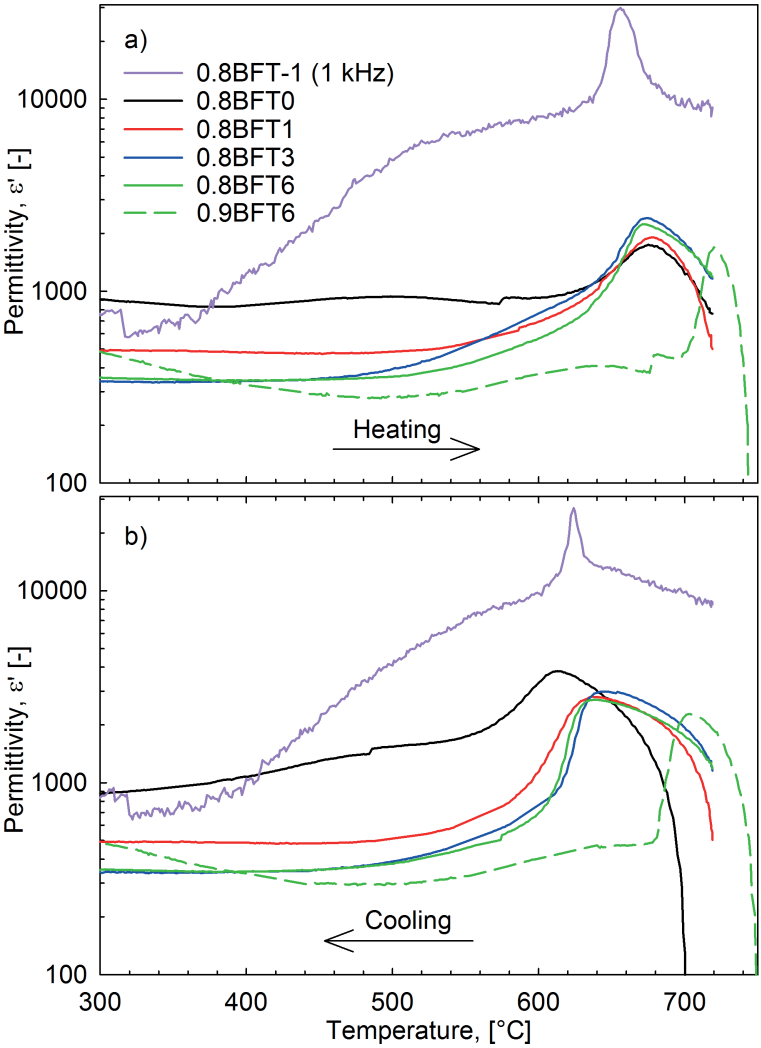

Figure 5.10: Real permittivity of 0.8BFTy and 0.9BFT6 (10 kHz) as a function of temperature during heating (a) and cooling (b).

Table 5.2: Phase transition temperatures for 0.8BFTy and 0.9BFTy as determined from XRD, DTA and permittivity.

Material	XRD	DTA heating		DTA cooling		Permittivity maximum	
	Heating [± 15 °C]	Onset [± 10 °C]	Maximum [± 1 °C]	Onset [± 10 °C]	Minimum [± 1 °C]	Heating [± 15 °C]	Cooling [± 15 °C]
0.8BFT-1	-	642	659	654	637	656	625
0.8BFT0	630	648	680	641	619	675	620
0.8BFT1	-	648	694	644	613	677	638
0.8BFT3	-	661	688	643	612	675	645
0.8BFT6	-	664	684	637	602	672	639
0.9BFT0	676	723	746	743	727	-	-
0.9BFT1	-	728	756	753	713	-	-
0.9BFT3	-	737	750	727	709	-	-
0.9BFT6	-	720	740	729	699	720	703

5.2 Discussion

5.2.1 Crystal Structure

The lattice distortion of ferroelectric and ferroelastic materials is important for the obtainable strain during non-180° domain reorientation. The addition of BKT to BFO was shown to decrease the lattice distortion (c_{pc}/a_{pc}) by ∼16 and ∼42 % for 0.9BFT0 and 0.8BFT0, respectively (Table 2.4 and 5.1). This decrease follows the reported evolution of the crystal structure where (1-x)BFO - xBKT becomes pseudo-cubic at $x \geq 0.4$ with a gradual disappearence of the rhombohedral splitting.[50] The lattice distortion was relatively constant below 550-600 °C, in line with the observed temperature stability of the lattice distortion of BFO which prevails up to near the ferroelectric to paraelectric phase transition (Figure 5.8b). The lattice distortion was found to decrease with increasing Ti-substitution for both the 0.8BFTy and the 0.9BFTy series, where the largest effect was observed for 0.8BFTy. The lattice distortion of 0.8BFT0 was decreased by ∼75 % (increased by ∼47 %) with only 1 mol% Ti-substitution for Fe (Fe substitution for Ti). The structural data presented here reveal that the lattice distortion of BFO-BKT materials, and hence the strain generated through movement of non-180° domain walls, can be tuned not only by the addition of BKT but also by relatively small changes in the Fe:Ti-ratio. A higher lattice distortion will provide a higher strain response during ferroelectric/ferroelastic domain switching but possibly also a higher resistance towards switching (higher energy barrier) as found for e.g. La-substituted BFO-PT.[96]

It is not clear why the effect of 1 mol% Ti-substitution on the lattice distortion for 0.8BFTy is larger compared to 0.9BFTy. The results presented by Zheng *et al.*[166] indicate that the lattice distortion did not decrease significantly with 10 mol% Ti-substitution. If the results for Ti-substituted pure BFO is seen in relation to 0.9BFTy and 0.8BFTy, it may indicate an increasing effect of Ti-substitution with increasing BKT-content. Furthermore, investigations of BNT have shown that relatively small variations of the nominal stoichiometry ($Bi_{0.5-x}Na_{0.5+x}TiO_3$ with x = -0.01 to 0.01) are required to change the long range order perceived by XRD to pseudo-cubic.[127] The nominal composition of the materials studied herein was confirmed by EDS. A large batch size of ∼50 g was used to decrease the effect of small deviations from the stoichiometric amount of precursors that may arise during weighing and further processing. Off stoichiometry may also arise due to loss of volatile elements during high temperature annealing. The observed variations of the crystal structure for the 0.8BFTy and 0.9BFTy series do not, however, correspond to any differences in the thermal history of the samples used for XRD analysis.

5.2.2 Phase Stability and Phase Diagram

Dense single phase perovskite (1-x)BFO - xBKT ceramics (x = 0.1, 0.2) were synthesized by a conventional solid state synthesis route. This infers that the addition of BKT to BFO has a stabilizing effect on the perovskite phase which inhibits the emergence of the commonly reported $Bi_2Fe_4O_9$ and $Bi_{25}FeO_{39}$ secondary phases, in line with earlier reports.[28,45,50,177] Figure 5.11a shows that addition of BKT, in addition to stabilizing the perovskite phase, can be used to tune T_C. A high T_C was determined for both 0.9BFT0 and 0.8BFT0, albeit somewhat reduced relative to that of pure BFO.

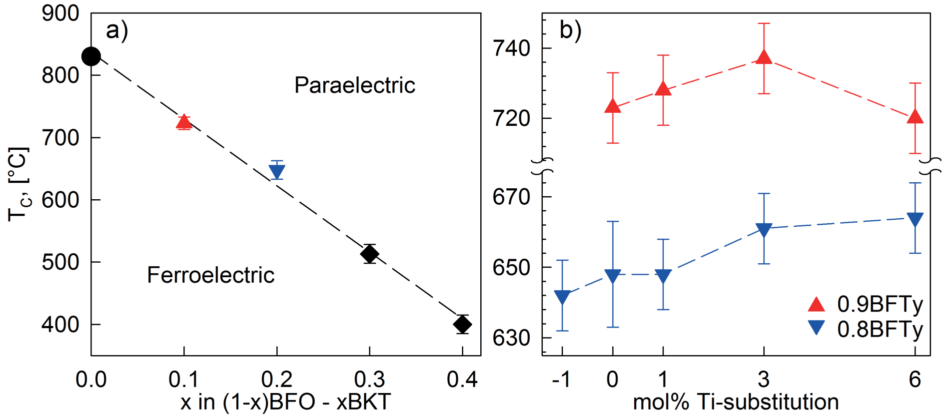

Figure 5.11: T_C (a); as a function of BKT content with pure BFO (x = 0, circle[133]), 0.9BFT0 and 0.8BFT0 (x = 0.1, 0.2, triangles, from this work), and 0.7BFO and 0.6BFO (x = 0.3, 0.4, diamonds, permittivity maximums[178]) and (b); as a function of Ti-substitution level in 0.8BFTy and 0.9BFTy (this work). The data from this work is taken from DTA.

Dense single phase perovskite 0.8BFTy ($y \leq 0.03$) and 0.9BFTy ($y \leq 0.06$) ceramics were also prepared where Fe was substituted by Ti (Figure 5.1 and 5.5). The solubility of substituents in BFO is known to be relatively low both on the A- and B-site (Chapter 2.5.5). A low solubility was also observed in this work where an Aurivillius phase emerged upon only 6 mol% substitution of Ti for Fe in 0.8BFTy. The Aurivillius phase also appeared in the XRD patterns of 0.8BFT3 and 0.9BFT6 after annealing above T_C (not apparent in XRD patterns of as-sintered samples). This suggests that the solubility limit was reached for the highest Ti-substitution levels (0.8BFT3, 0.8BFT6, 0.9BFT6). Moreover, the secondary phase that emerged in these materials is an Aurivillius phase and not the $Bi_2Fe_4O_9$ and $Bi_{25}FeO_{39}$ secondary phases which are commonly reported in pure BFO.[28,45] This again suggests that the stability of $Bi_2Fe_4O_9$ and $Bi_{25}FeO_{39}$ is significantly reduced relative to the perovskite phase also with donor substitition by Ti, as also indicated previously for pure BFO.[164,166] Donor substitution of Fe^{3+} by e.g. Ti^{4+} has been suggested by several authors as a method to reduce the inherent electrical conductivity of BFO.[149,150,152,166] The possibility to prepare stable single phase materials by conventional solid state synthesis may prove important for the future application of BFO-based materials.

The effect of Ti-substitution on T_C for 0.8BFT0 and 0.9BFT0 was less significant than the addition of 10 and 20 mol% BKT to BFO as is evident in Figure 5.11b. Nevertheless, some variation of T_C is observed and shows that the Fe:Ti-ratio of BFO-BKT can also be used to tune T_C on a smaller scale in these materials.

5.2.3 Microstructure

There are few reports on the grain size of BFO-rich materials in the (1-x)BFO - xBKT system. Morozov *et al.*[49] and Choi *et al.*[182] reported a grain size of ~1 μm and ~2 μm for BFO-BKT with 25 mol% and 60 mol% BFO, respectively, both which are considered to correspond well with the observations herein (Figure 5.4). Only small variations were observed with respect to the microstructure of 0.8BFTy and 0.9BFTy for $y \geq 0$. This is useful knowledge as the grain size is one factor that may affect the ferroelectric performance of a material as observed in BKT.[71]

The most apparent effect of Ti-substitution on the microstructure was the significantly larger grain size observed for 0.8BFT-1. The large grain size does not originate from the set of precursors used, as a large grain size was not observed in 0.8BFT0 (different batch than Figure 5.4b), 0.8BFT6 or 0.9BFT6 prepared from the same precursors as 0.8BFT-1. An increasing grain size from 2 to 4-5 μm was reported by Choi *et al.*[182] upon increasing the sintering temperature, but 0.8BFT-1 is sintered at the same temperature as the rest of the 0.8BFTy series. The origin of the large grain size was not investigated further.

Chapter 6

Electrical Conductivity and Point Defect Chemistry of BFO-BKT

6.1 Results

6.1.1 Isothermal DC Electrical Conductivity and Thermopower

The DC electrical conductivity (σ_{DC}) of 0.8BFT0 and 0.9BFT0 was measured as described in Chapter 3.2.6 and is shown as a function of temperature and P_{O_2} in Figure 6.1a and 6.1b, respectively. The conductivity increases with increasing BFO content, reflecting the higher conductivity of BFO relative to BKT.[110,121,136] Additionally, the conductivity increases with increasing temperature, in line with a semiconductor behavior. The isothermal conductivity decreases for both materials upon a decrease in P_{O_2} down to a distinct minimum (σ_{min}) before subsequently increasing again. The observed σ_{min} is typical for the change from p-type to n-type semiconductor behavior of oxides (Chapter 2.6) where 0.8BFT0 and 0.9BFT0 are p-type at high P_{O_2} (air and O_2) and n-type in low P_{O_2} (N_2). The p-type and n-type behavior is in line with earlier observations in BFO[138,153–155] but σ_{min} and $\sigma_{min}(P_{O_2})$ have not been reported previously. Furthermore, $\sigma_{min}(P_{O_2})$ is seen to shift towards higher P_{O_2} with increasing temperature, corresponding to observations in related LSF-materials and with conventional semiconductor behavior.[185,186]

The Seebeck coefficients (S) of 0.8BFT0 and 0.9BFT0 presented in Figure 6.2 as a function of temperature and atmosphere were measured to further confirm the shift from p-type to n-type conductivity for the materials. A positive S is observed in air and O_2, corresponding to p-type conductivity, while a negative S is observed in N_2, corresponding to n-type conductivity. The negative S is the first direct evidence of n-type conductivity in BFO-rich materials, to the best of the author's knowledge. The reported values of S in air are in line with the reported S of pure BFO of ~600 μV/K.[138]

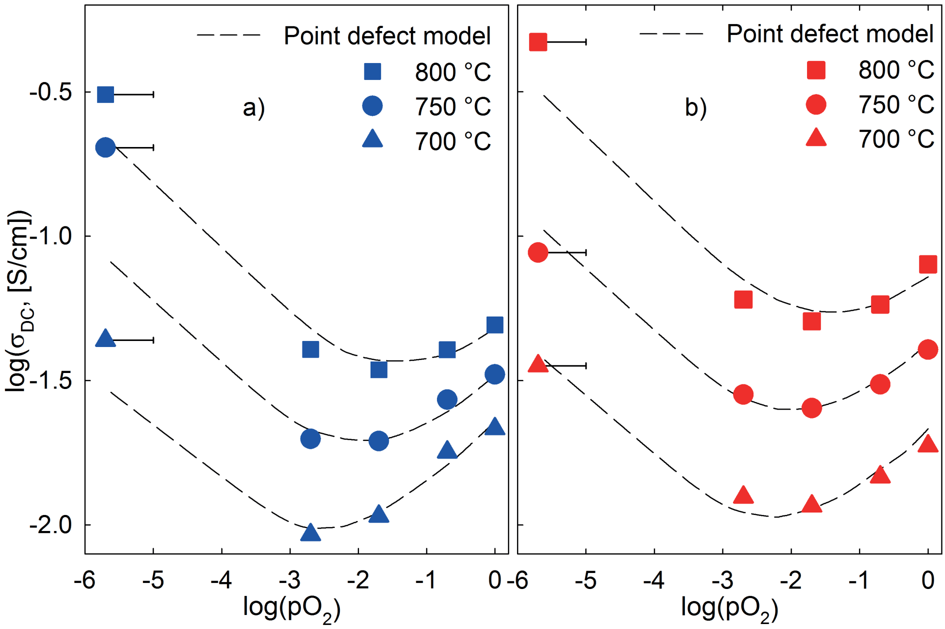

Figure 6.1: DC electrical conductivity of 0.8BFT0 (a) and 0.9BFT0 (b) as a function of P_{O_2} at 700, 750 and 800 °C. The dashed lines show the conductivity calculated by the point defect model introduced later in this chapter. The error bars are added as some uncertainty is associated with the P_{O_2} of pure N_2 gas.

6.1.2 Effect of Ti-substitution on Electrical Conductivity

The real AC conductivity (σ'_{AC}) of 0.8BFTy and 0.9BFTy was studied at room temperature (Figure 6.3) and during heating and cooling in different atmospheres (Figure 6.4-6.7). Figure 6.3 displays a significant reduction of σ'_{AC} for both 0.8BFTy and 0.9BFTy with the substitution of Fe^{3+} with Ti^{4+} (donor substitution) at room temperature. The conductivity was reduced by approximately four and two orders of magnitude with 1 mol% Ti-substitution for 0.8BFT0 and 0.9BFT0, respectively, at 10 mHz. Further Ti-substitution did not provide an additional reduction of σ'_{AC}. The conductivity of 0.8BFT-1 where Ti^{4+} was substituted by Fe^{3+} (acceptor substitution) was higher than that of 0.8BFT0.

The trend of reduced conductivity with donor substitution was also observed at high temperatures in air, as shown for 0.8BFTy and 0.9BFTy in Figure 6.4 and 6.5, respectively. The trend is apparent up to T_C where the conductivity and temperature dependence of the conductivity for non-substituted and

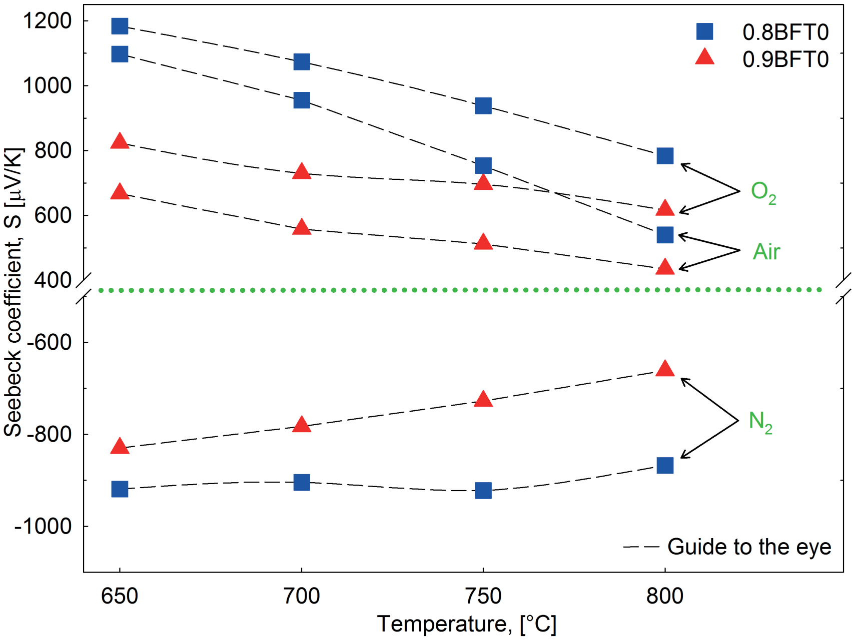

Figure 6.2: Seebeck coefficient of 0.8BFT0 and 0.9BFT0 as a function of temperature and atmosphere. Dashed lines are guides to the eye.

donor substituted materials converge towards a similar value within each series. The conductivity of the acceptor substituted 0.8BFT-1 material is significantly higher than that of 0.8BFT0 at all temperatures (Figure 6.4). The activation energy of σ'_{AC} was determined from an Arrhenius plot of the data and is included in Figure 6.4 and 6.5. All donor substituted materials display an upwards shift in the activation energy around 500 °C, except for 0.8BFT1 where the activation energy increases around 350 °C and 560 °C. The 0.8BFT-1 and 0.8BFT0 materials display a slightly decreasing conductivity while the other materials show a slightly increasing conductivity near the ferroelectric to paraelectric phase transition, as highlighted in the insets of Figure 6.4 and 6.5.

Figure 6.6 displays the real AC conductivity, σ'_{AC}, of 0.8BFT0, 0.8BFT1 and 0.8BFT3 measured in different atmospheres above 200 °C. σ'_{AC} of 0.8BFT0 (Figure 6.6a) possesses a clear decrease in the temperature range 400-500 °C when heating in N_2, relative to σ'_{AC} measured during the preceding cooling in air. The decrease in N_2 is less evident for 0.8BFT1 (Figure 6.6b) and not visible for 0.8BFT3 (Figure 6.6c). While σ'_{AC} measured for 0.8BFT0 in N_2

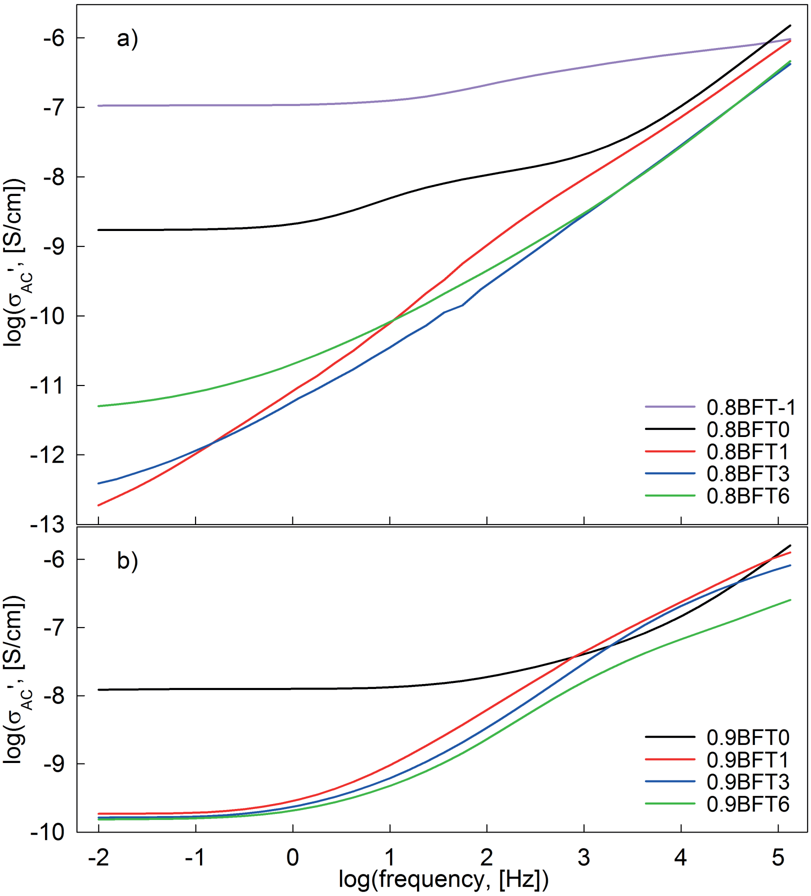

Figure 6.3: Room temperature real AC conductivity, σ'_{AC}, as a function of frequency for 0.8BFTy (a) and 0.9BFTy (b). The scale of the y-axis in (a) and (b) are the same to allow direct comparison.

remains lower than that in air up to 700 °C, the conductivity of 0.8BFT1 and 0.8BFT3 in N_2 starts to increase above 500 °C and has surpassed that of air at 700 °C. The higher conductivity in N_2 remains during the subsequent cooling in N_2. Cooling in N_2 was followed by heating in O_2 where the conductivity of 0.8BFT0 increased while the conductivity of 0.8BFT1 and 0.8BFT3 decreased. The conductivity in O_2 is slightly higher than the conductivity in air for all three materials. It is noteworthy that the effect of O_2 on σ'_{AC} is apparent already at ~270 °C, implying a significant oxygen mobility and change of the valence of Fe already at this low temperature.

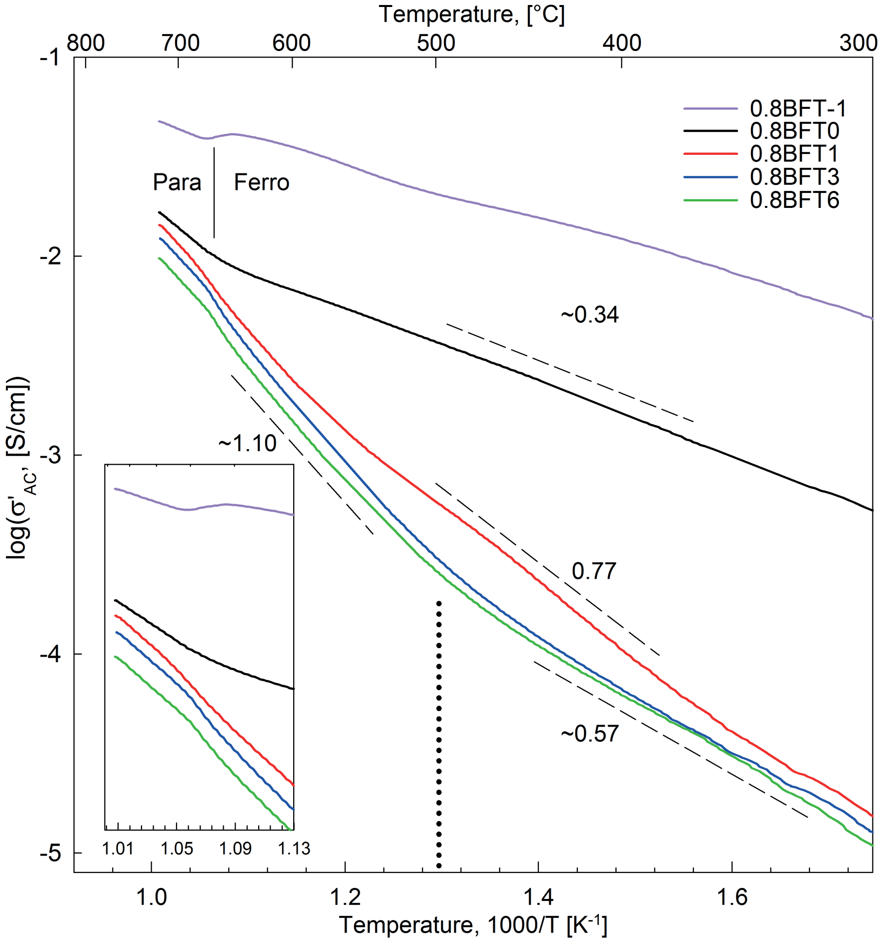

Figure 6.4: High temperature real AC conductivity, σ'_{AC} (100 Hz), of 0.8BFTy measured during heating in air above 300 °C where the conductivity was found to be independent of the frequency of the driving field. The activation energies are given in eV and the dotted line marks the shift in activation energy near 500 °C. The temperature region of the ferroelectric to paraelectric phase transition is also indicated and highlighted in the inset. Dashed lines are guides to the eye.

The conductivity in the region of the paraelectric to ferroelectric phase transition of 0.8BFT-1, 0.8BFT0, 0.8BFT1 and 0.8BFT3, measured during cooling in air, N_2 and O_2, is highlighted in Figure 6.7. The anomaly at the phase transition is seen to decrease in amplitude with increasing Ti-content in the materials, corresponding to the sharpness of the peaks observed by thermal analysis (Figure 5.9a). Moreover, the conductivity of 0.8BFT-1 and

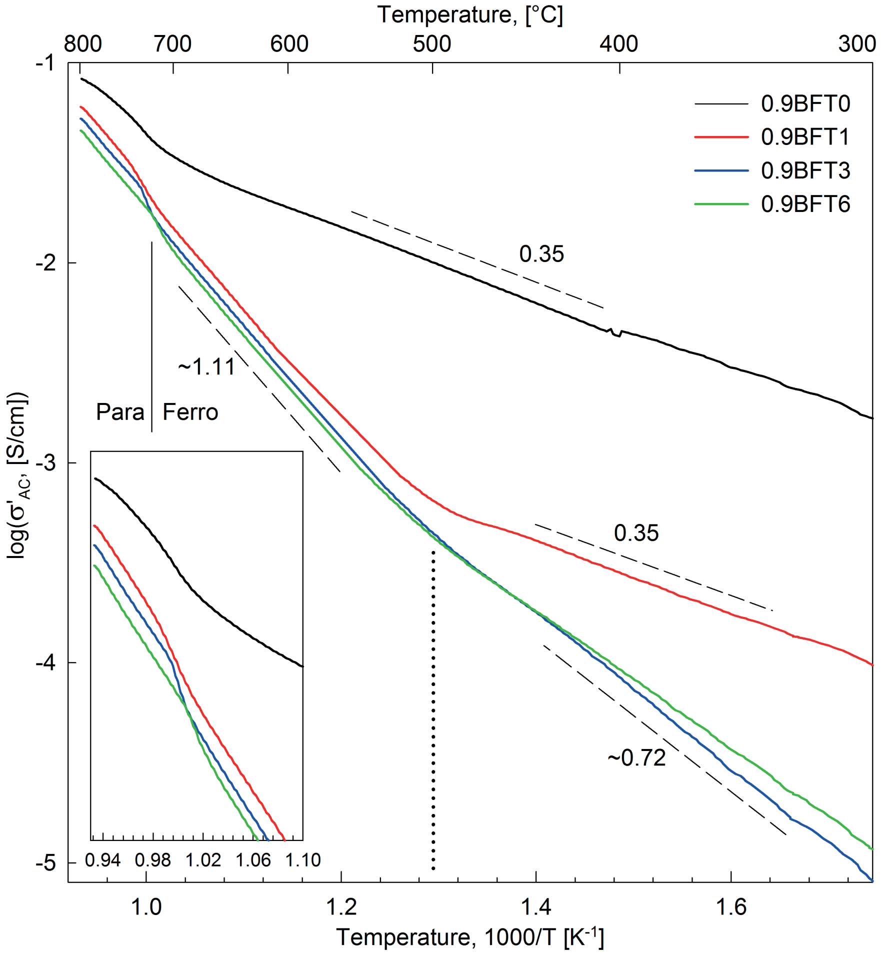

Figure 6.5: High temperature real AC conductivity, σ'_{AC} (100 Hz), of 0.9BFTy measured during heating in air above 300 °C where the conductivity was found to be independent of the frequency of the driving field. The activation energies are given in eV and the dotted line marks the shift in activation energy near 500 °C. The temperature region of the ferroelectric to paraelectric phase transition is also indicated and highlighted in the inset. Dashed lines are guides to the eye.

0.8BFT0 increases at the phase transition when cooling in O_2 and air while it decreases during cooling in N_2. The anomaly is strongly depressed in 0.8BFT1 whereas the conductivity of 0.8BFT3 is seen to decrease across the phase transition in all three atmospheres. The same trends are observed during heating but are not included to enhance clarity.

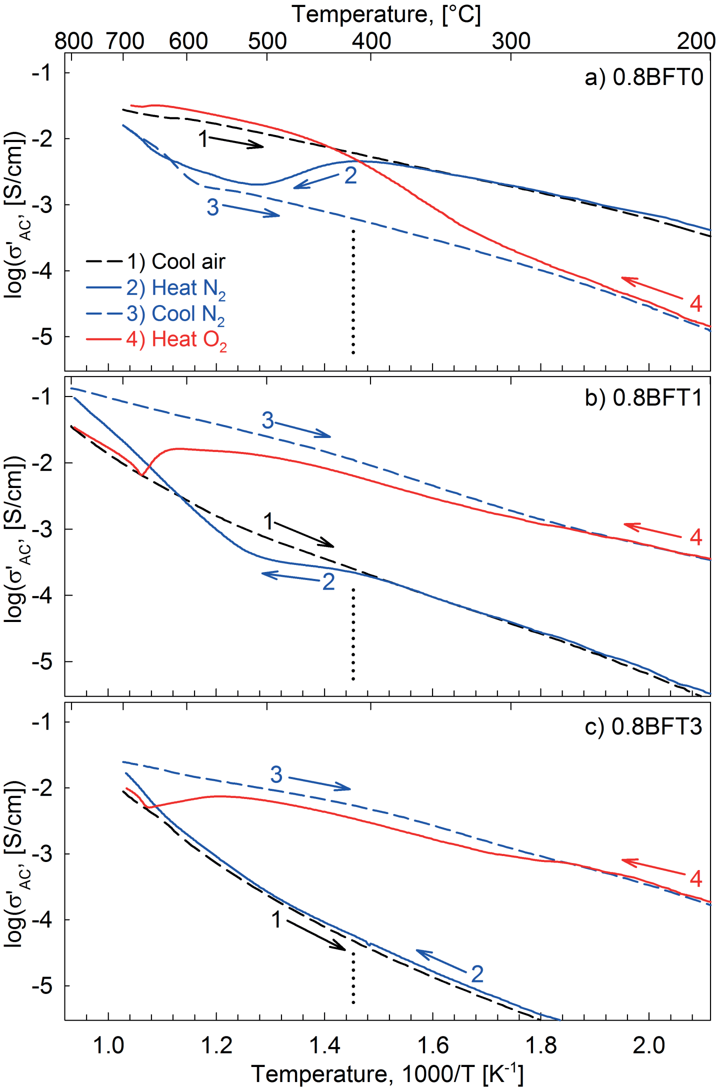

Figure 6.6: Real AC conductivity, σ'_{AC} (10 kHz), as a function of temperature and atmosphere for 0.8BFT0 (a), 0.8BFT1 (b) and 0.8BFT3 (c). The enumerated arrows refer to cooling in air (1), heating in N_2 (2), cooling in N_2 (3) and heating in O_2 (4). The dotted line is added as a guide to the eye and acts as a reference line positioned at the same temperature in all three figures.

6.2 Discussion

6.2.1 p/n-type Conductivity and Point Defect Model

The electrical conductivity of 0.8BFT0 and 0.9BFT0 was shown to be highly dependent on temperature and atmosphere (Figure 6.1), in line with earlier

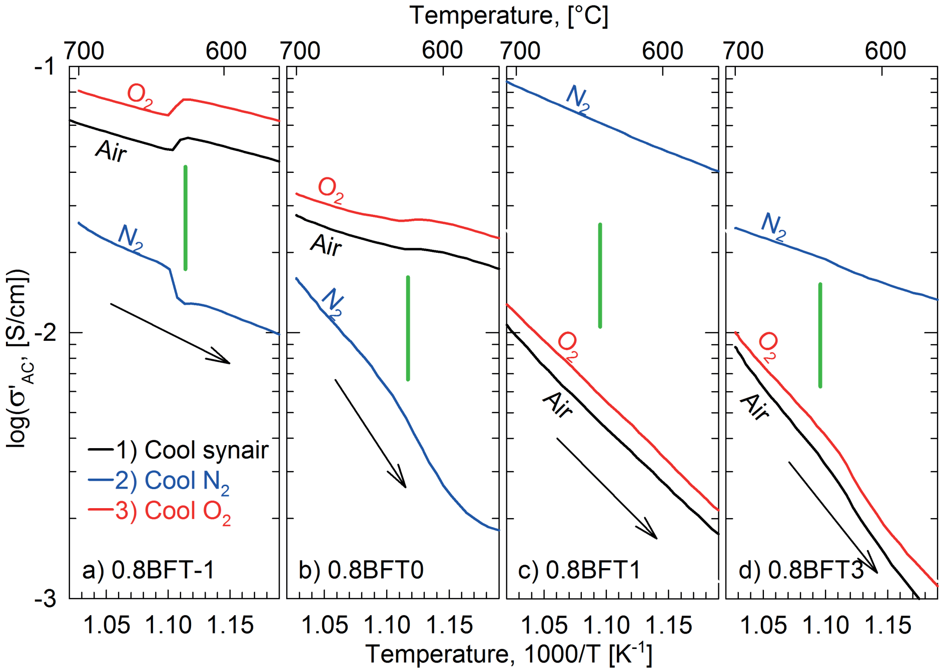

Figure 6.7: Real AC conductivity, σ'_{AC} (10 kHz), during cooling near the phase transition temperature of 0.8BFT-1 (a), 0.8BFT0 (b), 0.8BFT1 (c) and 0.8BFT3 (d). The conductivity was measured in air (1), then N_2 (2) and finally O_2 (3). The green line marks the phase transition temperature and the arrow denotes the cooling direction. The maximum temperature was 700 °C for all materials except 0.8BFT1 (c) which was heated to 800 °C.

reports on related materials.[51,167,178,180] The results present clear evidence for p-type conductivity in 0.8BFT0 and 0.9BFT0 at high P_{O_2} (O_2) where the conductivity decreases with *decreasing* P_{O_2}. Correspondingly, n-type conductivity at low P_{O_2} (N_2) was inferred as the conductivity decreases with *increasing* P_{O_2}. A minimum in the conductivity is observed at the shift from p-type to n-type behavior. Direct evidence of the shift between p-type and n-type conductivity, and hence from positive to negative charge carriers, was further provided by measurements of the Seebeck coefficient at high and low P_{O_2} (Figure 6.2).

The qualitative behavior of the electrical conductivity of both 0.8BFT0 and 0.9BFT0 presented in Chapter 6.1.1 (Figure 6.1 and 6.2) show great similarities with that of other Fe-based perovskites.[185,186] In Fe-based perovskites, the electrical conductivity can be described by a mass action type treatment of relevant point defect equilibria. A mass action type treatment of the conductivity of 0.8BFT0 and 0.9BFT0 based on the approach presented by Mizusaki *et al.*[185] for $LaFeO_3$ is presented in the following. The principle, including equations, was introduced in Chapter 2.5.5 and 2.6. However, the defect formation equation and electroneutrality is slightly altered due to the addition of BKT. All relevant equations are summarized here for convenience.

The substitution of BKT into BFO will introduce K^+ on the A-site and Ti^{4+} on the B-site resulting in acceptor (K''_{Bi}) and donor ($Ti^{\cdot}_{Fe}$) point defects, respectively. The overall charge balance for the substitution is maintained with a K:Ti-ratio of 1:2. The point defect chemistry of BFO-BKT can hence be described by the defect formation equations (Eqs. 6.1 and 6.2), the electroneutrality condition (Eq. 6.3) and the mass balance of iron (Eq. 6.4).

$$2Bi^{\times}_{Bi} + 3O^{\times}_{O} \xrightarrow{\text{Heat}} 2V'''_{Bi} + 3V^{\cdot\cdot}_{O} + 2Bi(g) + {}^{3}\!/_{2}O_2(g) \tag{6.1}$$

$$2K''_{Bi} + O^{\times}_{O} \xrightarrow{\text{Heat}} 2V'''_{Bi} + V^{\cdot\cdot}_{O} + 2K(g) + {}^{1}\!/_{2}O_2(g) \tag{6.2}$$

$$n + (3-x)\left[V_A^{(3-x)\prime}\right] = p + 2\left[V^{\cdot\cdot}_{O}\right] \tag{6.3}$$

$$\left[Fe_{Fe}\right] = n + \left[Fe^{\times}_{Fe}\right] + p \tag{6.4}$$

Here, n and p are the concentrations of Fe^{2+} and Fe^{4+}, respectively, and $[V_A^{(3-x)\prime}]$ is the concentration of A-site vacancies where the effective charge will depend on the amount of BKT (x = 0.1 for 0.9BFT0 and 0.2 for 0.8BFT0). Moreover, n and p will depend on the P_{O_2} as given by Eqs. 6.5 and 6.6, respectively.

$$2Fe'_{Fe} + {}^{1}\!/_{2}O_2(g) + V^{\cdot\cdot}_{O} \rightleftharpoons 2Fe^{\times}_{Fe} + O^{\times}_{O} \tag{6.5}$$

$$2Fe^{\times}_{Fe} + {}^{1}\!/_{2}O_2(g) + V^{\cdot\cdot}_{O} \rightleftharpoons 2Fe^{\cdot}_{Fe} + O^{\times}_{O} \tag{6.6}$$

The total electrical conductivity of a semiconductor (σ_{tot}, Eq. 6.7) depends on the concentration of charge carriers (C), the mobility of the charge carriers (μ) and the quantity of charge transported by each charge carrier (q).

$$\sigma_{tot} = \sum_i C_i \mu_i q_i \tag{6.7}$$

Here, i denotes the charge carrier species. The total conductivity can be divided into separate contributions from ions (σ_{ion}), electrons (σ_e) and electron-holes (σ_h) as presented in Eq. 6.8

$$\sigma_{tot} = \sigma_{ion} + \sigma_e + \sigma_h \tag{6.8}$$

where e and h denote electrons and electron-holes, respectively. The contribution from ionic conductivity is assumed to be small relative to the electronic contributions ($\sigma_{ion} \ll \sigma_e, \sigma_h$) such that σ_{ion} is neglected in the further calculations. Combining Eqs. 6.7 and 6.8 yields the total conductivity of 0.8BFT0 and 0.9BFT0 as

$$\sigma_{tot} \approx \sigma_e + \sigma_h = nq\mu_e + pq\mu_h \tag{6.9}$$

where μ_e/μ_h is the mobility of electrons/electron-holes. The equilibrium between electrons and electron-holes, and the corresponding equilibrium constant (K_i), is given by Eq. 6.10.

$$e + h \rightleftharpoons \text{null} \qquad\qquad K_i = np \tag{6.10}$$

μ_e and μ_h are taken to be constant at isothermal conditions with the assumption that n and p are sufficiently small.[185,186] This allows the combination of Eqs. 6.9 and 6.10 to give

$$\sigma_e\sigma_h = q^2\mu_e\mu_h np = q^2\mu_e\mu_h K_i = K_i' \tag{6.11}$$

where K_i' is a constant at isothermal conditions. Further combining Eqs. 6.9 and 6.11 yields an expression for the total conductivity as a function of K_i' and σ_e.

$$\sigma_{tot} = \sigma_e + \frac{K_i'}{\sigma_e} \tag{6.12}$$

Assuming an equal contribution from electrons and electron-holes to the total conductivity at $\sigma_{tot} = \sigma_{min}$ yields

$$\frac{\sigma_{min}}{2} = \sigma_e(\sigma_{min}) = \sigma_h(\sigma_{min}) = \sqrt{K_i'} \tag{6.13}$$

where $\sigma_e(\sigma_{min})$ and $\sigma_h(\sigma_{min})$ are the separate contributions to σ_{tot} from electrons and electron-holes at $\sigma_{tot} = \sigma_{min}$, respectively. The contributions to σ_{tot} from σ_e and σ_h at any given P_{O_2} are then obtained by treating Eq. 6.12 as a 2nd order polynomial which can be solved as shown in Eqs. 6.14 and 6.15.

$$\sigma_{tot} - \sigma_h = \sigma_e = \frac{\sigma_{tot} - \sqrt{\sigma_{tot}^2 - 4K_i'}}{2} \quad if \;\; \sigma_e \le \sigma_h \tag{6.14}$$

$$\sigma_{tot} - \sigma_h = \sigma_e = \frac{\sigma_{tot} + \sqrt{\sigma_{tot}^2 - 4K_i'}}{2} \quad if \quad \sigma_e \geq \sigma_h \tag{6.15}$$

The value of K_i' is calculated from Eq. 6.13 and σ_{tot} is the experimentally measured σ_{DC}.

The concentration of charge carriers (n and p) can now be quantified using Eq. 6.9 if μ_e and μ_h are known. The mobilities of electrons and electron-holes are not available for BFO-based materials but the mobilities found for $LaFeO_3$ were used as a first approximation[185] and the optimized mobilities estimated for 0.8BFT0 and 0.9BFT0 at each temperature are summarized in Table 6.1.

Table 6.1: μ_e and μ_h used for modeling σ_{tot} of 0.8BFT0 and 0.9BFT0.

Material	Temperature [°C]	μ_e [cm^2/Vs]	μ_h [cm^2/Vs]
0.8BFT0	700	0.052	0.05
	750	0.054	0.074
	800	0.056	0.107
0.9BFT0	700	0.046	0.03
	750	0.047	0.063
	800	0.056	0.107

Further modeling of the conductivity requires a quantification of either $[V_O^{\cdot\cdot}]$ or $[V_A^{(3-x)\prime}]$ which are not readily available for BFO-based materials. An assumption was introduced where $[V_A^{(3-x)\prime}] = 0.01$ based on preliminary data[179] which allows determination of $[V_O^{\cdot\cdot}]$ through Eq. 6.3.

The quantified n, p and $[V_O^{\cdot\cdot}]$ allows the determination of the equilibrium constant of Eqs. 6.5 and 6.6, given in Eq. 6.16 and 6.17, respectively.

$$K_{ox,1} = \frac{\left[Fe_{Fe}^{\times}\right]^2 \left[O_O^{\times}\right]}{\left[V_O^{\cdot\cdot}\right] n^2 P_{O_2}^{1/2}} \tag{6.16}$$

$$K_{ox,2} = \frac{p^2 \left[O_O^{\times}\right]}{\left[V_O^{\cdot\cdot}\right] \left[Fe_{Fe}^{\times}\right]^2 P_{O_2}^{1/2}} \tag{6.17}$$

$K_{ox,1}$ and $K_{ox,2}$ were calculated for all five P_{O_2}s used for measuring σ_{DC} (1 (O_2), 0.2, 0.02, 0.002 and 0.000002 (N_2)) and subsequently averaged because the equilibrium constant is constant (independent of P_{O_2}) at isothermal conditions. The equilibrium constants of the oxidation reactions are related to the enthalpy (Δ_rH), entropy (Δ_rS) and Gibbs free energy (Δ_rG) of reaction through Eq. 6.18[59]

$$\Delta_r G = \Delta_r H - T\Delta_r S = -RT \ln K_{ox} \tag{6.18}$$

where R is the gas constant. Rearranging Eq. 6.18 to give

$$\ln K_{ox} = -\frac{\Delta_r H}{RT} + \frac{\Delta_r S}{R} \tag{6.19}$$

allows the determination of an estimated Δ_rH for the two oxidation reactions (Eqs. 6.5 and 6.6) from an Arrhenius type plot of $\ln K_{ox}$ vs. 1/T. The entropy of the reactions was taken to be -130 kJ/mol, as argued by Bakken *et al.*[203] The estimated Δ_rH was subsequently adjusted along with μ_e and μ_h to obtain a best fit of the modeled conductivity to the experimental data. The optimized μ_e and μ_h were summarized in Table 6.1 and the optimized Δ_rH are presented in Table 6.2. Furthermore, the calculated n and p for 0.8BFT0 and 0.9BFT0 are shown in Figure 6.8 and the modeled conductivity is plotted as dashed lines in Figure 6.1. The value of $[V_O^{\cdot\cdot}]$ was found to vary little during the optimization of Δ_rH and the values determined from the experimental data (Eq. 6.3) were hence used to calculate the modeled n and p.

Table 6.2: Thermodynamic data for the point defect reactions of 0.8BFT0 and 0.9BFT0.

	Eq. 6.5	Eq. 6.6
Material	Δ_rH [kJ/mol]	Δ_rH [kJ/mol]
0.8BFT0	-343	-28
0.9BFT0	-340	-31

The presence of electrons and electron-holes as the major charge carriers in 0.8BFT0 and 0.9BFT0 is confirmed by the successful modeling of σ_{DC} by the point defect model introduced here. In addition, the importance of $V_O^{\cdot\cdot}$ and P_{O_2} is highlighted and provides important knowledge for the further development of BFO-based ferroelectrics. The presence of A-site vacancies are also substantiated and included in the model. Further improvement of

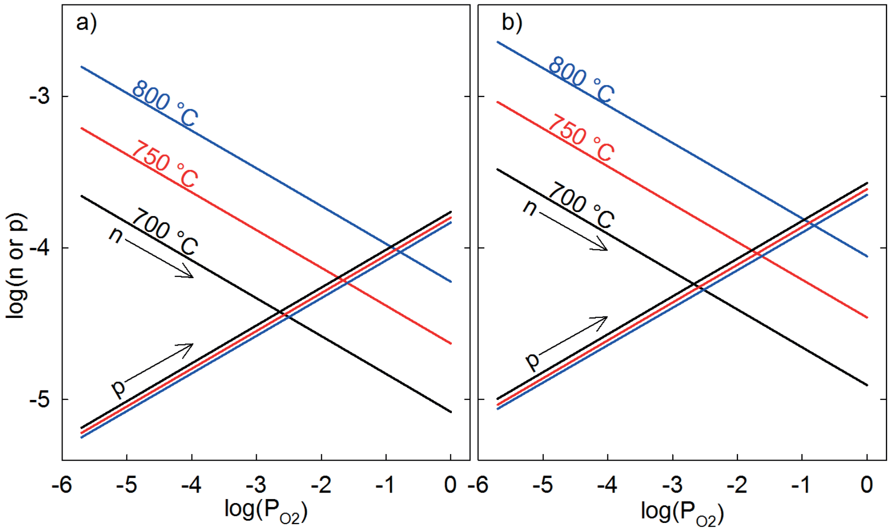

Figure 6.8: Concentration of electrons (n) and electron-holes (p) in 0.8BFT0 (a) and 0.9BFT0 (b) vs. P$_{O_2}$ and temperature, as calculated from the optimized Δ_rH, μ_e and μ_h.

the model is possible but requires more experimental data such as μ_e and μ_h or $[V_O^{\cdot\cdot}]$, and preferentially σ_{DC} over a wider P$_{O_2}$ range.

The point defect model can be used to rationalize certain aspects of the behavior of the Seebeck coefficient at isothermal or dynamic conditions. BFO-based materials can be considered extrinsic semiconductors as the evaporation of volatile elements in equivalent to acceptor substitution. The Seebeck coefficient of extrinsic semiconductors depends on the concentration of charge carriers as given by Eq. 6.20[187]

$$S \propto \ln \frac{1-C}{C} \tag{6.20}$$

where an increasing number of charge carriers will reduce the Seebeck coefficient. The trend where S$_{BFO}$ < S$_{0.9BFT0}$ < S$_{0.8BFT0}$ can be rationalized by the calculated concentration of charge carriers (Figure 6.8) and the assumption that BFO contains more charge carriers than 0.9BFT0. This assumption is reasonable considering that the conductivity of (1-x)BFO - xBKT increases with increasing BFO-content.[110] The decreasing absolute value of S with increasing temperature can be rationalized in the same way for the n-type regime where the charge carrier concentration increases with increasing temperature (Figure 6.8). The temperature and atmosphere dependence of

S in air and O_2 (p-type regime) is similar to observations reported for LSF but cannot be rationalized the same way as in the n-type regime.[186] This is probably because the P_{O_2} in air and O_2 is too close to the shift from p-type to n-type conductivity.

Recent investigations have revealed that the electrical conductivity at the domain wall of BFO thin films and ceramics is different from that in the bulk domain.[85,86,154,155,158] The conductivity of 71° domain walls in La-substituted BFO films has been described as n-type, and the currents at the domain wall was higher than in the domain, originating from a higher concentration of $V_O^{\cdot\cdot}$ on the wall. The domain wall conductivity was also found to change after annealing in different oxygen pressure.[155] Furthermore, it was recently shown for $CaMnO_{3-\delta}$ that the concentration of $V_O^{\cdot\cdot}$ can be influenced by strain.[204] It is hence apparent that the point defect model introduced herein is highly relevant not only for bulk materials but also for thin films.

6.2.2 Donor/Acceptor Substitution

The real AC conductivity, σ'_{AC}, of 0.8BFT0 and 0.9BFT0 was significantly reduced by donor substitution with Ti^{4+} as displayed in Figure 6.3-6.5. This behavior is in line with p-type semiconductor behavior and has been observed for both BFO and related materials.[150,152,165,169,205] The largest reduction of σ'_{AC} was seen for 0.8BFTy where σ'_{AC} was reduced by a maximum of four orders of magnitude within the investigated frequency range. This is among the largest reductions of conductivity by donor substitution reported in literature for BFO-based materials. σ'_{AC} was found to be frequency dependent for all investigated materials with the largest reduction of conductivity at low frequencies, indicating that the reduction is mainly related to a reduced σ_{DC}. An extrapolation of the measured σ'_{AC} to lower frequencies suggest that the reduction of the true σ_{DC} is even larger. The reduction of σ_{DC} is important as the application of ferroelectrics with a high coercive electric field (such as BFO) requires the use of high electric fields which may induce high leakage currents and eventually dielectric breakdown. The reduction of σ'_{AC} in 0.9BFTy is smaller and the conductivity becomes frequency independent at higher frequencies compared to that of 0.8BFTy. Furthermore, donor substitution of 0.8BFT0 and 0.9BFT0 is found to reduce the conductivity without large reductions of T_C (Figure 5.11b) which conserves the high temperature applicability of the materials.

As presented, the P_{O_2} dependence of σ_{DC} for 0.8BFT0 and 0.9BFT0 can be described by a point defect model. The model shows that electron-holes (Fe^{4+}) and electrons (Fe^{2+}) are the dominating charge carriers in the p-type regime (high P_{O_2}) and n-type regime (low P_{O_2}), respectively. Following this point defect model, the additional charge introduced by the substitution of Ti^{4+} for Fe^{3+} can be charge compensated by annihilation of $V_O^{\cdot\cdot}$, as illustrated by Eq. 6.21.

$$TiO_2 + Fe_{Fe}^{\times} + {}^{1}\!/_{2}V_O^{\cdot\cdot} \xrightarrow{\text{BFO}} Ti_{Fe}^{\cdot} + {}^{1}\!/_{2}Fe_2O_3 + {}^{1}\!/_{2}O_O^{\times} \qquad (6.21)$$

The concentrations of $V_O^{\cdot\cdot}$, Fe^{2+} and Fe^{4+} are directly related through Eqs. 6.5 and 6.6. Annihilation of $V_O^{\cdot\cdot}$ will shift Eqs. 6.5 and 6.6 to the left which effectively reduces the valence of Fe and lowers the concentration of Fe^{4+}, the major charge carrier in p-type conductors. The conductivity is hence reduced by donor substitution because of the lower concentration of the major charge carrier Fe^{4+}. The reduction of conductivity by donor substitution is analogous to a shift of σ_{min} towards higher P_{O_2} as is schematically illustrated in Figure 6.9. The conductivity in air (σ_{Air}) is seen to decrease upon donor substitution as σ_{min} is moved to a higher P_{O_2}. σ_{min} is kept at the same value in Figure 6.9 for simplicity.

The shift of σ_{min} to a higher P_{O_2} with donor substitution is further substantiated by the measurements of σ'_{AC} in different atmospheres (Figure 6.6). Although these measurements were performed during continuous heating and cooling (120 °C/h), the investigations by Morozov *et al.*[180] suggest that the oxygen mobility is sufficiently high to obtain equilibrium conditions at 700 °C. The assumption of equilibrium conditions allows the observed effects of atmosphere and donor substitution to be explained by the illustration of the isothermal conductivity in Figure 6.9. At 700 °C, the conductivity of 0.8BFT0 in air is higher than that in N_2 (Figure 6.6a), exemplified by $\sigma_{Air} > \sigma_{N2}$ given in black in Figure 6.9. In the donor substituted materials, σ_{min} is shifted to higher P_{O_2} resulting in a higher conductivity in N_2 relative to air (Figure 6.6b and 6.6c). This shift of σ_{min} is exemplified by $\sigma_{Air} < \sigma_{N2}$ given in red in Figure 6.9. A larger drop is observed for σ'_{AC} when heating the non-substituted material in N_2 relative to the donor substituted materials. The drop amplitude is related to $\Delta\sigma = \sigma_{Air}$ - σ_{min} which is larger for the non-substituted material, even though the materials may not be in equilibrium with the atmosphere at this temperature.

The increased conductivity observed for the acceptor substituted 0.8BFT-1 (Figure 6.3a and 6.4) can be rationalized by the same arguments based on

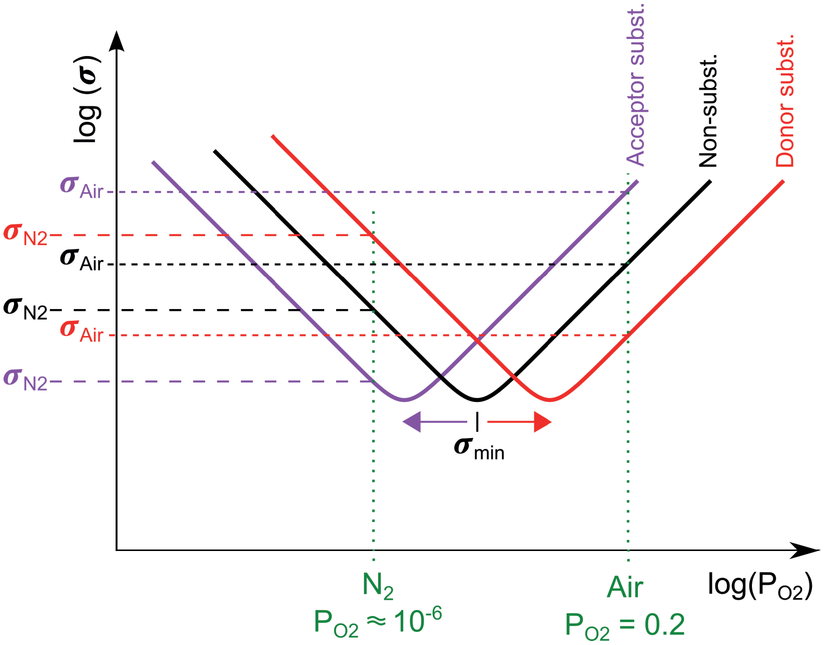

Figure 6.9: Schematic representation of how the P_{O_2} dependence of the electrical conductivity in semiconductors is affected by donor and acceptor substitution at isothermal conditions. The positions of the conductivity minima are chosen arbitrarily and σ_{min} for the three materials is kept at the same value for enhanced clarity.

point defect chemistry. Acceptor substitution was done by replacing Ti^{4+} with Fe^{3+} which increases the concentration of $V_O^{\cdot\cdot}$ according to Eq. 6.22.

$$1/2Fe_2O_3 + Ti_{Ti}^{\times} + 1/2O_O^{\times} \xrightarrow{\text{BFO}} Fe'_{Ti} + TiO_2 + 1/2V_O^{\cdot\cdot} \tag{6.22}$$

The reaction produces the opposite effect of that observed by donor substitution, hence Eqs. 6.5 and 6.6 are shifted to the right and Fe is oxidized. The oxidation of Fe increases the concentration of the major charge carrier Fe^{4+} and consequently the conductivity. The effect of acceptor substitution can also be illustrated by Figure 6.9 where a shift of σ_{min} towards lower P_{O_2} increases σ_{Air} relative to the non-substituted material.

6.2.3 Dynamic Conditions

The reversibility of the change from p-type to n-type conductivity was demonstrated by monitoring *in situ* the change in S when changing atmosphere from a high P$_{O_2}$ (O$_2$) via a low P$_{O_2}$ (N$_2$) and back to a high P$_{O_2}$ (air), as displayed in Figure 6.10a. The DC conductivity, σ_{DC}, of 0.9BFT0 was first measured in high P$_{O_2}$ and subsequently in low P$_{O_2}$ where p-type and n-type conductivity was observed (Figure 6.1b). p-type conductivity was again observed after reintroducing a high P$_{O_2}$ (Figure 6.10b) which further confirms the reversibility of the change from p-type to n-type semiconductor behavior.

The relaxation time of the red-ox reactions governing the oxygen content in 0.8BFT0 and 0.9BFT0 (Eqs. 6.5 and 6.6) is reflected in the measurements of σ_{DC}. Figure 6.10b displays the normalized σ_{DC} of 0.9BFT0 at 700 °C upon a change from air $\rightarrow$ O$_2$ and from O$_2$ $\rightarrow$ air (isothermal oxidation and reduction, respectively). The relaxation time upon oxidation and reduction is seen to be similar. An abrupt change in σ_{DC} of 0.9BFT0 is observed when shifting from N$_2$ to air at 550 °C (Figure 6.10b). This change is, however, not as abrupt as at 700 °C, which highlights the effect of temperature on the oxygen exchange relaxation time. This effect of temperature corresponds well to similar data presented by Morozov *et al.*[180] where the relaxation time upon a change of atmosphere was highly temperature dependent. Furthermore, an effect of a change in atmosphere is apparent for σ'_{AC} already at ~270 °C, suggesting a significant oxygen mobility already at such low temperatures (Figure 6.6). Because the measurements of σ'_{AC} are not done at isothermal conditions (continuous heating/cooling) it is difficult to assess whether the atmosphere effect at ~270 °C is due to a surface effect or a real bulk effect. The observed oxygen mobility is nevertheless important with respect to aging of BFO as a ferroelectric. The diffusion length of oxygen vacancies for aging by the bulk effect is within one unit cell (Chapter 2.2) which suggests that hardening of BFO may occur at temperatures below ~270 °C. Aging and hardening of 0.8BFT0 and 0.9BFT0 is further discussed in Chapter 7.

The activation energy of σ'_{AC} for the non-substituted and acceptor substituted materials is similar up to the ferroelectric to paraelectric phase transition (Figure 6.4 and 6.5). The activation energies are equal to those reported for 0.7BFT0e0[178] near 400 °C and comparable to those of Ca- and Nb-substituted BFO.[149,206] The activation energies are found to increase with donor substitution at low temperature and a further increase is apparent at ~500 °C in air. This increase at ~500 °C corresponds well with the temperature where σ'_{AC} starts to increase when the materials are heated in N$_2$ (Figure 6.6). The origin of the increased activation energy at ~500 °C can hence be attributed to the formation of new charge carriers.

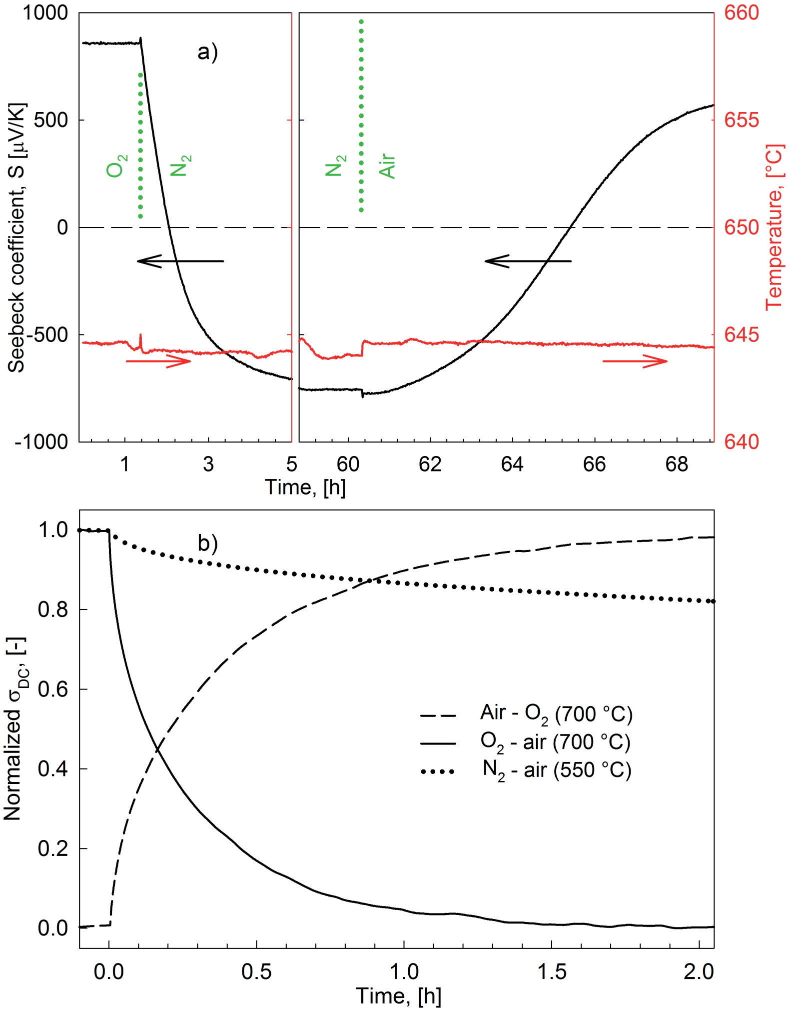

Figure 6.10: Variation of the Seebeck coefficient of 0.9BFT0 upon changing the atmosphere from oxygen rich (O_2) to oxygen poor (N_2) and back to oxygen rich (air) again (a), and the relaxation of normalized conductivity of 0.9BFT0 when changing between air to O_2 at 700 °C and from N_2 to air at 550 °C (b).

The anomaly observed for the conductivity during heating and cooling of 0.8BFTy (Figure 6.7) is attributed to the phase transition from the ferroelectric to paraelectric polymorphs. The amplitude of the anomaly decreases with increasing Ti-content which corresponds well with the less pronounced DTA peak at the phase transition (Figure 5.9a) and the decreasing lattice distortion (Figure 5.3b).

The real AC conductivity of 0.8BFT-1 and 0.8BFT0 displays a marked *increase* at T$_C$ when the materials are cooled in air and O_2 (p-type conductivity, Figure 6.7a and 6.7b). Interestingly, cooling in N_2 (n-type conductivity) has the opposite effect and σ'_{AC} *decreases* over the phase transition. The origin of the opposing behavior in oxidizing/intert atmosphere can be rationalized by considering the reducing character of increasing the temperature. The concentration of $V_O^{\cdot\cdot}$ in oxides increases with increasing temperature, and is highest at the maximum temperature of the experiment (700/800 °C). It is assumed that the materials were in equilibrium with the atmosphere at 700 °C based on earlier reports.[180] The material will consequently re-oxidize during cooling, i.e. oxygen will re-enter the lattice and Fe is oxidized. The result is an increasing conductivity for 0.8BFT-1 and 08BFT0 because both materials are p-type conductors in oxidizing atmospheres (air and O_2). The same reasoning applies during cooling in inert atmosphere, however, because the materials now are n-type conductors a re-oxidation will result in a reduced conductivity. Furthermore, the increase of the unit cell volume at T$_C$ during cooling (Figure 5.8a) is expected to give an abrupt reduction of the conductivity due to longer bond lengths, independently of atmosphere. The results suggest that the effect of oxidation in the p-type regime of 0.8BFT-1 and 0.8BFT0 dominates over the effect of increased unit cell volume. Moreover, the amount of oxygen in the N_2 atmosphere available for re-oxidation of the ceramic is very low which suggests that the conductivity change at the phase transition is dominated by the volume effect for n-type 0.8BFT-1 and 0.8BFT0. σ'_{AC} of 0.8BFT3 decreases slightly in *all* atmospheres at the phase transition (Figure 6.7d), inferring that the material is an n-type conductor also in oxidizing atmospheres. The increasing n-type character with increasing donor substitution corresponds to the suggested shift of σ_{min} to higher P_{O_2}, as described in Figure 6.9. The conductivity of 0.8BFT1 does not change at the phase transition in oxidizing atmosphere, in line with the gradual change of behavior with increasing donor substitution (Figure 6.7c).

The atmosphere dependent behavior of σ'_{AC} for 0.8BFT-1 and 0.8BFT0 at T$_C$ is similar to that observed when $BiFe_{0.7}Mn_{0.3}O_{3+\delta}$ is cooled from the cubic Pm$\bar{3}$m to the orthorhombic Pbnm polymorph.[207] This phase transition is associated with a decreasing unit cell volume in air whereas the paraelectric to ferroelectric transition of 0.8BFT0 was found to give an increasing unit cell volume (Figure 5.8a). Pure BFO also displays an increasing unit cell volume upon adopting the ferroelectric polymorph but this is accompanied by a decreasing conductivity upon cooling.[136] The varying behavior at the phase transition is attributed to the thermal history of the materials where the oxygen exchange kinetics of the electroded samples used in this work is faster[180] than for σ_{DC} measurements done on BFO and $BiFe_{0.7}Mn_{0.3}O_{3+\delta}$ (Figure 6.10).[136,207]

6.2.4 Thermal History

The observed minimum in conductivity and the change from p-type to n-type conductivity highlights the importance of thermal and atmospheric conditions during fabrication of BFO. The conductivity, and hence the leakage currents during application, can be readily reduced by selecting the appropriate atmosphere and temperature during sintering. The atmosphere must be chosen in accordance with the synthesis temperature as the P_{O_2} of σ_{min} is temperature dependent (Figure 6.1 and 6.8). The ferroelectric to paraelectric phase transition temperature was not influenced by annealing in different P_{O_2} (Figure 6.7). This is important as it allows the conductivity to be tuned by the appropriate atmosphere without loosing the high temperature applicability of the material.

The point defect model introduced above also elucidates the effect of Bi_2O_3-loss during fabrication of BFO at high temperature. Following Eq. 6.1, evaporation of Bi_2O_3 gives $V_O^{\cdot\cdot}$ which increases the concentration of electron-holes (Eqs. 6.5 and 6.6) and consequently the conductivity of p-type materials such as BFO. This further illustrates the challenge related to fabrication of BFO where the synthesis temperature should be higher than ∼770 °C to avoid secondary phases,[45] while at the same time it should be kept lower than ∼770 °C to reduce Bi_2O_3-loss and hence conductivity.[122]

The materials used to determine σ_{DC} and S were phase pure before starting the experiment. It should however be mentioned that Fe/Ti rich phases were found by XRD after the measurement was finished (Figure 6.11). It is argued that the secondary phases were concentrated on the surface, based on the comparison of the X-ray diffractograms obtained directly from the surface and the crushed part of the pellet (green and blue line in Figure 6.11). The origin of the secondary phases is most likely loss of Bi_2O_3 and K_2O during the measurement. A small decrease of the conductivity of 0.9BFT0 (∼8 %) was observed for $P_{O_2} = 1$ when comparing measurements in the beginning and the end of the experiment.

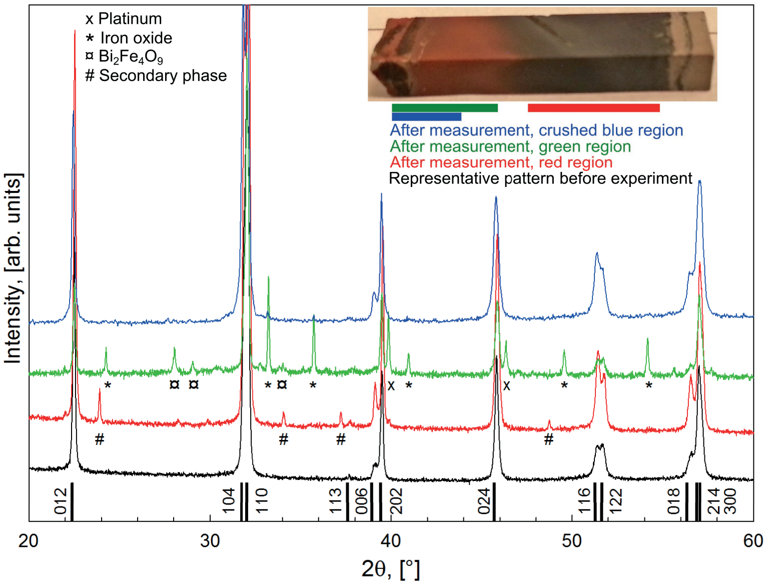

Figure 6.11: X-ray diffractograms of 0.8BFT0 powder (black) and different parts of the sample used for DC conductivity measurements (colors). The inset shows a picture of the sample after the measurement. The colors of the diffractograms correspond to the color bars below the inset. Secondary phases that evolved during the measurement are denoted by symbols and the lower indices refer to the room temperature structure of BFO (ICDD nr. 04-009-3445).

Chapter 7

Ferroelastic Properties of BFO-BKT

7.1 Results

7.1.1 Temperature Dependent Ferroelastic Behavior

The ferroelastic behavior of 0.8BFTy and 0.9BFTy materials was investigated by application of compressive stress and recording the strain response of the materials. The mechanical stress-strain curves of 0.8BFT0 and 0.8BFT3 ceramics, cooled by a rate of 300 °C/h, are displayed in Figure 7.1a. A close to linear relationship between mechanical stress and strain is evident. Quenching the materials in air from above T_C resulted in an increased hysteresis behavior and an increased remanent strain (Figure 7.1b). The opening of the hysteresis loop and the increase of ϵ_r observed after quenching was more pronounced for 0.8BFT0 than for 0.8BFT3.

The ferroelastic mechanical stress-strain behavior of air-quenched 0.8BFTy and 0.9BFTy from room temperature up to 400 °C in air is displayed in Figure 7.2. ϵ_r increases with temperature up to 200 °C for 0.8BFTy which substantiates a thermally activated ferroelastic domain switching behavior (Figure 7.3a). σ_c was, on the other hand, decreasing with increasing temperature up to 400 °C for all investigated materials (Figure 7.3b). 0.8BFT1 and 0.8BFT3 both display a low ϵ_r at room temperature where the maximum applied mechanical stress (σ_{max}) is lower than σ_c. At 100 °C, σ_{max} surpasses σ_c of 0.8BFT1 and ϵ_r increases with a similar temperature dependence as seen for 0.8BFT0. The remanent strain of 0.8BFT3 remains low at 100 °C but increases at 200 °C where σ_{max} surpasses σ_c of 0.8BFT3. The effect of temperature on the remanent strain is further illustrated by the similar ϵ_r obtained for 0.8BFT0 at 100 °C with $\sigma_{max} = 800$ MPa and at 400 °C with $\sigma_{max} = 400$ MPa (Figure 7.2a).

The coercive stresses of 0.8BFT0, 0.8BFT1, 0.8BFT3 and 0.9BFT0 decreased significantly with increasing temperature (Figure 7.3b), while substitution of Fe with Ti (donor substitution) increased σ_c resulting in ferroelastic hardening at all temperatures. The mechanical stress-strain curves of

0.8BFT0 cooled by a rate of 300 °C (Figure 7.1a, dashed line) and quenched 0.9BFT1 (Figure 7.2e) were measured at 400 °C up to 665 and 730 MPa, respectively, without surpassing σ_c. Based on these measurements, it is estimated that $\sigma_c > 800$ MPa for both materials. Annealing air-quenched 0.8BFT0 at 400 °C was found to increase the coercive stress as shown in the inset of Figure 7.3b. The observations gave no evidence for softening of the materials by repeated stress-strain cycles.

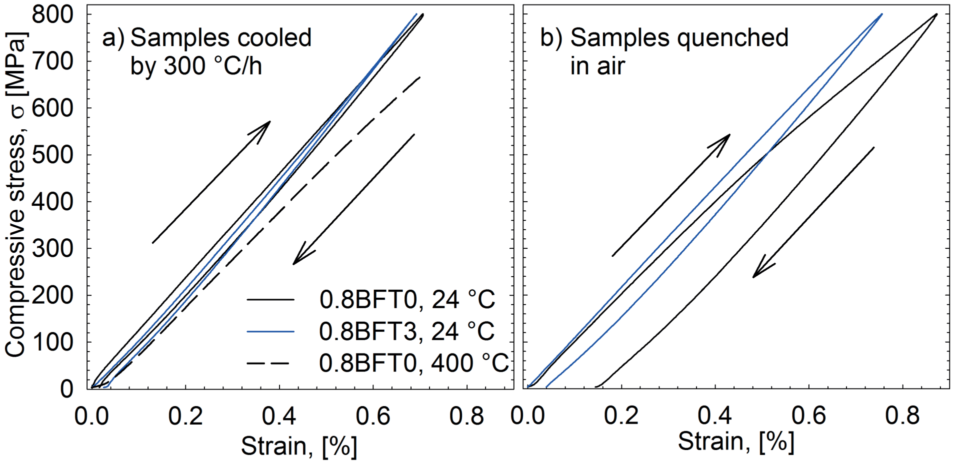

Figure 7.1: Mechanical stress-strain curves at room temperature in ambient air for 0.8BFT0 and 0.8BFT3 ceramics cooled at 300 °C/h (a) and air-quenched (b). The partial stress-strain loop of 0.8BFT0 (cooled at 300 °C/h) measured at 400 °C is also included in (a). The arrows denote the direction of stress progression.

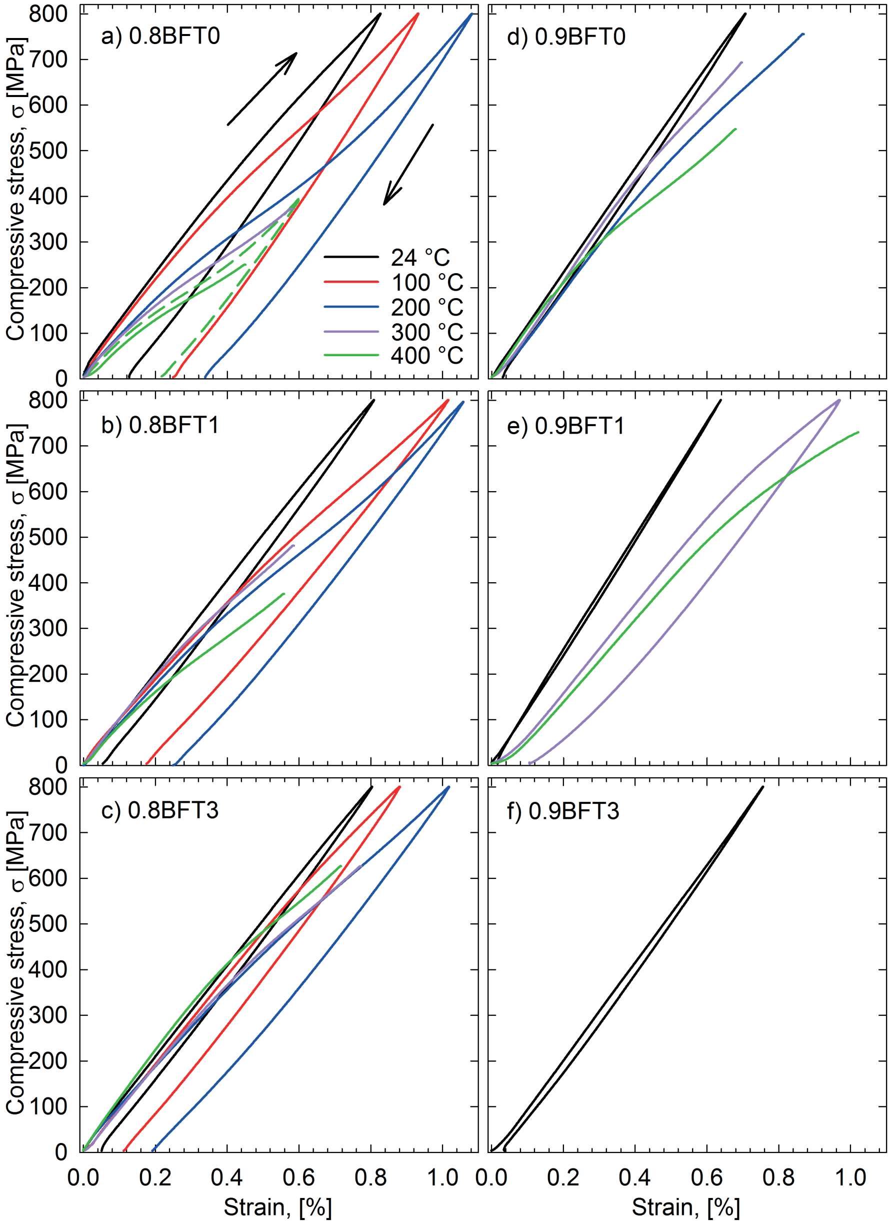

Figure 7.2: Mechanical stress-strain curves from room temperature to 400 °C for 0.8BFTy (a-c) and 0.9BFTy (d-f) ceramics quenched to ambient temperature from above T_C. The arrows denote the direction of stress progression and all measurements were done in ambient air.

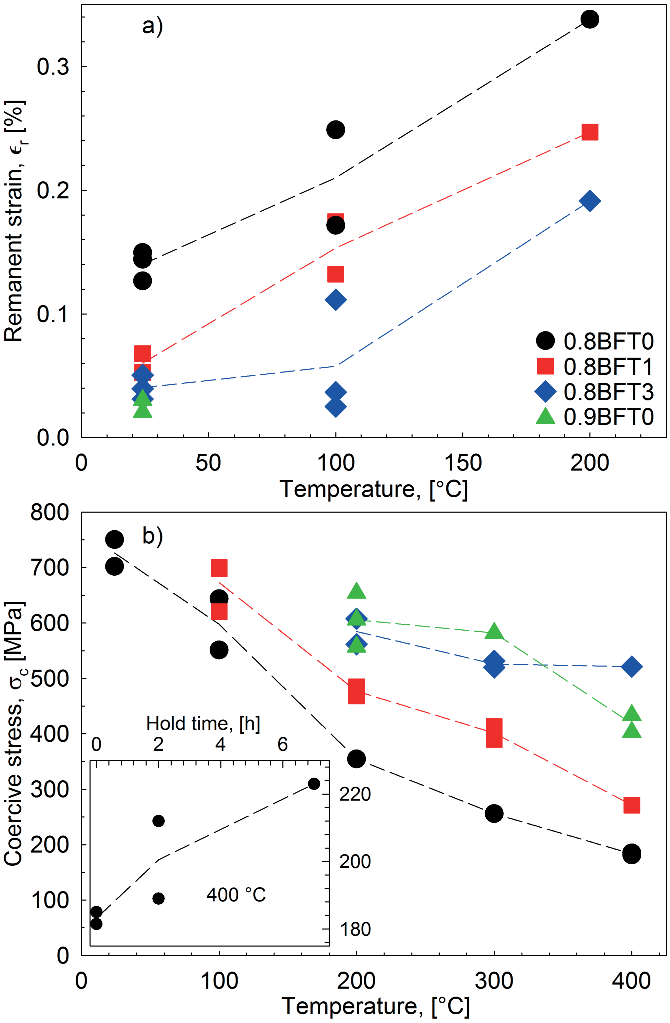

Figure 7.3: Remanent strain (a) and coercive stress (b) in ambient air as a function of temperature for 0.8BFTy and 0.9BFT0. The inset in (b) displays the coercive stress of 0.8BFT0 after annealing a quenched sample at 400 °C for 0, 2 and 7 h before testing. $\sigma = \sigma_{max} = 800$ MPa was used up to 200 °C and $\sigma_c < \sigma < \sigma_{max}$ for higher temperatures. The error in remanent strain and coercive stress was estimated to 5 % based on data scattering and previous measurements.[93,193] The dashed lines act as a guide to the eye.

7.1.2 Atmosphere Dependent Ferroelastic Behavior

It was established in Chapter 6 that annealing 0.8BFTy in varying P_{O_2} alters the concentration of $V_O^{\cdot\cdot}$ and the major charge carriers which consequently influences the electrical conductivity. The concentration of oxygen vacancies has been related to aging and hardening of ferroelectrics (Chapter 2.2) and a series of experiments were undertaken to elucidate the effect of annealing 0.8BFTy in different P_{O_2} on the mechanical stress-strain behavior. 0.8BFT0, 0.8BFT1 and 0.8BFT3 ceramics were quenched to ambient temperature after being annealed in air, N_2 and O_2 (Chapter 3.2.10). Large changes in P_{O_2} were applied to maximize any effect of the thermal annealing in controlled atmosphere.

The stress-strain behavior of 0.8BFT0, 0.8BFT1 and 0.8BFT3 annealed and subsequently quenched from air, N_2 and O_2 is displayed in Figure 7.4a-c, respectively. An atmosphere dependent opening of the stress-strain hysteresis loop is apparent for all three materials. The effect of annealing in different atmospheres is most pronounced for 0.8BFT3 (Figure 7.4c) where a significant opening of the hysteresis loop is observed after annealing in O_2, as elaborated below.

A 6th degree polynomial fitted to the $d\sigma/d\epsilon$ is plotted in Figure 7.4d-f. The $d\sigma/d\epsilon$ curves are provided to elucidate the hardening/softening effect of annealing in different atmospheres. σ_c is defined as the minimum of $d\sigma/d\epsilon$ and is used when $\sigma_{max} > \sigma_c$. If $\sigma_{max} < \sigma_c$, $d\sigma/d\epsilon$ is extrapolated to estimate σ_c (0.8BFT1, N_2) or used as an indication of increasing/decreasing σ_c (0.8BFT3, air and N_2). The donor substituted materials display an *increasing* σ_c upon quenching from N_2 relative to quenching from air, while a slight decrease is observed for 0.8BFT0 (Figure 7.5a and 7.4f). The subsequent quenching from O_2 *lowered* the coercive stress of all three materials (Figure 7.5c and 7.4f). σ_c of 0.8BFT3 quenched from O_2 was even lower than that of the air-quenched sample resulting in $\sigma_{max} > \sigma_c$ and significant opening of the hysteresis loop (Figure 7.4c). Based on the experiments with air-quenched samples described in Chapter 7.1.1 it is argued that the observations shown in Figure 7.4 are an effect of the annealing and not the result of repeated stress-strain cycles. The changes in σ_c and ϵ_r due to the annealing in different atmospheres are summarized in Figure 7.5.

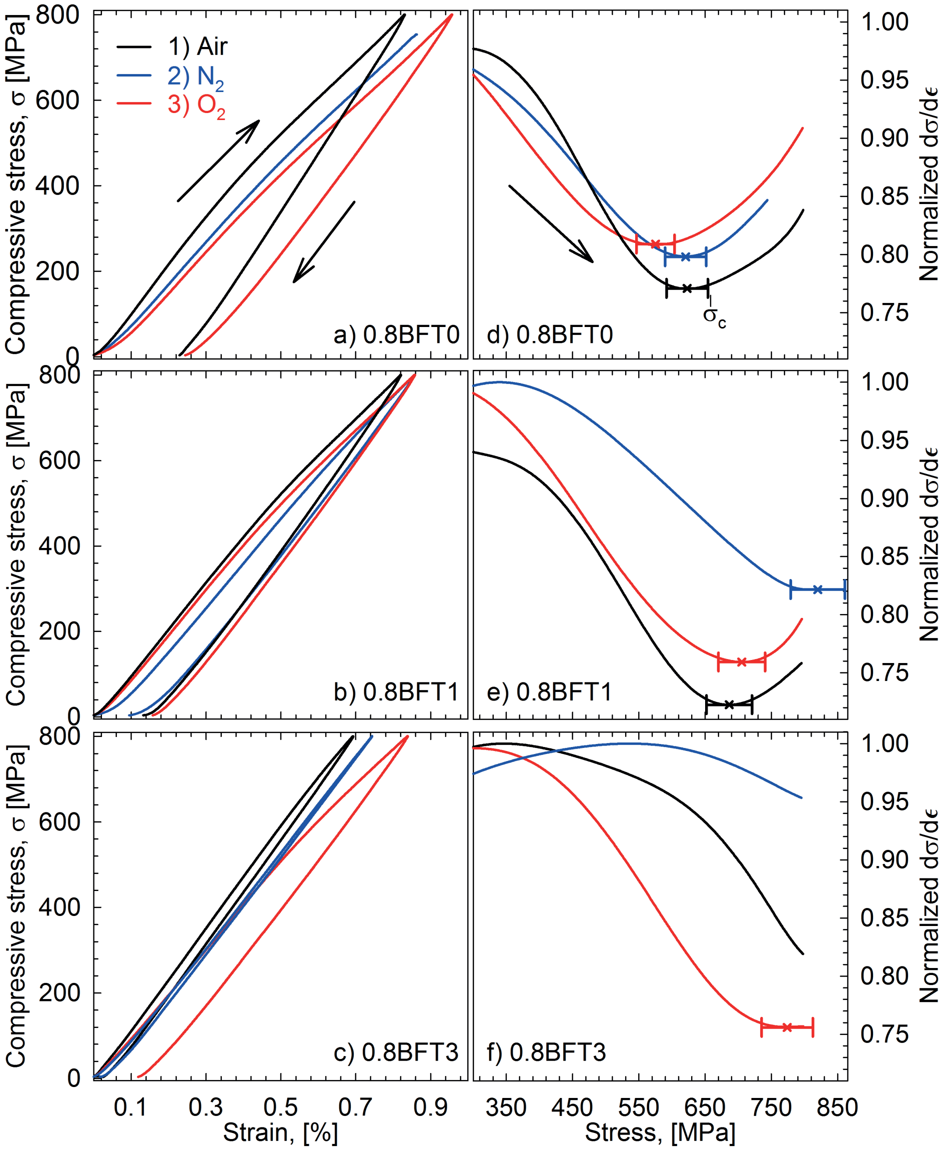

Figure 7.4: Mechanical stress-strain curves (a-c) and the corresponding $d\sigma/d\epsilon$ during increasing stress as a function of applied stress (d-f) for 0.8BFT0, 0.8BFT1 and 0.8BFT3 measured at 100 °C on samples that were quenched to ambient temperature after annealing in air (1), N_2 (2) and O_2 (3). The same sample was used for measurement in all three atmospheres. 5 % error bars are added to the minimum of the $d\sigma/d\epsilon$ curves at the position of the coercive stress.

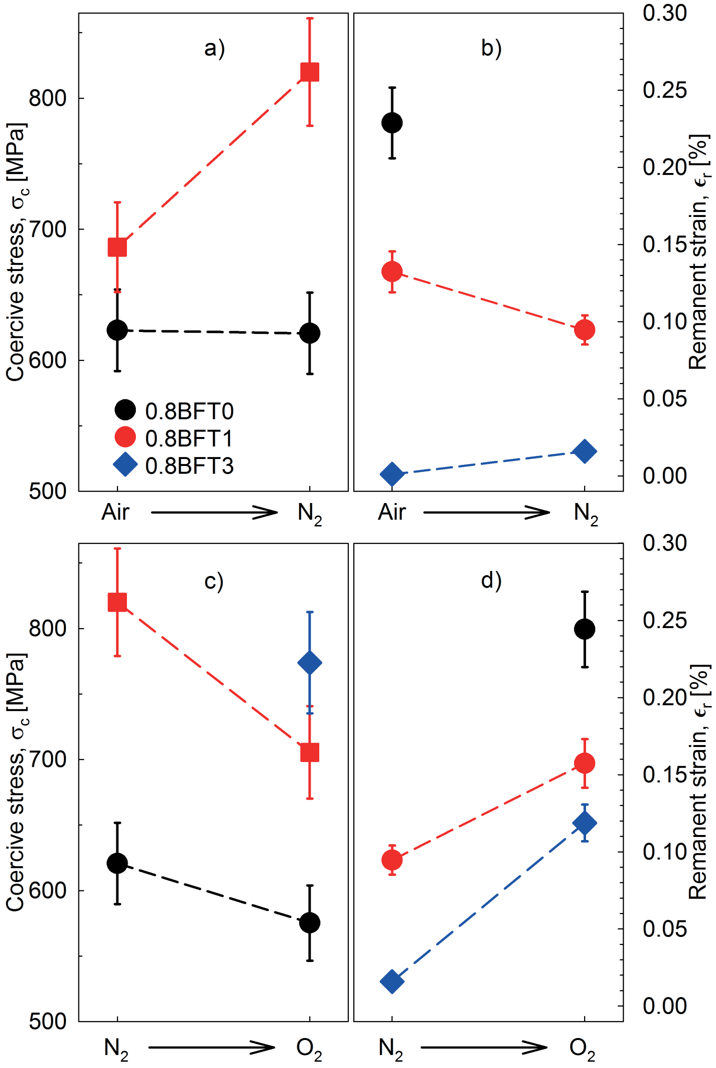

Figure 7.5: Coercive stress and remanent strain for air/N_2 annealed (a and b), and N_2/O_2 annealed (c and d) 0.8BFT0, 0.8BFT1 and 0.8BFT3 ceramics extracted from the measurements in Figure 7.4. All measurements were done at 100 °C. Dashed lines are guides to the eye.

7.2 Discussion

7.2.1 Aging

Ferroelastic softening, identified by an opened stress-strain hysteresis loop, reduced σ_c and increased ϵ_r, was observed after quenching 0.8BFT0 and 0.8BFT3 from above T_C (Figure 7.1). The point defects in a material are randomly distributed in the crystal lattice in its paraelectric and paraelastic state above T_C. Rapid cooling (quenching) will freeze in the random distribution due to the low mobility of the point defects at low temperature, which consequently reduces aging and pinning of domain walls and leaves a softer material. Slow cooling will, on the other hand, ensure the presence of point defect mobility below T_C where the driving force for aging is present. Slow cooling will hence allow the formation, and more importantly reorientation, of point defect clusters or defect dipoles and cause aging (Chapter 2.2). The observations correspond well with quenched vs. non-quenched ferroelectric properties of BFO and thermally annealed/non-annealed BT.[41,82] It also infers that point defects are the main reason for pinning of domain walls in BFO when considering corresponding observations for PZT.[208]

The ferroelastic softening (reduced aging) observed after quenching the materials infers that aging may be induced by annealing below T_C, but sufficiently above the temperature where point defects become immobile. Oxygen and oxygen vacancies were found to be mobile in 0.8BFTy down to at least ~270 °C where a change of the conductivity was observed upon changing atmosphere (Figure 6.6). Aging was observed through an increased σ_c upon annealing 0.8BFT0 at 400 °C (inset of Figure 7.3) which is analogous to the effect of annealing on BT presented by Zhang and Ren.[83] The aging of PZT and BT is suggested to be the result of oxygen vacancy migration where the driving force is the non-degenerate state of the oxygen lattice sites that arise with spontaneous polarization below T_C (Figure 2.8). Oxygen vacancies were shown to be an important part of the point defect chemistry of 0.8BFTy and 0.9BFTy in Chapter 6 and it was argued that this is the case for pure BFO as well. Based on the established point defect chemistry, and the relation between ferroelastic performance and thermal history, it is suggested that oxygen vacancies are an important constituent to aging observed in BFO. The data are not, however, sufficient to determine the mechanism behind the observed aging.

7.2.2 Hardening by Donor Substitution

Ferroelastic hardening with an increased σ_c and closing of the hysteresis loop was observed upon donor substitution (Ti^{4+} replacing Fe^{3+}) of 0.8BFTy and 0.9BFTy (Figure 7.2 and 7.3b). The decreasing permittivity with increasing Ti-substitution is furthermore an indication of a hardened ferroelectric (Figure 5.10).[1] This hardening effect is opposite to the well known softening observed upon donor substitution in PZT where the hard/soft properties are closely related to $V_O^{\cdot\cdot}$.[9,74,91,92] The origin of $V_O^{\cdot\cdot}$ in BFO and PZT is similar through the loss of Bi_2O_3 (Eq. 6.1) and PbO, respectively. Donor substitution can be charge compensated by annihilation of $V_O^{\cdot\cdot}$, as argued in Chapter 6.2.2 for 0.8BFTy and 0.9BFTy. This infers that the donor substituted materials should have a lower concentration of $V_O^{\cdot\cdot}$ that can take part in the pinning of domain walls. The ferroelastic performance of the donor substituted 0.8BFTy and 0.9BFTy consequently suggests that $V_O^{\cdot\cdot}$ cannot be the sole reason for domain wall pinning in BFO and BFO-based materials.

A hardening effect by donor substitution has not been reported previously to the best of the authors knowledge. Earlier reports on donor substituted BFO have shown that the P-E loop is less lossy, however, as sub-coercive electric fields are often used it is difficult to conclude on the hard/soft properties of the donor substituted materials.[41,148,150,209] Rojac *et al.*[41] suggest that loss of Bi_2O_3, and then presumably an increasing concentration of $V_O^{\cdot\cdot}$, is beneficial for the de-pinning of domain walls in BFO. These results are in line with the observed effect from donor substitution reported herein. Hagiwara and Fujihara[181] on the other hand presented a softening effect of CuO *doping* of BFO-BKT (60 mol% BFO), which is more in line with what is observed in PZT with donor *substitution*.

The removal of oxygen vacancies by donor substitution may also alter the concentration of charge carriers (related to the valence of Fe), as discussed in Chapter 6.2.2. The conductivity difference between domain walls and domains in thin film and ceramic BFO suggests a different concentration of $V_O^{\cdot\cdot}$ and charge carriers associated with the domain walls than the domains.[85,86,154] It was recently discussed whether the valence of Fe and the different electronic properties of domain walls and domains are of importance for migration of domain walls, possibly through a charge transfer mechanism.[28] While the results presented herein provide an important insight to the major point defects in BFO-materials, the results do not provide a direct clarification of the influence of the valence of Fe on domain wall pinning.

7.2.3 Influence of Lattice Distortion

The remanent strain increased with increasing temperature up to 200 °C (Figure 7.3a), opposite to what has been reported for both hard and soft PZT.[91] The temperature dependence of ϵ_r can be rationalized by considering σ_c and lattice distortion of the materials. The lattice distortion of 0.8BFT0 is relatively constant up to ∼400 °C which suggest that the induced strain from each non-180° domain switching event will produce a similar strain contribution. Furthermore, σ_c decreases with increasing temperature such that it becomes easier to reorient domains, subsequently resulting in an increasing remanent strain with increasing temperature. The lattice distortion of PZT on the other hand decreases continuously up to T_C which results in a gradual decrease of ϵ_r.[91] It is noted that the high σ_c prevents a saturated domain switching state during compression and that this will also influence the observed ϵ_r.

Reorientation of ferroelastic domains in a mechanical field occurs because it is energetically favorable.[90] However, if the lattice distortion (c_{pc}/a_{pc}) is small, it may be expected that the energy gain achieved by a switching event during mechanical loading is small. The low energy gain further implies that the critical stress needed for domain reorientation will be higher in materials with a low lattice distortion, such as 0.8BFT3. With donor substitution of 1 mol% Ti, σ_c increased more for 0.9BFT0 than for 0.8BFT0 ($>$ 90 % and 48 %, respectively) while the lattice distortion decreased significantly more for 0.8BFT0 than for 0.9BFT0. These results suggest that the increased σ_c observed with increased donor substitution (Figure 7.3b) is not the result of the decreasing lattice distortion (Figure 5.3). Investigations of La-substituted BFO-PT have shown a threshold value for the c_t/a_t-ratio below which an abrupt decrease of σ_c was observed.[96] Above this threshold, there were only small variations of σ_c. The threshold was related to the energy cost of a switching event which leads to a large structural deformation when the c_t/a_t-ratio is high. While no such threshold has been identified in this work, its existence cannot be ruled out but it is challenging to identify it due to the generally high σ_c of 0.8BFTy and 0.9BFTy.

The lattice distortion, which is important for the strain generated by non-180° domain wall movement in ferroelectrics/ferroelastics, was reduced by donor substitution (Figure 5.3). The reduction of ϵ_r with donor substitution is probably a combined effect of the lower lattice distortion and the higher σ_c. The domain switching rate is highest at σ_c which means that $\sigma_{max} > \sigma_c$

will give an abrupt increase of ϵ_r, as observed for 0.8BFT1 and 0.8BFT3 in Figure 7.3. Such an abrupt increase is also reported by Leist *et al.*[96] for La-substituted BFO-PT and by Marsilius *et al.*[91] for hard/soft PZT. The high σ_c prevented the acquisition of fully saturated stress-strain hysteresis loops for the investigated materials as this would require $\sigma_{max} \gg \sigma_c$. The smaller opening of the stress-strain hysteresis loop of 0.8BFT3 relative to 0.8BFT0 observed upon quenching (Figure 7.1) is hence proposed to result from the lower lattice distortion and $\sigma_{max} < \sigma_c$ for 0.8BFT3. Quenching is mainly related to a randomization of the point defect distribution that provides a reduced σ_c and the absolute reduction of σ_c upon quenching is assumed to be of the same magnitude for both 0.8BFT0 and 0.8BFT3. Furthermore, the influence of donor substitution on T_C of 0.8BFTy and 0.9BFTy was found to be modest (Table 5.2) which confirms that the different ϵ_r and σ_c is not the result of sub-T_C quenching.

The real maximum switching strain ($0.285 \times \epsilon^r_{sw}$) of 0.8BFT0, 0.8BFT1 and 0.8BFT3 is 0.22, 0.05 and 0.02 %, respectively, as calculated from room temperature lattice parameters (Chapter 2.4). The reported ϵ_r of 0.8BFT0 is ~0.14 % which suggest some degree of backswitching in addition to the stress-strain hysteresis loop not being fully saturated for $\sigma_{max} = 800$ MPa. The reported strain for 0.8BFT1 and 0.8BFT3 in Figure 7.3a is slightly higher than the calculated maximum and is probably related to challenges with resolving the lattice parameters from the diffraction data. The domain size in a ferroelectric may be influenced by the grain size.[70] The grain size for the materials was however relatively constant and the observed properties are most likely not related to grain size effects.

7.2.4 Atmosphere Dependent Stress-Strain Behavior

Annealing and quenching of 0.8BFTy ceramics from N_2 and O_2 resulted in ferroelastic hardening (increasing σ_c) and softening (decreasing σ_c), respectively, where the effect was most pronounced for the donor substituted materials (Figure 7.4 and 7.5). The observed hardening/softening is in line with the expected effect when considering the relation between point defects and the hard/soft properties of ferroelectrics/ferroelastics (Chapter 2.2). The concentration of $V_O^{\cdot\cdot}$ increases upon annealing 0.8BFTy in a low P_{O_2} (N_2), hence the concentration of point defects that can pin domain walls and result in ferroelastic hardening increases. The observed effect is analogous to acceptor substitution in PZT where the concentration of $V_O^{\cdot\cdot}$ is expected to increase, resulting in hard ferroelectric behavior.[9] Moreover, annealing in high P_{O_2} (O_2) reduces the concentration of $V_O^{\cdot\cdot}$, hence softening the material by removing point defects that may pin domain walls (lower σ_c). The effect of annealing in O_2 is analogous to donor substitution of PZT.[9] The increase (decrease) of σ_c was accompanied by a corresponding decrease (increase) of ϵ_r as the hysteresis loop closes for a harder material (higher σ_c) or opens for a softer material (lower σ_c), as demonstrated in Figure 7.5b and 7.5d.

The effect of annealing in different atmospheres was most pronounced in the donor substituted materials, which are expected to possess a lower concentration of $V_O^{\cdot\cdot}$ than 0.8BFT0 (Chapter 6.2.2). The lower concentration suggests that the relative change of the $V_O^{\cdot\cdot}$ concentration upon annealing in different atmospheres will be larger in the donor substituted materials. This may explain the seemingly larger effect of atmosphere on 0.8BFT1 and 0.8BFT3, and possibly why 0.8BFT0 is unaffected by annealing and quenching from N_2. A definite conclusion is, however, hindered by the high σ_c of 0.8BFT3.

Donor substitution and annealing in O_2 are both expected to reduce the concentration of $V_O^{\cdot\cdot}$ (Chapter 6.2.2) but only annealing in O_2 provides a reduced σ_c. This infers that the hardening induced by donor substitution with Ti^{4+} originates from an unknown effect that dominates over the effect of annihilating $V_O^{\cdot\cdot}$. Further investigations are required to determine the mechanism behind the hardening induced by donor substitution.

The coercive stress of 0.8BFT1 remains the same after air- and O_2-quenching (Figure 7.4e). This may reflect the small P_{O_2} difference between air and O_2 or that the material did not achieve equilibrium during the annealing. However, the results are still of importance as the trend when going from annealing in a high P_{O_2} via low P_{O_2} and back to high P_{O_2} shows a clear hardening and softening effect. The samples used for the measurements displayed in Figure 7.4 have the same atmospheric history meaning that they were only exposed to air before being annealed in N_2 and subsequently O_2. Several samples were investigated for each composition with slightly different atmospheric history and all show the same trends with respect to softening/hardening as presented above. The results confirm the importance of $V_O^{\cdot\cdot}$ in relation to the hard/soft characteristics of BFO-based ferroelastic/ferroelectric materials.

Chapter 8

Domains and Homogeneity of BFO-BKT Materials

8.1 Results

8.1.1 Domain and Crystal Structure

0.8BFT0 and 0.8BFT-1 ceramics were investigated by TEM, and a complex domain structure was generally identified with certain regions within some grains that display defined domains (Figure 8.1). The larger grain size of 0.8BFT-1 relative to 0.8BFT0 observed by SEM (Figure 5.4a and 5.4b) was confirmed by TEM and might be the reason for the more slightly more defined domain structure of 0.8BFT-1.

A rhombohedral R3c crystal structure was identified for both 0.8BFT0 and 0.8BFT-1 by electron diffraction, in accordance with XRD (Figure 5.1). SAED patterns from 0.8BFT0 and 0.8BFT-1 shown in Figure 8.2c and 8.2g, respectively, display the characteristic ($1/2$ $1/2$ $1/2$) super-reflection along the $[111]_{pc}$ directions which stem from the distortion of the rhombohedral R3c unit cell.

The TEM image of the 0.8BFT0 grain shown in Figure 8.2a display defined domains in the upper part of the grain. SAED patterns obtained from Region 1, 2 and 3 (defined in Figure 8.2a and 8.2b) are shown in Figure 8.2c-e, respectively. The characteristic ($1/2$ $1/2$ $1/2$) reflection along the $[111]_{pc}$ direction is observed for Region 1 (Figure 8.2c). The intensity of the reflection is reduced in Region 2 and is not visible in Region 3, as apparent in Figure 8.2d and 8.2e, respectively. Furthermore, no splitting is observed for the ($0\bar{3}\bar{3}$) diffraction spot in Region 1 while a clear splitting is apparent in Region 2 and 3, with that in Region 3 being the largest (insets in Figure 8.2c-e). The results confirm the general observation of a complex domain structure in 0.8BFT0 (Figure 8.1a-c).

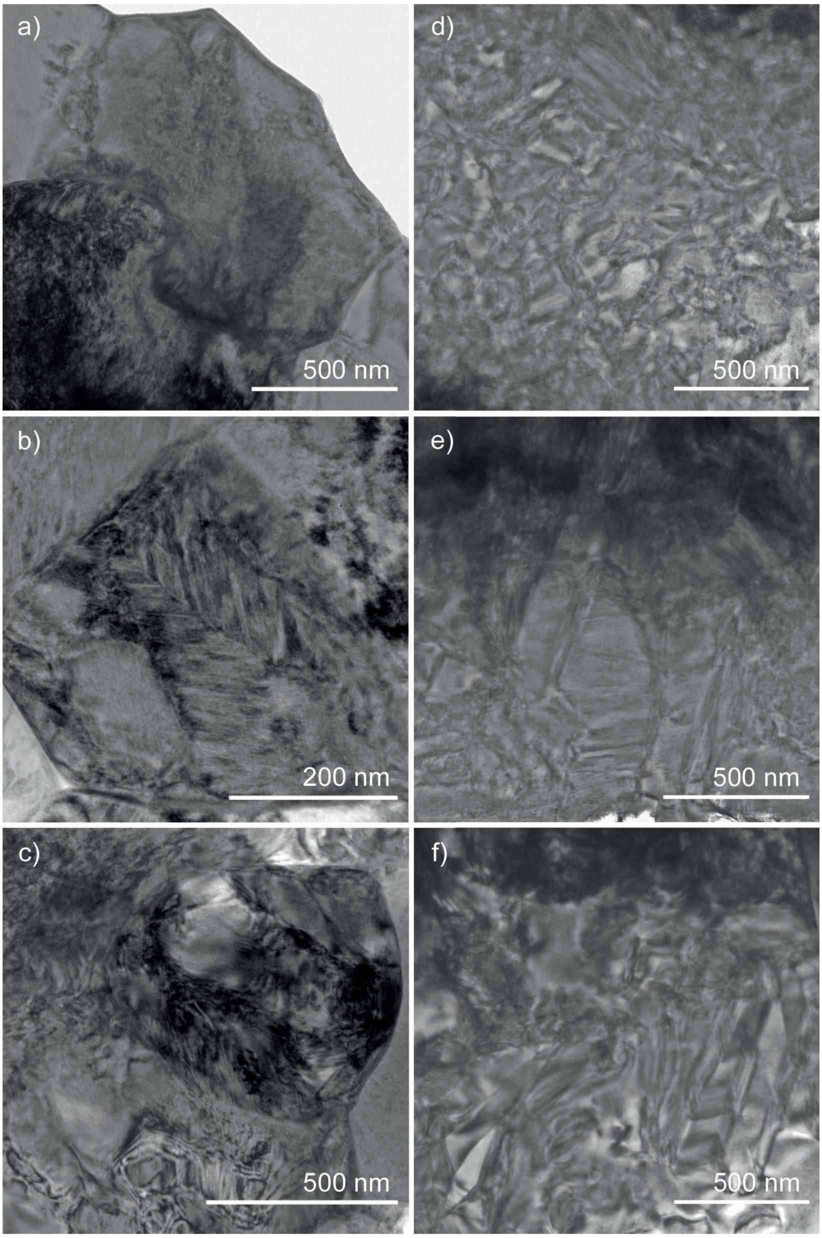

Figure 8.1: TEM images of three different grains in 0.8BFT0 with the zone axis oriented along the $[110]_{pc}$ (a), $[210]_{pc}$ (b) and $[1\bar{1}\bar{3}]_{pc}$ (c) directions; and 0.8BFT-1 with the zone axis oriented along the $[100]_{pc}$ (d), $[110]_{pc}$ (e) and $[111]_{pc}$ (f) directions.

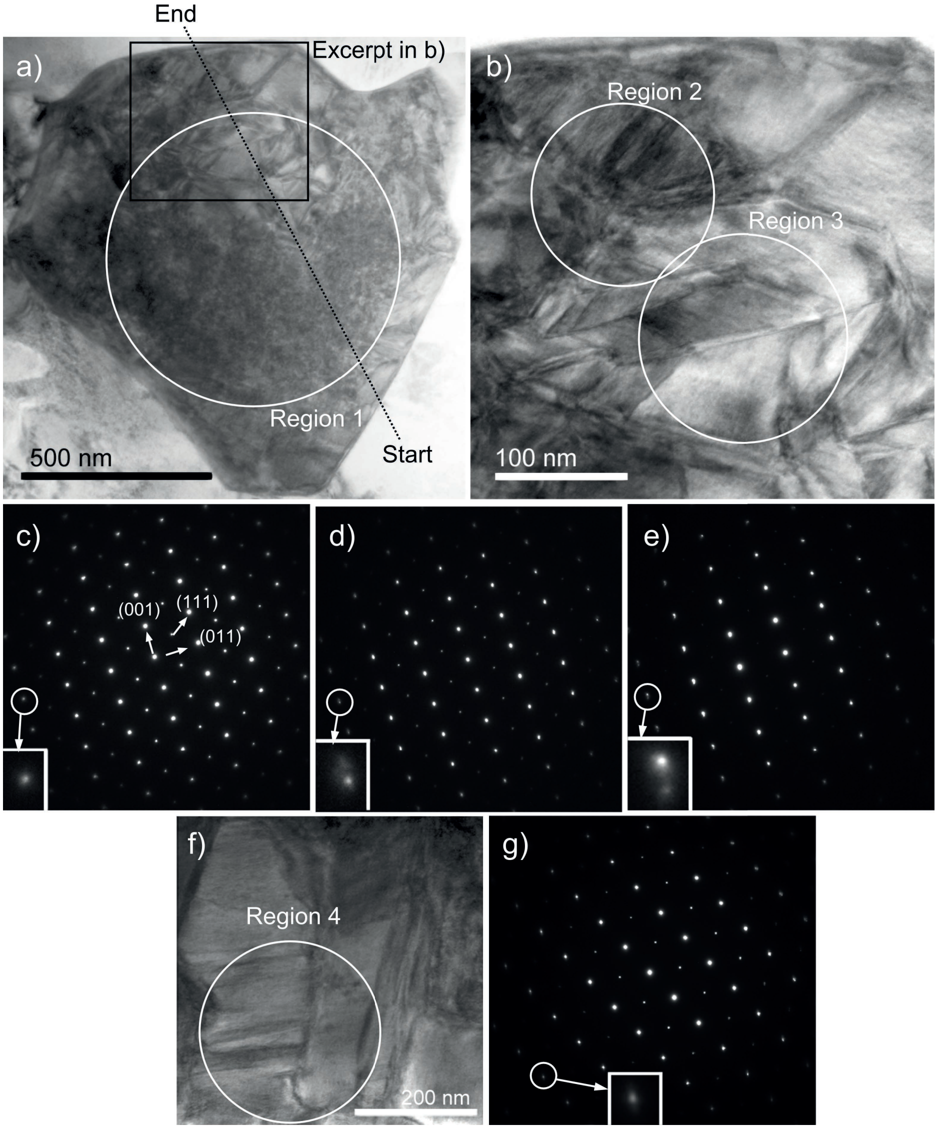

Figure 8.2: TEM image of a single grain in 0.8BFT0 (a); higher magnification TEM image of the area in (a) marked by a black square (b); SAED pattern of Region 1, 2 and 3 as defined in (a) and (b) by white rings (c, d and e, respectively); TEM image of a single grain in 0.8BFT-1 (f); SAED pattern of Region 4 as defined in (f) by a white ring (g). The insets in (c-e) and (g) display the magnified (0$\bar{3}\bar{3}$) reflection. The zone axis is oriented along the $[110]_{pc}$ direction. The black dotted line in (a) marks the trace of the EDS and EELS measurements presented in Figure 8.3.

8.1.2 Chemical Homogeneity

The chemical homogeneity of the 0.8BFT0 grain shown in Figure 8.2a was investigated by simultaneous EDS and EELS analysis along the dotted line. The upper part of the grain with clearly defined domains was found to be enriched with Fe relative to Ti by EELS analysis, as presented in Figure 8.3a. The region without clearly defined domains was correspondingly enriched with Ti relative to Fe while no variation was observed for the oxygen content. EDS analysis in TEM (Figure 8.3b) confirmed the Fe, Ti and O concentration profiles observed by EELS. In addition, the TEM-EDS analysis indicate that the Fe-rich region is also enriched with Bi while the Ti-rich region is enriched with K. The relative thickness of the sample provided in Figure 8.3c confirms that the observed non-homogeneous elemental distribution is not the result of thickness variations of the sample. The chemical homogeneity of 0.8BFT-1 was also investigated but no variations were observed in this sample.

8.2 Discussion

The TEM investigations presented here (Figure 8.2) demonstrate that both 0.8BFT0 and 0.8BFT-1 have a rhombohedral crystal structure, in line with XRD observations presented in Chapter 5.1.1. The structure is identified by the ($^1/_2$ $^1/_2$ $^1/_2$) superlattice reflections that are observed along the [111] direction in Figure 8.2c and 8.2g. The SAED patterns also correspond to those previously reported for 0.7BFT0e0, 0.8BFT0 and pure BFO.[144,176]

The disappearance of the ($^1/_2$ $^1/_2$ $^1/_2$) diffraction spots in 0.8BFT0 is not a result of chemical inhomogeneity (Fe-rich vs Ti-rich regions, Figure 8.3) but rather the local structure in regions with domains that are readily visible. The SAED patterns from Regions 2 and 3 (Figure 8.2d and 8.2e) where the ($^1/_2$ $^1/_2$ $^1/_2$) diffraction spots are visible and not visible, respectively, are both obtained from the Fe-rich part of the grain. There is, however, a less defined domain structure in Region 2 which apparently allow the appearance of the ($^1/_2$ $^1/_2$ $^1/_2$) spots. TEM-investigations by Ozaki *et al.*[176] revealed a gradual disappearance of the ($^1/_2$ $^1/_2$ $^1/_2$) diffraction spots when increasing the BKT content from 40 to 50 mol% in BFO-BKT. The gradual disappearance was attributed to a decreasing rhombohedral distortion of the crystal lattice and the emergence of polar nanoregions within a non-polar matrix.

The complex domain structure observed by TEM might to some extent be

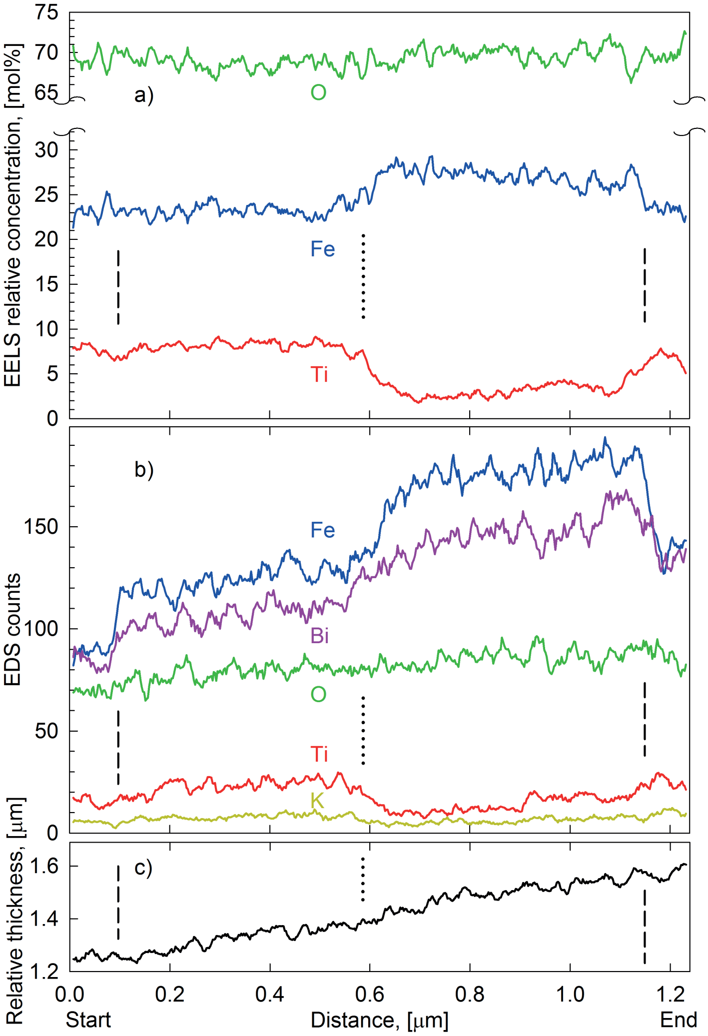

Figure 8.3: Distribution of elements along the dotted line in Figure 8.2a as determined by EELS (a) and EDS (b) in STEM mode, and the relative thickness of the same sample along the line (c). The dashed lines mark crossing of the grain boundary in each end and the dotted line marks border of the region of clearly defined domains. The data are smoothed by a 7 point moving average.

caused by the observed inhomogeneous chemical distribution of elements. A complex domain structure was also observed for 0.7BFT0e0 by Ozaki *et al.*[176] while relatively well defined domains were reported for pure BFO by Rojac *et al.*[144] Reorientation of ferroelectric and ferroelastic domains depend on domain wall movement which is expected to be easier with a well defined domain structure. The TEM-observations hence infer that the hard ferroelastic behavior observed for 0.8BFT0 (Chapter 7) stems from the complicated domain structure in the material.

Lead-free ferroelectrics often include volatile elements such as Bi, K and Na which motivates short synthesis times and low temperatures to limit evaporation. A complex chemical composition in the perovskite lattice is quite typical for many promising lead-free material systems. Despite the complex chemistry, the degree of chemical homogeneity in synthesized materials has not received much attention. Materials prepared by the solid state method are especially prone to be chemically inhomogeneous due to potentially long diffusion distances and slow cation diffusion. The observations by TEM presented herein suggest that the ferroelectric/ferroelastic properties of BFO-based materials may depend on the chemical homogeneity of the ceramics. These results motivated further investigations into the effect of chemical homogeneity and its influence on the functional properties of BFO-BKT materials.

Chapter 9

The Effect of Sintering Procedure and Varying the A:B-ratio in BFO-BKT

9.1 Results

9.1.1 Microstructure and Chemical Homogeneity

The effect of sintering procedure and small variations of the A:B and Fe:Ti-ratio was investigated in a third composition series, 0.7BFTyez. The composition with 70 mol% BFO was chosen based on the high strain recently reported by Morozov *et al.*[180] The donor substitution level of 1 mol% (y) was chosen based on the observed effect in 0.8BFTy and 0.9BFTy (Chapter 6) and 0.5 mol% excess A-cations (z) was added based on the findings reported by Christensen.[179] The compositional variations are illustrated in Figure 9.1 and the compositions are defined in Table 3.2 (page 50).

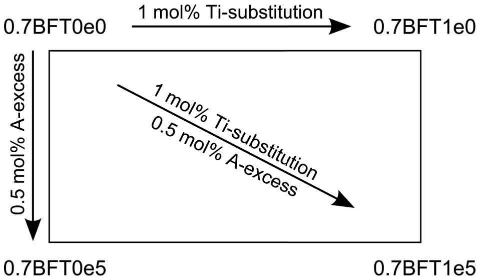

Figure 9.1: Visual representation of the synthesized 0.7BFTyez compositions investigated. Note that 0.7BFT0e0 corresponds to 0.7BFO - 0.3BKT.

0.7BFTyez ceramics with density $\geq$ 96 % were prepared by the solid state method as described in Chapter 3.1.2. The grain size increased by increasing the sintering time from 2 to 10 h and further to 20 h, as summarized in Table 9.1. The three sintering times correspond to sintering procedures S1, S2 and S3 defined in Table 3.3. SEM micrographs obtained by backscattered electrons from polished ceramics (not thermally etched) are presented in Figure 9.2. The micrographs confirm a dense microstructure and increasing

Table 9.1: Grain size [μm] of 0.7BFTyez ceramics after 2, 10 and 20 h sintering time (sintering procedure S1, S2 and S3, respectively).

Material	2 h	10 h	20 h
0.7BFT0e0	0.8 ± 0.04	1.4 ± 0.05	1.6 ± 0.06
0.7BFT1e0	-	1.4 ± 0.09	1.7 ± 0.07
0.7BFT0e5	-	1.5 ± 0.1	1.9 ± 0.2
0.7BFT1e5	-	1.2 ± 0.2	1.8 ± 0.1

grain size with increasing sintering time. Only the grain size of 0.7BFT0e0 was investigated after 2 h sintering. However, this grain size was similar to the one found for 0.8BFTy and 0.9BFTy (Table 5.1) and it is inferred that the grain size is similar for all of the 0.7BFTyez materials sintered for 2 h.

The chemical homogeneity of the 0.7BFTyez materials was significantly improved by increasing the sintering time from 2 to 10 h, as reflected by the reduced atomic number contrast in Figure 9.2 (bright and dark regions with backscatter electrons in the grain centers, highlighted by arrows). The nominal composition was confirmed by SEM-EDS. Increasing the sintering time to 20 h further improved the homogeneity of each individual grain (Figure 9.2). A bright Bi_2O_3-rich grain boundary phase emerged after 20 h sintering in all the materials. No significant effect of donor substitution or A-excess was observed with respect to the chemical homogeneity or the presence of the grain boundary phase (Figure 9.2 and 9.3). EDS mapping in SEM was used to elucidate the elemental distribution in the darker and brighter regions of a polished ceramic sintered for 10 h (Figure 9.4). The EDS-maps reveal that bright regions are enriched with Fe while darker regions are enriched with Ti and K. A systematic variation of the Bi distribution was not observed. Finally, the Fe-rich regions were always surrounded by (Ti,K)-rich regions while the (Ti,K)-rich regions were not surrounded by Fe-rich regions.

Figure 9.5 displays a SEM micrograph of the polished surface of 0.7BFT0e0 where small inclusions of iron oxide (determined by EDS) are highlighted. The inclusions, with a size of $\sim$10 μm, were observed in 0.7BFT0e0 prepared by sintering procedure S1. The inclusions are not considered as secondary phases but rather unreacted Fe_2O_3 originating from minor agglomeration of Fe_2O_3 during mixing of precursors in the powder processing, and were not observed after longer sintering times. Similar agglomerates were also found in 0.8BFTy and 0.9BFTy sintered by procedure S1 for $y \leq 0.03$.

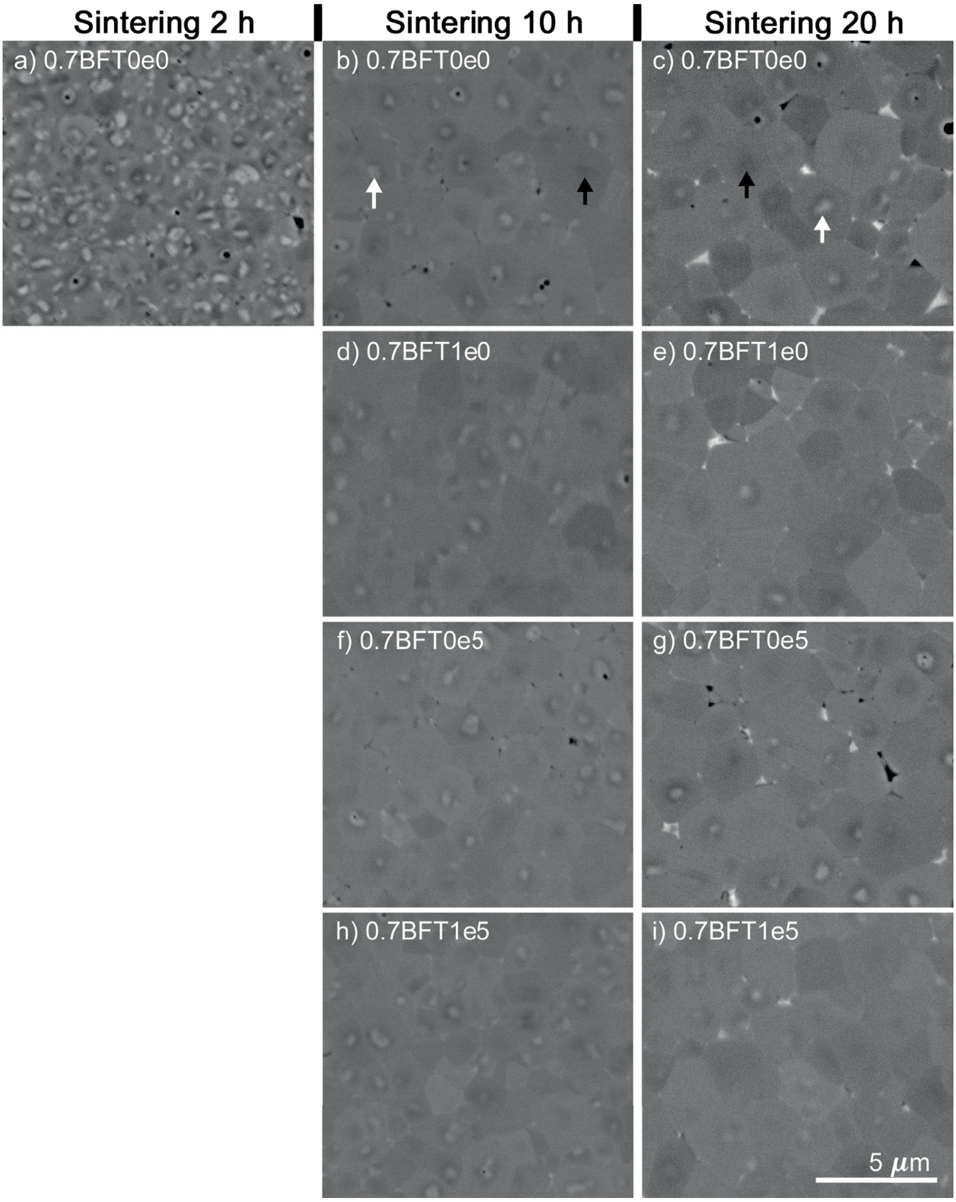

Figure 9.2: SEM micrographs (backscattered electrons) of polished 0.7BFT0e0 ceramics sintered for 2 (a), 10 (b) and 20 h (c) by sintering procedure S1, S2 and S3, respectively. Also shown are polished 0.7BFT1e0 (d/e), 0.7BFT0e5 (f/g) and 0.7BFT1e5 (h/i) ceramics, sintered for 10/20 h (S2/S3). The white/black arrows highlight bright/dark atomic number contrast in the grain centers and correspond to the arrows in Figure 9.4.

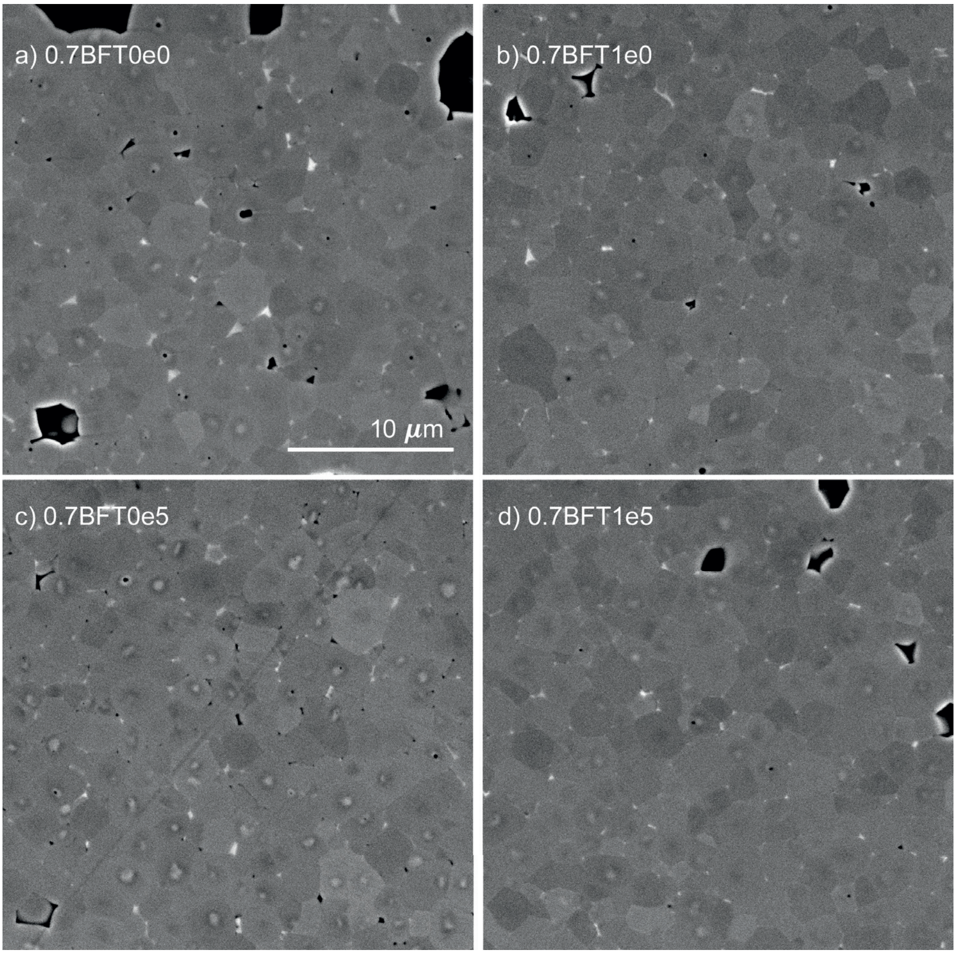

Figure 9.3: SEM micrographs (backscattered electrons) of polished 0.7BFTyez ceramics sintered for 20 h by sintering procedure S3 with a lower magnification than Figure 9.2.

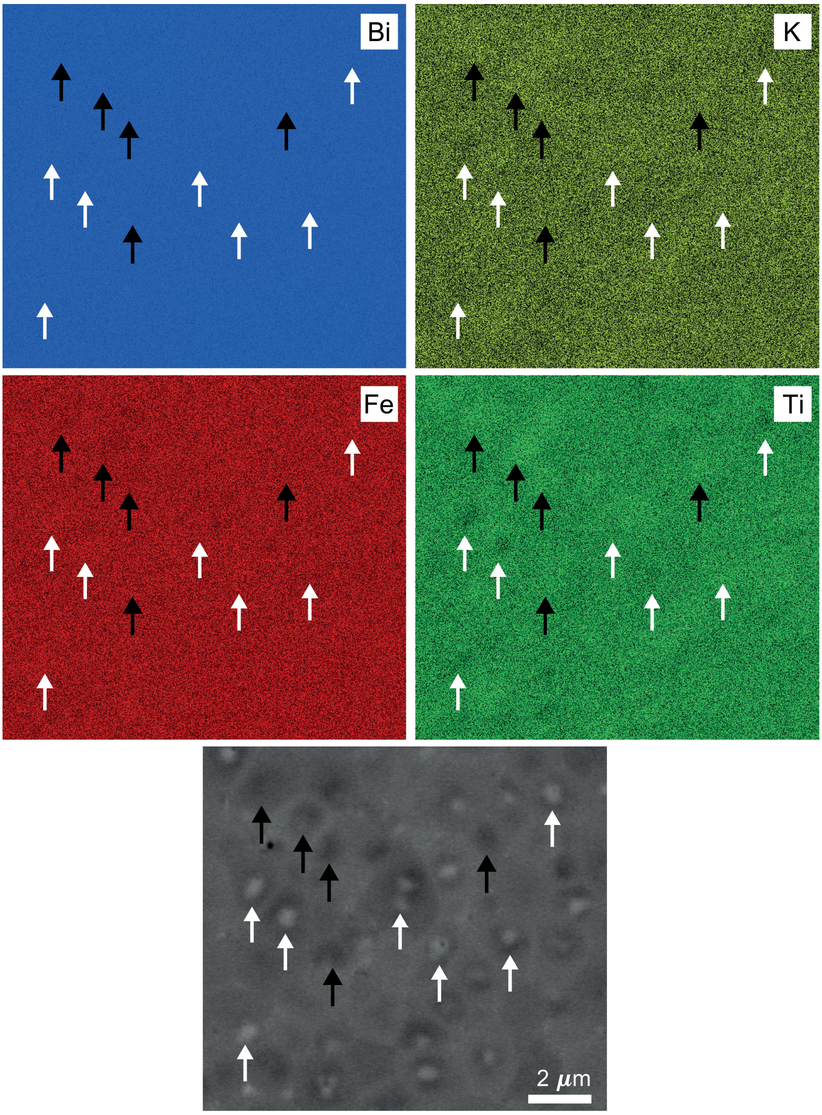

Figure 9.4: EDS maps showing the distribution of Bi, K, Fe and Ti in the mapped area shown in the lower micrograph (backscatter electrons) for 0.7BFT0e0 sintered for 10 h (S2). The white and black arrows pointing towards brighter (Fe-rich) and darker (Ti,K-rich) regions in the micrograph, respectively, are added as a guide to the eye.

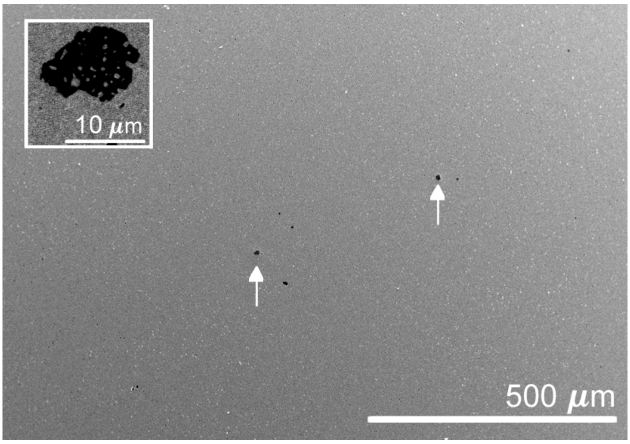

Figure 9.5: SEM micrograph (secondary electrons) of a polished 0.7BFT0e0 ceramic. The white arrows mark small inclusions of iron oxide. The inset shows an iron oxide inclusion at higher magnification (backscatter electrons).

9.1.2 Crystal Structure and Lattice Distortion

0.7BFTyez ceramics sintered for 10 h appeared cubic and phase pure upon XRD-analysis of powder from crushed pellets. The materials still appeared cubic after the powder was annealed above T_C to remove residual stresses from the crushing (Figure 9.6). The annealing above T_C introduced Bi_2O_3-rich secondary phases that were not present directly after sintering. The amount of $Bi_{25}FeO_{39}$ decreases with both Ti-substitution and A-excess and was not observed for 0.7BFT1e5.

The cubic like crystal structure was also observed for 0.8BFT0 and 0.8BFT1 after sintering for 10 h, in contrast to the clear rhombohedral splitting of diffraction lines observed after 2 h of sintering (Figure 9.6). The apparent cubic structure after 10 h of sintering prevented a meaningful refinement of the diffraction patterns using a rhombohedral space group.

Thermal analysis of 0.7BFTyez displays a weak endothermic (exothermic) peak upon heating (cooling) at ∼640 °C (∼ 610 °C), presented in Figure 9.7a. Much more pronounced endothermic (exothermic) peaks were observed for 0.8BFT0 and 0.8BFT1 during heating (cooling) as displayed in Figure 9.7b. The endothermic/exothermic peaks clearly show the presence of a phase transition although the materials appear cubic from the XRD-analysis. The higher amplitude of the peaks for 0.8BFTy relative to those of 0.7BFTyez

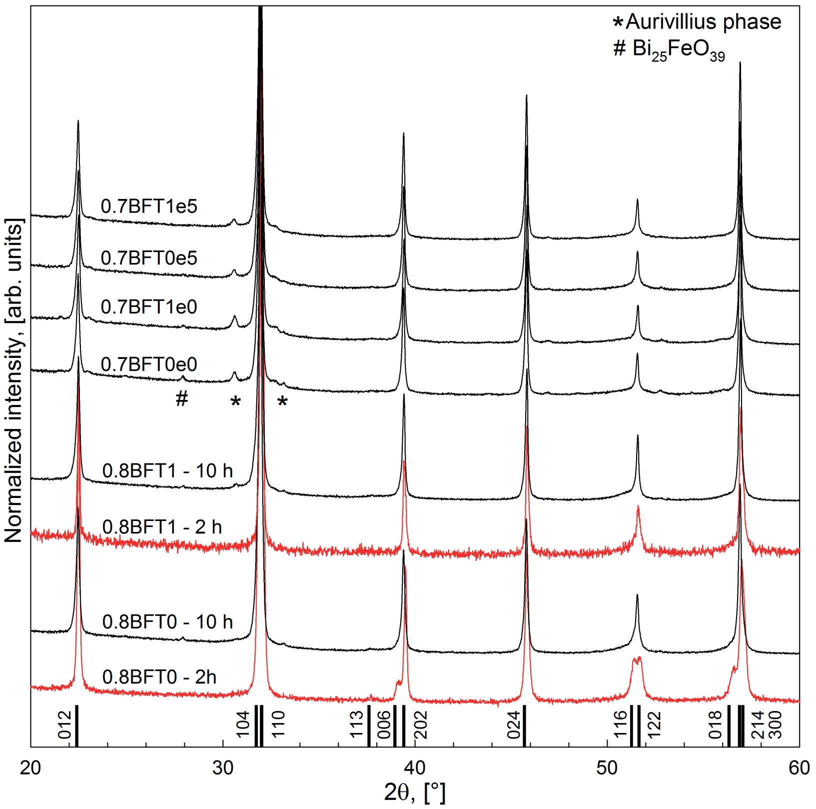

Figure 9.6: X-ray diffractograms of 0.7BFTyez, 0.8BFT0 and 0.8BFT1 sintered for 10 h (S2); and 0.8BFT0 and 0.8BFT1 sintered for 2 h (red lines, S1). The diffractograms were normalized to the maximum intensity of the (110) diffraction line where the indices refer to the room temperature structure of BFO (ICDD nr. 04-009-3445).

suggest a more pronounced transition with a higher BFO-content. The heat trace of 0.8BFT0 displays two peaks upon cooling during the first heating cycle. Two peaks were again observed during both heating and cooling upon a second heating cycle (Figure 9.7b).

9.1.3 Dielectric Performance

The permittivity and conductivity measured for ceramics prepared by the different sintering procedures are presented in Figure 9.8. The room temperature σ'_{AC} at low frequencies was reduced by ~2 orders of magnitude by

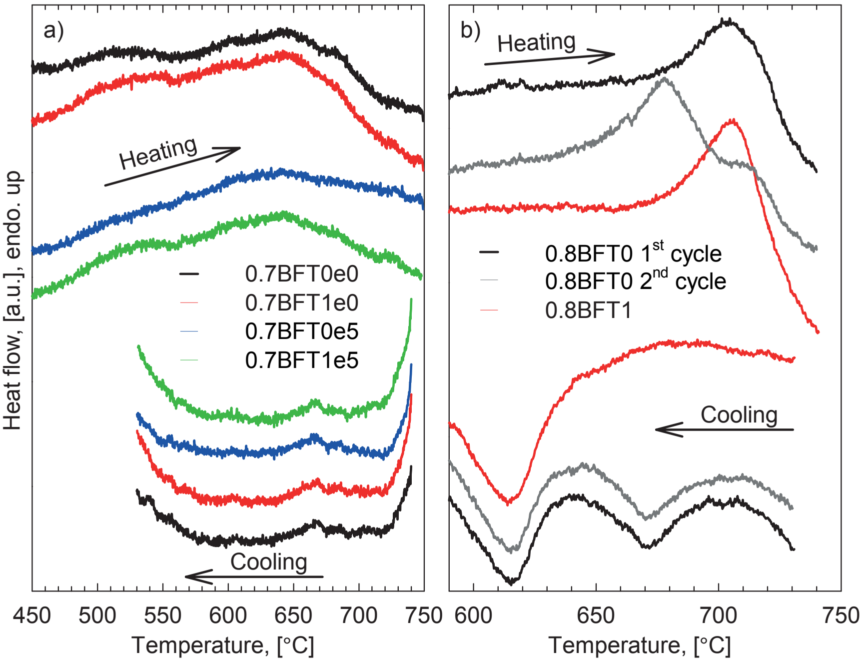

Figure 9.7: DTA heat flow during heating and cooling for 0.7BFTyez (a), and 0.8BFT0 and 0.8BFT1 (b) materials sintered for 10 h (S2). The 0.8BFT0 sample was heated two consecutive times without removing the sample in between the cycles. The DTA data were processed by subtracting a signal with a constant slope. The heating/cooling rate was 40 °C/min.

increasing the sintering time from 2 to 10 h (Figure 9.8a). Furthermore, covering the sample with sacrificial powder during sintering lowered σ'_{AC} by up to one order of magnitude relative to sintering without sacrificial powder. σ'_{AC} was also reduced by increasing the sintering temperature from 1010 to 1020 °C. Finally, it was observed that σ'_{AC} of a sample sintered with sacrificial powder at 1010 °C displayed the same σ'_{AC} as a sample sintered at 1020 °C without sacrificial powder. All the effects described here for σ'_{AC} at room temperature are also observed at higher temperature up to T_C, as evident from Figure 9.8b. The conductivity of the materials sintered at different conditions converge towards a nearly similar value above T_C.

The room temperature permittivity of ceramics prepared by all the sintering procedures displays a slight increase with decreasing frequency down to ~1 Hz (Figure 9.8c). Below ~1 Hz, the permittivity of the 10 h sintered samples demonstrate a significant increase. A processing dependent room

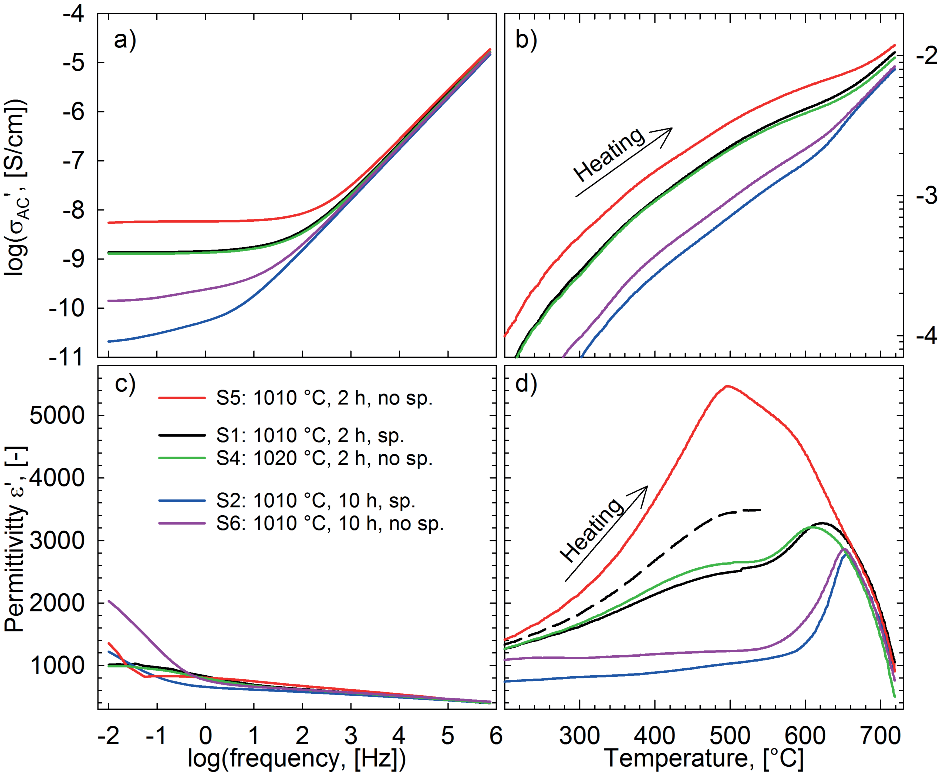

Figure 9.8: Real AC conductivity, σ'_{AC}, (a) and the permittivity (c) as a function of frequency at room temperature for 0.7BFT0e0 ceramics sintered at different temperature, times and with (sp.) or without (no sp.) sacrificial powder. Also displayed is σ'_{AC} (b) and permittivity (d) recorded at 10 kHz during heating for the same sintering procedures. The dashed line in (d) shows the permittivity of the S1 sample during the second heating to 550 °C, corresponding to the first heating to 720 °C for the other sintering procedures. The sintering procedures are defined in Table 3.3 and all measurements were performed in synthetic air.

temperature permittivity has also been reported for pure BFO and BFO-BKT (60 mol% BFO).[28,182] The effect of using different sintering procedures is more pronounced at high temperature where two peaks in the permittivity can be observed around 500 and 650 °C (Figure 9.8d) upon heating. The most striking feature is that the peak around 500 °C is removed by increasing the sintering time from 2 to 10 h. The single peak observed in the 10 h sintered ceramics is observed at the same temperature as the endothermic peak during thermal analysis, confirming the probability of a phase transition at this temperature. Furthermore, the maximum in permittivity was frequency independent for all the materials, which demonstrates that the maximum is not related to a relaxor-type behavior. The ceramics with the higher permittivity also possess the higher conductivity, while the lower permittivity ceramics also demonstrate a lower conductivity. This reflects the contribution from σ'_{AC} to the permittivity as described in Chapter 2.1.5.

The effect of thermal cycling on the permittivity and σ'_{AC} of ceramics sintered for 2 and 10 h is presented in Figure 9.9. A gradual decrease of the permittivity maximum near 500 °C is observed for the 2 h sintered sample upon repeated heating to 550 °C (Figure 9.9a). The gradual decrease starts

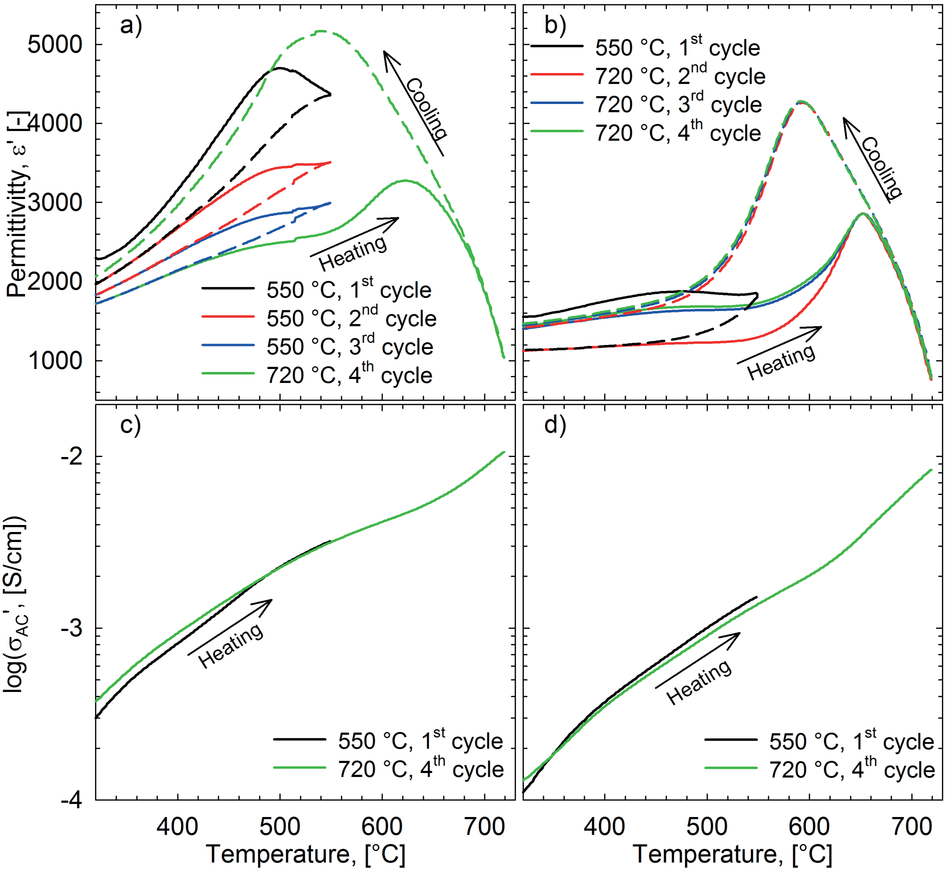

Figure 9.9: Permittivity and real AC conductivity, σ'_{AC} (10 kHz), as a function of temperature for 0.7BFT0e0 ceramics sintered for 2 h (a and c, S1) and 10 h (b and d, S6). Solid and dashed lines refer to heating and cooling, respectively, and all measurements were performed in synthetic air.

at ∼400 °C where the permittivity during heating (solid lines) depart from the permittivity recorded during the preceding cooling (dashed lines). A corresponding reduction of the permittivity was also observed for the 10 h sintered ceramic upon heating to 550 °C (Figure 9.9b). The permittivity of the 10 h sintered sample did not change upon repeated heating to 720 °C and stabilized at values higher than the permittivity observed during cooling from 550 °C. Furthermore, thermal cycling gave only small variations of σ'_{AC} for both samples, as presented in Figure 9.9c and 9.9d. The hysteresis between the temperature of the permittivity maximum upon heating and cooling is in line with the observations from thermal analysis and indicate a 1^{st} order phase transition.

The separate and combined effects of donor substitution and excess A-cations on the dielectric properties are presented in Figure 9.10. The results show that donor substitution reduces both permittivity and σ'_{AC} while excess A-cations increase both permittivity and σ'_{AC}. It is further apparent that the increase of σ'_{AC} is smaller in the donor substituted material. The effects of both donor substitution and excess A-cations remain up to the phase transition temperature where the conductivity converges close to a common value for all four materials. The phase transition temperature is not strongly dependent on donor substitution and excess A-cations based on the maximum in the permittivity (Figure 9.10b). Moreover, no frequency dependence was observed at the transition, which confirms that the materials are not relaxor ferroelectrics.

Figure 9.11a presents σ'_{AC} measured during heating and cooling in air, N_2 and O_2 of 0.7BFT0e0 sintered for 10 h. It is apparent that the atmosphere dependent σ'_{AC} behaves qualitatively the same as observed for 0.8BFT1 sintered for 2 h (Figure 6.6b, S1). The corresponding permittivity of 0.7BFT0e0 in air and N_2 is shown in Figure 9.11b where a small peak is apparent at ∼470 °C in N_2 (enlarged in the inset). This peak is in the same temperature range where a high permittivity was observed in the samples sintered for 2 h (Figure 9.8d).

9.1.4 Electromechanical Performance

The electric field induced strain and polarization of 0.7BFTyez ceramics are presented in Figure 9.12. Compared to the as-sintered ceramics, the observed strain increases significantly with an opening of the butterfly-loop

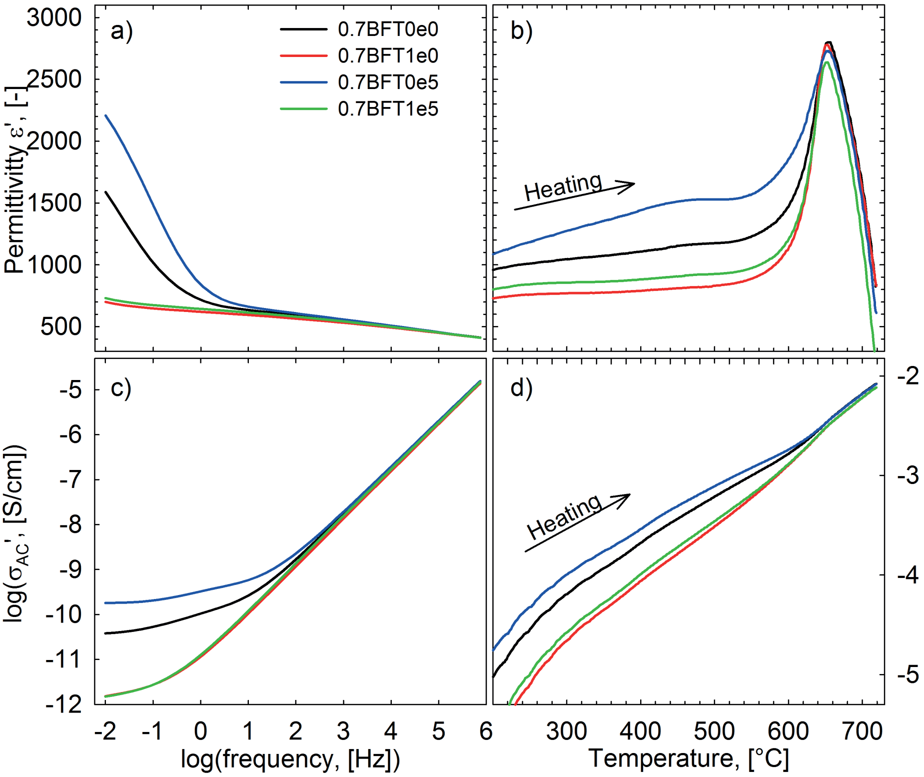

Figure 9.10: Dielectric permittivity (a) and real AC conductivity, σ'_{AC}, (c) as a function of frequency at room temperature for 0.7BFTyez ceramics sintered for 10 h (S2). Also displayed is the dielectric permittivity (b) and σ'_{AC} (d) recorded at 10 kHz during heating for the same sintering procedure. All measurements were performed in synthetic air.

after quenching the materials from above T_C. A negative strain is observed which confirms a ferroelectric contribution to the strain response. The strain increased significantly when increasing the electric field from 70 to 80 kV/cm for 0.7BFT0e5. This increase suggests that the coercive electric field is in this field range, as reported previously for 0.7BFT0e0.[110,180] The strain of 0.7BFT0e5 is on the level of that reported by Bennett *et al.*[177] in non-quenched 0.7BFT0e0 ceramics. The electric field induced polarization of the as-sintered samples was low with little opening of the hysteresis loop (Figure 9.12c). The P-E loop of the quenched ceramics appear leaky inferring that the conductivity was higher in the quenched ceramics (Figure 9.12d). The leaky character of the samples was confirmed by measuring σ'_{AC} af-

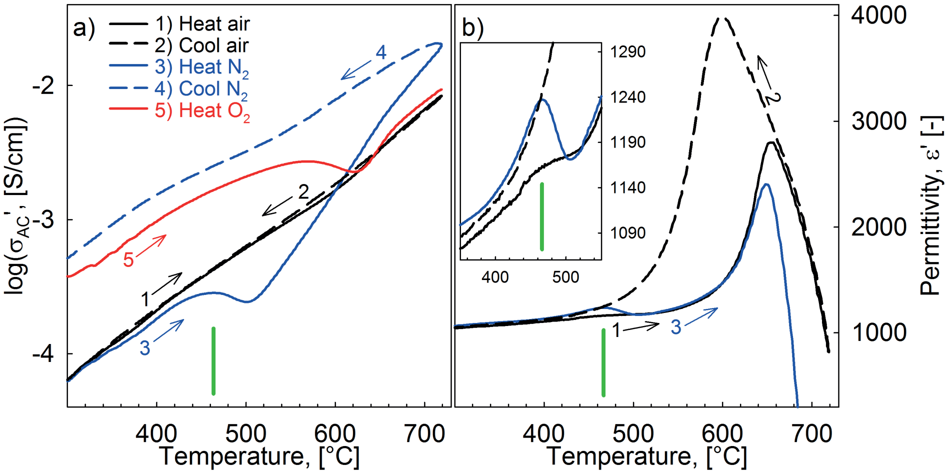

Figure 9.11: Real AC conductivity, σ'_{AC}, (a) and permittivity (b) of 0.7BFT0e0 (10 kHz) sintered for 10 h (S2) and measured upon heating in air (1), cooling in air (2), heating in N_2 (3), cooling in N_2 (4) and heating in O_2 (5). The permittivity during cooling in N_2 and heating in O_2 is omitted for clarity. The inset shows a magnified section of (b) and the green line is a guide to the eye placed at the same temperature in both (a) and (b).

ter the electromechanical experiments. No significant effects were observed due to donor substitution and addition of excess A-cations with respect to electromechanical performance.

In addition to the investigation of electromechanical properties presented in Figure 9.12, 0.7BFTyez ceramics were quenched after annealing for 30 min at 1000 °C in air, 24 h at 710 °C in air and 30 min at 710 °C in $P_{O_2} = 0.01$ (with and without electrode). All these experiments resulted in ceramics with a higher conductivity than the as-sintered, where the conductivity of samples quenched from 1000 °C and 710 °C (24 h) was the highest. The conductivity of the sample annealed in $P_{O_2} = 0.01$ were similar to the one quenched from air after 30 min annealing at 710 °C (Figure 9.12).

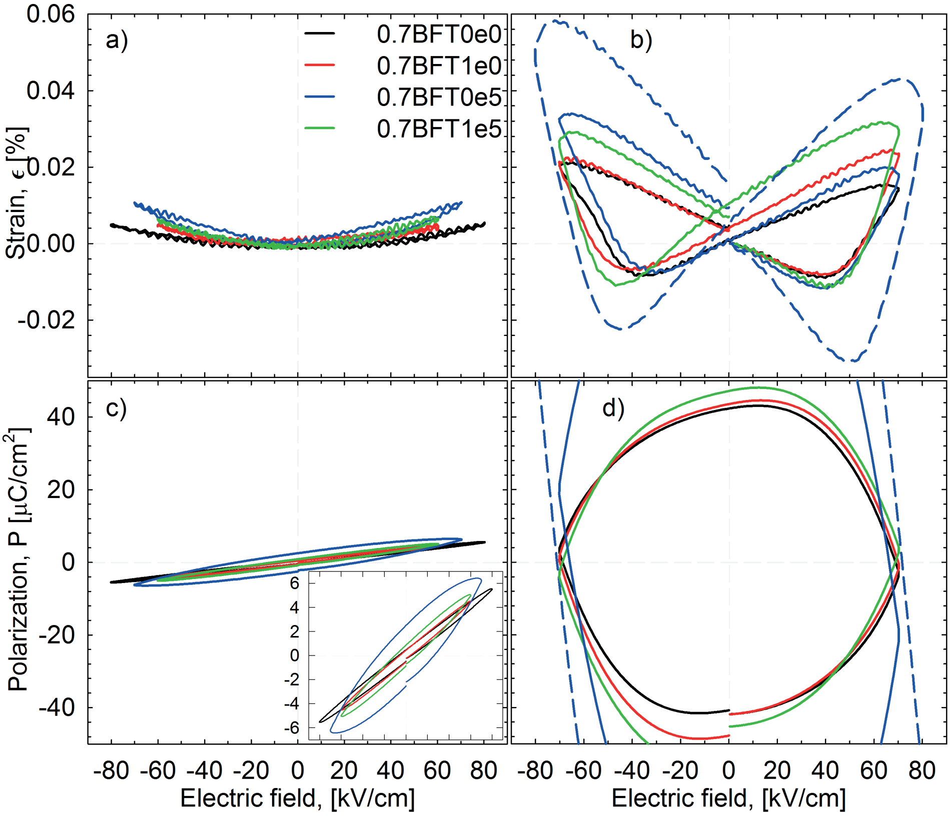

Figure 9.12: Electric field induced strain of 0.7BFTyez ceramics sintered for 10 h (S2) measured after sintering (a) and after quenching to ambient temperature from 710 °C (b). The corresponding P-E loops are shown in (c) and (d), respectively. The inset in (c) displays the P-E loops with a different scale on the y-axis. The dashed lines refer to 0.7BFT0e5 at a higher electric field than the solid line. All measurements were performed at 0.25 Hz.

9.2 Discussion

9.2.1 Chemical Homogeneity and Sintering Procedure

The sintering procedure used to prepare 0.7BFTyez ceramics was found to be important both for the grain size and the chemical homogeneity. The chemical homogeneity of the ceramics was significantly improved by increasing the sintering time from 2 to 10 h (Figure 9.2). The element mapping of 0.7BFT0e0 revealed Fe-rich and (Ti,K)-rich regions, which corresponds well with the observation by TEM-EDS on 0.8BFT0 (Figure 9.4 and 8.3). The Fe- and (Ti,K)-rich regions are a part of the matrix grains and not separate grains of different composition/secondary phases, based on the observations by both SEM and TEM (Figure 8.2a and 9.2). The X-ray diffractograms that demonstrate a single phase perovskite (as-sintered) for both 0.8BFT0 and 0.7BFTyez further support this conclusion.

The chemical homogeneity of individual 0.7BFT0e0 grains was further improved by increasing the sintering time from 10 to 20 h along with and increasing grain size (Figure 9.2). While the grains are more homogeneous, a Bi_2O_3-rich grain boundary phase emerged, which was not observed by SEM or TEM in ceramics sintered for shorter times. The grain boundary phase is most likely a liquid phase at high temperature based on how it wets the surrounding grains and the melting temperature of Bi_2O_3 (825 °C).[210] It is suggested that the origin of this Bi_2O_3-rich grain boundary phase is that the as-synthesized materials have a slightly A-cation excess. The grain boundary phase is not observed after short sintering times because of the inhomogeneous distribution of elements and the small grains. As the grains grow, the chemical homogeneity improves and the Bi_2O_3-rich phase segregates to the grain boundaries. Based on observations by SEM and XRD, the amount of grain boundary phase is not found to vary significantly with donor substitution or excess A-cations (Figure 9.2, 9.3 and 9.6).

Similar observations to what is reported here were earlier reported by Christensen[179] where 0.8BFT0 sintered at 1010 °C for 2 h gave small inhomogeneous grains analogous to Figure 9.2a. Adding 1 mol% A-excess and sintering at 1030 °C increased the grain size, but also introduced a Bi_2O_3-rich grain boundary phase analogous to the grain boundary phase observed in this work (Figure 9.2). The increased sintering temperature for the A-excess materials is expected to provide grain growth and may have the corresponding influence as increased sintering time in the case of 0.7BFTyez (Figure 9.2). The observations by Christensen are, however, not sufficient to conclude unambiguously on whether the Bi_2O_3-rich phase emerged due to a too high A:B-ratio or the increased sintering temperature.

The peritectic decomposition of BFO to a Bi_2O_3-rich liquid phase and Fe_2O_3 is reported at ∼960 °C, which is below the sintering temperature used in this work (Figure 2.17). A peritectic decomposition is considered unlikely as the Bi_2O_3-rich grain boundary phase was not observed together with an Fe_2O_3 phase. Small inclusions of Fe_2O_3 were observed after 2 h sintering but not after 20 h sintering, where the Bi_2O_3-rich grain boundary phase was observed. Furthermore, a decomposition to the commonly observed $Bi_2Fe_4O_9$ and $Bi_{25}FeO_{39}$ is also unlikely as only the Bi_2O_3-rich phase is observed by XRD (Figure 9.6).

The Bi_2O_3-rich secondary phases were observed by XRD in 0.7BFTyez only after annealing above T_C (800 °C). This annealing temperature is in the vicinity of the stability region of $Bi_{25}FeO_{39}$ as reported by Selbach *et al.*[45] and the eutectic temperature in the Bi_2O_3 - Fe_2O_3 phase diagram (Figure 2.17). The Bi_2O_3-rich grain boundary phase discussed above is in a liquid state during sintering and may not be fully crystallized after cooling from the sintering temperature. The annealing near the eutectic temperature may, however, facilitate crystallization of the grain boundary phase to such an extent that it is observed by XRD.

The investigated 0.7BFTyez materials were not completely homogenized after 20 h sintering, and it is considered unlikely that further grain growth will remove the inhomogeneities (Figure 9.2 and 9.3). The Fe/(Ti,K)-enriched regions are mainly located in the middle of the grains, while the outer parts of the grains appear relatively homogeneous as a result of the grain growth. Further grain growth will hence not affect the grain interior significantly. Moreover, Fe and Ti occupy the same lattice site in BFO-BKT and both form stable perovskites, BFO and BKT. The mobility and driving force for counter-diffusion of Fe and Ti is relatively small and homogenization by thermal annealing is unlikely. The Fe-rich regions were always surrounded by (Ti,K)-rich regions while the (Ti,K)-rich regions were not surrounded by Fe-rich regions (Figure 9.2). This distribution of Fe/(Ti,K) infers that the reactivity/mobility of Ti^{4+} may be a limiting factor during the synthesis or sintering. Bernardo *et al.*[135] have suggested a reaction mechanism for the synthesis of BFO which was controlled by the diffusion of Bi^{3+} into Fe_2O_3 particles, resulting in the commonly observed $Bi_2Fe_4O_9$. This phase was, however, not been observed in this work.

The temperature during synthesis of BFO-based materials is ideally kept above ~770 °C to limit the formation of the secondary phases $Bi_2Fe_4O_9$ and $Bi_{25}FeO_{39}$.[45] At the same time, the potential loss of e.g. Bi_2O_3 and K_2O promotes a low synthesis temperature and short exposure time to high temperature.[122] The work presented herein shows that chemical homogeneity must also be taken into account when synthesizing materials where more than one element can occupy the A- or B-site. Although the material appears phase pure by e.g. XRD, there may be significant chemical inhomogeneity that requires longer sintering time or higher temperature to remove. The chemical homogeneity is especially relevant to consider when materials are synthesized by the solid state method where the diffusion distances are relatively long compared to when using e.g. wet chemical methods. Moreover, chemical homogeneity is important not only for BFO-based materials but for lead-free piezoelectrics in general where several elements are commonly mixed on the same lattice site in the search for MPBs.

9.2.2 Conductivity and Sintering Procedure

The effect of A:B-ratio on the conductivity is illustrated by considering the conductivity of 0.7BFTyez prepared by different sintering procedures. The higher σ'_{AC} of ceramics prepared without sacrificial powder compared to ceramics prepared with can be rationalized by loss of volatile A-site elements. Loss of Bi_2O_3 and K_2O at high temperature will increase the concentration of $V_O^{\cdot\cdot}$ and consequently the concentration of electron-holes, following the point defect model introduced in Chapter 6.2.1. Electron-holes are the main charge carriers in p-type conductors and σ'_{AC} will hence increase. Addition of excess A-cations was proposed to reduce σ'_{AC} by compensating for loss of Bi_2O_3 and K_2O during synthesis, but σ'_{AC} was observed to increase in contradiction to the expectation (Figure 9.10c and 9.10d). The higher conductivity is probably related to the slight A-excess stoichiometry of the as-synthesized materials as discussed in the previous chapter. The minimum conductivity in materials where polaron hopping conductivity dominates will be at A:B-ratio = 1 with Fe in a single valence state. A deviation from the A:B-ratio = 1 will hence induce oxidation/reduction of Fe and increase the conductivity. The observations above suggest that the amount of A-site elements lost when sintering without sacrificial powder is higher than the initial A-excess content of the material. The loss of Bi_2O_3 and K_2O was not quantified in this work, but a 6 wt% volatilization has been reported for BKT after 20 h at 1030 °C.[122]

The reduced σ'_{AC} upon increased sintering time or temperature (Figure 9.8a and 9.8b) is proposed to be the result of the improved homogeneity with increasing grain size (Figure 9.2). The improved homogeneity may remove point defects present in the inhomogeneous ceramics, and an increased grain size reduces any contribution from grain boundary conductivity. The conductivity increased more when adding excess A-cations to 0.7BFT0e0 than to the donor substituted 0.7BFT1e0. This may be an indication that donor substitution slightly destabilizes the Bi_2O_3-rich grain boundary phase. The effect of donor substitution on σ'_{AC} is qualitatively the same for 0.7BFTyez, 0.8BFTy and 0.9BFTy (Figure 9.10, 6.4 and 6.5, respectively) despite different sintering procedures (S1 and S2). The results show that both microstructure and loss of Bi_2O_3 and K_2O associated with longer sintering times/higher temperatures is important for the electrical conductivity of BFO-BKT ceramics.

The P_{O_2} dependence of σ'_{AC} of *non*-substituted 0.7BFT0e0 is qualitatively similar to that of *donor* substituted 0.8BFT1 (Figure 9.11a and 6.6b). The similar behavior is probably not an effect of the sintering procedure but rather a manifestation of a reduced p-type character in BFO-BKT with increasing BKT content, as reported by Morozov *et al.*[180] A reduced p-type character is analogous to a shift of σ_{min} to higher P_{O_2} in Figure 6.9 with increasing BKT-content. The results further confirm that the point defect model introduced in Chapter 6.2.1 is valid irrespective of chemical homogeneity and microstructure.

9.2.3 Dielectric Permittivity and Sintering Procedure

The ferroelectric to paraelectric phase transition, T_C, of 0.7BFTyez can be identified by the coinciding temperature of the permittivity maximum and the DTA-peak at ∼650 °C (Figure 9.10b and 9.7a). The transition temperature is not very sensitive to donor substitution or excess A-cations. A small variation of T_C was observed upon donor substitution of 0.8BFTy and 0.9BFTy but this can possibly be attributed to a lower chemical homogeneity of the sintered ceramics. Morozov *et al.*[178] reported a sharp peak for the permittivity of 0.7BFT0e0 at ∼500 °C in a first heating cycle up to 700 °C, indicating that T_C is ∼500 °C. Bennett *et al.*[177] on the other hand reported a $T_C = 472$ °C for 0.7BFT0e0 based on permittivity measurements up to 520 °C. The broadness of the peak and lack of permittivity data at higher temperatures may suggest that this peak is related to the high permittivity observed in this work at ∼500 °C, which is discussed further below.

The permittivity maximum at ∼ 500 °C for 0.7BFT0e0 ceramics sintered for 2 h originates from conductivity and chemical homogeneity of the ceramic (Figure 9.8d). The measured real permittivity of a material is affected by σ'_{AC} where a higher conductivity contributes to a higher permittivity (Chapter 2.1.5). The contribution from conductivity is apparent when comparing the two samples sintered at the same temperature but with and without sacrificial powder. Both conductivity and permittivity is higher for the sample without sacrificial powder. The major difference between these two samples is the conductivity as it is inferred that the microstructure is not readily affected by the use of sacrificial powder. The contribution from chemical homogeneity can be separated from the contribution of conductivity by the observed effect of increasing the sintering temperature to 1020 °C. The permittivity at ∼500 °C of the sample sintered at 1020 °C (S4) is lower than for that sintered at 1010 °C (S1, dashed line) while the conductivity is the same (Figure 9.8b and 9.8d). The major difference between these samples is hence the chemical homogeneity which clearly contributes to the permittivity.

A third contribution to the observed permittivity of BFO-BKT ceramics relates to movement of oxygen and oxygen vacancies, where the origin is the temperature dependent oxygen stoichiometry, as briefly outlined below. The concentration of $V_O^{\cdot\cdot}$ increases with increasing temperature, and re-oxidation of the material is expected during cooling. The re-oxidation will take place down to a temperature where the cooling rate is too fast for the oxygen content to remain in equilibrium with the atmosphere. This results in an as-sintered ceramic where the sub-stoichiometric oxygen content is frozen in due to low oxygen mobility or slow surface oxygen-exchange kinetics. The material may also have oxygen gradients for the same reasons. The actual temperature where the stoichiometry is frozen in is not known but it is estimated to be 700-800 °C for non-electroded samples (Figure 6.10) and lower for electroded samples.[180]

The gradual decrease of the permittivity with thermal cycling above ∼400 °C (Figure 9.9) originates in the dependence of oxygen content on thermal history. Significant oxygen mobility is observed in the electroded samples at 400 °C (Figure 6.6 and 9.11). Above this temperature the samples re-oxidize, any gradients in the oxygen content is reduced and aging by migration of oxygen vacancies can take place. The influence on permittivity is probably related most to movement of oxygen vacancies or other point defects in the material and less to re-oxidation. This statement is based on the reproducibility of σ'_{AC} upon thermal cycling and the relatively small permittivity peak at ∼470 °C when heating 0.7BFT0e0 in N_2. The gradual reduction of permittivity observed for 2 and 10 h sintered samples is hence not an effect of changes in the chemical homogeneity involving cations. Thermal cycling to 720 °C shows that the permittivity does not change after the first cycle. It is assumed that the oxygen exchange kinetics are fast enough at 720 °C for the ceramic to obtain equilibrium with the atmosphere. The equilibrium oxygen content is hence re-established and any aging effect is removed before the material is cooled from 720 °C (above T_C), resulting in a similar permittivity for every cycle.

9.2.4 Long Range Crystallographic Order

The lattice distortion of 0.8BFT0 and 0.8BFT1 ceramics was sensitive to the sintering time, as observed by XRD (Figure 9.6). The X-ray diffractograms of samples sintered for 2 h display a clear rhombohedral splitting of the diffraction lines while the samples sintered for 10 h appear cubic. The reduced rhombohedral splitting is illustrated by the FWHM of the (116)/(122) diffraction lines plotted in Figure 9.13 (obtained from Figure 9.6). Little or no effect of donor substitution or excess A-cations was observed for the FWHM after 10 h sintering, as also shown for 0.8BFTy and 0.7BFTyez in Figure 9.13. The diffractograms presented in Figure 9.6 were also compared to diffractograms obtained before annealing the powders above T_C but no significant variation was observed.

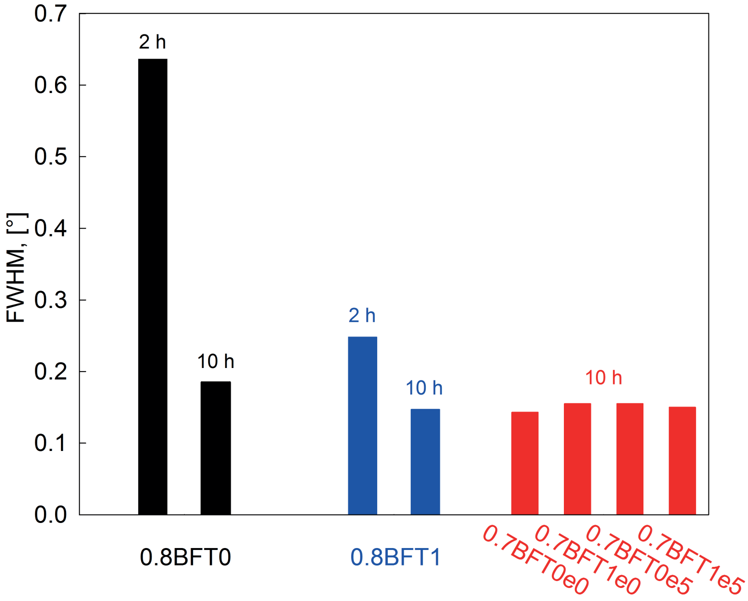

Figure 9.13: Full-width-half-maximum of the (116)/(122) diffraction lines for 0.8BFT0 and 0.8BFT1 sintered for 2 and 10 h (S1 and S2, black and blue) and FWHM for 0.7BFTyez sintered for 10 h (S2, red).

DTA confirmed the presence of a phase transition for the 10 h sintered materials which means that the symmetry is most likely lower than observed by XRD. The DTA data are in line with the observations for the samples sintered for 2 h (Figure 9.7b and 5.9). Furthermore, the observed negative strain response of 0.7BFTyez to an applied electric field and a clear permittivity maximum at the phase transition temperature confirm the non-cubic symmetry of 0.7BFTyez (Figure 9.12b and 9.10b). The frequency independent permittivity peak at the phase transition is further evidence that the material is not pseudo-cubic with a relaxor-type behavior.

The reduced lattice distortion after 10 h sintering is suggested to mainly result from loss of Bi_2O_3 and K_2O during the prolonged sintering. Previous reports have shown that relatively small deviations from stoichiometric composition in the related BNT may result in significant changes to the long range order.[126,127] The crystal structure of 0.8BFT0 has been reported to be close to cubic with up to 1 mol% excess A-cations and clearly rhombohedral with 2 mol% excess A-cations. Loss of Bi_2O_3 and K_2O will be most probable before a dense microstructure is formed during sintering due to the high surface area and open porosity. The weight loss will increase with increasing sintering time, but will not be proportional to the time due to the effect of closed porosity. Once the dense microstructure is formed, the losses require diffusion of cations to the surface which possibly favors loss of K_2O due to the lower charge of K^+ compared to Bi^{3+}. The nominal composition of the materials investigated in this work was confirmed by EDS, but further work is needed to accurately quantify the loss of Bi_2O_3 and K_2O and how it affects the crystal structure.

The observed lattice distortion may also be influenced by the microstructure of the materials in addition to the loss of volatile elements. The local crystal structure of the Fe-rich regions (Figure 9.4) is probably closer to the rhombohedral structure of pure BFO. Correspondingly, the local structure of the (Ti,K)-rich regions is closer to the pseudo-cubic structure which is adopted at high BKT content. The presence of the Fe-rich regions will contribute to the rhombohedral splitting of diffraction lines in the diffractogram. The (Ti,K)-rich and the stoichiometric regions will on the other hand provide cubic diffraction lines which do not show the same degree of rhombohedral splitting. The cubic diffraction lines overlap with the rhombohedral diffraction reflections and cannot be separated from the rhombohedral contribution by e.g. Pawley or Rietveld refinement. Sintering for 10 h improves the homogeneity and reduces the contribution from Fe-rich regions, resulting in a near cubic crystal structure. This discussion may indicate that the observed rhombohedral to pseudo-cubic transition for BFO-BKT materials in reality is highly dependent on the synthesis conditions and the resulting chemical homogeneity. It is reasonable to assume that the amount of Fe-rich regions decreases with decreasing Fe-content in the material, i.e. with Ti-substitution or an increasing BKT content. BFO-BKT has been reported to transform from rhombohedral to pseudo-cubic below both 60 and 40 mol% BFO-content[50,111] where the differing compositions may be the result of different synthesis parameters. The sensitivity of long range order on synthesis parameters and composition also offers an indication of the origin of the different sensitivity of 0.8BFT0 and 0.9BFT0 to 1 mol% Ti-substitution for Fe. In 0.9BFT1, the amount of Fe is still high enough for a significant amount of Fe-rich regions to be present but this is not the case for 0.8BFT1, resulting in an apparent reduction of lattice distortion. The crystal structure of a (K,Ti)-rich phase in 0.9BFTy is likely more rhombohedrally distorted than in 0.8BFTy and will hence contribute more to the rhombohedral distortion observed by XRD.

9.2.5 Thermal and Atmospheric History

Aging is apparent from the comparison of electric field induced strain for as-sintered and quenched 0.7BFTyez ceramics (Figure 9.12a and 9.12b). This behavior corresponds well with the aging observed during ferroelastic characterization (Chapter 7). The low strain originates from a combination of the small lattice distortion of ceramics sintered for 10 h and dielectric breakdown in the vicinity of the coercive electric field. The significant increase of strain for 0.7BFT0e5 upon increasing the electric field from 70 to 80 kV/cm infers that the coercive electric field is in this field range. This field range corresponds well with data reported for non-quenched 0.7BFT0e0 ceramics.[110,180] The low strain amplitudes hinder a conclusion on whether ferroelectric hardening occurs with donor substitution analogous to ferroelastic hardening observed previously (Chapter 7). The effect of compensating for loss of volatile elements with excess A-cations is also not clear due to the low strain.

The P-E loops of 0.7BFTyez show a significantly higher leakage current for the quenched compared to the as-sintered ceramics (Figure 9.12c and 9.12d). Additional experiments were performed with different annealing atmosphere, temperature and time before the ceramics were quenched, but all quenched materials were leaky and independent of atmosphere. The higher conductivity of the quenched materials was confirmed by measurement of σ'_{AC} which infers that a higher charge carrier concentration is frozen in upon quenching compared to the as-sintered ceramic. All materials in this work are n-type conductors at the sintering temperature (1010 °C) based on an extrapolation of σ_{min} of Figure 6.1 to higher temperatures. In addition, the charge carrier concentration increases with increasing temperature. The fast cooling rate upon quenching hinders re-oxidation of the ceramic and freezes in a higher charge carrier and $V_O^{\cdot\cdot}$ concentration than the equilibrium conditions, as previously discussed in Chapter 9.2.3.

The observed effects of quenching 0.7BFTyez highlight the challenges presented by the close relation between ferroelectric performance, thermal history and point defects. It was established in Chapter 6 that the conductivity is intimately connected to the concentration of $V_O^{\cdot\cdot}$, and that there exists a temperature specific σ_{min} at a given P_{O_2}. To ensure a low leakage current, the ceramics should be annealed in the P_{O_2} of σ_{min} at an as low temperature as possible, because σ_{min} decreases with decreasing temperature. This temperature will, however, be lower than T_C which facilitates aging and the material will harden, as established in Chapter 7. Thermal annealing in a high P_{O_2} atmosphere will decrease the concentration of $V_O^{\cdot\cdot}$ and consequently soften the material as there are less point defects that pin domain walls. However, annealing in a high P_{O_2} will also increase the conductivity of the material and prevent application as a ferroelectric. Additionally, the short/low sintering times/temperatures employed to minimize evaporation of volatile elements during synthesis of BFO-based materials facilitate an inhomogeneous distribution of elements. Chemical inhomogeneity may cause a complex domain structure that eventually makes the material behave as a hard ferroelectric. The chemical homogeneity of BFO-BKT could be significantly improved by increasing the sintering time or temperature, but this also decreases the lattice distortion which is important for the ferroelectric/ferroelastic performance.

9.2.6 Effect of A:B-ratio

A variation in the A:B-ratio was introduced in this chapter to investigate the effects on the functional properties. The small amount of A-excess (0.5 mol%) was chosen as the work by Christensen[179] suggested that the optimum A-excess content was between 0 and 1 mol%. An influence of the

A:B-ratio was observed for σ'_{AC} where both the effect of evaporation and excess A-cations were demonstrated. Other properties such as microstructure, crystal structure, phase transition temperature and ferroelectric performance were found to not depend significantly on the A:B-ratio. The small amount of A-excess introduced may be too small for any effect to be observed. Additionally, it is also possible that the slight A-excess composition of the as-synthesized materials may dominate over the small A-excess which was deliberately introduced.

In summary, the considerations discussed in this chapter demonstrate the complexity of fabricating BFO-based ferroelectric materials which are readily applicable as lead-free alternatives to PZT. It is apparent that the thermal and atmospheric history, starting with the sintering of ceramics, is important to consider when an optimized synthesis route is developed. Finally it is noted that the factors that influence the ferroelectric/ferroelastic properties also present interesting opportunities to tailor the material to specific applications.

Chapter 10

Conclusions

Dense and phase pure (1-x)BKT - xBNZ ceramics, including pure BKT, were successfully prepared using a conventional solid state synthesis route. The crystal structure was found to be tetragonal for x $\leq$ 0.1 and pseudo-cubic for x = 0.15-0.80. The electromechanical properties for x = 0-0.50 were investigated, with 0.10BNZ showing the highest bipolar polarization and strain and a unipolar $\epsilon_{u,max}/\mathrm{E}_{max}$ = 116 pm/V. The dielectric performance was investigated for x = 0-0.50 and all materials demonstrated relaxor-like behavior where the dielectric dispersion increased with increasing BNZ content. The highest dielectric constant was measured for 0.15BNZ with $\varepsilon' = 3507$ (10 kHz) at 255 °C. The best performance of the dielectric and electromechanical properties was demonstrated near the tetragonal to pseudo-cubic phase transition (x = 0.10-0.15), in line with other BKT-rich piezoelectrics. The performance of BKT-BNZ is however not as good as other BKT-based materials. The dielectric performance throughout the BKT-BNZ ternary reciprocal system was mapped, and it was concluded that the best properties are obtained for Ti-rich compositions. The permittivity contour coincides with the proposed phase diagram for the BKT-BNZ ternary reciprocal system, with a large pseudo-cubic region for intermediate compositions. Based on the findings, the properties of BKT can be improved by BNZ but the BKT-BNZ composition joint does probably not provide the most promising lead-free alternative to PZT.

Dense and phase pure 0.8BFTy and 0.9BFTy materials were synthesized by the solid state method with up to 6 mol% donor substitution (Ti^{4+}) and 1 mol% acceptor substitution (Fe^{3+}). A rhombohedral R3c crystal structure was observed by XRD for all materials after 2 h sintering with a decreasing lattice distortion with increasing BKT-content and donor substitution. The temperature dependent lattice distortion was relatively constant up to 550-600 °C for 0.8BFT0 and 0.9BFT0. The microstructure was similar for both composition series with a sub-micron grain size except for 0.8BFT-1 and 0.8BFT6. The ferroelectric to paraelectric phase transition temperature decreased with increasing BKT content, but remained relatively high. Only small variations of T_C were observed with donor/acceptor substitution. The results demonstrate that BKT stabilizes the perovskite phase and allows synthesis of BFO-rich materials by the conventional solid state method without the evolution of commonly observed parasitic phases. A high T_C and lattice distortion is maintained which retains the high temperature applicability of BFO also with BKT-substitution.

The DC electrical conductivity of 0.8BFT0 and 0.9BFT0 was measured as a function of temperature and atmosphere. A P_{O_2}-dependent minimum was observed in the conductivity reflecting a change from p-type conductivity in oxidizing atmosphere (air and O_2) to n-type conductivity in inert atmosphere (N_2). The change from p-type to n-type conductivity corresponds to a change from positive to negative major charge carriers. A positive/negative Seebeck coefficient in oxidizing/inert atmosphere confirmed the change of the main charge carriers. A negative Seebeck coefficient in inert atmosphere is the first direct evidence of n-type bulk BFO-based ceramics. A point defect model was introduced which successfully described the measured DC conductivity. The model was based on a mass action law treatment of relevant point defect equilibria, and established electrons and electron-holes as major charge carriers. Oxygen and A-site vacancies were included as additional point defects. Donor substitution of 0.8BFTy and 0.9BFTy decreased the room temperature conductivity by several orders of magnitude in both composition series. Correspondingly, acceptor substitution increased the conductivity of 0.8BFTy. The effect of donor/acceptor substitution is in good accord with the point defect model. The results show that the electrical conductivity of BFO is closely related to the point defect chemistry, and by that, the thermal and atmospheric history of the material.

The ferroelastic behavior of BFO-rich materials was investigated for the first time by measuring the mechanical stress-strain hysteresis loop of 0.8BFTy and 0.9BFTy up to 400 °C. Aging of the materials was demonstrated by varying the thermal history of the samples. The materials behaved ferroelastically softer if the aging process was hindered by quenching, but a high coercive stress (>700 MPa) was still observed at room temperature. Thermally activated domain switching was inferred by a lowering of the coercive stress and an increase of remanent strain with increasing temperature. Donor substitution resulted in ferroelastic hardening of both 0.8BFTy and 0.9BFTy. This was surprising given the well-known softening effect of donor substitution in PZT. Finally, it was demonstrated that the ferroelastic behavior of 0.8BFTy could be tuned by varying the atmospheric history of the materials. The atmosphere dependence corresponds well with the established point defect chemistry of the materials and the role of oxygen vacancies in relation to aging generally accepted for e.g. PZT and BT.

A complex domain structure was observed in dense 0.8BFT-1 and 0.8BFT0 along with an inhomogeneous chemical distribution of elements. The complex domain structure was suggested to contribute to the high coercive stress of the materials. The effect of longer sintering times on chemical homogeneity was investigated in a third composition series 0.7BFTyez ceramics. The influence of donor substitution and excess A-cations was also elucidated. The chemical homogeneity was significantly improved by increasing the sintering time, and the permittivity and electrical conductivity were clearly reduced up to the phase transition temperature. The rhombohedral lattice distortion was significantly reduced and the materials appeared cubic by XRD analysis after longer sintering time. However, a lower symmetry than cubic was inferred by DTA, permittivity and electromechanical performance. Donor substitution in 0.7BFTyez demonstrated a lowered electrical conductivity and permittivity, analogous to 0.8BFTy and 0.9BFTy. Excess A-cations increased the electrical conductivity and permittivity, contradictory to expectations. This increase was attributed to a slight A-excess stoichiometry of the 0.7BFTyez materials. The observed chemical homogeneity, phase transition temperature, lattice distortion and electromechanical performance were not very dependent on donor substitution and excess A-cations.

The work presented in this thesis demonstrates the importance of considering thermal and atmospheric history of BFO-materials. While the results are obtained on BKT-substituted BFO, it is argued that the findings are relevant also for pure BFO and other BFO-rich materials. The results show that the electrical conductivity can be minimized by selecting an appropriate sintering procedure with respect to atmosphere, temperature and time. The demonstrated relationship between aging, electrical conductivity, point defects and thermal history further highlight the opportunities to tune the material properties according to specific needs.

Chapter 11

Outlook

A number of different materials have been investigated in recent years in the search for lead-free piezoelectrics to replace PZT. The present work has investigated the solid solutions of BKT-BNZ and BFO-BKT. It was concluded that BKT-BNZ is probably not the most promising lead-free piezoelectric materials system and further investigations in this system are not recommended. This chapter therefore aims to address the implications of the results obtained for the BFO-BKT materials. Observations that require further attention to improve the understanding of BFO-BKT are particularly addressed.

The high electrical conductivity is one of the main challenges that need to be overcome to realize piezoelectric application of BFO-based materials. The work included in this thesis has demonstrated the existence of a temperature and atmosphere dependent minimum in electrical conductivity which is closely related to the concentration of oxygen vacancies (Chapter 6). The work also determined the main mechanism for the decreased electrical conductivity of donor-substituted BFO. Moreover, the work showed hardening through aging, and that the high coercive stress was highly dependent on the thermal and atmospheric history of the materials (Chapter 7). The findings demonstrate that the ferroelectric performance of BFO can be significantly improved by carefully selecting an appropriate sintering procedure and atmosphere where both minimization of the electrical conductivity (point defects) and aging must be taken into account. In a wider perspective, the multivalent Fe-cation and its close relation to point defect chemistry and ferroelectric/ferroelastic performance offers an opportunity for tuning material properties. This opportunity is not present in other lead-free piezoelectrics and further manifests BFO and BFO-based materials as highly interesting potential replacements for PZT.

This thesis provides insight to the importance of the point defect chemistry in BFO, especially with respect to oxygen vacancies. The concentration of oxygen vacancies is clearly important for the electrical conductivity due to the close link with the concentration of major charge carriers. The dependence of ferroelastic and ferroelectric behavior on thermal and atmospheric history has been established. This dependence demonstrates that the distribution of oxygen vacancies is important, in addition to the concentration. It is however not clear whether the ferroelastic properties are directly affected by the concentration of oxygen vacancies or the concentration of major charge carriers. Most of the investigations related to aging and hard/soft ferroelectrics are conducted on PZT and BT. An important difference between PZT/BT and BFO is the multivalent Fe-cation which forms the important relationship between charge carriers and oxygen vacancies. Investigations on BFO-based thin films and bulk BFO ceramics have shown that the conductivity along a domain wall is different from that of the domain, possibly due to a higher concentration of oxygen vacancies.[85,86,154] As the conductivity depends on the concentration of charge carriers, this may suggest that the movement of domain walls depends on a charge transfer mechanism. Further investigations are required to determine the relation between domain wall movement, major charge carriers and oxygen vacancies.

Donor substitution is well-known for softening the ferroelectric/ferroelastic properties of PZT,[9] while donor substitution of 0.8BFTy and 0.9BFTy was shown to harden the materials. According to the introduced point defect model, donor substitution leads to a reduced concentration of oxygen vacancies. A reduced vacancy concentration upon annealing in an oxidizing atmosphere was indeed shown to soften 0.8BFTy in Chapter 7. Rojac *et al.*[86] suggested in a recent report that the mechanism for domain wall movement in BFO is different from that in PZT. Further investigations are however required to determine the origin of hardening by donor substitution in BFO.

Increasing the sintering time was shown to improve the chemical homogeneity of 0.7BFTyez significantly, but also removed most of the rhombohedral lattice distortion. This is worth investigating further as it has potential implications for the obtainable strain and the composition of the rhombohedral to pseudo-cubic transition in BFO-BKT. This could be performed through a systematic study where the sintering procedure is varied with respect to time and with/without sacrificial powder. Sintering for longer times will give insight to the effect of chemical homogeneity and the sacrificial powder will elucidate the effect of volatilization of Bi_2O_3 and K_2O. Furthermore, it was surprising to find a Bi_2O_3-rich phase after the longest sintering time, where the loss of volatile elements is expected to be largest. Elemental analysis should be performed to determine if this phase emerges due to an as-synthesized A-excess composition or if this is related to A:B-ratio $\neq 1$ in the primary phase of BFO-BKT. Such analysis could e.g. be performed by wavelength-dispersive X-ray spectroscopy.

Finally, this thesis has highlighted the importance of considering the chemical homogeneity of materials, including materials that appear phase pure by XRD and SEM. Perovskites are the most studied materials in the search for prominent lead-free piezoelectric materials. The motivation behind the synthesis of many new materials, including BKT-BNZ and BFO-BKT, is the prospect of finding an MPB where enhanced piezoelectric properties are expected. The perovskite structure is versatile with respect to accommodating a large variety of different cations both at the A- and B-site. However, the chemical homogeneity of the materials is rarely commented on although the composition is such that several elements occupy the same lattice site. Materials produced by the solid state method are especially prone to chemical inhomogeneity due to potentially long diffusion distances. Other wet chemistry based methods such as spray pyrolysis and sol-gel derived methods offer a better control of distribution of elements before calcination and sintering. Wet chemical methods could therefore be preferential when preparing perovskite solid solutions where several elements occupy the same lattice site.

References

1. Jaffe B, Cook WR, and Jaffe HL, *Piezoelectric ceramics*, volume 3 of *Non-metallic solids* (Academic Press, London and New York, 1971).
2. Haugen AB, *Synthesis and characterisation of textured lead-free piezoelectric ceramics*, Ph.D. thesis, Norwegian University of Science and Technology (2014).
3. Haertling GH, “Ferroelectric ceramics: History and technology,” *J. Am. Ceram. Soc.*, **82**, 797–818 (1999).
4. “JEM-ARM200F Transmission electron microscope,” *http://www.jeol.co.jp/en/products/detail/JEM-ARM200F.html*, JEOL USA, INC. (Accessed Jan 15th, 2015).
5. “Piezoelectric ceramic, polymer and ceramic/polymer composite devices - types, materials, apllications, new developments, industry structure and global markets,” *Press release*, Innovative Research and Products Inc. (Jan 2014).
6. Anton SR and Sodano HA, “A review of power harvesting using piezoelectric materials (2003-2006),” *Smart Mater. Struct.*, **16**, R1 (2007).
7. Jo W, Dittmer R, Acosta M, Zang J, Groh C, Sapper E, Wang K, and Rödel J, “Giant electric-field-induced strains in lead-free ceramics for actuator applications - status and perspective,” *J. Electroceram.*, **29**, 71–93 (2012).
8. Shenck NS and Paradiso JA, “Energy scavenging with shoe-mounted piezoelectrics,” *IEEE Micro*, **21**, 30–42 (2001).
9. Morozov MI and Damjanovic D, “Charge migration in $Pb(Zr,Ti)O_3$ ceramics and its relation to ageing, hardening, and softening,” *J. Appl. Phys.*, **107**, 034106 (2010).
10. Cohen RE, “Origin of ferroelectricity in perovskite oxides,” *Nature*, **358**, 136–138 (1992).
11. Kuroiwa Y, Aoyagi S, Sawada A, Harada J, Nishibori E, Takata M, and Sakata M, “Evidence for Pb-O covalency in tetragonal $PbTiO_3$,” *Phys. Rev. Lett.*, **87**, 217601 (2001).
12. Shrout TR and Zhang SJ, “Lead-free piezoelectric ceramics: Alternatives for PZT?” *J. Electroceram.*, **19**, 113–126 (2007).
13. Rödel J, Jo W, Seifert KTP, Anton EM, Granzow T, and Damjanovic D, “Perspective on the development of lead-free piezoceramics,” *J. Am. Ceram. Soc.*, **92**, 1153–1177 (2009).

14. Flora G, Gupta D, and Tiwari A, “Toxicity of lead: A review with recent updates,” *Interdiscip. Toxicol.*, **5**, 47–58 (2012).

15. Rödel J, Webber KG, Dittmer R, Jo W, Kimura M, and Damjanovic D, “Transferring lead-free piezoelectric ceramics into application,” *J. Eur. Ceram. Soc.*, **35**, 1659–1681 (2015).

16. European Parliament, “EU-directive 2002/95/EC: Restriction of the use of certain hazardous substances in electrical and electronic equipment (RoHS),” *Off. J. Eur. Union*, **46**, 19–23 (2003).

17. European Parliament, “EU-directive 2011/65/EU: Restriction of the use of certain hazardous substances in electrical and electronic equipment (RoHS),” *Off. J. Eur. Union*, **54**, 89–110 (2011).

18. European Parliament, “EU-directive 2002/96/EC: Waste electrical and electronic equipment (WEEE),” *Off. J. Eur. Union*, **46**, 24–39 (2003).

19. European Parliament, “EU-directive 2012/19/EU: Waste electrical and electronic equipment (WEEE),” *Off. J. Eur. Union*, **55**, 38–71 (2012).

20. Maeder MD, Damjanovic D, and Setter N, “Lead free piezoelectric materials,” *J. Electroceram.*, **13**, 385–392 (2004).

21. Takenaka T, Nagata H, and Hiruma Y, “Current developments and prospective of lead-free piezoelectric ceramics,” *Jpn. J. Appl. Phys.*, **47**, 3787–3801 (2008).

22. Aksel E and Jones JL, “Advances in lead-free piezoelectric materials for sensors and actuators,” *Sensors*, **10**, 1935–1954 (2010).

23. Leontsev SO and Eitel RE, “Progress in engineering high strain lead-free piezoelectric ceramics,” *Sci. Tech. Adv. Mater.*, **11**, 044302 (2010).

24. Safari A and Abazari M, “Lead-free piezoelectric ceramics and thin films,” *IEEE Trans. Ultrason., Ferroelect., Freq. Control*, **57**, 2165–2176 (2010).

25. Eichel RA and Kungl H, “Recent developments and future perspectives of lead-free ferroelectrics,” *Funct. Mater. Lett.*, **3**, 1–4 (2010).

26. Jardiel T, Caballero AC, and Villegas M, “Aurivillius ceramics: $Bi_4Ti_3O_{12}$-based piezoelectrics,” *J. Ceram. Soc. Jpn.*, **116**, 511–518 (2008).

27. Panda PK, “Review: Environmental friendly lead-free piezoelectric materials,” *J. Mater. Sci.*, **44**, 5049–5062 (2009).

28. Rojac T, Bencan A, Malic B, Tutuncu G, Jones JL, Daniels JE, and Damjanovic D, “$BiFeO_3$ ceramics: Processing, electrical, and electromechanical properties,” *J. Am. Ceram. Soc.*, **97**, 1993–2011 (2014).

29. Sasaki A, Chiba T, Mamiya Y, and Otsuki E, "Dielectric and piezoelectric properties of $(Bi_{0.5}Na_{0.5})TiO_3$-$(Bi_{0.5}K_{0.5})TiO_3$ systems," *Jpn. J. Appl. Phys.*, **38**, 5564–5567 (1999).

30. Takenaka T, Maruyama K, and Sakata K, "$(Bi_{1/2}Na_{1/2})TiO_3$-$BaTio_3$ system for lead-free piezoelectric ceramics," *Jpn. J. Appl. Phys.*, **30**, 2236–2239 (1991).

31. Neaton JB, Ederer C, Waghmare UV, Spaldin NA, and Rabe KM, "First-principles study of spontaneous polarization in multiferroic $BiFeO_3$," *Phys. Rev. B.*, **71**, 014113 (2005).

32. Ravindran P, Vidya R, Kjekshus A, Fjellvåg H, and Eriksson O, "Theoretical investigation of magnetoelectric behavior in $BiFeO_3$," *Phys. Rev. B.*, **74**, 224412 (2006).

33. Ivanova V, Kapyshev A, Venevtsev Y, and Zhdanov G, "X-ray determination of the symmetry of elementary cells of the ferroelectric materials $(K_{0.5}Bi_{0.5})TiO_3$ and $(Na_{0.5}Bi_{0.5})TiO_3$ and of high-temperature phase transitions in $(K_{0.5}Bi_{0.5})TiO_3$," *Izv. Akad. Nauk SSSR*, **26**, 354–356 (1962).

34. Hiruma Y, Aoyagi R, Nagata H, and Takenaka T, "Ferroelectric and piezoelectric properties of $(Bi_{1/2}K_{1/2})TiO_3$ ceramics," *Jpn. J. Appl. Phys.*, **44**, 5040–5044 (2005).

35. Dorcet V, Trolliard G, and Boullay P, "Reinvestigation of phase transitions in $Na_{0.5}Bi_{0.5}TiO_3$ by TEM. Part I: First order rhombohedral to orthorhombic phase transition," *Chem. Mater.*, **20**, 5061–5073 (2008).

36. Trolliard G and Dorcet V, "Reinvestigation of phase transitions in $Na_{0.5}Bi_{0.5}TiO_3$ by TEM. Part II: Second order orthorhombic to tetragonal phase transition," *Chem. Mater.*, **20**, 5074–82 (2008).

37. Dorcet V, Marchet P, and Trolliard G, "Structural and dielectric studies of the $Na_{0.5}Bi_{0.5}TiO_3BiFeO_3$ system," *J. Eur. Ceram. Soc.*, **27**, 4371–4374 (2007).

38. Jaiban P, Rachakom A, Buntham S, Jiansirisomboon S, and Watcharapasorn A, "Fabrication of $Bi_{0.5}Na_{0.5}ZrO_3$ powder by mixed oxide method," *Mater. Sci. Forum*, **695**, 49–52 (2011).

39. Ivanov S, "ICDD grant-in-Aid," *Technical Report 00-057-0823*, Karpov Institute of Physical Chemistry (2005).

40. Hussain A, Ahn CW, Lee JS, Ullah A, and Kim IW, "Large electric-field-induced strain in Zr-modified lead-free $Bi_{0.5}(Na_{0.78}K_{0.22})_{0.5}TiO_3$ piezoelectric ceramics," *Sensor. Actuat. A-Phys.*, **158**, 84–89 (2010).

41. Rojac T, Kosec M, Budic B, Setter N, and Damjanovic D, "Strong ferroelectric domain-wall pinning in $BiFeO_3$ ceramics," *J. Appl. Phys.*, **108**, 074107 (2010).

42. Rojac T, Kosec M, and Damjanovic D, “Large electric-field induced strain in $BiFeO_3$ ceramics,” *J. Am. Ceram. Soc.*, **94**, 4108–4111 (2011).

43. Lebeugle D, Colson D, Forget A, and Viret M, “Very large spontaneous electric polarization in $BiFeO_3$ single crystals at room temperature and its evolution under cycling fields,” *Appl. Phys. Lett.*, **91**, 022907 (2007).

44. Catalan G and Scott JF, “Physics and applications of bismuth ferrite,” *Adv. Mater.*, **21**, 2463–2485 (2009).

45. Selbach SM, Einarsrud MA, and Grande T, “On the thermodynamic stability of $BiFeO_3$,” *Chem. Mater.*, **21**, 169–173 (2009).

46. Selbach SM, Tybell T, Einarsrud MA, and Grande T, “The ferroic phase transitions of $BiFeO_3$,” *Adv. Mater.*, **20**, 3692–3696 (2008).

47. Selbach SM, Tybell T, Einarsrud MA, and Grande T, “Phase transitions, electrical conductivity and chemical stability of $BiFeO_3$ at high temperatures,” *J. Solid State Chem.*, **183**, 1205–1208 (2010).

48. Selbach SM, *Structure, stability and phase transitions of multiferroic $BiFeO_3$*, Ph.D. thesis, Norwegian University of Science and Technology (2009).

49. Morozov MI, Einarsrud MA, Grande T, and Damjanovic D, “Lead-free relaxor-like $0.75Bi_{0.5}K_{0.5}TiO_3$-$0.25BiFeO_3$ ceramics with large electric field-induced strain,” *Ferroelectrics*, **439**, 88–94 (2012).

50. Morozov MI, Einarsrud MA, and Grande T, “Polarization and strain response in $Bi_{0.5}K_{0.5}TiO_3$-$BiFeO_3$ ceramics,” *Appl. Phys. Lett.*, **101**, 252904 (2012).

51. Masó N and West AR, “Electrical properties of Ca-doped $BiFeO_3$ ceramics: From p-type semiconduction to oxide-ion conduction,” *Chem. Mater.*, **24**, 2127–2132 (2012).

52. Zhang Z, Wu P, Chen L, and Wang JL, “Density functional theory plus U study of vacancy formations in bismuth ferrite,” *Appl. Phys. Lett.*, **96**, 232906 (2010).

53. Pham KN, *Potassium sodium niobate thin films by chemical solution deposition*, Ph.D. thesis, Norwegian University of Science and Technology (2014).

54. Damjanovic D, “Ferroelectric, dielectric and piezoelectric properties of ferroelectric thin films and ceramics,” *Rep. Prog. Phys.*, **61**, 1267–1324 (1998).

55. Safari A and Akdoğan EK (editors), *Piezoelectric and acoustic materials for transducer applications* (Springer, US, 2008).

56. Damjanovic D, “Piezoelectric properties of perovskite ferroelectrics: unsolved problems and future research,” *Ann. Chim. Sci. Mat.*, **26**, 99–106 (2001).

57. Goodenough JB, "Electronic and ionic transport properties and other physical aspects of perovskites," *Rep. Prog. Phys.*, **67**, 1915–1993 (2004).

58. Goldschmidt VM, "Geochemische verteilungsgesetze der elemente. VII: Die gesetze der krystallochemie," *Skr. Nor. Vidensk.-Akad. Oslo*, **2**, 5–116 (1926).

59. Stølen S and Grande T, *Chemical thermodynamics of materials: macroscopic and microscopic aspects* (J. Wiley & Sons, West Sussex, England, 2004).

60. Suchomel MR and Davies PK, "Predicting the position of the morphotropic phase boundary in high temperature $PbTiO_3$-Bi(B'B")O_3 based dielectric ceramics," *J. Appl. Phys.*, **96**, 4405–4410 (2004).

61. Eitel R, Randall C, Shrout T, Rehrig P, Hackenberger W, and Park SE, "New high temperature morphotropic phase boundary piezoelectrics based on Bi(Me)O_3-$PbTiO_3$ ceramics," *Jpn. J. Appl. Phys.*, **40**, 5999–6002 (2001).

62. Surez DY, Reaney IM, and Lee WE, "Relation between tolerance factor and T_c in Aurivillius compounds," *J. Mater. Res.*, **16**, 3139–3149 (2001).

63. Marton P, Rychetsky I, and Hlinka J, "Domain walls of ferroelectric $BaTiO_3$ within the Ginzburg-Landau-Devonshire phenomenological model," *Phys. Rev. B.*, **81**, 144125 (2010).

64. Damjanovic D, "Contributions to the piezoelectric effect in ferroelectric single crystals and ceramics," *J. Am. Ceram. Soc.*, **88**, 2663–2676 (2005).

65. Ahn CW, Song HC, Nahm S, Park SH, Uchino K, Priya S, Lee HG, and Kang NK, "Effect of MnO_2 on the piezoelectric properties of (1-x)($Na_{0.5}K_{0.5}$)NbO_3-x$BaTiO_3$ ceramics," *Jpn. J. Appl. Phys.*, **44**, L1361–L1364 (2005).

66. Zuo R, Fang X, Ye C, and Li L, "Phase transitional behavior and piezoelectric properties of lead-free ($Na_{0.5}K_{0.5}$)NbO_3-($Bi_{0.5}K_{0.5}$)TiO_3 ceramics," *J. Am. Ceram. Soc.*, **90**, 2424–2428 (2007).

67. Yoshii K, Hiruma Y, Nagata H, and Takenaka T, "Electrical properties and depolarization temperature of $Bi_{1/2}Na_{1/2}TiO_3$-$Bi_{1/2}K_{1/2}TiO_3$ lead-free piezoelectric ceramics," *Jpn. J. Appl. Phys.*, **45**, 4493–4496 (2006).

68. Lines ME and Glass AM, *Principles and applications of ferroelectrics and related materials*, Oxford classic texts in the physical sciences (Clarendon Press; Oxford University Press, Oxford New York, 2001).

69. Rørvik PM, Grande T, and Einarsrud MA, "One-dimensional nanostructures of ferroelectric perovskites," *Adv. Mater.*, **23**, 4007–4034 (2011).

70. Cao WW and Randall CA, "Grain size and domain size relations in bulk ceramic ferroelectric materials," *J. Phys. Chem. Solids*, **57**, 1499–1505 (1996).

71. Hiruma Y, Nagata H, and Takenaka T, "Grain-size effect on electrical properties of $(Bi_{1/2}K_{1/2})TiO_3$ ceramics," *Jpn. J. Appl. Phys.*, **46**, 1081–1084 (2007).

72. Zhao Z, Buscaglia V, Viviani M, Buscaglia MT, Mitoseriu L, Testino A, Nygren M, Johnsson M, and Nanni P, "Grain-size effects on the ferroelectric behavior of dense nanocrystalline $BaTiO_3$ ceramics," *Phys. Rev. B.*, **70**, 024107 (2004).

73. Jin L, Li F, and Zhang SJ, "Decoding the fingerprint of ferroelectric loops: Comprehension of the material properties and structures," *J. Am. Ceram. Soc.*, **97**, 1–27 (2014).

74. Morozov M, *Softening and hardening transitions in ferroelectric Pb(Zr,Ti)O*$_3$ *ceramics*, Ph.D. thesis, Ècole Polytechnique Fèdèrale de Lausanne (2005).

75. Bokov AA and Ye ZG, "Dielectric relaxation in relaxor ferroelectrics," *J. Adv. Dielectr.*, **2**, 1241010 (2012).

76. Ogihara H, Randall CA, and Trolier-McKinstry S, "Weakly coupled relaxor behavior of $BaTiO_3$-$BiScO_3$ ceramics," *J. Am. Ceram. Soc.*, **92**, 110–118 (2009).

77. Morozov MI and Damjanovic D, "Hardening-softening transition in Fe-doped $Pb(Zr,Ti)O_3$ ceramics and evolution of the third harmonic of the polarization response," *J. Appl. Phys.*, **104**, 034107 (2008).

78. Carl K and Härdtl KH, "Electrical after-effects in $Pb(Ti,Zr)O_3$ ceramics," *Ferroelectrics*, **17**, 473–486 (1978).

79. Chandrasekaran A, Damjanovic D, Setter N, and Marzari N, "Defect ordering and defect-domain-wall interactions in $PbTiO_3$: A first-principles study," *Phys. Rev. B.*, **88**, 214116 (2013).

80. Erhart P, Eichel RA, Traskelin P, and Albe K, "Association of oxygen vacancies with impurity metal ions in lead titanate," *Phys. Rev. B.*, **76**, 174116 (2007).

81. Zhang XL, Chen ZX, Cross LE, and Schulze WA, "Dielectric and piezoelectric properties of modified lead titanate zirconate ceramics from 4.2 K to 300 K," *J. Mater. Sci.*, **18**, 968–972 (1983).

82. Ren XB, "Large electric-field-induced strain in ferroelectric crystals by point-defect-mediated reversible domain switching," *Nature Mater.*, **3**, 91–94 (2004).

83. Zhang LX and Ren X, "*In situ* observation of reversible domain switching in aged Mn-doped $BaTiO_3$ single crystals," *Phys. Rev. B.*, **71**, 174108 (2005).

84. Postnikov VS, Pavlov VS, and Turkov SK, "Internal friction in ferroelectrics due to interaction of domain boundaries and point defects," *J. Phys. Chem. Solids*, **31**, 1785–1791 (1970).

85. Seidel J, Martin LW, He Q, Zhan Q, Chu YH, Rother A, Hawkridge ME, Maksymovych P, Yu P, Gajek M, Balke N, Kalinin SV, Gemming S, Wang F, Catalan G, Scott JF, Spaldin NA, Orenstein J, and Ramesh R, "Conduction at domain walls in oxide multiferroics," *Nature Mater.*, **8**, 229–234 (2009).

86. Rojac T, Ursic H, Bencan A, Malic B, and Damjanovic D, "Mobile domain walls as a bridge between nanoscale conductivity and macroscopic electromechanical response," *Adv. Funct. Mater.*, **25**, 2099–2108 (2015).

87. Genenko YA, "Space-charge mechanism of aging in ferroelectrics: An analytically solvable two-dimensional model," *Phys. Rev. B.*, **78**, 214103 (2008).

88. Cross LE, "Relaxor ferroelectrics," *Ferroelectrics*, **76**, 241–267 (1987).

89. Bokov AA and Ye ZG, "Recent progress in relaxor ferroelectrics with perovskite structure," *J. Mater. Sci.*, **41**, 31–52 (2006).

90. Salje EKH, *Phase transitions in ferroelastic and co-elastic crystals: an introduction for mineralogists, material scientists, and physicists - student edition*, Cambridge topics in mineral physics and chemistry (Cambridge University Press, Cambridge England ; New York, 1993).

91. Marsilius M, Webber KG, Aulbach E, and Granzow T, "Comparison of the temperature-dependent ferroelastic behavior of hard and soft lead zirconate titanate ceramics," *J. Am. Ceram. Soc.*, **93**, 2850–2856 (2010).

92. Schäufele AB and Härdtl KH, "Ferroelastic properties of lead zirconate titanate ceramics," *J. Am. Ceram. Soc.*, **79**, 2637–2640 (1996).

93. Webber KG, Aulbach E, Key T, Marsilius M, Granzow T, and Rödel J, "Temperature-dependent ferroelastic switching of soft lead zirconate titanate," *Acta Mater.*, **57**, 4614–4623 (2009).

94. Seo YH, Franzbach DJ, Koruza J, Bencan A, Malic B, Kosec M, Jones JL, and Webber KG, "Nonlinear stress-strain behavior and stress-induced phase transitions in soft $\mathrm{Pb(Zr_{1-\mathit{x}}Ti_{\mathit{x}})O_3}$ at the morphotropic phase boundary," *Phys. Rev. B.*, **87**, 094116 (2013).

95. Jones JL, Hoffman M, and Bowman KJ, "Saturated domain switching textures and strains in ferroelastic ceramics," *J. Appl. Phys.*, **98**, 024115 (2005).

96. Leist T, Webber KG, Jo W, Granzow T, Aulbach E, Suffner J, and Rödel J, "Domain switching energies: Mechanical versus electrical loading in La-doped bismuth ferrite-lead titanate," *J. Appl. Phys.*, **109**, 054109 (2011).

97. Kounga AB, Granzow T, Aulbach E, Hinterstein M, and Rödel J, "High-temperature poling of ferroelectrics," *J. Appl. Phys.*, **104**, 024116 (2008).

98. Jones GO and Thomas PA, "Investigation of the structure and phase

transitions in the novel A-site substituted distorted perovskite compound $Na_{0.5}Bi_{0.5}TiO_3$," *Acta Crystallogr., Sect. B: Struct. Sci*, **58**, 168–178 (2002).

99. Hiruma Y, Yoshii K, Nagata H, and Takenaka T, "Phase transition temperature and electrical properties of $(Bi_{1/2}Na_{1/2})TiO_3$-$(Bi_{1/2}A_{1/2})TiO_3$ (A=Li and K) lead-free ferroelectric ceramics," *J. Appl. Phys.*, **103**, 084121 (2008).

100. Tabuchi K, Inoue Y, Nagata H, and Takenaka T, "Effects of starting raw materials for fabricating dense $(Bi_{1/2}K_{1/2})TiO_3$ ceramics," *Ferroelectrics*, **457**, 124–130 (2013).

101. Otoničar M, Škapin SD, Spreitzer M, and Suvorov D, "Compositional range and electrical properties of the morphotropic phase boundary in the $Na_{0.5}Bi_{0.5}TiO_3$-$K_{0.5}Bi_{0.5}TiO_3$ system," *J. Eur. Ceram. Soc.*, **30**, 971–979 (2010).

102. Kubel F and Schmid H, "Structure of a ferroelectric and ferroelastic monodomain crystal of the perovskite $BiFeO_3$," *Acta Crystallogr., Sect. B: Struct. Sci*, **46**, 698–702 (1990).

103. Liu W and Ren X, "Large piezoelectric effect in Pb-free ceramics," *Phys. Rev. Lett.*, **103**, 257602 (2009).

104. Shirane G, Newnham R, and Pepinsky R, "Dielectric properties and phase transitions of $NaNbO_3$ and $(Na,K)NbO_3$," *Phys. Rev.*, **96**, 581–588 (1954).

105. Baker DW, Thomas PA, Zhang N, and Glazer AM, "A comprehensive study of the phase diagram of $K_xNa_{1-x}NbO_3$," *Appl. Phys. Lett.*, **95**, 091903 (2009).

106. Saito Y, Takao H, Tani T, Nonoyama T, Takatori K, Homma T, Nagaya T, and Nakamura M, "Lead-free piezoceramics," *Nature*, **432**, 84–87 (2004).

107. Leontsev SO and Eitel RE, "Origin and magnitude of the large piezoelectric response in the lead-free (1-x)$BiFeO_3$-x$BaTiO_3$ solid solution," *J. Mater. Res.*, **26**, 9–17 (2011).

108. Kumar MM, Srinivas A, and Suryanarayana SV, "Structure property relations in $BiFeO_3/BaTiO_3$ solid solutions," *J. Appl. Phys.*, **87**, 855–862 (2000).

109. Leontsev SO and Eitel RE, "Dielectric and Piezoelectric Properties in Mn-Modified (1-x)$BiFeO_3$-x$BaTiO_3$ Ceramics," *J. Am. Ceram. Soc.*, **92**, 2957–2961 (2009).

110. Matsuo H, Noguchi Y, Miyayama M, Suzuki M, Watanabe A, Sasabe S, Ozaki T, Mori S, Torii S, and Kamiyama T, "Structural and piezoelectric properties of high-density $(Bi_{0.5}K_{0.5})TiO_3$-$BiFeO_3$ ceramics," *J. Appl. Phys.*, **108**, 104103 (2010).

111. Bennett J, Shrout TR, Zhang SJ, Owston HE, Stevenson TJ, Esat F, Bell AJ, and Comyn TP, "Variation of piezoelectric properties and mechanisms across

the relaxor-like/ferroelectric continuum in $BiFeO_3$-$(K_{0.5}Bi_{0.5})TiO_3$-$PbTiO_3$ ceramics," *IEEE Trans. Ultrason., Ferroelect., Freq. Control*, **62**, 33–45 (2015).

112. Smolenskii GA, Isupov VA, Agranovskaya AI, and Krainik NN, "New ferroelectrics of complex composition. IV," *Sov. Phys.-Sol. State*, **2**, 2651–2654 (1961).

113. Buhrer CF, "Some properties of bismuth perovskites," *J. Chem. Phys.*, **36**, 798–803 (1962).

114. Otoničar M, Škapin SD, Jančar B, Ubic R, and Suvorov D, "Analysis of the phase transition and the domain structure in $K_{0.5}Bi_{0.5}TiO_3$ perovskite ceramics by *in situ* XRD and TEM," *J. Am. Ceram. Soc.*, **93**, 4168–4173 (2010).

115. Li ZF, Wang CL, Zhong WL, Li JC, and Zhao ML, "Dielectric relaxor properties of $K_{0.5}Bi_{0.5}TiO_3$ ferroelectrics prepared by sol-gel method," *J. Appl. Phys.*, **94**, 2548–2552 (2003).

116. Elkechai O, Manier M, and Mercurio JP, "$Na_{0.5}Bi_{0.5}TiO_3$-$K_{0.5}Bi_{0.5}TiO_3$ (NBT-KBT) system: A structural and electrical study," *Phys. Status Solidi A*, **157**, 499–506 (1996).

117. Jones GO, Kreisel J, and Thomas PA, "A structural study of the $(Na_{1-x}K_x)_{0.5}Bi_{0.5}TiO_3$ perovskite series as a function of substitution (x) and temperature," *Powder Diffr.*, **17**, 301–319 (2002).

118. Shannon R, "Revised effective ionic-radii and systematic studies of interatomic distances in halides and chalcogenides," *Acta Crystallogr., Sect. A: Found. Crystallogr.*, **32**, 751–67 (1976).

119. Bengagi M, Morini F, Maaoui ME, and Marchet P, "Structure and electrical properties in the $K_{0.5}Bi_{0.5}TiO_3$-$K_{0.5}Bi_{0.5}ZrO_3$ solid solution (KBT-KBZ)," *Phys. Status Solidi A*, **209**, 2063–2072 (2012).

120. Wada T, Fukui A, and Matsuo Y, "Preparation of $(K_{0.5}Bi_{0.5})TiO_3$ ceramics by polymerized complex method and their properties," *Jpn. J. Appl. Phys.*, **41**, 7025–7028 (2002).

121. Rao PVB, Ramana EV, and Sankaram TB, "Electrical properties of $K_{0.5}Bi_{0.5}TiO_3$," *J. Alloys Compd.*, **467**, 293–298 (2009).

122. König J, Spreitzer M, Jančar B, Suvorov D, Samardžija Z, and Popovič A, "The thermal decomposition of $K_{0.5}Bi_{0.5}TiO_3$ ceramics," *J. Eur. Ceram. Soc.*, **29**, 1695–1701 (2009).

123. Gorfman S and Thomas PA, "Evidence for a non-rhombohedral average structure in the lead-free piezoelectric material $Na_{0.5}Bi_{0.5}TiO_3$," *J. Appl. Crystallogr.*, **43**, 1409–1414 (2010).

124. Aksel E, Forrester JS, Jones JL, Thomas PA, Page K, and Suchomel MR, “Monoclinic crystal structure of polycrystalline $Na_{0.5}Bi_{0.5}TiO_3$,” *Appl. Phys. Lett.*, **98**, 152901 (2011).

125. Shvartsman VV and Lupascu DC, “Lead-free relaxor ferroelectrics,” *J. Am. Ceram. Soc.*, **95**, 1–26 (2012).

126. Spreitzer M, Valant M, and Suvorov D, “Sodium deficiency in $Na_{0.5}Bi_{0.5}TiO_3$,” *J. Mater. Chem.*, **17**, 185–192 (2007).

127. Carter J, Aksel E, Iamsasri T, Forrester JS, Chen J, and Jones JL, “Structure and ferroelectricity of nonstoichiometric $(Na_{0.5}Bi_{0.5})TiO_3$,” *Appl. Phys. Lett.*, **104**, 112904 (2014).

128. Shuvaeva VA, Zekria D, Glazer AM, Jiang Q, Weber SM, Bhattacharya P, and Thomas PA, “Local structure of the lead-free relaxor ferroelectric $(K_xNa_{1-x})_{0.5}Bi_{0.5}TiO_3$,” *Phys. Rev. B.*, **71**, 174114 (2005).

129. Yamada Y, Akutsu T, Asada H, Nozawa K, Hachiga S, Kurosaki T, Ikagawa O, Fujiki H, Hozumi K, Kawamura T, Amakawa T, Hirota K, and Ikeda T, “Effect of B-ions substitution in $[(K_{1/2}Bi_{1/2})\text{-}(Na_{1/2}Bi_{1/2})](Ti\text{-}B)O_3$ system with B=Zr, $Fe_{1/2}Nb_{1/2}$, $Zn_{1/3}Nb_{2/3}$ or $Mg_{1/3}Nb_{2/3}$,” *Jpn. J. Appl. Phys.*, **34**, 5462–5466 (1995).

130. Rachakom A, Jaiban P, Jiansirisomboon S, and Watcharapasorn A, “Crystal structure and electrical properties of bismuth sodium titanate zirconate ceramics,” *Nanoscale Res. Lett.*, **7**, 57 (2012).

131. Kumari L, Kumari K, Prasad K, and Choudhary RNP, “Impedance spectroscopy of $(Na_{0.5}Bi_{0.5})(Zr_{0.25}Ti_{0.75})O_3$ lead-free ceramic,” *J. Alloys Compd.*, **453**, 325–331 (2008).

132. Watcharapasorn A and Jiansirisomboon S, “Dielectric and piezoelectric properties of zirconium-doped bismuth sodium titanate ceramics,” *Adv. Mat. Res.*, **55-57**, 133–136 (2008).

133. Palai R, Katiyar RS, Schmid H, Tissot P, Clark SJ, Robertson J, Redfern SAT, Catalan G, and Scott JF, “β phase and γ-β metal-insulator transition in multiferroic $BiFeO_3$,” *Phys. Rev. B.*, **77**, 014110 (2008).

134. Silva J, Reyes A, Esparza H, Camacho H, and Fuentes L, “$BiFeO_3$: A review on synthesis, doping and crystal structure,” *Integr. Ferroelectr.*, **126**, 47–59 (2011).

135. Bernardo MS, Jardiel T, Peiteado M, Caballero AC, and Villegas M, “Reaction pathways in the solid state synthesis of multiferroic $BiFeO_3$,” *J. Eur. Ceram. Soc.*, **31**, 3047–3053 (2011).

136. Selbach SM, Tybell T, Einarsrud MA, and Grande T, "Structure and properties of multiferroic oxygen hyperstoichiometric $BiFe_{1-x}Mn_xO_{3+\delta}$," *Chem. Mater.*, **21**, 5176–5186 (2009).

137. Arnold DC, Knight KS, Catalan G, Redfern SAT, Scott JF, Lightfoot P, and Morrison FD, "The β-to-γ transition in $BiFeO_3$: A powder neutron diffraction study," *Adv. Funct. Mater.*, **20**, 2116–2123 (2010).

138. Yokota T, Aoyagi R, and Gomi M, "Thermoelectric properties of Co-doped $BiFeO_3$ and $Bi_{24}CoO_{37}$-$BiFeO_3$ compound systems," *J. Ceram. Soc. Jpn.*, **121**, 675–678 (2013).

139. Faaland S, Grande T, Einarsrud MA, Vullum PE, and Holmestad R, "Stress-strain behavior during compression of polycrystalline $La_{1-x}Ca_xCoO_3$ ceramics," *J. Am. Ceram. Soc.*, **88**, 726–730 (2005).

140. Kamba S, Nuzhnyy D, Savinov M, Šebek J, Petzelt J, Prokleška J, Haumont R, and Kreisel J, "Infrared and terahertz studies of polar phonons and magnetodielectric effect in multiferroic $BiFeO_3$ ceramics," *Phys. Rev. B.*, **75**, 024403 (2007).

141. Yuan GL, Or SW, Wang YP, Liu ZG, and Liu JM, "Preparation and multi-properties of insulated single-phase $BiFeO_3$ ceramics," *Solid State Commun.*, **138**, 76–81 (2006).

142. Teague JR, Gerson R, and James WJ, "Dielectric hysteresis in single crystal $BiFeO_3$," *Solid State Commun.*, **8**, 1073–1074 (1970).

143. Wang J, Neaton JB, Zheng H, Nagarajan V, Ogale SB, Liu B, Viehland D, Vaithyanathan V, Schlom DG, Waghmare UV, Spaldin NA, Rabe KM, Wuttig M, and Ramesh R, "Epitaxial $BiFeO_3$ multiferroic thin film heterostructures," *Science*, **299**, 1719–1722 (2003).

144. Rojac T, Bencan A, Drazic G, Kosec M, and Damjanovic D, "Piezoelectric nonlinearity and frequency dispersion of the direct piezoelectric response of $BiFeO_3$ ceramics," *J. Appl. Phys.*, **112**, 064114 (2012).

145. Kubel F, "The absolute configuration of an as-grown and a mechanically switched single crystal of the perovskite $BiFeO_3$," *Z. Kristallogr.*, **210**, 5–8 (1995).

146. Yuan GL, Yang Y, and Or SW, "Aging-induced double ferroelectric hysteresis loops in $BiFeO_3$ multiferroic ceramic," *Appl. Phys. Lett.*, **91**, 122907 (2007).

147. Wang X, Hu G, Cheng L, Yang C, and Wu W, "Comparative study on aging effect in $BiFeO_3$ thin films substituted at A- and B-sites," *Appl. Phys. Lett.*, **99**, 262901 (2011).

148. Bernardo MS, Jardiel T, Peiteado M, Mompean FJ, Garcia-Hernandez M,

Garcia MA, Villegas M, and Caballero AC, "Intrinsic compositional inhomogeneities in bulk Ti-doped $BiFeO_3$: Microstructure development and multiferroic properties," *Chem. Mater.*, **25**, 1533–1541 (2013).

149. Jun YK, Moon WT, Chang CM, Kim HS, Ryu HS, Kim JW, Kim KH, and Hong SH, "Effects of Nb-doping on electric and magnetic properties in multiferroic $BiFeO_3$ ceramics," *Solid State Commun.*, **135**, 133–137 (2005).

150. Qi XD, Dho J, Tomov R, Blamire MG, and MacManus-Driscoll JL, "Greatly reduced leakage current and conduction mechanism in aliovalent-ion-doped $BiFeO_3$," *Appl. Phys. Lett.*, **86**, 062903 (2005).

151. Makhdoom AR, Akhtar MJ, Khan RTA, Rafiq MA, Hasan MM, Sher F, and Fitch AN, "Association of microstructure and electric heterogeneity in $BiFeO_3$," *Mater. Chem. Phys.*, **143**, 256–262 (2013).

152. Kalantari K, Sterianou I, Karimi S, Ferrarelli MC, Miao S, Sinclair DC, and Reaney IM, "Ti-Doping to reduce conductivity in $Bi_{0.85}Nd_{0.15}FeO_3$ ceramics," *Adv. Funct. Mater.*, **21**, 3737–3743 (2011).

153. Perejón A, Masó N, West AR, Sanchez-Jiménez PE, Poyato R, Criado JM, and Pérez-Maqueda LA, "Electrical properties of stoichiometric $BiFeO_3$ prepared by mechanosynthesis with either conventional or spark plasma sintering," *J. Am. Ceram. Soc.*, **96**, 1220–1227 (2013).

154. Farokhipoor S and Noheda B, "Conduction through 71° domain walls in $BiFeO_3$ thin films," *Phys. Rev. Lett.*, **107**, 127601 (2011).

155. Seidel J, Maksymovych P, Batra Y, Katan A, Yang SY, He Q, Baddorf AP, Kalinin SV, Yang CH, Yang JC, Chu YH, Salje EKH, Wormeester H, Salmeron M, and Ramesh R, "Domain wall conductivity in La-doped $BiFeO_3$," *Phys. Rev. Lett.*, **105**, 197603 (2010).

156. Paudel TR, Jaswal SS, and Tsymbal EY, "Intrinsic defects in multiferroic $BiFeO_3$ and their effect on magnetism," *Phys. Rev. B.*, **85**, 104409 (2012).

157. Xu Q, Sobhan M, Yang Q, Anariba F, Ong KP, and Wu P, "The role of Bi vacancies in the electrical conduction of $BiFeO_3$: a first-principles approach," *Dalton Trans.*, **43**, 10787–10793 (2014).

158. Maksymovych P, Seidel J, Chu YH, Wu PP, Baddorf AP, Chen LQ, Kalinin SV, and Ramesh R, "Dynamic conductivity of ferroelectric domain walls in $BiFeO_3$," *Nano Lett.*, **11**, 1906–1912 (2011).

159. Baek SH, Folkman CM, Park JW, Lee S, Bark CW, Tybell T, and Eom CB, "The nature of polarization fatigue in $BiFeO_3$," *Adv. Mater.*, **23**, 1621–1625 (2011).

160. Li Z, Wu H, and Cao W, “Piezoelectric response of charged non-180° domain walls in ferroelectric ceramics,” *J. Appl. Phys.*, **111**, 024106 (2012).

161. Karimi S, Reaney IM, Han Y, Pokorny J, and Sterianou I, “Crystal chemistry and domain structure of rare-earth doped $BiFeO_3$ ceramics,” *J. Mater. Sci.*, **44**, 5102–5112 (2009).

162. Fujino S, Murakami M, Anbusathaiah V, Lim SH, Nagarajan V, Fennie CJ, Wuttig M, Salamanca-Riba L, and Takeuchi I, “Combinatorial discovery of a lead-free morphotropic phase boundary in a thin-film piezoelectric perovskite,” *Appl. Phys. Lett.*, **92**, 202904 (2008).

163. Walker J, Bryant P, Kurusingal V, Sorrell C, Kuscer D, Drazic G, Bencan A, Nagarajan V, and Rojac T, “Synthesis-phase-composition relationship and high electric-field-induced electromechanical behavior of samarium-modified $BiFeO_3$ ceramics,” *Acta Mater.*, **83**, 149–159 (2015).

164. Bernardo MS, Jardiel T, Peiteado M, Caballero AC, and Villegas M, “Sintering and microstuctural characterization of W^{6+}, Nb^{5+} and Ti^{4+} iron-substituted $BiFeO_3$,” *J. Alloys Compd.*, **509**, 7290–7296 (2011).

165. Wang Y and Nan CW, “Enhanced ferroelectricity in Ti-doped multiferroic $BiFeO_3$ thin films,” *Appl. Phys. Lett.*, **89**, 052903 (2006).

166. Zheng XH, Ma ZH, Chen PJ, Tang DP, and Ma N, “Decomposition behavior and dielectric properties of Ti-doped $BiFeO_3$ ceramics derived from molten salt method,” *J. Mater. Sci.: Mater. Electron.*, **23**, 1533–1537 (2012).

167. Hu GD, Fan SH, Yang CH, and Wu WB, “Low leakage current and enhanced ferroelectric properties of Ti and Zn codoped $BiFeO_3$ thin film,” *Appl. Phys. Lett.*, **92**, 192905 (2008).

168. Azough F, Freer R, Thrall M, Cernik R, Tuna F, and Collison D, “Microstructure and properties of Co-, Ni-, Zn-, Nb- and W-modified multiferroic $BiFeO_3$ ceramics,” *J. Eur. Ceram. Soc.*, **30**, 727–736 (2010).

169. Abe K, Sakai N, Takahashi J, Itoh H, Adachi N, and Ota T, “Leakage current properties of cation-substituted $BiFeO_3$ ceramics,” *Jpn. J. Appl. Phys.*, **49**, 09MB01 (2010).

170. Pradhan AK, Zhang K, Hunter D, Dadson JB, Loutts GB, Bhattacharya P, Katiyar R, Zhang J, Sellmyer DJ, Roy UN, Cui Y, and Burger A, “Magnetic and electrical properties of single-phase multiferroic $BiFeO_3$,” *J. Appl. Phys.*, **97**, 093903 (2005).

171. Wang YP, Zhou L, Zhang MF, Chen XY, Liu JM, and Liu ZG, “Room-temperature saturated ferroelectric polarization in $BiFeO_3$ ceramics synthesized by rapid liquid phase sintering,” *Appl. Phys. Lett.*, **84**, 1731–1733 (2004).

172. Poghossian AS, Abovian HV, Avakian PB, Mkrtchian SH, and Haroutunian VM, “Bismuth ferrites - new materials for semiconductor gas sensors,” *Sensor. Actuat. B-Chem.*, **4**, 545–549 (1991).

173. Masó N, Beltrán H, Prades M, Cordoncillo E, and West AR, “Field-enhanced bulk conductivity and resistive-switching in Ca-doped $BiFeO_3$ ceramics,” *Phys. Chem. Chem. Phys.*, **16**, 19408–19416 (2014).

174. Li MC and MacManus-Driscoll JL, “Phase stability, oxygen nonstoichiometry and magnetic properties of $BiFeO_{3-\delta}$,” *Appl. Phys. Lett.*, **87**, 252510 (2005).

175. Kim JM, Sung YS, Cho JH, Song TK, Kim MH, Chong HH, Park TG, Do D, and Kim SS, “Piezoelectric and dielectric properties of lead-free (1-x)$(Bi_{0.5}K_{0.5})TiO_3$-x$BiFeO_3$ ceramics,” *Ferroelectrics*, **404**, 88–92 (2010).

176. Ozaki T, Matsuo H, Noguchi Y, Miyayama M, and Mori S, “Microstructures related to ferroelectric properties in $(Bi_{0.5}K_{0.5})TiO_3$-$BiFeO_3$,” *Jpn. J. Appl. Phys.*, **49**, 09MC05 (2010).

177. Bennett J, Bell AJ, Stevenson TJ, Smith RI, Sterianou I, Reaney IM, and Comyn TP, “Multiferroic properties of $BiFeO_3$-$K_{0.5}Bi_{0.5}TiO_3$ ceramics,” *Mater. Lett.*, **94**, 172–175 (2013).

178. Morozov MI, Einarsrud MA, and Grande T, “Atmosphere controlled conductivity and Maxwell-Wagner relaxation in $Bi_{0.5}K_{0.5}TiO_3$-$BiFeO_3$ ceramics,” *J. Appl. Phys.*, **115**, 044104 (2014).

179. Christensen M, *On the effect of A to B stoichiometry variation on conductivity and phase purity in 0.8*$BiFeO_3$*-0.2*$Bi_{0.5}K_{0.5}TiO_3$, Master, Norwegian University of Science and Technology (2013).

180. Morozov MI, Einarsrud MA, and Grande T, “Control of conductivity and electric field induced strain in bulk $Bi_{0.5}K_{0.5}TiO_3$-$BiFeO_3$ ceramics,” *Appl. Phys. Lett.*, **104**, 122905 (2014).

181. Hagiwara M and Fujihara S, “Effects of CuO addition on electrical properties of 0.6$BiFeO_3$-0.4$(Bi_{0.5}K_{0.5})TiO_3$ lead-free piezoelectric ceramics,” *J. Am. Ceram. Soc.*, **98**, 469–475 (2015).

182. Choi J, Kim J, and Cheon C, “Effect of process condition on the ferroelectric properties in $BiFeO_3$-(Bi,K)TiO_3 ceramics,” *J. Korean Phys. Soc.*, **65**, 382–386 (2014).

183. Bennett J, Bell AJ, Stevenson TJ, and Comyn TP, “Exceptionally large piezoelectric strains in $BiFeO_3$-$(K_{0.5}Bi_{0.5})TiO_3$-$PbTiO_3$ ceramics,” *Scripta Mater.*, **68**, 491–494 (2013).

184. Bennett J, Bell AJ, Stevenson TJ, and Comyn TP, “Tailoring the structure

and piezoelectric properties of $BiFeO_3$-$(K_{0.5}Bi_{0.5})TiO_3$-$PbTiO_3$ ceramics for high temperature applications," *Appl. Phys. Lett.*, **103**, 152901 (2013).

185. Mizusaki J, Sasamoto T, Cannon WR, and Bowen HK, "Electronic conductivity, seebeck coefficient, and defect Structure of $LaFeO_3$," *J. Am. Ceram. Soc.*, **65**, 363–368 (1982).

186. Mizusaki J, Sasamoto T, Cannon WR, and Bowen HK, "Electronic conductivity, seebeck coefficient, and defect structure of $La_{1-x}Sr_xFeO_3$ (x=0.1, 0.25)," *J. Am. Ceram. Soc.*, **66**, 247–252 (1983).

187. Goodenough JB, "Metallic oxides," *Prog. Solid State Ch.*, **5**, 145–399 (1971).

188. Bruker AXS, "Topas," (2009), URL www.bruker.com, version 4.2.

189. Bruker AXS, "DIFFRAC.EVA," (2012), URL www.bruker.com, version 3.1.

190. Eberg E, Monsen ÅF, Tybell T, van Helvoort ATJ, and Holmestad R, "Comparison of TEM specimen preparation of perovskite thin films by tripod polishing and conventional ion milling," *J. Electron Microsc.*, **57**, 175–179 (2008).

191. Wærnhus I, *Defect chemistry, conductivity and mass transport properties of* $La_{1-x}Sr_xFeO_3$ *(x = 0 and 0.1)*, Ph.D. thesis, Norwegian University of Science and Technology (2003).

192. "Seebeck measurement sample mounting," http://www.norecs.com/index.php?page=Seebeck+coefficient (2015), accessed: February 16th, 2015.

193. Seo YH, Vogler M, Isaia D, Aulbach E, Rödel J, and Webber KG, "Temperature-dependent R-curve behavior of $Pb(Zr_{1-x}Ti_x)O_3$," *Acta Mater.*, **61**, 6418–6427 (2013).

194. Sorokina SL and Sleight AW, "New phases in the ZrO_2-Bi_2O_3 and HfO_2-Bi_2O_3 systems," *Mat. Res. Bull.*, **33**, 1077–1081 (1998).

195. Martin-Arias L, Castro A, and Alguero M, "Ferroelectric phases and relaxor states in the novel lead-free (1-x)$Bi_{1/2}K_{1/2}TiO_3$ - x$BiScO_3$ system ($0 \leq x \leq 0.3$)," *J. Mater. Sci.*, **47**, 3729–3740 (2012).

196. Kreisel J, Glazer AM, Jones G, Thomas PA, Abello L, and Lucazeau G, "An x-ray diffraction and Raman spectroscopy investigation of A-site substituted perovskite compounds: the $(Na_{1-x}K_x)_{0.5}Bi_{0.5}TiO_3$ ($0 \leq x \leq 1$) solid solution," *J. Phys.-Condens. Mat.*, **12**, 3267–3280 (2000).

197. Pronin IP, Parfenova NN, Zaitseva NV, Isupov VA, and Smolenskii GA, "Phase transitions in solid solutions of sodium-bismuth and potassium-bismuth titanates," *Sov. Phys.-Sol. State*, **24**, 1060–1062 (1982).

198. Jaiban P, Rachakom A, Jiansirisomboon S, and Watcharapasorn A, "In-

fluences of phase transition and microstructure on dielectric properties of $Bi_{0.5}Na_{0.5}Zr_{1-x}Ti_xO_3$ ceramics," *Nanoscale Res. Lett.*, **7**, 45 (2012).

199. Lily, Kumari K, Prasad K, and Yadav KL, "Dielectric and impedance study of lead-free ceramic: $(Na_{0.5}Bi_{0.5})ZrO_3$," *J. Mater. Sci.*, **42**, 6252–6259 (2007).

200. Jaiban P, Jiansirisomboon S, and Watcharapasorn A, "Effect of lanthanum substitution on microstructure and electrical properties of $(Bi_{0.5}Na_{0.5})_{(1-1.5x)}La_xTi_{0.41}Zr_{0.59}O_3$ ceramics," *Ceram. Int.*, **38**, S379–S383 (2012).

201. Scott JF, "Ferroelectrics go bananas," *J. Phys.-Condens. Mat.*, **20**, 021001 (2008).

202. Reisman A, "Heterogeneous equilibria in the system K_2CO_3-Na_2CO_3," *J. Am. Chem. Soc.*, **81**, 807–811 (1959).

203. Bakken E, Norby T, and Stolen S, "Redox energetics of perovskite-related oxides," *J. Mater. Chem.*, **12**, 317–323 (2002).

204. Aschauer U, Pfenninger R, Selbach SM, Grande T, and Spaldin NA, "Strain-controlled oxygen vacancy formation and ordering in $CaMnO_3$," *Phys. Rev. B.*, **88**, 054111 (2013).

205. Lohne OF, Phung TN, Grande T, Bouwmeester HJM, Hendriksen PV, Søgaard M, and Wiik K, "Oxygen non-stoichiometry and electrical conductivity of $La_{0.2}Sr_{0.8}Fe_{0.8}B_{0.2}O_{3-\delta}$, B= Fe, Ti, Ta," *J. Electrochem. Soc.*, **161**, F176–F184 (2014).

206. Chen WT, Williams AJ, Ortega-San-Martin L, Li M, Sinclair DC, Zhou WZ, and Attfield JP, "Robust antiferromagnetism and structural disorder in $Bi_xCa_{1-x}FeO_3$ perovskites," *Chem. Mater.*, **21**, 2085–2093 (2009).

207. Selbach SM, Tybell T, Einarsrud MA, and Grande T, "High-temperature semiconducting cubic phase of $BiFe_{0.7}Mn_{0.3}O_{3+\delta}$," *Phys. Rev. B.*, **79**, 214113 (2009).

208. Schader FH, Morozov MI, Wefring ET, Grande T, and Webber KG, "Mechanical stability of polar defects in ferroelectric perovskites," *J. Appl. Phys. (submitted)* (2015).

209. Kim SJ, Han SH, Kim HG, Kim AY, Kim JS, and Cheon CI, "Multiferroic properties of Ti-doped $BiFeO_3$ ceramics," *J. Korean Phys. Soc.*, **56**, 439–442 (2010).

210. Haynes WM (editor), *CRC Handbook of Chemistry and Physics* (CRC Press, Taylor & Francis Group, Florida, USA, 2012), 93^{rd} edition.

Appendices

Appendix A

Scientific Papers

Paper I (reprinted by permission of John Wiley and Sons):
Wefring ET, Morozov MI, Einarsrud M-A and Grande T, ”Solid-state synthesis and properties of relaxor (1-x)BKT-xBNZ ceramics,” *J. Am. Ceram. Soc.*, **97**, 2928-2935 (2014)

Paper II (reprinted by permission of the PCCP Owner Societies):
Wefring ET, Einarsrud M-A and Grande T, ”Electrical conductivity and thermopower of (1-x)$BiFeO_3$ - $xBi_{0.5}K_{0.5}TiO_3$ (x = 0.1, 0.2) ceramics near the ferroelectric to paraelectric phase transition,” *Phys. Chem. Chem. Phys.*, **17**, 9420-9428 (2015)

Journal

J. Am. Ceram. Soc., **0** [9] 2928–2935 (2014)
DOI: 10.1111/jace.13066

Solid-State Synthesis and Properties of Relaxor $(1-x)$BKT–xBNZ Ceramics

Espen T. Wefring, Maxim I. Morozov, Mari-Ann Einarsrud, and Tor Grande[†]

Department of Materials Science and Engineering, Norwegian University of Science and Technology,
Trondheim N-7491, Norway

Conventional solid-state synthesis was used to synthesize dense and phase pure ceramics in the $(1-x)$ $Bi_{0.5}K_{0.5}TiO_3$–$xBi_{0.5}Na_{0.5}ZrO_3$ (BKT–BNZ) system. Structural characterization was done using X-ray diffraction at both room temperature and elevated temperatures, identifying a transition from tetragonal $xBi_{0.5}Na_{0.5}ZrO_3$ (xBNZ, x = 0–0.10) to pseudo cubic xBNZ for x = 0.15–0.80. Dielectric properties were investigated with respect to both temperature (RT = 600°C) and frequency (1–10^6 Hz). Relaxor-like behavior was retained for all the materials investigated, evident by the broadening of the relative dielectric permittivity peaks at transition temperatures as well as frequency dispersion at their maximum. The maximum dielectric constant at elevated temperature was found for 0.15 BNZ. Electric field-induced strain and polarization response were also investigated for several compositions at RT and the largest field-induced strain was observed for the 0.10 BNZ ceramics. The composition range with best performance coincides with the transition from tetragonal to cubic crystal structure.

I. Introduction

Development of lead-free piezoelectric ceramics has attained significant attention in recent years.[1] There is a need to replace the state of the art lead containing piezoceramics such as $Pb(Zr_{1-x}Ti_x)O_3$ (PZT) with lead-free alternatives due to environmental concerns. Among others, the European Union has passed legislations limiting the amount of lead in electronics, with the exception of piezoelectrics until lead-free alternatives are available.[1,2]

Two of the lead-free alternatives to PZT are $Bi_{0.5}K_{0.5}TiO_3$ (BKT) and $Bi_{0.5}Na_{0.5}TiO_3$ (BNT). Both BKT and BNT, as well as their solid solution have been intensively studied.[3–11] Other lead-free systems based on BKT or BNT, such as BKT-$Bi_{0.5}K_{0.5}ZrO_3$[12] (BKT-BKZ), BKT-$BiFeO_3$[13,14] (BKT-BFO), BKT-$BaTiO_3$[15] (BKT-BT), BKT-$K_{0.5}Na_{0.5}NbO_3$[16] (BKT-KNN), BKT-$BiScO_3$[17] (BKT-BS), BNT-$BaTiO_3$,[18] BNT-$K_{0.5}Na_{0.5}NbO_3$[19], and BNT-$NaNbO_3$[20] have also been investigated.

$Bi_{0.5}K_{0.5}TiO_3$ is a tetragonal ferroelectric perovskite. It transforms to a pseudo cubic crystal structure around 300°C (T_2) resulting in relaxor properties and finally it becomes cubic and paraelectric above 380°C.[3–5,8] BNT is a ferroelectric relaxor, which shows a gradual phase transition from RT rhombohedral ($R3c$) to tetragonal crystal structure between 200°C and 320°C.[6,7] It has been suggested that the transition from tetragonal to cubic phase does not occur until 620°C.[7]

Separate studies have been conducted on BKT and BNT, where Ti is replaced with Zr. The tetragonality of BKT has been found to prevail up to 5–11 mol% substitution of Zr for Ti[12,21], whereas pure $Bi_{0.5}K_{0.5}ZrO_3$ (BKZ) is found to be cubic $Pm\bar{3}m$.[12,22] A transition from rhombohedral to orthorhombic structure has been observed for BNT upon 58–60 mol% substitution of Zr for Ti.[21,23,24] The crystal structure of $Bi_{0.5}Na_{0.5}ZrO_3$ (BNZ) has been reported to be orthorhombic *Pnma*.[25]

The effect of Zr substitution on the piezoelectric and dielectric properties of BNT and BKT has not been reported to a large extent. A slight increase of the dielectric constant (ε') with 5–10 mol% substitution of Zr for Ti in BKT and BNT has been observed.[21,26] The piezoelectric coefficient (d_{33}) has been found to decrease from 68 to 40 pC/N when substituting 20 mol% Zr for Ti in BNT.[26]

Compositions near a morphotropic phase boundary (MPB) in a solid solution of two or more compounds are known to give enhanced piezoelectric properties, as in PZT where the MPB is found at a Zr:Ti ratio corresponding to 52:48.[27] An MPB in the systems BKT-BNT and BNT–BT has been reported at 16–20 mol% BKT and 6 mol% BT, respectively.[11,18] A general decrease of the transition temperatures relative to pure BNT is observed at the MPB in BKT-BNT, in addition to increased piezoelectric properties relative to both end-members.[10,11] The MPB in the above-mentioned materials is found in the composition region where the symmetry changes from tetragonal to rhombohedral.[27] Although the symmetry of the end-members in this study is orthorhombic (BNZ) and tetragonal (BKT), a BKT–BNZ solid solution could possibly involve an MPB or similar phenomena such as a "morphotropic phase".[1,28] No MPB has been reported close to pure BKT.

Here, we report on the solid-state synthesis and structural, dielectric, and piezoelectric properties of the $(1-x)$BKT–xBNZ materials system, which have not been reported on previously although BNZ was suggested as a ferroelectric already in 1961.[9] Both the large difference in tolerance factor and the different symmetry of the end-members suggest a possible MPB along the BKT–BNZ composition line.

II. Experimental Procedure

A conventional solid-state synthesis route was used to obtain dense ceramic samples of the composition $(1-x)$BKT - xBNZ with x = 0, 0.05, 0.10, 0.15, 0.20, 0.30, 0.40, and 0.50. Ceramics with x = 0.60, 0.70, 0.80, 0.90, and 1 were also prepared, but this samples could not prepared with sufficient density and phase purity. The precursors, Bi_2O_3 (99.9%; Aldrich, Steinheim, Germany), TiO_2 (99.9%; Aldrich), ZrO_2 (Tosoh, Shunan-shi, Yamaguchi, Japan), Na_2CO_3 (99.99%; Aldrich), and K_2CO_3 (99.99%; Aldrich) were first dried in a vacuum furnace (195°C, ~12 h). Stoichiometric amounts of precursors were mixed and ball-milled (24 h, isopropanol) using 5- mm yttrium-stabilized ZrO_2 balls. Prior to this, ZrO_2 was ball-milled by the same procedure, but separately, to break down ZrO_2 agglomerates. The calcination temperature was optimized for all compositions ranging from 700°C to 750°C, and the calcined powders were ball-milled by the same procedure as the precursor mixture. The calcined

---

S. E. Trolier-McKinstry—contributing editor

Manuscript No. 34300. Received December 31, 2013; approved May 10, 2014.
[†] Author to whom correspondence should be addressed. e-mail: grande@ntnu.no

powders were dried and sieved (250 μm sieve). Pellets (10 mm diameter) were prepared using uniaxial pressing (50–100 MPa) followed by cold isostatic pressing (200 MPa). The sintering temperature and time was optimized for all compositions to produce dense and phase pure ceramics. The pellets were surrounded with sacrificial powder inside an alumina crucible closed with a lid during sintering. Detailed calcination and sintering programs for each composition are summarized in Table I.

The relative density was taken as the ratio between the absolute density of the pellets, measured by Archimedes method [ISO 5017:1998(E)], and the theoretical density, calculated from lattice parameters determined as described below.

Crystal structure was studied using X-ray diffraction (XRD; Siemens D5005 diffractometer with CuK_α-radiation and secondary monochromator, Karlsruhe, Germany). The diffractograms were obtained from crushed sintered pellets annealed at 600°C for 12 h to relieve mechanical stresses introduced during crushing (no annealing was performed prior to XRD of $x = 0.9$ and 1.0). Lattice parameters of the investigated compositions were determined by Pawley refinement using the Topas software for $0 \leq x \leq 1$.[29] High-temperature XRD [HTXRD; Bruker D8Advance (Karlsruhe, Germany) with an mri high-temperature camera] of BKT ($x = 0$) was performed up to 600°C.

The microstructure of sintered ceramics was studied by scanning electron microscopy (SEM; Hitachi S-3400N, Ibaraki, Japan). Pellets were polished, thermally etched, and coated with carbon. The grain size was measured by the intercept method, measuring ~30 grains for each sample. The chemical composition of the samples was investigated using energy-dispersive X-ray spectroscopy (EDS; X-MAX, Oxford Instruments, Oxfordshire, UK).

The piezoelectric and dielectric characterization was performed using samples with ≥96% density. The samples were polished with grade #1200 silicon carbide grinding paper to thicknesses from 0.69 to 2.32 mm. Electrodes were applied on the pellet faces prior to electrical testing. Dosilac spray on silver electrode (Doduco, Pforzheim, Germany) was used for RT piezoelectric testing (cured at 200°C, 12 h). Sputtered gold electrodes were used for dielectric measurements at elevated temperatures.

Dielectric properties were characterized using a frequency analyzer (Alpha-A High Performance Frequency Analyzer; Novocontrol Technologies, Montabaur, Germany) connected to a heating unit (for $0.30 \leq x \leq 0.50$: combined furnace and electrode setup, Novotherm, Novocontrol Technologies; for $0 \leq x \leq 0.20$: tubular furnace with Probostat, NorECs, Oslo, Norway). All samples (both for dielectric and piezoelectric testing) were subject to a RT-scan at frequencies 10^7–10^{-2} Hz to confirm sufficient sample quality before further characterization. Two samples of each composition were initially tested and the sample with the lowest loss tangent was used for the piezoelectric measurements.

Dielectric spectroscopy at elevated temperatures (RT-600°C) was performed with constant heating rate (2°C/min) and a measurement was done every 30 s at frequencies 1–10^6 Hz with 1 V (AC).

Piezoelectric properties were determined by studying the electric field-induced polarization and strain response of the samples at RT, with the samples submerged in silicone fluid (Wacker AK 100; Drawin Vertriebs, Riemerling, Germany), using an aixPES - Piezoelectric Evaluation System (aixACCT, Aachen, Germany). All samples were subject to bipolar measurements with subsequent unipolar measurements at a constant frequency (0.25 Hz). Dielectric breakdown was typically observed for electric fields above 60 kV/cm.

III. Results

Dense ceramics in the composition region $0 \leq x \leq 0.50$ were successfully prepared by the conventional solid-state synthesis method. The calcination and sintering temperatures were optimized for all compositions and densities ≥96% were subsequently obtained for $0 \leq x \leq 0.50$ as summarized in Table I.

X-ray diffractograms of powder samples are shown in Fig. 1. The reflections can be indexed to the tetragonal or the cubic perovskite crystal structure for $x \leq 0.8$. The reflections shift to lower 2θ angles as the BNZ content increases, demonstrating an increasing size of the unit cell with increasing BNZ content. The increasing unit cell volume is confirmed by the unit cell parameters determined by Pawley refinement, as shown in Fig. 2 and listed in Table II. The unit cell of xBNZ ($x = 0$–0.10) was refined using the tetragonal $P4mm$ symmetry, in accordance with what is reported for BKT.[8] The diffractograms were refined using cubic $Pm\bar{3}m$ unit cell for xBNZ ($x = 0.15$–0.80), while BNZ ($x = 1$) was refined using the orthorhombic $Pnma$ unit cell.[25] At high BKT content no secondary phases could be observed by XRD, but from $x = 0.2$ traces of secondary phases could be observed. The ceramics with $x = 0.80$ and 1 contained a secondary phase suggested to be $Bi_2Zr_2O_7$ based on findings by EDS.[30]

Selected HTXRD diffractograms for pure BKT up to 600°C are shown in Fig. 3. The tetragonal splitting of the $(100)_{pc}$ diffraction line gradually vanishes and the tetragonal splitting is not possible to identify above 300°C in line with previous reports.[31]

The final density and grain size of the ceramics are summarized in Table I. The grain size increased slowly from $x = 0$ to 0.30 before a significant increase was seen for $x = 0.40$ and 0.50. SEM micrographs of the thermally etched pellets are presented in Fig. 4, demonstrating the significant grain size increase observed for $x = 0.50$. The micrographs also demonstrate that the grain size is not homogeneous due to exaggerated grain growth. The nominal chemical composition of all the compositions was confirmed by EDS.

Table I. Optimized Synthesis Temperatures and Relative Density and Grain Size for the $(1-x)$BKT–xBNZ Materials

Composition (x)	Calcination	Sintering	Density (%)	Grain size (μm)
0 (BKT)	700°C - 3 h	1060°C - 3 h	97 ± 0.6	0.2 ± 0.01
0.05	700°C - 3 h	1050°C - 10 h	97 ± 0.4	0.2 ± 0.02
0.10	700°C - 3 h	1050°C - 3 h	96 ± 0.9	0.3 ± 0.03
0.15	700°C - 3 h	1050°C - 10 h	98 ± 0.8	0.4 ± 0.01
0.20	700°C - 3 h	1050°C - 10 h	96 ± 0.7	0.5 ± 0.05
0.30	750°C - 3 h	1000°C - 10 h	96 ± 1	0.6 ± 0.06
0.40	750°C - 3 h	980°C - 10 h	96 ± 0.7	2.0 ± 0.1
0.50	750°C - 3 h	980°C - 10 h	96 ± 0.6	4.8 ± 0.5
0.60	750°C - 3 h	980°C - 10 h	92 ± 2	—
0.70	750°C - 3 h	980°C - 10 h	93 ± 0.5	—
0.80	750°C - 3 h	875°C - 3 h	96 ± 0.5	—
0.90	700-1050°C - 3 h	—	—	—
1 (BNZ)	750°C - 3 h	850°C - 3 h	96 ± 1	—

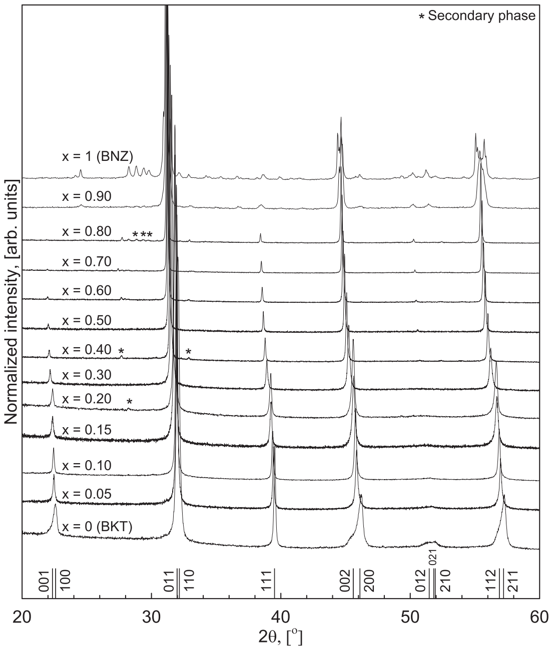

Fig. 1. X-ray diffractograms of sintered compositions $(1-x)$BKT–xBNZ ($x = 0$–1). The intensity is normalized to the maximum intensity. The lower indices refer to tetragonal BKT.

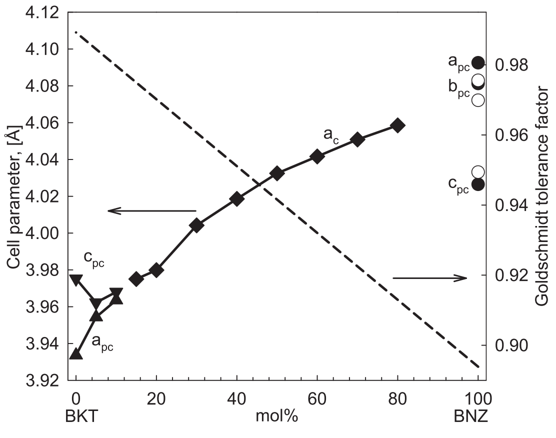

Fig. 2. Pseudo cubic (a_{pc}, b_{pc}, and c_{pc}) and cubic (a_c) unit cell parameters as a function of composition for $(1-x)$BKT–xBNZ ($c_{pc} = 2^{1/2}c_{orth}$). The orthorhombic unit cell parameters for $x = 1.0$ are normalized as follows; $a_{pc} = 2^{-1/2}a_{orth}$, $b_{pc} = 0.5b_{orth}$, and $c_{pc} = 2^{-1/2}c_{orth}$. Filled symbols from this work, open circles from elsewhere.[25] Also shown is the Goldschmidt tolerance factor (dashed line).[32]

The variation of the relative dielectric permittivity, ε', was investigated for $0 \leq x \leq 0.50$ with respect to temperature and frequency. Figures 5(a) and (b) show how ε' varies with temperature at 10 kHz. The ε' maximum (ε'_{max}) becomes less pronounced as the BNZ content exceed 15 mol% ($x = 0.15$), and for $x = 0.40$ and 0.50 it is difficult to establish the temperature at the maximum. The temperature of maximum relative permittivity (T_m) decreases with increasing BNZ content and $x = 0.15$ displays the highest ε' of 3507 at 255°C (10 kHz). The maximum value of ε' is given in Table II, together with T_m.

The frequency dependence of ε' and dielectric loss versus temperature for $x = 0.15$ are shown in Figs. 5(c) and (d), respectively. Relaxor type behavior is evident by the significant shift in ε' with frequency. The same behavior was observed for all compositions investigated. The room temperature ε' and dielectric losses as a function of frequency and composition for the samples used to characterize the piezoelectric properties are shown in Fig. 6.

The polarization versus applied electric field curves for $0 \leq x \leq 0.50$ compositions are displayed in Figs. 7(a) and (b). The maximum polarization (P_{max}) was obtained for the $x = 0.10$ composition with 20.5 μC/cm^2 at 60 kV/cm. The shape of the hysteresis loop did not depend on the maximum electric field in the range 25–60 kV/cm. The polarization decreased significantly and the hysteresis loop became gradually more closed as $x \rightarrow 0.50$ with $P_{max} = 4.4$ μC/cm^2 at 60 kV/cm for $x = 0.50$. The same trend was also apparent in strain versus electric field curves as shown in Figs. 7(c) and (d). The highest strain ($S_{max,b}$) obtained was 0.08 % for $x = 0.1$. Following the reduced polarization with increasing BNZ content, the strain was also significantly reduced. P_{max} and $S_{max,b}$ for all compositions are included in Table II together with the unipolar electric field-induced strain, where $S_{max,u}$ is the maximum obtained strain (with remanent strain subtracted) and E_{max} is the maximum applied electric field.

IV. Discussion

The dielectric and piezoelectric properties for xBNZ ($x = 0$–0.50) demonstrated a peak in performance for $x = 0.15$ and 0.10, respectively. These compositions coincide with the transition from tetragonal to cubic symmetry (Fig. 2). We have calculated the Goldschmidt tolerance factor, t, for the different compositions using the Shannon radii[32] with A and B cations of coordination number (CN) 12 and 6, respectively. For Bi CN = 8 was used, giving a tolerance factor for the present end-members of 0.99 (BKT) and 0.89 (BNZ). BKT loses its tetragonality at $t \approx 0.96$–0.98 when substituting with BKZ,[12,21] BFO,[13] KNN,[16] BS,[17] and BNT,[11,33,34] and $t = 0.98$ for $x = 0.1$. There is no consensus on the exact composition for the transition from tetragonal to cubic or rhombohedral symmetry in the BKT–BNT system.[34] A tentative structural phase diagram of the ternary reciprocal system BKT–BNZ is shown in Fig. 8. This is based on this study and literature data.[11,12,21,33–35] The diagram shows a dominating cubic/pseudo cubic region suggesting that significant substitution in the BKT–BNZ system is not beneficial. The tetragonal area of BKT is mainly constrained to the Ti-rich region of the diagram. This is the region with higher tolerance factor and corresponds to the t-range given above for which BKT loses its tetragonality. The loss of tetragonality occurs at $x \sim 0.10$ along the $(1-x)$BKT–xBNZ composition joint. This transition does not show the characteristics of an MPB as the tetragonal and orthorhombic phase regions are separated by a large area with cubic symmetry.

Figure 5(c) shows that T_m is a function of frequency for the $x = 0.15$ ceramics. The broad temperature and frequency dependence of ε' is typical of relaxor materials. However, our data are not sufficient to attribute the investigated materials to any specific class of relaxors (see e.g., Bokov and Ye[36]), hence relaxor-like is used. Relaxor-like behavior was maintained for all levels of BNZ substitution. The same has been observed when substituting BKT with BKZ, BS and BFO.[12,14,17] The dielectric dispersion increases as the BNZ content is increased along with the general decrease of ε' and T_m. These trends are most likely related to the structural development with composition.

RT dielectric constants of the ternary reciprocal BKT–BNZ materials system are summarized in Fig. 9. ε'_{RT} for BKT ($x = 0$) correspond to literature data (450–720).[5,12,33,37,38] It is apparent from the contour plot that the Ti-rich compositions exhibit the highest dielectric constants, and that addition of large amounts of Zr in general suppresses ε'_{RT}. The maximum ε'_{RT} observed for the BKT–BNT

Table II. Tabulated Unit Cell Parameters, Piezoelectric, and Dielectric Data for the (1 – x)BKT–xBNZ Materials System

	Cell parameters (Å)			P_{max}	$S_{max,b}$	$S_{max,u}/E_{max}$	ε'_{max}
Composition (x)	a	b	c	(μC/cm)	(%)	(pm/V)	@ 10 kHz
0 (BKT)	3.933 (3)	—	3.975 (4)	12	0.03	46	2575 (368°C)
0.05	3.954 (6)	—	3.962 (8)	14	0.04	62	2954 (319°C)
0.10	3.96 (2)	—	3.96 (2)	21	0.08	116	3296 (298°C)
0.15	3.975 (1)	—	—	13	0.04	61	3507 (255°C)
0.20	3.9799 (8)	—	—	14	0.04	61	2555 (233°C)
0.30	4.0042 (7)	—	—	10	0.02	36	1788 (212°C)
0.40	4.0186 (4)	—	—	7	0.01	16	1217 (232°C)
0.50	4.0325 (4)	—	—	4	0.01	9	906 (251°C)
0.60	4.0416 (3)	—	—	—	—	—	—
0.70	4.0508 (2)	—	—	—	—	—	—
0.80	4.0585 (3)	—	—	—	—	—	—
1 (BNZ)	5.787 (4)	8.162 (5)	5.694 (3)	—	—	—	—

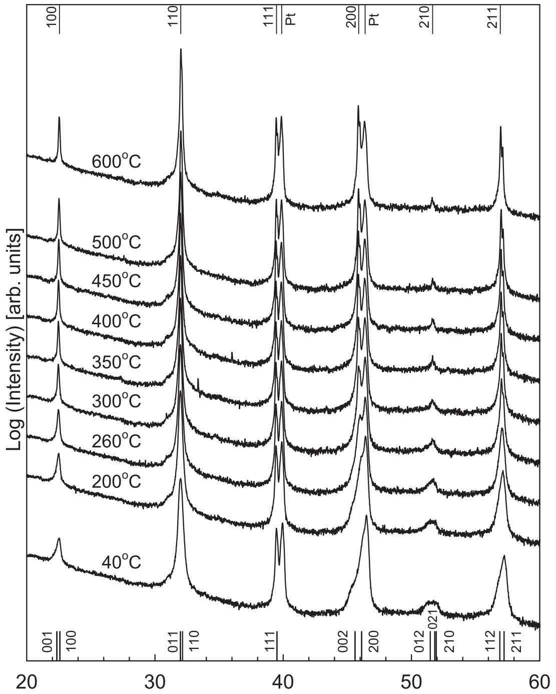

Fig. 3. X-ray diffractograms for BKT ($x = 0$) at selected temperatures. The lower indices refer to tetragonal BKT and upper indices to cubic BKT. The reflections due to the platinum sample stage is shown at ~39.8° and ~46.3°.

system is found near the MPB at ~20 mol% BKT in BNT.[10,33] A 15 mol% substitution of BNZ to BKT is currently the second best composition investigated in the ternary reciprocal BKT–BNZ system at RT.

Solid solutions of BKT–BNT (80% BNT), BKT–BFO (25% BFO), BKT–BNZ (15% BNZ) and BKT–BS (15% BS) all show similar ε'_{RT}, which is higher than the ε'_{RT} of the end-members.[10,12,14,16,17] The BKT–KNN and BKT–BKZ systems do not show any increase of the maximum ε' at elevated temperatures relative to BKT ($x = 0$) and are hence not seen as a viable alternative to improve the properties of BKT. At elevated temperatures the BKT–BNT and BKT–BFO solid solutions show an ε' two to three times higher than what is observed for BKT–BNZ and BKT–BS.

The relaxor behavior observed above ~300°C for BKT ($x = 0$) is in accordance with earlier reports.[12,17] Full-width half-maximum (FWHM) values of selected diffraction lines from the HTXRD experiment performed on BKT ($x = 0$, Fig. 3) are shown in Fig. 10(a). The data show an abrupt drop of FWHM near 300°C in agreement with where T_2 has been reported earlier followed by a more gradual decrease as the temperature rises to ~400°C.[3,8,31] The region between ~300°C and ~400°C is the pseudo cubic region of BKT where the relaxor behavior is observed.

The observed polarization and strain response to the applied electric field of BKT ($x = 0$) is in good accord with previous reports.[17,38] The increase of polarization and strain response is though much lower than what has been obtained both for the BKT–BFO and BKT–BNT systems.[10,13,14] The reduced opening of the hysteresis loops as x increases is attributed to the increasing cubic character of the materials with increasing BNZ content. Other solid solutions such as BKT–BFO also show reduced opening, but this is probably related to domain pinning.[1,13] Another factor to consider is that the average size of the A-site cation decreases while the average size of the B-site cation increases as more BNZ is added to BKT. This reduces the tolerance factor and the structure adapts by tilting the BO_6 octahedra (BNZ is orthorhombic due to octahedral tilting). This also reduces the structures ability to accommodate the ferroelectric displacement of Ti^{4+} which consequently reduces the overall ferroelectric response of the material.[39]

By examining the strain response of $0 \leq x \leq 0.50$ ceramics [Figs. 7(c) and (d)] it is apparent that the response becomes more electrostrictive as x increases, identified by the transition from ferroelectric butterfly loops to almost parabolic strain–electric field curves. The domain structure of the pseudo cubic phase observed for $0.15 \leq x \leq 0.50$ is probably a combination of a cubic matrix phase with embedded local polar nanodomains. These polar domains will provide piezoelectric response in an inherently cubic centrosymmetric matrix phase.[36] The nanodomains will disappear gradually as x increases and will eventually vanish completely, leaving behind a cubic paraelectric state where only electrostriction can be observed. The same gradual microstructural changes are observed as BKT ($x = 0$) is heated from RT to above T_C where disappearance of the ferroelectric domains occur gradually between 280°C and 450°C.[31] Tetragonal-to-pseudo cubic transition has also been suggested for BKT–BNT[40] [as referred by Ref. (34)], BKT–BKZ[12], BKT-BFO[13], and BKT–BS[17] solid solutions when moving away from the BKT rich region.

The P–E loops in Figs. 7(a) and (b) show a limited degree of saturation with some evidence of non-ferroelectric contributions due to dielectric loss at high fields. These losses will manifest as an overestimation of the polarization (Table II) but do not alter the observed trend between compositions. Measurements of polarization versus electric field strength

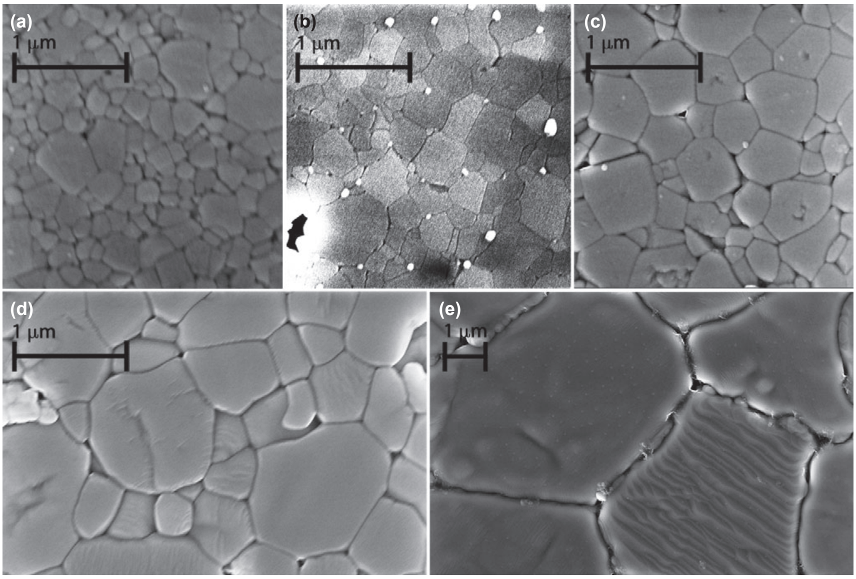

Fig. 4. SEM micrographs of thermally etched pellet surfaces, (a) BKT ($x = 0$); (b) 0.1BNZ; (c) 0.15BNZ; (d) 0.3BNZ; (e) 0.5BNZ (note larger scale).

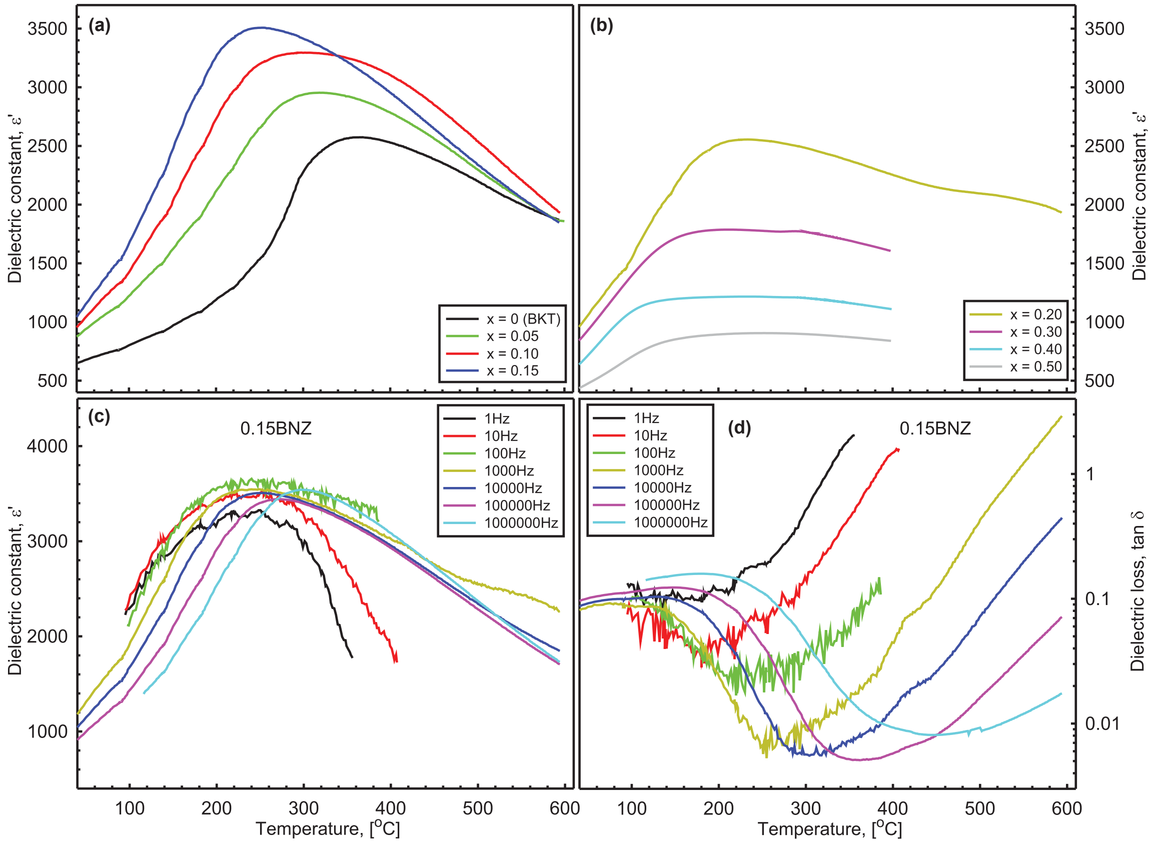

Fig. 5. Temperature dependence of the dielectric constant for $(1-x)$BKT–xBNZ ($x = 0$–0.5) at 10 kHz (a) and (b), and frequency and temperature dispersion of the dielectric permittivity and loss of 0.15BNZ (c) and (d).

were normally stopped at fields of 60 kV/cm as higher fields typically gave dielectric breakdown. One sample ($x = 0.05$) was exposed to 70 kV/cm and one ($x = 0.10$) was exposed to 80 kV/cm without any significant change of the hysteresis loop. As the coercive field of BKT is ∼50 kV/cm and the tetragonality is reduced with increasing BNZ content, it is

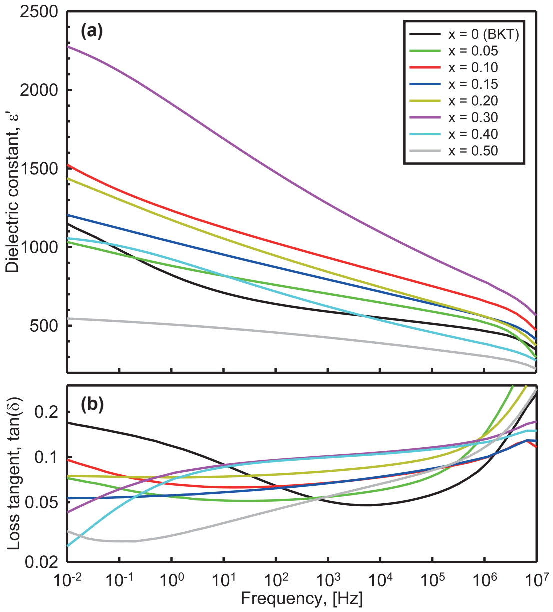

Fig. 6. Room temperature dielectric constant (a) and loss (b) as a function of frequency of the samples used for electromechanical testing for (1−*x*)BKT–*x*BNZ (*x* = 0–0.5).

proposed that the applied fields are sufficient to make the data relevant.[5,41] It should be noted that the increasing polarization observed with increasing BKT content is not a manifestation of losses.[42] There is no systematic indication when examining the dielectric loss of samples used for piezoelectric characterization that the observed polarization is manifestation of conductivity rather than real polarization, see Fig. 6.

The FWHM of two X-ray diffraction lines is shown as a function of *x*BNZ in Fig. 10(b). Both these diffraction lines show tetragonal splitting at ambient temperatures for pure BKT. A drop of FWHM is, as expected, observed at $x = 0.10$ where the transition from tetragonal to pseudo cubic crystal structure occurs. The increase of FWHM at $x = 0.15$ may be due to the polar nanodomains distributed throughout the cubic matrix phase. It is possible that these nanodomains introduce nonuniform stresses that may act to disturb the long range order seen by the X-rays and cause a "size effect" giving peak broadening. As the nanodomains gradually disappear, the "size effect" diminishes and the FWHM decrease down to a close to constant level at $x = 0.50$–0.80. It is also possible that there is a symmetry change for this composition that was not resolved by the XRD analysis, offering an alternative explanation to the broadening between $x = 0.15$ and 0.40.

It has been noted by others that densification of BKT during sintering is difficult and hot pressing has been suggested as one measure to overcome this.[5,38] Problems were not observed with respect to sinterability of BKT ($x = 0$) in this work. A study was conducted to first find the lowest calcination

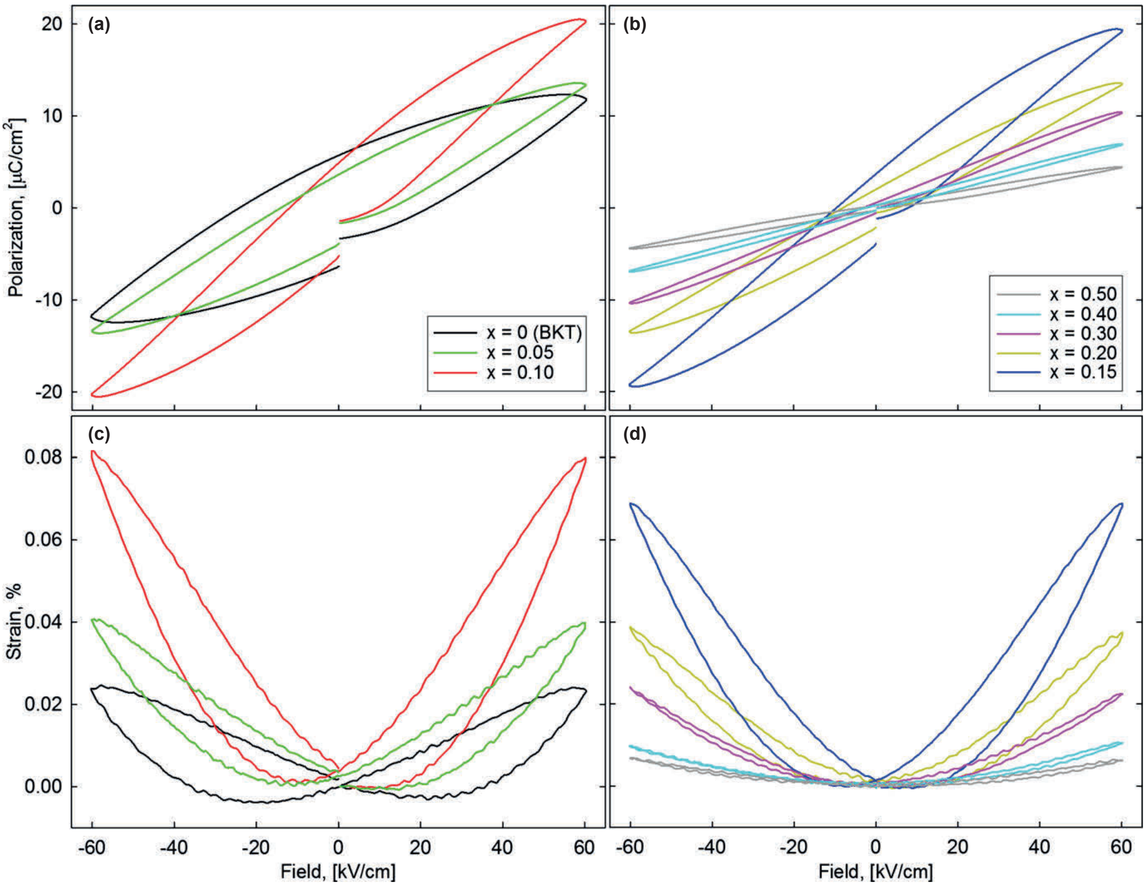

Fig. 7. Bipolar polarization (a) and (b), and strain (c) and (d) for sintered ceramics of composition (1−*x*)BKT–*x*BNZ (*x* = 0–0.5).

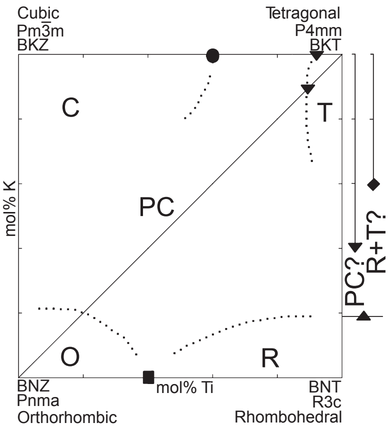

Fig. 8. Tentative structural phase diagram in the ternary reciprocal system BKT–BNZ based on reported crystal symmetries. Solid marks along the binary joints represent reported phase transitions (PC = pseudo cubic); circle PC-C,[12] triangle down T-PC[12] and[40] as reported by Ref. [34] and this work, diamond T-(R + T?),[33] triangle up (PC?)/(R + T?)/T-R[11,33] and[40] as reported by Ref. [34], and square R–O.[21,35] Dotted lines possible phase dominance areas.

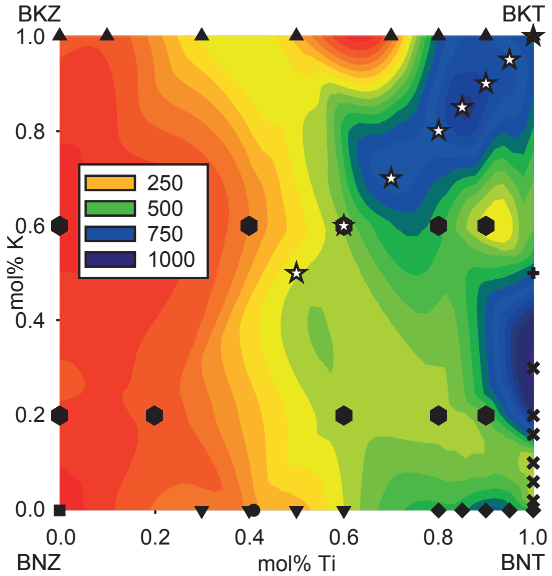

Fig. 9. Contour plot of RT dielectric constants in the BKT–BNZ system. Data are gathered from the following literature (frequency = 10 kHz if not stated otherwise): stars (this work), triangle up,[12] triangle down,[35] hexagons (100 kHz),[21] plus (1 MHz),[37] cross,[10] diamond,[26] square,[44] circle.[45]

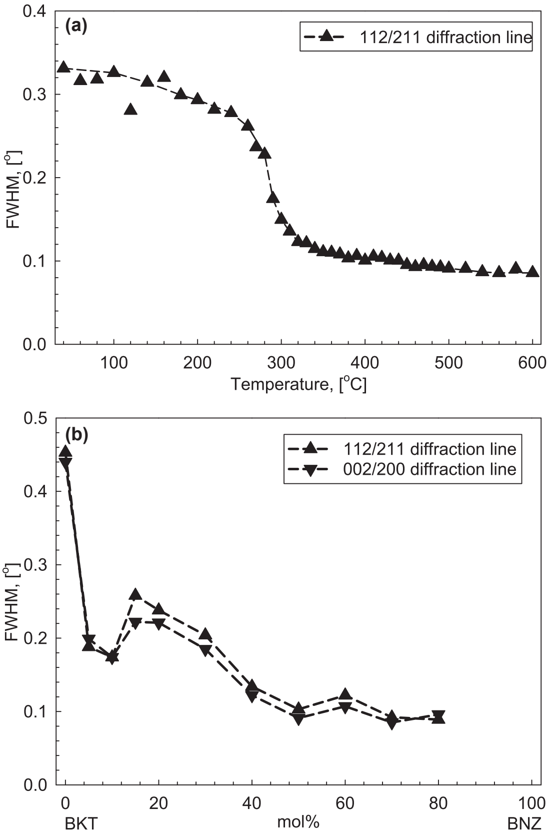

Fig. 10. FWHM of the (a) 112/211 XRD reflections as a function of temperature for BKT ($x = 0$) and (b) 112/211 and 002/200 XRD reflections as a function of composition of $(1-x)$BKT–xBNZ ($x = 0$-0.8). Dashed line added as guide to the eye.

temperature which gave a pure perovskite phase. A subsequent milling step was performed to obtain small particles, resulting in a higher driving force for densification during sintering. The resulting microstructure shows grain sizes similar to what has been reported elsewhere.[4,5] The grain size increases gradually for $0 \le x \le 0.30$ and then increases significantly for $x = 0.40$ and 0.50. As x increases from 0, the ratio of the alkali precursors K_2CO_3 and Na_2CO_3 approach their eutectic composition at 55–58 mol% Na_2CO_3 and the liquidus temperature of this carbonate mixture hence decreases with increasing BNZ content.[43] The liquidus temperature of the K_2CO_3 : Na_2CO_3 ratio in the precursor mixture for $x = 0.40$ and 0.50 is 746°C and 719°C, respectively, showing that the two materials, when calcined at 750°C, were made in the presence of a transient liquid, not as a purely solid-state synthesis. Such synthesis conditions allow for much higher ion mobility and may result in significant grain growth during calcination. The solidus and liquidus temperature of the carbonates in the precursor mixture for $x = 0.30$ is 750°C and 783°C, respectively, and hence only a very small amount of liquid can be expected at this composition and less grain growth is observed.[43]

Based on experimental results it is proposed that the transition from pseudo cubic to orthorhombic symmetry of the $(1-x)$BKT–xBNZ system occurs at $0.80 \le x \le 0.90$ as orthorhombic superstructure reflections were observed for $x = 0.90$. This transition range also corresponds to a similar tolerance factor to that of the rhombohedral–orthorhombic transition of BNT–BNZ. The dielectric and piezoelectric properties of $x = 0.60$–1.0 were not studied in detail due to the low response observed for $x = 0.5$ and the challenge to prepare materials with sufficient quality.

V. Conclusion

Dense and phase pure materials of the composition $(1-x)$ $Bi_{0.5}K_{0.5}TiO_3$–$xBi_{0.5}Na_{0.5}ZrO_3$ were fabricated using conventional solid-state synthesis. The route gave dense and fine-grained ceramics, also for pure BKT. The crystal structure was found to be tetragonal for $0 \le x \le 0.10$ and pseudo cubic for $0.15 \le x \le 0.80$. The piezoelectric and dielectric response to an applied electric field was investigated, showing relaxor-like behavior for all materials. The maximum dielectric performance was observed for $x = 0.15$ with $\varepsilon'_{\max} = 3507$ at 255°C and the maximum converse piezoelectric performance was observed for $x = 0.10$ with $S_{\max}/E_{\max} = 116$ pm/V. The functional properties in all show maximum performance in the composition region of phase transition from tetragonal to pseudo cubic crystal structure. This is in line with what has been observed for other BKT-based piezoelectrics, although not the best. The reported dielectric properties of the BKT–BNZ materials system demonstrated that the Ti-rich compositions show the highest performance. A tentative structural phase diagram for the reciprocal BKT–BNZ system was suggested based on reported crystal symmetries and shows a large pseudo cubic region for intermediate compositions. Although the functional properties of BKT were improved by BNZ substitution, the BKT–BNZ composition joint does not provide lead-free alternatives to PZT.

Acknowledgments

Dr. Sverre Magnus Selbach is acknowledged for suggesting BKT–BNZ as a possible novel piezoelectric materials system. The Research Council of Norway (FRINATEK project no. 197497/F20) is acknowledged for financial support.

References

[1] J. Rödel, W. Jo, K. T. P. Seifert, E. M. Anton, T. Granzow, and D. Damjanovic, “Perspective on the Development of Lead-Free Piezoceramics,” *J. Am. Ceram. Soc.*, **92** [6] 1153–77 (2009).

[2] “EU-DIRECTIVE 2011/65/EU: Restriction of the Use of Certain Hazardous Substances in Electrical and Electronic Equipment (RoHS),” *Off. J. Eur. Union.*, **54** [L174] 89–110 (2011).

[3] C. F. Buhrer, “Some Properties of Bismuth Perovskites,” *J. Chem. Phys.*, **36** [3] 798–803 (1962).

[4] Y. Hiruma, H. Nagata, and T. Takenaka, “Grain-Size Effect on Electrical Properties of $Bi_{0.5}K_{0.5}TiO_3$ Ceramics,” *Jpn. J. Appl. Phys. Pt. 1*, **46** [3A] 1081–4 (2007).

[5] Y. Hiruma, R. Aoyagi, H. Nagata and T. Takenaka, “Ferroelectric and Piezoelectric Properties of $Bi_{0.5}K_{0.5}TiO_3$ Ceramics,” *Jpn. J. Appl. Phys. Pt. 1*, **44** [7A] 5040–44 (2005).

[6] V. Dorcet, G. Trolliard, and P. Boullay, “Reinvestigation of Phase Transitions in $Na_{0.5}Bi_{0.5}TiO_3$ by TEM. Part I: First Order Rhombohedral to Orthorhombic Phase Transition,” *Chem. Mater.*, **20** [15] 5061–73 (2008).

[7] G. Trolliard and V. Dorcet, “Reinvestigation of Phase Transitions in $Na_{0.5}Bi_{0.5}TiO_3$ by TEM. Part II: Second Order Orthorhombic to Tetragonal Phase Transition,” *Chem. Mater.*, **20** [15] 5074–82 (2008).

[8] V. V. Ivanova, A. G. Kapyshev, Y. N. Venevtsev, and G. S. Zhdanov, “X-ray Determination of the Symmetry of Elementary Cells of the Ferroelectric Materials $(K_{0.5}Bi_{0.5})TiO_3$ and $(Na_{0.5}Bi_{0.5})TiO_3$ and of High-temperature Phase Transitions in $(K_{0.5}Bi_{0.5})TiO_3$,” *Izv. Akad. Nauk. SSSR*, **26**, 354–6 (1962).

[9] G. A. Smolenskii, V. A. Isupov, A. I. Agranovskaya, and N. N. Krainik, “New Ferroelectrics of Complex Composition IV,” *Sov. Phys. - Solid State*, **2** [11] 2651–4 (1961).

[10] Y. Hiruma, K. Yoshii, H. Nagata, and T. Takenaka, “Phase Transition Temperature and Electrical Properties of $(Bi_{0.5}Na_{0.5})TiO_3$-$(Bi_{0.5}A_{0.5})TiO_3$ (A=Li and K) Lead-Free Ferroelectric Ceramics,” *J. Appl. Phys.*, **103** [8] 084121, 7pp. (2008).

[11] A. Sasaki, T. Chiba, Y. Mamiya, and E. Otsuki, “Dielectric and Piezoelectric Properties of $(Bi_{0.5}Na_{0.5})TiO_3$-$(Bi_{0.5}K_{0.5})TiO_3$ Systems,” *Jpn. J. Appl. Phys. Pt. 1*, **38** [9B] 5564–7 (1999).

[12] M. Bengagi, F. Morini, M. El Maaoui, and P. Marchet, “Structure and Electrical Properties in the $K_{0.5}Bi_{0.5}TiO_3$-$K_{0.5}Bi_{0.5}ZrO_3$ Solid Solution (KBT-KBZ),” *Phys. Status Solidi A*, **209** [10] 2063–72 (2012).

[13] M. I. Morozov, M.-A. Einarsrud, and T. Grande, “Polarization and Strain Response in $Bi_{0.5}K_{0.5}TiO_3$-$BiFeO_3$ Ceramics,” *Appl. Phys. Lett.*, **101** [25] 252904, 4pp. (2012).

[14] M. I. Morozov, M.-A. Einarsrud, T. Grande, and D. Damjanovic, “Lead-Free Relaxor-Like $0.75Bi_{0.5}K_{0.5}TiO_3$ - $0.25BiFeO_3$ Ceramics with Large Electric Field-Induced Strain,” *Ferroelectrics*, **439** [1] 88–94 (2012).

[15] Y. Hiruma, R. Aoyagi, H. Nagata, and T. Takenaka, “Piezoelectric Properties of $BaTiO_3$ - $(Bi_{0.5}K_{0.5})TiO_3$ Ferroelectric Ceramics,” *Jpn. J. Appl. Phys. Pt. 1*, **43** [11A] 7556–9 (2004).

[16] H. L. Du, W. C. Zhou, F. Luo, D. M. Zhu, S. B. Qu, Y. Li, and Z. B. Pei, “Polymorphic Phase Transition Dependence of Piezoelectric Properties in $(K_{0.5}Na_{0.5})NbO_3$-$(Bi_{0.5}K_{0.5})TiO_3$ Lead-Free Ceramics,” *J. Phys. D. Appl. Phys.*, **41** [11] 115413, 5pp. (2008).

[17] L. Martin-Arias, A. Castro, and M. Alguero, “Ferroelectric Phases and Relaxor States in the Novel Lead-Free $(1-x)(Bi_{0.5}K_{0.5})TiO_3$-$xBiScO_3$ System ($0 \le x \le 0.3$),” *J. Mater. Sci.*, **47** [8] 3729–40 (2012).

[18] T. Takenaka, K. Maruyama, and K. Sakata, “$(Bi_{0.5}Na_{0.5})TiO_3$ - $BaTiO_3$ System for Lead-Free Piezoelectric Ceramics,” *Jpn. J. Appl. Phys. Pt. 1*, **30** [9B] 2236–9 (1991).

[19] R. Z. Zuo, X. S. Fang, and C. Ye, “Phase Structures and Electrical Properties of New Lead-Free $(Na_{0.5}K_{0.5})NbO_3$-$(Bi_{0.5}Na_{0.5})TiO_3$ Ceramics,” *Appl. Phys. Lett.*, **90** [9] 092904, 3pp. (2007).

[20] T. Takenaka, T. Okuda, and K. Takegahara, “Lead-Free Piezoelectric Ceramics Based on $(Bi_{0.5}Na_{0.5})TiO_3$-$NaNbO_3$,” *Ferroelectrics*, **196** [1–4] 495–8 (1997).

[21] Y. Yamada, T. Akutsu, H. Asada, K. Nozawa, S. Hachiga, T. Kurosaki, O. Ikagawa, H. Fujiki, et al., “Effect of B-Ions Substitution in $[(K_{0.5}Bi_{0.5})$-$(Na_{0.5}Bi_{0.5})](Ti\text{-}B)O_3$ System with B = Zr, $Fe_{1/2}Nb_{1/2}$, $Zn_{1/3}Nb_{2/3}$ or $Mg_{1/3}Nb_{2/3}$,” *Jpn. J. Appl. Phys. Pt. 1*, **34** [9B] 5462–6 (1995).

[22] S. Ivanov, ICDD Grant-in-Aid, Technical Report 00-057-0823, Karpov Institute of Physical Chemistry (2005).

[23] A. Rachakom, P. Jaiban, S. Jiansirisomboon, and A. Watcharapasorn, “Crystal Structure and Electrical Properties of Bismuth Sodium Titanate Zirconate Ceramics,” *Nanoscale. Res. Lett.*, **7** 57, 5pp. (2012).

[24] L. Kumari, K. Kumari, K. Prasad, and R. N. P. Choudhary, “Impedance Spectroscopy of $(Na_{0.5}Bi_{0.5})(Zr_{0.25}Ti_{0.75})O_3$ Lead-Free Ceramic,” *J. Alloy. Compd.*, **453** [1–2] 325–31 (2008).

[25] P. Jaiban, A. Rachakom, S. Buntham, S. Jiansirisomboon, and A. Watcharapasorn, “Fabrication of $Bi_{0.5}Na_{0.5}ZrO_3$ Powder by Mixed Oxide Method,” *Mater. Sci. Forum*, **695**, 49–52 (2011).

[26] A. Watcharapasorn and S. Jiansirisomboon, “Dielectric and Piezoelectric Properties of Zirconium-Doped Bismuth Sodium Titanate Ceramics,” *Adv. Mat. Res.*, **55–57**, 133–6 (2008).

[27] D. A. Berlincourt, C. Cmolik, and H. Jaffe, “Piezoelectric Properties of Polycrystalline Lead Titanate Zirconate Compositions,” *P. IRE.*, **48** [2] 220–9 (1960).

[28] N. Zhang, H. Yokota, A. M. Glazer, and P. A. Thomas, “Neutron Powder Diffraction Refinement of $PbZr_{1-x}Ti_xO_3$,” *Acta Cryst. B*, **67** [5] 386–98 (2011).

[29] Bruker AXS, “Topas,” Version 4.2 (2009), URL http://www.bruker-axs.com.

[30] S. L. Sorokina and A. W. Sleight, “New Phases in the ZrO_2-Bi_2O_3 and HfO_2-Bi_2O_3 Systems,” *Mater. Res. Bull.*, **33** [7] 1077–81 (1998).

[31] M. Otoničar, S. D. Škapin, B. Jančar, R. Ubic, and D. Suvorov, “Analysis of the Phase Transition and the Domain Structure in $K_{0.5}Bi_{0.5}TiO_3$ Perovskite Ceramics by *in situ* XRD and TEM,” *J. Am. Ceram. Soc.*, **93** [12] 4168–73 (2010).

[32] R. D. Shannon, “Revised Effective Ionic-Radii and Systematic Studies of Interatomic Distances in Halides and Chalcogenides,” *Acta Crystallogr., Sect. A: Found. Crystallogr.*, **32** [Sep 1] 751–67 (1976).

[33] O. Elkechai, M. Manier, and J. P. Mercurio, “$Na_{0.5}Bi_{0.5}TiO_3$-$K_{0.5}Bi_{0.5}TiO_3$ (NBT-KBT) System: A Structural and Electrical Study,” *Phys. Status Solidi A*, **157** [2] 499–506 (1996).

[34] J. Kreisel, A. M. Glazer, G. Jones, P. A. Thomas, L. Abello, and G. Lucazeau, “An X-ray Diffraction and Raman Spectroscopy Investigation of A-Site Substituted Perovskite Compounds: The $(Na_{1-x}K_x)_{0.5}Bi_{0.5}TiO_3$ ($0 \le x \le 1$) Solid Solution,” *J. Phys.: Condens. Matter.*, **12** [14] 3267–80 (2000).

[35] P. Jaiban, A. Rachakom, S. Jiansirisomboon, and A. Watcharapasorn, “Influences of Phase Transition and Microstructure on Dielectric Properties of $Bi_{0.5}Na_{0.5}Zr_{1-x}Ti_xO_3$ Ceramics,” *Nanoscale Res. Lett.*, **7** [1] 45, 5pp. (2012).

[36] A. A. Bokov and Z.-G. Ye, “Recent Progress in Relaxor Ferroelectrics with Perovskite Structure,” *J. Mater. Sci.*, **41** [1] 31–52 (2006).

[37] M. Otoničar, S. D. Škapin, M. Spreitzer, and D. Suvorov, “Compositional Range and Electrical Properties of the Morphotropic Phase Boundary in the $Na_{0.5}Bi_{0.5}TiO_3$-$K_{0.5}Bi_{0.5}TiO_3$ System,” *J. Eur. Ceram. Soc.*, **30** [4] 971–9 (2010).

[38] T. Wada, A. Fukui, and Y. Matsuo, “Preparation of $(K_{0.5}Bi_{0.5})TiO_3$ Ceramics by Polymerized Complex Method and Their Properties,” *Jpn. J. Appl. Phys. Pt. 1*, **41** [11B] 7025–8 (2002).

[39] V. A. Shuvaeva, D. Zekria, A. M. Glazer, Q. Jiang, S. M. Weber, P. Bhattacharya, and P. A. Thomas, “Local Structure of the Lead-Free Relaxor Ferroelectric $(K_xNa_{1-x})_{0.5}Bi_{0.5}TiO_3$,” *Phys. Rev. B*, **71** [17] 174114, 8pp. (2005).

[40] I. P. Pronin, N. N. Parfenova, N. V. Zaitseva, V. A. Isupov, and G. A. Smolenskii, “Phase Transitions in Solid Solutions of Sodium-bismuth and Potassium-bismuth Titanates,” *Sov. Phys.-Solid State*, **24**, 1060–2 (1982).

[41] A. B. Kounga, S. T. Zhang, W. Jo, T. Granzow, and J. Rodel, “Morphotropic Phase Boundary in $(1-x)Bi_{0.5}Na_{0.5}TiO_3$-$xK_{0.5}Na_{0.5}NbO_3$ Lead-Free Piezoceramics,” *Appl. Phys. Lett.*, **92** [22] 222902, 3pp (2008).

[42] J. F. Scott, “Ferroelectrics Go Bananas,” *J. Phys.-Condens. Mat.*, **20** [2] 021001, 2pp. (2008).

[43] A. Reisman, “Heterogeneous Equilibria in the System K_2CO_3-Na_2CO_3,” *J. Am. Chem. Soc.*, **81** [4] 807–11 (1959).

[44] Lily, K. Kumari, K. Prasad, and K. L. Yadav, “Dielectric and Impedance Study of Lead-Free Ceramic: $(Na_{0.5}Bi_{0.5})ZrO_3$,” *J. Mater. Sci.* , **42** [15] 6252–9 (2007).

[45] P. Jaiban, S. Jiansirisomboon, and A. Watcharapasorn, “Effect of Lanthanum Substitution on Microstructure and Electrical Properties of $(Bi_{0.5}Na_{0.5})_{1-1.5x}La_xTi_{0.41}Zr_{0.59}O_3$ Ceramics,” *Ceram. Int.*, **38**, S379–83 (2012). □

PCCP

PAPER

View Article Online
View Journal | View Issue

Cite this: Phys. Chem. Chem. Phys., 2015, 17, 9420

Electrical conductivity and thermopower of $(1 - x)$ $BiFeO_3 - xBi_{0.5}K_{0.5}TiO_3$ ($x = 0.1, 0.2$) ceramics near the ferroelectric to paraelectric phase transition

E. T. Wefring, M.-A. Einarsrud and T. Grande*

Received 16th January 2015,
Accepted 2nd March 2015

DOI: 10.1039/c5cp00266d

www.rsc.org/pccp

Ferroelectric $BiFeO_3$ has attractive properties such as high strain and polarization, but a wide range of applications of bulk $BiFeO_3$ are hindered due to high leakage currents and a high coercive electric field. Here, we report on the thermal behaviour of the electrical conductivity and thermopower of $BiFeO_3$ substituted with 10 and 20 mol% $Bi_{0.5}K_{0.5}TiO_3$. A change from p-type to n-type conductivity in these semi-conducting materials was demonstrated by the change in the sign of the Seebeck coefficient and the change in the slope of the isothermal conductivity *versus* partial pressure of O. A minimum in the isothermal conductivity was observed at $\sim 10^{-2}$ bar O_2 partial pressure for both solid solutions. The strong dependence of the conductivity on the partial pressure of O_2 was rationalized by a point defect model describing qualitatively the conductivity involving oxidation/reduction of Fe^{3+}, the dominating oxidation state of Fe in stoichiometric $BiFeO_3$. The ferroelectric to paraelectric phase transition of 80 and 90 mol% $BiFeO_3$ was observed at 648 ± 15 and 723 ± 15 °C respectively by differential thermal analysis and confirmed by dielectric spectroscopy and high temperature powder X-ray diffraction.

1. Introduction

Legislations, prohibiting the use of lead in electronics, have been passed by the European Union and other countries due to environmental concerns.[1,2] Lead-free piezoelectric materials have therefore received significant interest in recent years to replace the state of the art lead-containing piezoelectric $Pb(Zr,Ti)O_3$ (PZT).[2] Bismuth containing perovskite-based materials are among the most promising lead-free alternatives, and among these bismuth ferrite, $BiFeO_3$ (BFO), and bismuth potassium titanate, $Bi_{0.5}K_{0.5}TiO_3$ (BKT), have been investigated intensively.[2,3] BFO with a rhombohedral structure has attracted tremendous interest due to its multiferroic properties,[3,4] including the potential as a ferro- or piezoelectric material with high polarization, lattice strain and Curie temperature (T_C, 830 °C), the latter being important for high temperature applications.[5–7] The prospects of applying BFO are though hampered by parasitic secondary phases formed during synthesis,[8,9] and a high coercive electric field and high dielectric losses stemming from conductivity.[3,10] BKT is a tetragonal ferroelectric which shows a relatively high piezoelectric constant and T_C (380 °C).[11,12] Challenges with the fabrication of dense BKT ceramics have been reported[13] but dense single phase materials can be obtained by solid state synthesis.[14] BKT is also an important constituent in solid solution systems, which may possess a morphotropic phase boundary (MPB) similar to the one known for PZT.[2]

Solid solutions of BFO and BKT have recently been investigated due to a possible MPB.[12,13,15–20] Solid solutions of BFO with BKT suppresses the formation of the parasitic phases well known in pure BFO and phase pure BFO–BKT materials are obtain by conventional solid state synthesis.[8,15] BFO–BKT materials are isostructural with BFO at a high BFO content. A maximum in the dielectric and electromechanical properties is reported at 25 mol% BFO, and the piezoelectric properties such as electric field induced polarization and strain decreases towards a high BFO content.[15,17] This is probably due to the high coercive electric field and dielectric loss of BFO relative to that of BKT.[5,13] Morozov *et al.* have recently shown that the conductivity of BFO–BKT materials can be reduced by annealing in an inert atmosphere improving the electromechanical performance.[20] A Maxwell–Wagner type relaxation in BFO–BKT, coupled to the electrical conductivity and point defects, has also been reported.[21]

One of the main challenges with to BFO is the high electrical conductivity giving rise to dielectric loss.[3] Pure and acceptor substituted BFO shows the characteristics of p-type conductivity in air, relating conductivity to the presence of Fe^{4+}.[22–26] The conductivity of 0.7BFO–0.3BKT can be manipulated by thermal treatment in an oxidizing or an inert atmosphere.[20,21] The aliovalent

---

Department of Materials Science and Engineering, Norwegian University of Science and Technology, Trondheim, 7491 Trondheim, Norway. E-mail: grande@ntnu.no

substitution of Fe^{3+} with *e.g.* Ti^{4+} and Ni^{2+} on the perovskite B site has profound effect on the conductivity of BFO[27–29] where tetravalent cations reduce the conductivity and divalent cations increase the conductivity. Particularly, substitution with Ti has shown great promise to reduce the conductivity of BFO.[27,29,30] The observed effects are discussed in relation to the presence of Fe^{2+} and oxygen vacancies, and coulometric titration has shown that 2 mol% Fe^{2+} can be present in BFO before decomposition of BFO occurs under reducing conditions.[31] However, the effect of the presence of Fe^{2+} on the conductivity of bulk BFO has yet to be established.

Evaporation of Bi_2O_3 during synthesis increases the point defect concentration in BFO materials.[10] Bi vacancies can be charge compensated by oxygen vacancies or oxidation of Fe^{3+}. The presence of multivalent Fe will strongly influence the electrical conductivity of BFO, as it depends on small polaron hopping.[27,28,32] P-type (in air) and n-type (reducing conditions) semiconductor behaviour has previously been reported for several related Fe-containing perovskites, including $La_{1-x}Sr_xFeO_{3-\delta}$[33–35] and $LnFeO_3$ (Ln = Pr, Nd, Sm, Eu and Gd).[36,37] In these materials the electronic conductivity is strongly linked to polaron hopping and the oxidation state of Fe, which is strongly dependent on the partial pressure of oxygen ($p(O_2)$).

Here we report on the electrical conductivity and thermopower of BFO substituted with 10 and 20 mol% BKT. This solid solution was chosen as the model system to obtain physical insight into the electrical conductivity of BFO-based materials, avoiding the influence of secondary phases typically found in pure bulk BFO. We provide experimental evidence for the change of the conductivity from p-type to n-type when going from oxidizing to inert conditions, demonstrating clearly for the first time why the electrical conductivity can be minimized by annealing at controlled partial pressure of oxygen. The ferroelectric phase transition of the materials is investigated by high temperature X-ray diffraction, dielectric spectroscopy/electrical conductivity and differential thermal analysis. Finally, a conventional point defect model is applied to describe the dependence of the electrical conductivity on $p(O_2)$.

2. Experimental

Ceramics with composition $(1-x)$ $BiFeO_3$ – $xBi_{0.5}K_{0.5}TiO_3$ (x = 0.2, 0.1, denoted 0.8BFO and 0.9BFO) were prepared by solid state synthesis as reported by Morozov *et al.*[17] Stoichiometric amounts of dried Bi_2O_3 (Aldrich, 99.9% or 99,99%), K_2CO_3 (Aldrich, 99.99%), TiO_2 (Aldrich, 99.9% or 99,99%) and Fe_2O_3 (Aldrich, 99.999%) precursors were mixed and ball milled in isopropanol (18 h). The precursor mixture was calcined (5 h) in air at 820 °C (x = 0.2) and 800 °C (x = 0.1). The calcined powders were ball milled in isopropanol (18 h), dried and sieved (250 μm sieve), and further pressed into pellets/bars by uniaxial pressing and cold isostatic pressing (200 MPa). The samples were sintered in air (2 h) covered by a sacrificial powder at 1010 °C (x = 0.2) and 980 °C (x = 0.1). Powders for X-ray diffraction (XRD) were prepared by crushing the sintered pellets followed by annealing the powders above the Curie temperature.

The density of the materials was measured by the Archimedes method (ISO 5017:1998(E)) and the relative density was calculated with respect to the crystallographic density determined by XRD. The grain size was determined by the intercept method from polished and thermally etched samples (880 °C, 5 min) using a scanning electron microscope (SEM; Hitachi S-3400N).

Electronic conductivity was measured using a direct current (DC) four-point method, as previously described by Wærnhus *et al.*[38] The surface of sintered bars was ground using a grade #220 silicon carbide grinding paper to dimensions of about 22 × 4.5 × 3 mm. A constant voltage was applied over the current circuit and the distance between the voltage electrodes on the sample was 5 mm. Pt-paste was used to ensure sufficient contact between the current electrodes and the sample. The DC electrical conductivity was measured at 700, 750 and 800 °C at a constant $p(O_2)$. The temperature was reduced to 650 °C before a new $p(O_2)$ was introduced. The conductivity relaxation was observed and the conductivity was allowed to stabilize under the specific conditions before the temperature or the atmosphere was altered. The temperature was measured by using an S-type thermocouple and the partial pressure of oxygen (O_2, 0.2, 0.02, 0.002, N_2) was controlled by mixing O_2 and N_2 (Yara Praxair, 5.0) at flow rates of 50, 250 or 500 mL min^{-1}.

The Seebeck-coefficient (Q) was measured at 650, 700, 750 and 800 °C using a ProboStat™ setup (NorECs AS) in a vertical tubular furnace with a vertical bar analogous to the bar used to measure the electrical conductivity. The temperature gradient was measured by two S-type thermocouples (20–25 °C) and the voltage across the sample was measured using Pt-electrodes. The atmosphere was varied by manual flow control of O_2, N_2 and synthetic air (Yara Praxair, 5.0).

Dielectric properties were investigated in synthetic air (Yara Praxair, 5.0) using a frequency analyzer (Alpha-A High Performance Frequency Analyser, Novocontrol Technologies) connected to a ProboStat™ setup in a vertical tubular furnace. Gold electrodes were sputtered onto ground and cleaned faces of a sintered pellet, and measurements were performed during continuous heating/cooling (2 °C min^{-1}) every 30 second at frequencies 1–10^6 Hz. The electroded sample was first heated/cooled to/from 400 °C to remove Maxwell–Wagner contributions to the permittivity.[21] The reported data are obtained from the 2nd heating cycle to 720 °C and 800 °C for 0.8BFO and 0.9BFO, respectively.

High temperature X-ray diffraction (HTXRD) was performed using a θ–θ Bruker D8 ADVANCE diffractometer utilizing Cu K_α radiation and a VANTEC-1 position sensitive detector. Powders for investigation were contained within an alumina sample holder and heated using a radiant heater mounted within an MRI Physikalische Geräte GmbH high temperature camera. Calibration of the system against an Al_2O_3 standard gave an estimated temperature error of ±15 °C. Diffraction patterns were collected from room temperature to 760 °C (every 50 degrees up to 510 °C, every 10 degrees above 510 °C), across an angular range 20–75° 2θ with a step size of 0.016° (1 second/step).

Lattice parameters for each diffraction pattern were determined by Pawley fitting using the Topas software.[39] A hexagonal model (*R3c*) was adopted below the Curie temperature and a cubic model ($Pm\bar{3}m$) above, as previously described for $BiFeO_3$ and Mn-doped $BiFeO_3$.[40,41] Peak shapes were described using a Pseudo-Voigt model (TCHZ) and a Chebychev polynomial background function was used. Sample displacement and lattice parameters were refined for each temperature.

Differential thermal analysis (DTA) was used to determine the ferroelectric to paraelectric phase transition (STA 449 C, Netzsch). The powder used for DTA was prepared the same way as the powder for XRD, from the same sintered pellet. The powder was packed in alumina crucibles and heated to 750 °C (0.8BFO) and 800 °C (0.9BFO) at 10 °C min^{-1} in synthetic air (30 mL min^{-1}). The samples were kept at T_{max} for 5 minutes before cooling.

3. Results

Dense (97 ± 1% of theoretical density) and phase pure ceramics with compositions 0.8BFO and 0.9BFO were successfully prepared by conventional solid state synthesis. No secondary phases could be observed in the sintered specimens by X-ray diffraction in agreement with previous work.[17] The microstructure of the dense and single phase materials, shown in Fig. 1, is relatively homogeneous with the submicron grain size (Table 1). No evidence for the presence of any secondary phases could be observed by SEM/back scattered electrons. The room temperature unit cell parameters determined from the diffraction pattern (not shown) are given in Table 1.

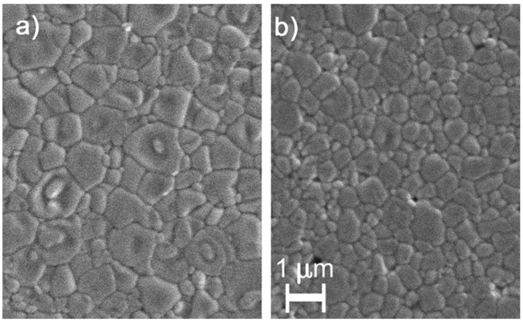

Fig. 1 SEM micrographs (secondary electrons) of polished and thermally etched 0.8BFO (a) and 0.9BFO (b) ceramics.

The DC electrical conductivity of 0.8BFO and 0.9BFO is shown as a function of temperature and $p(O_2)$ in Fig. 2a and b, respectively. The conductivity increases with increasing BFO content, reflecting a higher conductivity of BFO relative to BKT,[42,43] and it increases with increasing temperature in line with a semiconductor behaviour. A distinct minimum in the isothermal conductivity *versus* $\log p(O_2)$, typical for the p-type to n-type transition of oxide semiconductors, is evident for both compositions. P-type conductivity is characteristic for the materials in oxidizing atmosphere, while n-type is typical for inert or reducing conditions. A similar p-type behaviour is observed for Ca-substituted, $BiFeO_3$,[26] but the minimum in the conductivity as well as the n-type conductivity in bulk BFO-materials has not been reported previously.

While the materials were single phase after sintering, it is worth noting that an Fe/Ti-rich secondary phase was observed on the surface of the materials after a long period of electrical DC conductivity measurement (640 and 770 hours for 0.8BFO and 0.9BFO respectively). The formation of the secondary phase on the surface is most likely related to the loss of Bi_2O_3 during the measurements as shown previously for pure BFO.[4]

The Seebeck coefficients in the temperature range 650–800 °C in three different atmospheres, shown in Fig. 3, demonstrate clearly the p-type conductivity in air and oxygen and n-type conductivity in an inert atmosphere. The negative Seebeck coefficient is to the author's knowledge the first direct evidence for n-type conductivity of bulk BFO-rich materials. The positive Seebeck coefficient for BFO at 650 °C in air has been reported as ~600 μV K^{-1} in reasonable agreement with the present data. It is clear that the Seebeck coefficient increases with increasing BKT content.[43]

The real part of the permittivity of 0.8BFO during heating (10 kHz, 100 kHz, 1 MHz) and cooling (10 kHz) in synthetic air is shown in Fig. 4a. No temperature dispersion of the maximum

Table 1 Lattice parameters, grain size and phase transition temperature of 0.8BFO and 0.9BFO

		0.8BFO	0.9BFO
Room temperature lattice parameters	*a* [Å]	5.591(8)	5.584(6)
	c [Å]	13.80(6)	13.840(8)
Grain size	[μm]	0.9 ± 0.05	0.6 ± 0.03
Permittivity heating	Temp. of perm. max [°C] 10 kHz	675 ± 15	—
Permittivity cooling		620 ± 15	—
Phase transition HTXRD	[°C]	630 ± 15	676 ± 15
DTA heating	Peak onset [°C]	648 ± 15	723 ± 10
	Peak max [°C]	680 ± 1	746 ± 1
DTA cooling	Peak onset [°C]	641 ± 5	743 ± 10
	Peak min [°C]	619 ± 1	713 ± 1

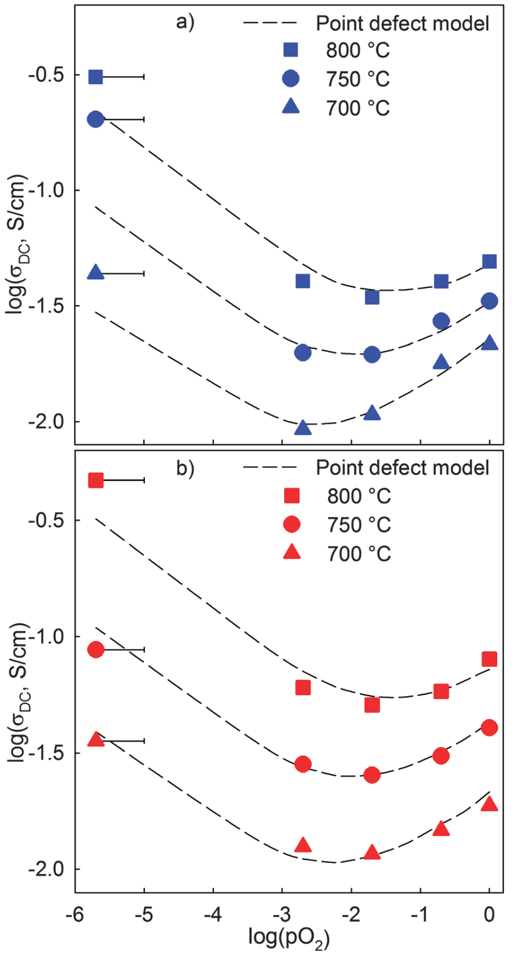

Fig. 2 DC conductivity of 0.8BFO (a) and 0.9BFO (b) as a function of $p(O_2)$ at 700, 750 and 800 °C. The dashed lines are the conductivity calculated by the point defect model introduced in the discussion section. The uncertainty associated with the $p(O_2)$ in N_2 is shown by error bars.

permittivity ($\varepsilon'_{\max}$) is observed during heating, pointing to a true ferroelectric phase transition in line with what is previously reported.[21] The temperature of $\varepsilon'_{\max}$ is included in Table 1. The shift in the maximum permittivity observed during cooling points to a first order phase transition. Permittivity data for 0.9BFO are not reported due to the high conductivity of this particular material close to the phase transition.

The real part of the AC conductivity (10 kHz) during heating is shown for 0.8BFO and 0.9BFO in Fig. 4b. The conductivity increases with temperature and changes slope around 240 °C and in the temperature range of the ferroelectric to paraelectric phase transition for all frequencies. The DC conductivity measured during heating is in good accordance with the data measured under isothermal conditions (Fig. 2).

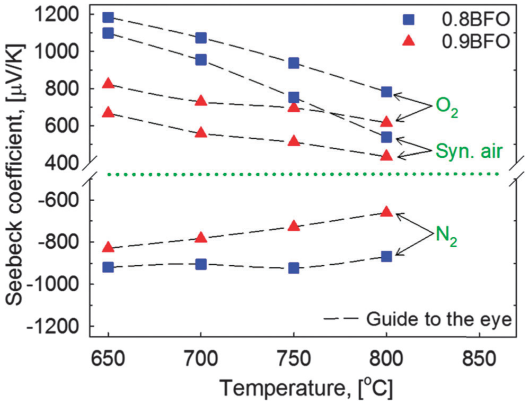

Fig. 3 The Seebeck coefficient of 0.8BFO and 0.9BFO as a function of temperature in three different atmospheres.

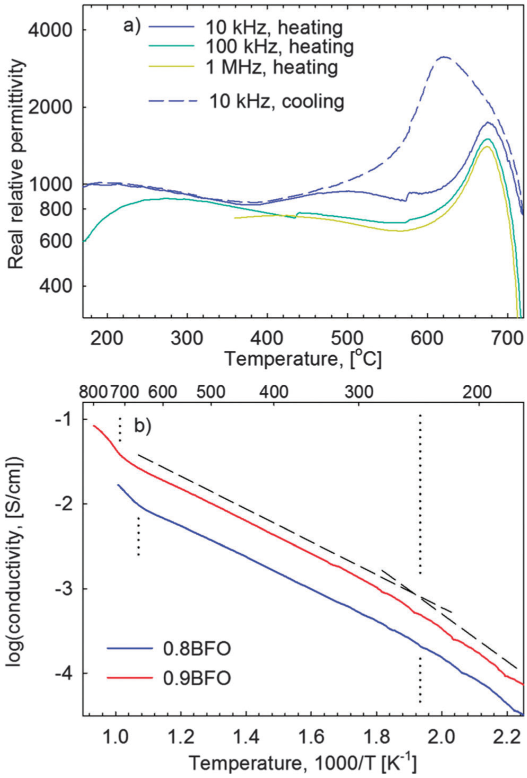

Fig. 4 The real permittivity during heating (solid lines) and cooling (dashed line) of 0.8BFO (a) and the real part of the AC conductivity (10 kHz) for 0.8BFO and 0.9BFO during heating (b). In (b), the dashed lines show the slope and dotted lines mark temperature ranges of the changing slope. All measurements were performed in synthetic air.

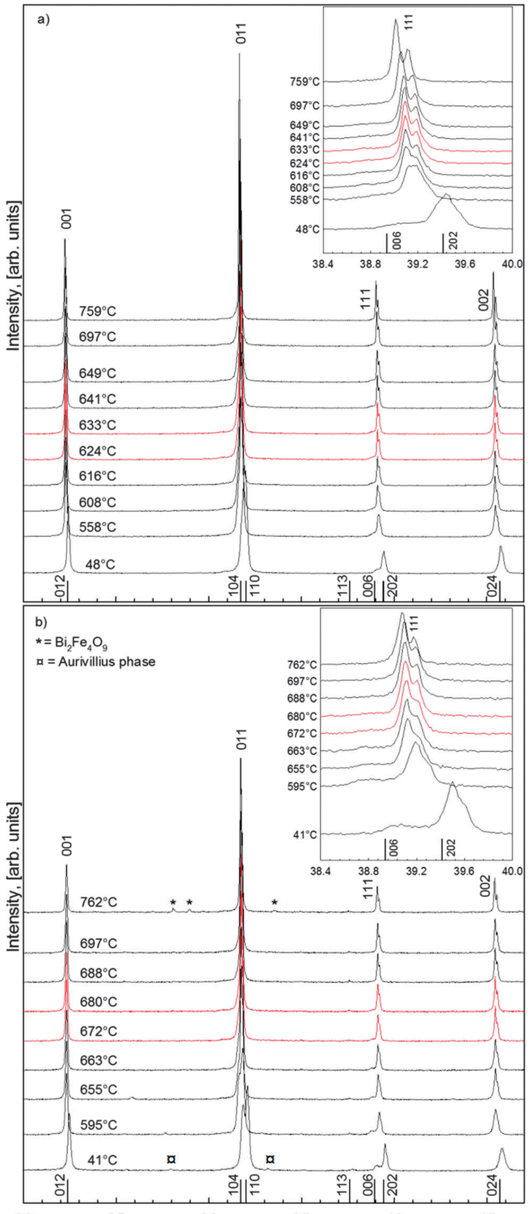

Fig. 5 X-ray diffractograms of 0.8BFO (a) and 0.9BFO (b) at selected temperatures. The vertical bars show the reflections with indices for rhombohedral BFO. The Miller indices above the reflections refer to the cubic symmetry at a high temperature. The phase transition occurs in the temperature range of the red diffractograms (624 and 633 °C for 0.8BFO, 672 and 680 °C for 0.9BFO). The inset shows the 006/202 diffraction lines in detail. The secondary phase (¤) seen at low temperature in 0.9BFO was not present after sintering, but appeared after thermal annealing above T_C prior to the HTXRD analysis.

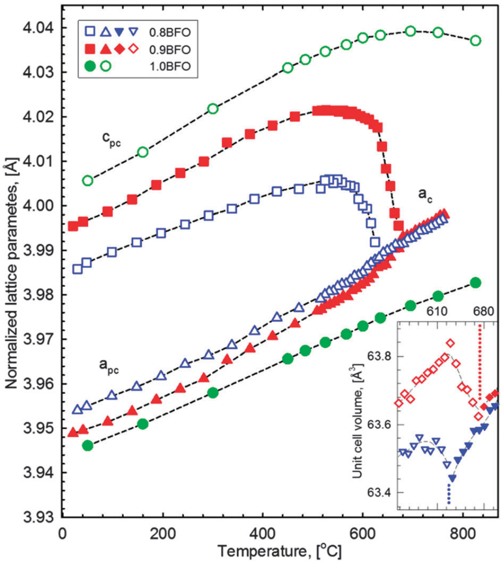

Fig. 6 Refined and pseudo cubic (normalized) lattice parameters for 0.8BFO, 0.9BFO and BFO (1.0BFO).[45] Dashed lines serve as a guide to the eye. The inset shows unit cell volume below (open symbols) and above (filled symbols) the ferroelectric phase transition (marked by dotted lines).

The thermal evolution of the HTXRD diffractograms of 0.8BFO and 0.9BFO is shown in Fig. 5a and b, respectively. Both materials were indexed to the $R3c$ space group from room temperature up to the ferroelectric to paraelectric phase transition temperature. The most pronounced change with temperature is the reduced splitting of the (006) and (202) reflections (inset in Fig. 5a and b). Above the phase transition the diffraction patterns were indexed using the space group $Pm\bar{3}m$. Pure BFO is known to be orthorhombic $Pbnm$ above T_C,[44] but no super reflections due to tilting of the octahedra could be observed and the cubic space group was therefore used. The phase transition temperatures were estimated to be 630 ± 15 °C (0.8BFO) and 676 ± 15 °C (0.9BFO) based on the diffraction data (Table 1).

The thermal evolution of the pseudo cubic unit cell parameters for 0.9BFO and 0.8BFO is compared to the lattice parameters of pure BFO in Fig. 6.[45] The unit cell parameters are normalized as follows: $a_{pc} = 2^{-1/2}\, a_h$ and $c_{pc} = 12^{-1/2}\, c_h$, where pc and h refer to pseudo cubic and hexagonal, respectively. The thermal expansion of a_{pc} and c_{pc} is close to linear far below the phase transition. A strong contraction of the c-axis is evident close to T_C as reported for $BiFeO_3$ due to the ferroelectric to paraelectric phase transition.[44,45] The unit cell volume is discontinuous at the phase transition (inset Fig. 6) demonstrating a 1st order phase transition as reported for BFO.[44,45]

The phase transition of 0.8BFO and 0.9BFO observed by DTA is presented in Fig. 7. An endothermic peak upon heating and an exothermic peak during cooling are clearly evident.

The temperature for the onset of the peaks is included in Table 1 along with the temperature of the peak maximum/minimum. The hysteresis between the heating and cooling curves confirms the 1st order of the phase transition.

4. Discussion

The qualitative behaviour of the electrical conductivity at different $p(\mathrm{O_2})$ for 0.8BFO and 0.9BFO shows great similarities to the properties reported for similar Fe-based perovskite materials.[33–37] The electrical conductivity of these materials has previously been modelled with success by a mass action type treatment of point defect equilibria. A mass action type model adapted for 0.8BFO and 0.9BFO is introduced here based on the approach presented by Mizusaki *et al.*[35] for $\mathrm{LaFeO_3}$. The substitution of $\mathrm{K^+}$ into the A-site and $\mathrm{Ti^{4+}}$ into the B-site of BFO can be seen as acceptor and donor substitution, respectively, resulting in $\mathrm{K}_{\mathrm{Bi}}''$ and $\mathrm{Ti}_{\mathrm{Fe}}^{\bullet}$ as point defects using the Kröger-Vink notation. These two point defects are charge balanced by the K : Ti substitution ratio of 1 : 2, and can therefore be neglected for a first approximation. The point defect chemistry in $(1-x)$BFO–xBKT can, analogous to $\mathrm{LaFeO_3}$, be described by a model based on 5 equations. First, the point defect equilibria related to the volatility of $\mathrm{Bi_2O_3}$ (1), the principle of electro neutrality (2) and the mass balance of Fe (3), are defined.

$$2\mathrm{Bi}_{\mathrm{Bi}}^{\times} + 3\mathrm{O}_{\mathrm{O}}^{\times} \rightarrow 2V_{\mathrm{Bi}}^{'''} + 3V_{\mathrm{O}}^{\bullet\bullet} + 2\mathrm{Bi(g)} + \frac{3}{2}\mathrm{O_2(g)} \qquad (1)$$

$$p + 2\left[V_{\mathrm{O}}^{\bullet\bullet}\right] = n + 3\left[V_{\mathrm{Bi}}^{'''}\right] \qquad (2)$$

$$[\mathrm{Fe}_{\mathrm{Fe}}] = n + \left[\mathrm{Fe}_{\mathrm{Fe}}^{\times}\right] + p \qquad (3)$$

Here, $V_{\mathrm{Bi}}^{'''}$ is Bi vacancy, $V_{\mathrm{O}}^{\bullet\bullet}$ is an oxygen vacancy and n and p are concentrations of electrons and holes, respectively. The electrons and holes correspond to the concentration of $\mathrm{Fe^{2+}}$ and $\mathrm{Fe^{4+}}$ respectively, where the valence of Fe is connected to $p(\mathrm{O_2})$ through the oxidation reactions (4) and (5).

$$V_{\mathrm{O}}^{\bullet\bullet} + 2\mathrm{Fe}_{\mathrm{Fe}}' + \frac{1}{2}\mathrm{O_2(g)} = 2\mathrm{Fe}_{\mathrm{Fe}}^{\times} + \mathrm{O}_{\mathrm{O}}^{\times} \qquad (4)$$

$$V_{\mathrm{O}}^{\bullet\bullet} + 2\mathrm{Fe}_{\mathrm{Fe}}^{\times} + \frac{1}{2}\mathrm{O_2(g)} = 2\mathrm{Fe}_{\mathrm{Fe}}^{\bullet} + \mathrm{O}_{\mathrm{O}}^{\times} \qquad (5)$$

The total electrical conductivity (σ_{tot}) of the material is described by eqn (6)

$$\sigma_{\mathrm{tot}} = \sigma_{\mathrm{ion}} + \sigma_{\mathrm{e}} + \sigma_{\mathrm{h}} \approx ne\mu_{\mathrm{e}} + pe\mu_{\mathrm{h}} \qquad (6)$$

where σ_{ion} is the ionic conductivity, σ_{e} and σ_{h} are the contributions from electrons and holes, respectively, e is the charge of an electron, and μ_{e} and μ_{h} are the mobilities of electrons and holes respectively. For further calculations it is assumed that $\sigma_{\mathrm{ion}} \ll \sigma_{\mathrm{e}}, \sigma_{\mathrm{h}}$. At the $p(\mathrm{O_2})$ corresponding to the minimum in the (σ_{min}) see Fig. 2a and b, the contribution from electrons and holes can be expressed by eqn (7)

$$\frac{\sigma_{\mathrm{min}}}{2} = \sigma_{\mathrm{h}}(\sigma_{\mathrm{min}}) = \sigma_{\mathrm{e}}(\sigma_{\mathrm{min}}) = \left(\mathrm{K}_{\mathrm{i}}'\right)^{0.5} \qquad (7)$$

where $\mathrm{K}_{\mathrm{i}}' = \sigma_{\mathrm{e}} \cdot \sigma_{\mathrm{h}}$. A combination of eqn (6) and (7) allows for determining $\sigma_{\mathrm{h}}(p(\mathrm{O_2}))$ and $\sigma_{\mathrm{e}}(p(\mathrm{O_2}))$. Following this, eqn (6) can be used to determine n and p. The mobility of electrons and holes (Table 2) was adjusted to fit the model, based on the corresponding data reported for $\mathrm{LaFeO_3}$.[23]

Accurate data on the extent of A-site cation deficiency due to evaporation of $\mathrm{Bi_2O_3}$ (and/or $\mathrm{K_2O}$) during solid state reaction and sintering have so far not been determined, but accurate data on the cation non-stoichiometry are critical for further development of the model. Here, an assumption that $V_{\mathrm{Bi}}^{'''} = 0.01$ was introduced based on preliminary data.[46]

The optimized enthalpies for reactions (4) and (5) are listed in Table 2. The Gibbs energy was estimated by assuming that the entropy of the reactions is equal to −130 kJ mol^{-1} as argued by Bakken *et al.*[47]

The model for the conductivity, shown by the dashed lines in Fig. 2, shows that the dominating charge carriers in 0.8BFO and 0.9BFO are electrons or holes. While a positive Seebeck coefficient was measured in oxygen and air, a negative value was measured at low $p(\mathrm{O_2})$ proving the change of the sign of the main charge carrier (Fig. 3). The decreasing Seebeck coefficient with increasing temperature in oxygen and air can be rationalized

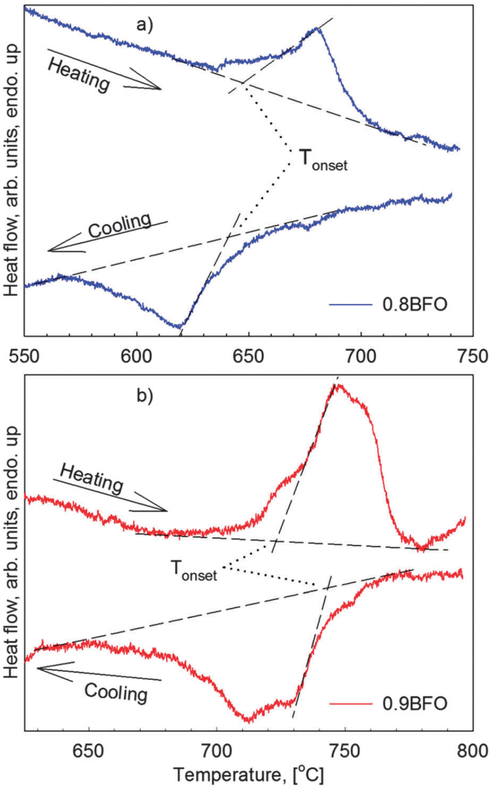

Fig. 7 DTA heat flow signal for 0.8BFO (a) and 0.9BFO (b). The black lines give the determination of T_{onset}.

Table 2 Mobility of electrons and holes respectively used in the point defect model, and thermodynamic data for the point defect reactions for 0.8BFO and 0.9BFO

	Temperature [°C]	μ_e [cm^2 V^{-1} s^{-1}]	μ_h [cm^2 V^{-1} s^{-1}]	$\Delta_r H$ (eqn (4)) [kJ mol^{-1}]	$\Delta_r S$ (eqn (4)) [J mol^{-1}]	$\Delta_r G$ (eqn (4)) [kJ mol^{-1}]	$\Delta_r H$ (eqn (5)) [kJ mol^{-1}]	$\Delta_r S$ (eqn (5)) [J mol^{-1}]	$\Delta_r G$ (eqn (5)) [kJ mol^{-1}]
0.8BFO	700	0.052	0.050	−343	−130	−216	−28	−130	99
	750	0.054	0.074			−210			105
	800	0.056	0.107			−203			112
0.9BFO	700	0.046	0.030	−340	−130	−213	−31	−130	96
	750	0.047	0.063			−207			102
	800	0.056	0.107			−200			109

by a conventional semiconductor behaviour related to the number of charge carriers. The apparent increase of the Seebeck coefficient with temperature at low $p(O_2)$ is not fully understood. The importance of $V_O^{\bullet\bullet}$ in these BFO-rich materials is confirmed by the $p(O_2)$ dependence of the conductivity and the Seebeck coefficient. It is proposed that V_{Bi}''' is also an important point defect, but further work must be carried out to quantify the concentration of the cation vacancies.

The behaviour of the conductivity shown in Fig. 2 illustrates that the sintering atmosphere during fabrication of the ceramics is important for the conductivity, which falls in line with previous reports showing that conductivity can be reduced significantly by annealing in an inert or reducing atmosphere.[21] Although the results presented herein are on BKT substituted BFO, we propose that the present observations give valuable insight into the thermal evolution of the electrical conductivity of bulk pure BFO.[22–25]

The ferroelectric phase transition temperatures of 0.8BFO and 0.9BFO were determined by three different methods in reasonable agreement. The Curie temperature decreases upon decreasing BFO content in $(1-x)$BFO–xBKT as shown in Fig. 8. T_C values for 0.8BFO and 0.9BFO are still high making these materials interesting for high temperature applications. T_C is at the level of pure BKT for $x > \sim 0.4$, where a relaxor-type behaviour has been reported for pseudo cubic $(1-x)$BFO–xBKT solid solutions.[17,21]

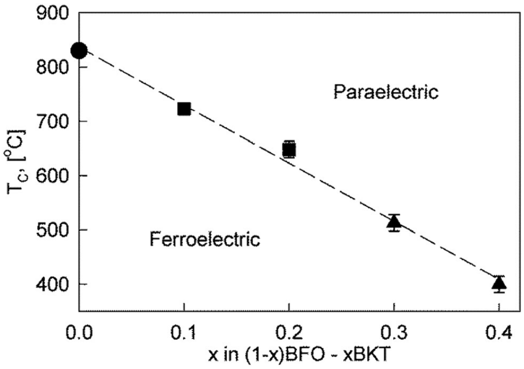

Fig. 8 The Curie temperature as a function of BFO-content in $(1-x)$BFO–xBKT. Squares from this work (DTA), circles[7] and triangles[21] from elsewhere. Dashed line is a guide to the eye.

The relaxation time for the redox driven point defect equilibria can be qualitatively derived from the DC conductivity and thermopower measurements although this was not the primary goal of the experiments. The electrical relaxation for 0.9BFO at 700 °C is shown in Fig. 9a where the normalized conductivity upon switching between O_2 and synthetic air are given as a function of time.

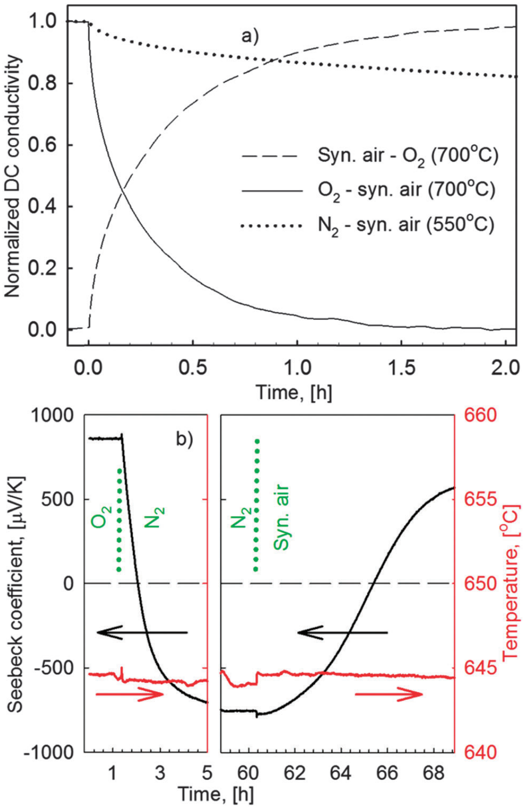

Fig. 9 (a) The relaxation of normalized conductivity upon switching between O_2 and synthetic air at 700 °C for 0.9BFO. Also shown is relaxation upon a shift from N_2 to synthetic air at 550 °C. (b) The material response for the Seebeck coefficient upon switching atmospheres from O_2 *via* N_2 to synthetic air at 650 °C (0.9BFO).

The relaxation time for oxidation and reduction was found to be comparable. Relaxation is an activated process and the relaxation time increases significantly with decreasing temperatures as illustrated by the relaxation curve at 550 °C, also depicted in Fig. 9a. The rapidly increasing relaxation time with decreasing temperature is in good agreement with similar data reported for 0.7BFO–0.3BKT by Morozov *et al.*[20] An important observation is the immediate response from the material to a shift in the atmosphere, even at 550 °C, implying a significant mobility of point defects at temperatures significantly below T_C. Fast relaxation was also observed during measurements of the Seebeck coefficient (Fig. 9b). The figure shows the reversible response going from p-type (in O_2) *via* n-type (in N_2) and back to p-type (in synthetic air) semiconductor behaviour.

The hardness of ferroelectric PZT can be tuned by acceptor and donor substitution,[48,49] and the hardening of acceptor substituted PZT has been explained by defect ordering due to rearrangement of oxygen vacancies.[50] Such ordering has also been studied in *e.g.* $BaTiO_3$ by long term aging at elevated temperatures ($<T_C$).[51] The driving force for point defect ordering and the formation of "defect dipoles" is minimization of electrostatic and probably also elastic energy that arises below T_C. Above T_C the material will have a paraelectric centrosymmetric structure with no driving force for ordering of charged point defects. Below T_C, a spontaneous polarization develops and the point defects will energetically prefer specific sites and form *i.e.* defect dipoles. These ordered defects subsequently act as effective pining centres for domain wall movement.[51] The hard ferroelectric characteristics of BFO have been related to point defects, though the mechanism is not yet clear.[4] Because the T_C of BFO is 830 °C, the driving force for point defect ordering will emerge already at high temperatures ($<T_C$). It is evident from the electrical relaxation curves shown in Fig. 9a that there is a significant oxygen ion mobility at temperatures as low as 550 °C. Since these measurements were performed on bulk materials, the diffusion length scale of the process involving a shift in the conductivity is on an mm scale.[52] The length scale of oxygen vacancy diffusion required for defect dipole formation is only within a unit cell. It is therefore reasonable to assume that oxygen vacancy mobility is sufficient at temperatures much lower than 550 °C. This is important because defect ordering in high T_C materials will start immediately below T_C if the point defects are sufficiently mobile. The high T_C of these materials and the mobility, evidenced by the relaxation data, show that point defect ordering likely occurs in BFO materials, possibly explaining the hard ferroelectric properties reported for these materials.[4]

The unit cell volume of $(1-x)$BFO–xBKT decreases with the addition of BKT, along with a decrease in lattice distortion (c_{pc}/a_{pc}, Fig. 6). The lattice distortions of 1.0BFO,[45] 0.9BFO and 0.8BFO are ~1.015, 1.013 and 1.009, respectively. The large intrinsic lattice distortion (strain) observed for 1.0BFO is one factor contributing to the large piezoelectric response observed. The large strain in BFO may cause problems in the electromechanical performance. The introduction of BKT not only reduces the challenges to secondary phases during synthesis but do also offer the possibility of adjusting T_C as well as the crystallographic strain. $(1-x)$BFO–xBKT becomes pseudo cubic $x > \sim 0.4$ which implies that most of the lattice distortion is suppressed by substitution, hence a low BKT content is preferable.[17] On the other hand, a low polarization and strain response to an applied electric field was observed for $x < \sim 0.4$. This reflects the hard ferroelectric characteristics of BFO making a wider range of applications of BFO as a piezoelectric or ferroelectric material challenging.[10] The understanding of the point defect chemistry presented herein offers a path to understand both hardening of BFO as well as reduction of the electrical conductivity and thereby the dielectric loss.

Finally, we address the relation of the major charge carriers and charged domain walls in BFO.[4,53,54] The conductivity along 71° domain walls has been described as n-type[54] (La-substituted BFO) and the concentration of oxygen vacancies has been shown to influence the domain wall conductivity[53] (pure BFO). The work described herein shows that both p- and n-type behaviour and electrical conductivity can be easily changed by annealing at different partial pressures of oxygen. The point defect equilibria, controlling the valence of Fe, can also be influenced by strain as recently shown for $CaMnO_{3-\delta}$.[55] The thermal processing of BFO, also in the case of BFO thin films, may therefore strongly affect the electrical properties.

5. Conclusions

Minima in the DC electrical conductivity of 0.8BFO and 0.9BFO were observed as a function of $p(O_2)$, which reflects a shift from p-type to n-type conductivity upon decreasing the partial pressure of oxygen. The change in the majority charge carrier was confirmed by the change in the sign of the Seebeck coefficient measured at different atmospheres. The conductivity was successfully described by a conventional mass action type point defect model by using electrons and holes as major charge carriers and oxygen vacancies and A-site vacancies as additional point defects. A high Curie temperature of BFO was retained with the introduction of 10 and 20 mol% BKT, and the ferroelectric to the paraelectric phase was established by a combination of dielectric spectroscopy thermal analysis and high temperature XRD.

Acknowledgements

The Research Council of Norway (FRINATEK project no. 197497/F20) is acknowledged for financial support. We acknowledge discussion concerning the interpretation of the data with Dr Maxim Morozov.

Notes and references

1 European Parliament, *Off. J. Eur. Union*, 2011, **54**(L174), 89.
2 J. Rödel, W. Jo, K. T. P. Seifert, E. M. Anton, T. Granzow and D. Damjanovic, *J. Am. Ceram. Soc.*, 2009, **92**, 1153.
3 G. Catalan and J. F. Scott, *Adv. Mater.*, 2009, **21**, 2463.

4 T. Rojac, A. Bencan, B. Malic, G. Tutuncu, J. L. Jones, J. E. Daniels and D. Damjanovic, *J. Am. Ceram. Soc.*, 2014, **97**, 1993.

5 T. Rojac, M. Kosec and D. Damjanovic, *J. Am. Ceram. Soc.*, 2011, **94**, 4108.

6 D. Lebeugle, D. Colson, A. Forget and M. Viret, *Appl. Phys. Lett.*, 2007, **91**, 022907.

7 R. Palai, R. S. Katiyar, H. Schmid, P. Tissot, S. J. Clark, J. Robertson, S. A. T. Redfern, G. Catalan and J. F. Scott, *Phys. Rev. B: Condens. Matter Mater. Phys.*, 2008, **77**, 014110.

8 S. Selbach, M.-A. Einarsrud and T. Grande, *Chem. Mater.*, 2009, **21**, 169.

9 M. Valant, A. K. Axelsson and N. Alford, *Chem. Mater.*, 2007, **19**, 5431.

10 T. Rojac, M. Kosec, B. Budic, N. Setter and D. Damjanovic, *J. Appl. Phys.*, 2010, **108**, 074107.

11 Y. Hiruma, H. Nagata and T. Takenaka, *Jpn. J. Appl. Phys.*, 2007, **46**, 1081.

12 C. F. Buhrer, *J. Chem. Phys.*, 1962, **36**, 798.

13 Y. Hiruma, R. Aoyagi, H. Nagata and T. Takenaka, *Jpn. J. Appl. Phys.*, 2005, **44**, 5040.

14 E. T. Wefring, M. I. Morozov, M.-A. Einarsrud and T. Grande, *J. Am. Ceram. Soc.*, 2014, **97**, 2928.

15 J. Bennett, A. J. Bell, T. J. Stevenson, R. I. Smith, I. Sterianou, I. M. Reaney and T. P. Comyn, *Mater. Lett.*, 2013, **94**, 172.

16 M. I. Morozov, M.-A. Einarsrud, T. Grande and D. Damjanovic, *Ferroelectrics*, 2012, **439**, 88.

17 M. I. Morozov, M.-A. Einarsrud and T. Grande, *Appl. Phys. Lett.*, 2012, **101**, 252904.

18 H. Matsuo, Y. Noguchi, M. Miyayama, M. Suzuki, A. Watanabe, S. Sasabe, T. Ozaki, S. Mori, S. Torii and T. Kamiyama, *J. Appl. Phys.*, 2010, **108**, 104103.

19 J. M. Kim, Y. S. Sung, J. H. Cho, J. K. Song, M. H. Kim, H. H. Chong, T. G. Park, D. Do and S. S. Kim, *Ferroelectrics*, 2010, **404**, 88.

20 M. I. Morozov, M.-A. Einarsrud and T. Grande, *Appl. Phys. Lett.*, 2014, **104**, 122905.

21 M. I. Morozov, M.-A. Einarsrud and T. Grande, *J. Appl. Phys.*, 2014, **115**, 044104.

22 T. R. Paudel, S. S. Jaswal and E. Y. Tsymbal, *Phys. Rev. B: Condens. Matter Mater. Phys.*, 2012, **85**, 104409.

23 A. S. Poghossian, H. V. Abovian, P. B. Avakian, S. H. Mkrtchian and V. M. Haroutunian, *Sens. Actuators, B*, 1991, **4**, 545.

24 Z. Dai and Y. J. Akishige, *J. Phys. D: Appl. Phys.*, 2010, **43**, 445403.

25 Z. Zhang, P. Wu, L. Chen and J. L. Wang, *Appl. Phys. Lett.*, 2010, **96**, 232906.

26 N. Masó and A. R. West, *Chem. Mater.*, 2012, **24**, 2127.

27 K. Kalantari, I. Sterianou, S. Karimi, M. C. Ferrarelli, S. Miao, D. C. Sinclair and I. M. Reaney, *Adv. Funct. Mater.*, 2011, **21**, 3737.

28 X. D. Qi, J. Dho, R. Tomov, M. G. Blamire and J. L. MacManus-Driscoll, *Appl. Phys. Lett.*, 2005, **86**, 062903.

29 K. Abe, N. Sakai, J. Takahashi, H. Itoh, N. Adachi and T. Ota, *Jpn. J. Appl. Phys.*, 2010, **49**, 09MB01.

30 Y. Wang and C.-W. Nan, *Appl. Phys. Lett.*, 2006, **89**, 052903.

31 M. C. Li and J. L. MacManus-Driscoll, *Appl. Phys. Lett.*, 2005, **87**, 252510.

32 S. Hunpratub, P. Thongbai, T. Yamwong, R. Yimnirun and S. Maensiri, *Appl. Phys. Lett.*, 2009, **94**, 062904.

33 V. L. Kozhevnikov, I. A. Leonidov, M. V. Patrakeev, E. B. Mitberg and K. R. Poeppelmeier, *J. Solid State Chem.*, 2001, **158**, 320.

34 J. Mizusaki, M. Yoshihiro, S. Yamauchi and K. Fueki, *J. Solid State Chem.*, 1985, **58**, 257.

35 J. Mizusaki, T. Sasamoto, W. R. Cannon and H. K. Bowen, *J. Am. Ceram. Soc.*, 1982, **65**, 363.

36 T. Arakawa, S. Tsuchi-ya and J. Shiokawa, *Mater. Res. Bull.*, 1981, **16**, 97.

37 M. Siemons, A. Leifert and U. Simon, *Adv. Funct. Mater.*, 2007, **17**, 2189.

38 I. Wærnhus, P. E. Vullum, R. Holmestad, T. Grande and K. Wiik, *Solid State Ionics*, 2005, **176**, 2783.

39 A. A. Coelho, *TOPAS Academic: General Profile and Structure Analysis Software for Powder Diffraction Data*, Bruker AXS, Karlsruhe, Germany, 2004.

40 S. M. Selbach, T. Tybell, M. A. Einarsrud and T. Grande, *Phys. Rev. B: Condens. Matter Mater. Phys.*, 2009, **79**, 214113.

41 S. M. Selbach, T. Tybell, M.-A. Einarsrud and T. Grande, *Chem. Mater.*, 2009, **21**, 5176.

42 P. V. B. Rao, E. V. Ramana and T. B. Sankaram, *J. Alloys Compd.*, 2009, **467**, 293.

43 T. Yokota, R. Aoyagi and M. Gomi, *J. Ceram. Soc. Jpn.*, 2013, **121**, 675.

44 D. C. Arnold, K. S. Knight, G. Catalan, S. A. T. Redfern, J. F. Scott, P. Lightfoot and F. D. Morrison, *Adv. Funct. Mater.*, 2010, **20**, 2116.

45 S. M. Selbach, T. Tybell, M.-A. Einarsrud and T. Grande, *Adv. Mater.*, 2008, **20**, 3692.

46 M. Christensen, Master thesis, Norwegian University of Science and Technology, Trondheim, Norway, 2013.

47 E. Bakken, T. Norby and S. Stølen, *J. Mater. Chem.*, 2002, **12**, 317.

48 M. I. Morozov and D. Damjanovic, *J. Appl. Phys.*, 2008, **104**, 034107.

49 M. I. Morozov and D. Damjanovic, *J. Appl. Phys.*, 2010, **107**, 034106.

50 A. Chandrasekaran, D. Damjanovic, N. Setter and N. Marzari, *Phys. Rev. B: Condens. Matter Mater. Phys.*, 2013, **88**, 214116.

51 X. B. Ren, *Nat. Mater.*, 2004, **3**, 91.

52 T. Grande, J. R. Tolchard and S. M. Selbach, *Chem. Mater.*, 2012, **24**, 338.

53 J. Seidel, P. Maksymovych, Y. Batra, A. Katan, S. Y. Yang, Q. He, A. P. Baddorf, S. V. Kalinin, C. H. Yang, J. C. Yang, Y. H. Chu, E. K. H. Salje, H. Wormeester, M. Salmeron and R. Ramesh, *Phys. Rev. Lett.*, 2010, **105**, 197603.

54 S. Farokhipoor and B. Noheda, *Phys. Rev. Lett.*, 2011, **107**, 127601.

55 U. Aschauer, R. Pfenninger, S. M. Selbach, T. Grande and N. A. Spaldin, *Phys. Rev. B: Condens. Matter Mater. Phys.*, 2013, **88**, 054111.